Control Designs for Low-Loss Active Magnetic Bearings: Theory and Implementation

A Thesis
Presented to
The Academic Faculty

by

Brian Christopher David Wilson

In Partial Fulfillment
of the Requirements for the Degree
Doctor of Philosophy

School of Electrical and Computer Engineering
Georgia Institute of Technology
April, 2004

Control Designs for Low-Loss Active Magnetic Bearings: Theory and Implementation

Approved by:

Dr. Panagiotis Tsiotras, Advisor

Dr. Nader Sadegh

Dr. Bonnie Heck-Ferri, Advisor

Dr. Thomas Habetler

Dr. David Taylor

Date Approved: 12 April 2004

... to my parents, who taught me the meaning of unconditional love and the value of hard work.

ACKNOWLEDGEMENTS

I would first like to express my appreciation to my advisors, Dr. Bonnie Heck-Ferri and Dr. Panagiotis Tsiotras, for whom I have the utmost respect. They have guided me well on my journey towards professional maturity and have helped me grow as a person. I am very appreciative for all your encouragement and your genuine concern for my future and well-being. I am deeply indebted to you for the considerable and positive influence you have had on my life. In addition, I thank the other Ph.D. committee members Dr. David G. Taylor, Dr. Nader Sadegh, Dr. Paul Steffes, and Dr. Thomas G. Habetler for taking time from their busy schedules to participate in my graduation process. Furthermore, I value the numerous post-lecture conversations with Dr. Sadegh and Dr. Taylor which have greatly expanded my knowledge of control systems design.

I also extend my gratitude to Dr. Jerry Fausz and all the associates at the Air Force Research Laboratories (AFRL) for my opportunity to participate in the 2001 Space Scholars Program. This was a very enriching and rewarding experience in which I had the good fortune to interact with several talented and professional individuals. I would particularly like to thank Dr. Mark Balas, Dr. George T. Flowers, Dr. Robert Fuentes, and Dr. R. Scott Erwin for their camaraderie and advice. In addition to supplying several essential pieces of laboratory equipment and the PREMAG reaction wheel, which is used for experimental validation, Dr. Fausz and AFRL has funded my research efforts from 2001-2004. I further thank Dr. Robert Bartlett and American Flywheel Systems Inc. for their financial support during 1998-2000.

I acknowledge the insightful comments in the preparation of [82] made by Dr. Eric Maslen, Dr. Carl Knospe, and Dr. M. S. de Queiroz. I further thank Dr. Carl

Knospe for providing the high-fidelity AMB Simulink Model.

I am very appreciative of the technical troubleshooting advice that Dr. W. Marshall Leach Jr. provided to me in the construction of the printed circuit board filters. Furthermore, I recognize the contributions of Scott Mosley, Harry Rudd, and Wayne Springfield of the Georgia Tech Aerospace Engineering Machine Shop for the retrofitting work they conducted on my experimental apparatus.

A special thanks is extended to my high school Physics teacher John Burgholzer at Amherst Central High School. His enthusiasm for Physics was infectious and was a source of inspiration during my Junior and Senior year. His good-humored nurturing manner and infinite patience allowed me to unabashedly ask *any* question in the search to satisfy my curiosity. This country is indebted to him and to other teachers like him.

I would like to recognize the efforts of Marilou Mycko and the other dedicated workers in the Electrical Engineering Graduate Office and the Aerospace Engineering Accounting Office. They were always helpful in ensuring that my paycheck arrived at the end of each month. Marilou Mycko in particular, solved countless administrative and scheduling problems for me in addition to providing a warm smile from day one in the otherwise cold academic hallways.

I would like to thank Peter Jackson and George Lucas for making the Lord of the Rings and Star Wars movies. These films kept me company for many uncounted sleepless nights.

This acknowledgement is incomplete until I mention my comrades-in-arms. My laboratory mates Ancil Marshal, David Richie, Haijun Shen, Xiping Zhang, Efstathios Velenis, and Dongwon "Thomas" Jung listened to my problems, successes, and offered advice, even when they probably were not all that interested. My friends Dr. Raye Sosseh and his wife Madeline, Dr. Ben Damiani and wife Jennifer, and Dr. Scott Clements were always there to keep my sanity intact with companionship, advice and

laughter. I would like to personally thank my close friends Dr. James P. Hoffman and his wife Kristen whom I have known since I started my undergraduate education. I don't think I could have made the journey without friends like these.

My family's support throughout my academic endeavors has never wavered. They have shared my successes and their patient ears have been a sanctuary during times of need. I would especially like to thank my brothers who took a keen interest in my work. They would tirelessly ask insightful questions like "Are you finished yet?" and "How long have you been in school?"

And finally, to my wife Bernice and my furry little boy Barley. Your embrace lends me courage and strength, your smile makes me laugh, your determination and passion inspires me, your cooking satisfies me, your dedication to the truth in all things centers me, and your love fulfills me. Through you I'm learning that the most important resources in our life are the people standing right next to us. You are the best thing that has ever happened to me.

My sincere thanks to all of you,

Brian Christopher David Wilson

March 19, 2004

TABLE OF CONTENTS

LIST OF TABLES

LIST OF FIGURES

SUMMARY

This work theoretically develops and experimentally verifies zero- and low-bias control laws that globally asymptotically stabilize an active magnetic bearing (AMB). In addition, the control laws are constructed with the largest domain of definition possible while minimizing the AMB operating losses. AMB losses are minimized by reducing the total square flux required for regulation [35]. This suggests operation with zero-bias (ZB) or low-bias flux (LB). In service of these goals, a flux-based model for a one-degree-of-freedom (1-DOF) AMB is derived using a generalized complementary flux condition (gcfc). This condition is imposed in both ZB and LB modes of operation. A convenient model structure results, in which the ZB mode is a limiting case of the more general LB mode of operation. Nonlinear ZB and LB control laws are developed which stem from the theory of integrator backstepping, feedback linearization, control Lyapunov functions (clf's), and passivity. The standard nonlinear techniques of feedback linearization and integrator backstepping suffer from a singularity in ZB operation which manifests itself as an infinite voltage command. The clf control law also has a singularity in ZB operation, but has a much larger domain of definition than the standard nonlinear techniques. The passivity-based control law is nonsingular. In addition to evaluating the performance of each control design through numerical simulation, they are experimentally verified on a 6-DOF magnetically suspended reaction wheel. Many practical issues such as velocity and flux estimation, flux-bias implementation, gcfc implementation, passive magnetic bearing construction, coil resistance compensation, and signal conditioning have been addressed to successfully implement the nonlinear control laws on the 6-DOF AMB. Theoretical

analysis and experimental results furnish evidence that under typical operating circumstances, the gcfc bias strategy is more efficient in producing the forces required for regulation than the standard constant-flux-sum (cfs) bias scheme. Furthermore, the frequency content of the control signal is used to evaluate operation near the ZB singularity. Large spikes are produced in the voltage control signal when the control law becomes singular. Consequently, the control laws with the smallest domain of definition produce control signals with the largest frequency content. In addition, a trade-off exists between the bearing stiffness, the operating losses, and power consumption as one varies the level of flux bias. Larger bias implies an increase in bearing stiffness, but at the cost of higher operating losses. Interestingly, the power consumption does not necessarily increase with bias. In fact, there are circumstances when operation with large bias consumes less power than when operating with a small bias.

This thesis is organized as follows. Chapter 1 introduces the importance of AMB's in several applications, including the flywheel battery (FWB), the motivating application for the study of low-loss AMB design. It also serves to summarize and criticize the current literature as well as clearly define the goals and contributions of this work. The place this research holds in the development of the multi-disciplinary FWB technology is also outlined. Chapter 2 presents the modelling of the 1-DOF AMB, conducts an AMB power analysis, and summarizes the AMB and FWB power loss mechanisms. Chapter 3 introduces the generalized complementary flux condition (gcfc) biasing scheme and compares it to the standard constant-flux-sum strategy. Chapter 4 gives detailed derivations of several nonlinear ZB and LB control laws. Chapter 5 gives an overview of the experimental apparatus used to verify the control laws presented in Chapter 4. Chapter 6 presents a strategy for flux measurement and verifies the implementation of a flux bias and the gcfc condition. Chapter 7 presents the 6-DOF modelling and decentralized linear control of the magnetically suspended reaction wheel. Chapter 8 presents the experimental verification of the control laws

developed in Chapter 4. Conclusions and future work is outlined in Chapter 9

Several appendices are included: properties of the function $x^{[q]}$, background electromagnetic theory, generation of electromagnetic force, magnetic circuit energy analysis, and filter construction.

CHAPTER I

INTRODUCTION

Bearings are essential components of all rotating machinery. By definition, the bearing is the static part of the machine (often called the stator) that supports the moving part (often called the rotor). While air and fluid bearings may be found in multi-degree-of-freedom ball and socket joint machines, ball bearings, which allow for pure rotation, are by far the most popular. They are widely available, cheap, and can handle very large static loads. However, the most common failures in rotating machinery are ball-bearing failures. For example, such a failure may be due to over-stress from imbalance loads, lubrication thermal breakdown, or lubrication contamination.

Magnetic bearings are an alternative to ball, air, or fluid bearings. Magnetic bearings are constructed from permanent magnets (PM), electromagnets (EM), or combinations of both. Active magnetic bearings (AMB) use stator mounted electromagnets and feedback control to generate forces on the rotor so that it spins without touching the stator. That is, the magnetic bearing is frictionless! In addition, feedback control may actively adjust the system stiffness and damping characteristics to reduce vibrations caused by rotor imbalance. The elimination of lubrication, operation in a vacuum, and the non-contacting nature allows for low-maintenance, long life-span, high-speed bearings. Furthermore, advances in power electronics have resulted in AMB's constructed in compact packages with little external hardware. In spite of the long list of benefits, magnetic bearings do have some limitations that traditional bearings do not. The most fundamental limitations are the electromagnet force saturation (resulting in limited load capacity) and the force slew-rate limits. For further introductory material, see [38, 36, 35], for example.

The next few figures show some examples of magnetic bearing systems. Magnetic bearings typically support two different types of rotors: the elongated shaft type or the flat "pancake" type. Figure 1.1 shows a shaft type rotor supported by two sets of 4-poled[1] AMBs. The most active areas of magnetic bearing research are currently driven by high-speed operation, lower power loss, greater use of the bearing airgap, and disturbance rejection due to rotor imbalance and flexibility [38]. The MBRotor^{TM} test stand is supplied by Revolve Magnetic Bearings Inc. and is useful for studying and controlling the flexible modes of shafts. The motor can spin the rotor up to 15,000 rpm while the AMBs allow for frictionless operation. Each AMB has a backup ("catcher") ball bearing in the case of a failure. The position of the AMBs, the shaft length, and balance disk location can be changed to study the flexible modes of the shaft. This test stand could also be fitted with an additional "thrust" AMB to create forces along the rotor axis.

Figure 1.2 illustrates a "pancake" configuration of a AMB flywheel. This particular AMB flywheel utilizes a conical bearing which provides thrust in the axial direction as well as actuation in the radial direction. Also shown are the radial "catcher" bearings, the vacuum housing, and a rotor made of composite materials. In high-speed flywheel testing, rotors may burst creating an extremely dangerous situation, and therefore require expensive containment systems. When a composite rotor bursts, the energy is dissipated in the shredding of the composite fibers and a safer failure results.

AMB's have enjoyed successful application in many industrial and scientific settings [17]. They have been considered for various applications such as vacuum pumps, hard disk drives, high-speed centrifuges, high-speed turbines, machine tools, voltage

[1]Since electromagnets can only produce an attractive force on a ferromagnetic target, two electromagnets are required per control axis to generate positive and negative forces. Thus 4 electromagnets are required to actuate the horizontal and vertical directions in each of the AMBs shown in Figure 1.1

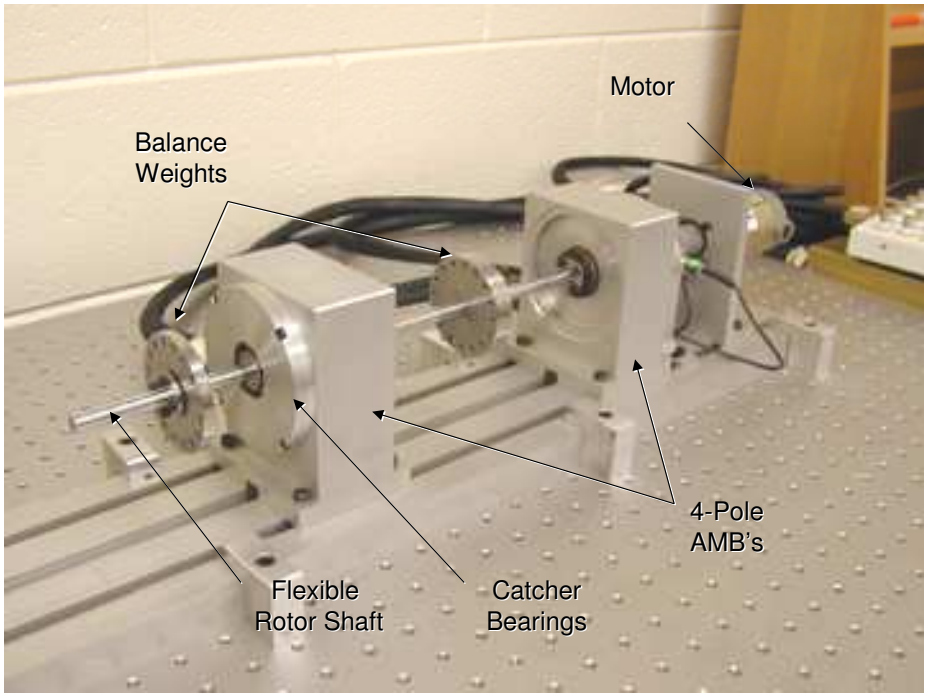

Figure 1.1: The MBRotor^{TM} test stand from Revolve Magnetic Bearings Inc.

regulation, un-interruptible power supplies, magnetic catapults, and magnetically levitated trains. In [79], the suspension of a steel tube is studied as a prototype for a non-contacting industrial processes. For example, in industrial processes such as plastic film production, paper production, coating and painting, it is advantageous to be able to handle the product without directly touching it [79]. A similar application is presented in [68] where magnetic levitation is used in the deployment of spacecraft solar arrays to simulate the weightlessness of space. The use of AMBs in high speed milling (cutting) machines shows great potential for reduction of drill bit chatter and enables high-precision cutting [39, 70]. A heavy-weight industrial application is the use of magnetic bearings in the reduction of propeller-induced vibrations in ship transmission shafts [14]. The lack of lubrication makes magnetically levitated machines especially suitable for "clean" environments. For example, a magnetically suspended stepper motor and magnetic levitation linear motion Silicon wafer transporter have been developed for use in clean-rooms and ultra-high vacuum environments [24, 61].

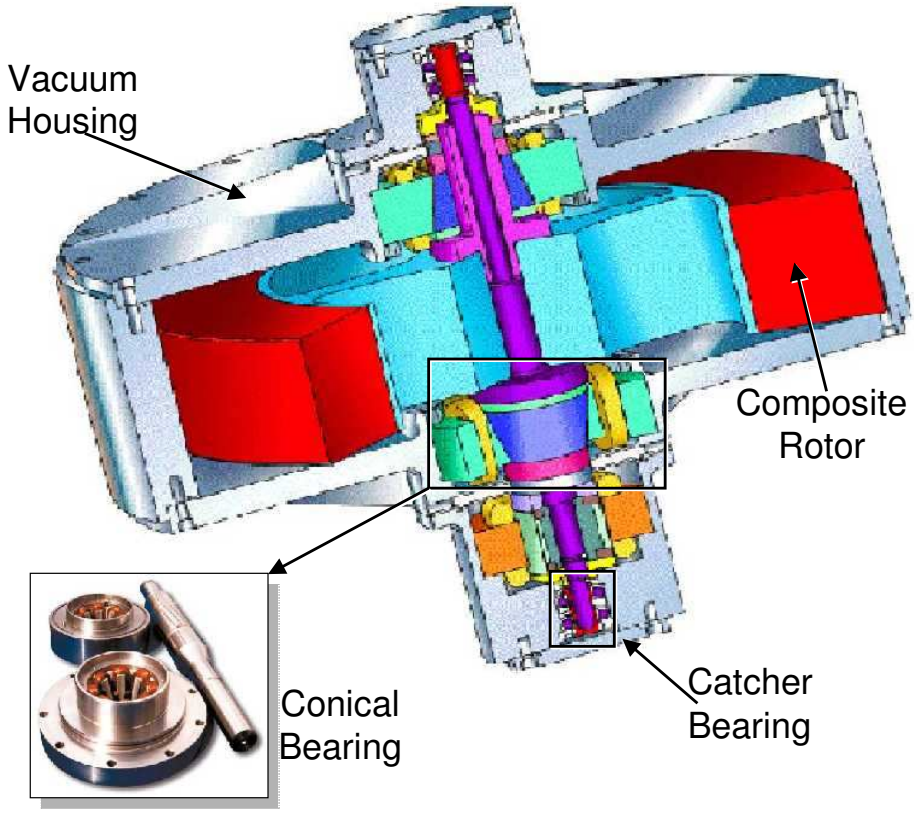

Figure 1.2: This particular bearing utilizes a conical bearing which provides thrust in the axial direction as well as actuation in the radial direction. This figure is courtesy of Dr. Jerry Fausz, Flywheel Program Manager, Air Force Research Labs [19].

One application in particular, the flywheel battery (FWB), serves as the main focus of this research. In the FWB application, kinetic energy is stored in the rotating flywheel and converted back and forth to electrical energy via a motor/generator. Since the axial moment of inertia of the pancake configuration is typically larger than the shaft configuration for a given a rotor mass, the pancake rotor configuration is typically better for energy storage[2]. Note however that the control of a pancake-type rotor is more challenging as the angular velocity increases because the gyroscopic effects are more dramatic [56, 54].

A good introduction to flywheel battery applications may be found in [5, 23]. In

[2]The energy, or "state-of-charge" in a flywheel is $E = 1/2\ I\omega^2$ where I is the moment of inertia and ω is the angular velocity.

addition to having the ability to store energy, a FWB can also deliver high power. That is, it can deliver its stored energy in a short period of time[3]. Figure 1 in reference [5] compares the energy density (Wh/kg) and power density (W/kg) for several competing energy storage technologies. Energy storage technologies such as gasoline and H_2 fuel cells rank among the highest in energy density, but have limited power density and peak power capabilities. On the other hand, super capacitors and AMB flywheel batteries are the highest ranking peak power devices available. Note that AMB FWB has a higher energy density than that of the super capacitor. Existing electric utility companies have used FWB's to augment their ability to meet peak power demands and to improve power quality. In such a configuration, the overall power supply system can be designed to meet lower average power specifications. The energy stored in the FWB is delivered during peak demand hours. A similar use of the FWB has been proposed for the hybrid electric vehicles and military combat vehicles[62, 26]. Another peak power application, for instance, is the Incredible Hulk Roller Coaster at Universal Studios Florida which uses a team electric motors (requiring as much as 6000 amps) and a system of three flywheels (not AMB supported) to launch its riders *up* the lift hill. This type of energy pulse generation has also been suggested for military applications such as a magnetic rail gun used to replace the steam catapult on aircraft carriers [23]. One of the most interesting applications is use of FWBs on spacecraft: for a further discussion see Section 1.1.

Minimization of all AMB operating losses is essential for successful implementation of a flywheel battery. There are several energy dissipation mechanisms that make the AMB enabled FWB application far from efficient. Due to the lack of contact friction and operation in a vacuum, all AMB mechanical losses are eliminated.

[3]The electrical power that the flywheel can deliver is, assuming no loss, equal to the mechanical power $dE/dt = I\omega\dot{\omega} = I\alpha\omega = \tau\omega$. That is, the electrical power delivered by the flywheel depends on the angular velocity and the deceleration torque. In other words, the power capacity of the flywheel depends only on how fast one can change the rotor speed.

Table 1.1: Summary of AMB power losses [35].

Loss	**Relation to flux**
Ohmic power loss in coil	$\propto \Phi^2,\ i^2R$
Eddy-Current Drag power loss	$\propto \Phi^2, \omega^2$
Alternating Hysteresis power loss in core	$\propto \Phi_{max}^{1.5-2.5}$
Rotational Hysteresis power loss in core	$\propto \Phi$
Eddy-Current power loss in core	$\propto \Phi_{max}^2$

However, electromagnetic losses are still significant, especially at high operational speeds. The loss mechanisms include resistive power dissipation, eddy-current core loss, eddy-current drag, and hysteretic core loss. The adjective "eddy-current" is often used imprecisely in the literature. Eddy currents which appear in the EM core are generated by the AC variation of the magnetic flux used for rotor control. Eddy currents are also generated on the surface of a spinning rotor in the presence of a magnetic field. These currents are generated in such a way as to produce a drag force (i.e. proportional to speed) and consequently reduce the angular velocity [2, 89]. In this report, eddy-current loss will refer to core loss and eddy-current drag will refer to the motion induced drag force. Note that eddy-currents generated in the rotor lead to rotor heating, and consequently, thermal expansion of the rotor and degeneration of the nominal airgap. This can lead to a decrease in bearing stiffness complicate the control design. Observe that even though the AMB eliminates all mechanical losses, the eddy-current drag reduces the angular velocity of the rotor. Consequently, the "charge" or energy stored in the mechanical FWB dissipates with time. As Table 1.1 shows, each[4] of the electromagnetic power losses are proportional to the square of the flux required by the bearings. Often a bias flux (or current) is introduced into the electromagnets to increase the bearing stiffness, $\Phi = \Phi_0 + \phi$. Thus, minimization of the flux bias Φ_0 (or current bias) when used is imperative for designing efficient AMB's for flywheel batteries.

[4]Rotating hysteresis is not significant in the FWB problem.

The control of an AMB *with low-loss design in mind* is not a trivial problem. In a customary AMB control design, a large flux (current) bias is introduced into the electromagnets to linearize the nonlinear force-flux (force-current) characteristic. Instead of a standard Jacobian linearization approach, a biasing scheme called the "normal" or "constant flux (current) sum" is typically used [46, 47, 48]. A *global* linearization of the force nonlinearity is achieved by a novel input transformation: a bias is introduced into both electromagnets and a net force is generated by adding a control flux (current) to one electromagnet while subtracting the same control flux (current) from the opposing electromagnet. Once the system is linearized, any convenient classical or modern linear control technique may be used to provide closed-loop stability. A large flux (current) bias – often one third to one half of the saturation flux (current) of the electromagnets – is used to provide adequate bearing stiffness. However, since electrical losses are directly proportional to the flux bias, operation with very small or zero flux bias is imperative for efficiency. As will be seen in the sequel, reduction of the flux bias to zero results in an *uncontrollable* linearization. This is due to the fact that the AMB exhibits a dead-zone-like characteristic for zero-bias (ZB) operation which results in a reduced force slew-rate capability [47, 53, 4]. Thus, ZB operation requires one to deviate from classical approaches and investigate *nonlinear control techniques*.

ZB operation of the AMB is implemented with *complementary* strategies which completely eliminate the flux (or current) bias. Since current and flux depend on each other, either one may be used as the electrical state. When using current, this strategy is called the complementary current condition (ccc). When using flux, it is called the complementary flux condition (cfc). In these methods, a constraint is imposed on the operation of the opposing electromagnets that constitute a control axis of the AMB. Along a given control axis, only one electromagnet at any given time is allowed to pull on the rotor. That is, one electromagnet is turned off while

the other is active. In this way, power is saved because the opposing electromagnets do not fight each others efforts to accelerate the rotor in a given direction.

Standard nonlinear control techniques, such as feedback linearization (FBL) and integrator backstepping (IB), suffer from a singularity in ZB voltage-amplifier mode. This singularity manifests itself as an infinite voltage command when the control flux is zero [8, 7, 15, 45]. This singularity arises from the dead-zone-like characteristic that the force-flux nonlinearity has when operated in ZB. As a means to alleviate the force slew-rate limitations of the ZB designs, a *new* bias scheme called the *generalized complementary flux condition* (gcfc) is introduced which allows for a flux bias while at the same time keeps the power-saving switching strategy of the cfc bias scheme. Note that this bias improves the bearing stiffness and removes the singularity but at the cost of increased electrical system losses. Thus, it is typical that a low-bias (LB) will be implemented.

Note that when the bias is reduced to zero, the gcfc bias scheme coincides with the cfc bias scheme. Consequently, control laws developed for LB operation will realize a ZB implementation when the flux-bias is reduced to zero. There are applications where one may desire a time-varying bias level to meet changing system requirements or perhaps to optimize some performance index. While this thesis does lay the groundwork for a time-varying bias implementation, the selection of an optimal bias policy is deferred to future research. For these reasons, the ZB mode of operation is revisited with the goal of removing the singularity from the control laws. To this end, a *new* control algorithm based on the theory of control Lyapunov functions (clf) is constructed that has a larger domain of definition than the standard nonlinear techniques in ZB. Even better, a *new* passivity-based control design is developed that is completely nonsingular in ZB.

The performance of the AMB depends on the flux bias. Performance is measured in terms of bearing stiffness, power consumption and power losses. Bearing stiffness

refers to the rate of change of the closed-loop actuator force with respect to a change in position. It is closely related to the controller's ability to regulate the rotor against disturbances. The power consumption of the bearing is measured as the electrical power supplied to the bearing $V_{app}I_{coil}$ where V_{app} is the voltage applied across the coil and I_{coil} is the current through the coil. This power supplied is consumed in three ways: (1) it produces the control forces, (2) it implements the bias flux, or (3) gets dissipated as heat in one of the previously mentioned loss mechanisms. As the bias increases, bearing stiffness increases, the power required to implement the bias increases, and the loss mechanisms dissipate more power. However, the corresponding increase in bearing stiffness reduces the amount of power required to implement the control forces. Thus, the total power consumption may actually decrease as the bias increases. Therefore, a trade-off exists between the bearing stiffness, the power consumption, and power losses.

The above control techniques are studied extensively through simulation and their applicability to real-world AMBs is verified by experimental testing on a 6-DOF, magnetically suspended AMB flywheel. This apparatus is illustrated in Figure 1.3. It was originally constructed by Precision Magnetic Bearings Systems, Inc. (PREMAG) [64] for use by the Air Force Research Laboratories (AFRL) as a light-weight magnetically suspended reaction wheel for a small satellite. It is passively supported in the vertical z direction and a motor built into the hub of the rotor provides the z axis rotation. Horizontal regulation of the rotor position away from the housing is achieved by two sets of four electromagnets stacked on top of each other. The stacked electromagnet configuration allows for regulation of the rotor tilt about the horizontal axes. For simplicity, the rotor regulation is implemented with four independent SISO control laws instead of one MIMO control law. Furthermore, three of the four horizontal control axes are implemented with standard linear controllers with servo-amplifiers operating in current-mode. The fourth axis operates in voltage-mode and serves as

the test bed for the nonlinear control validation.

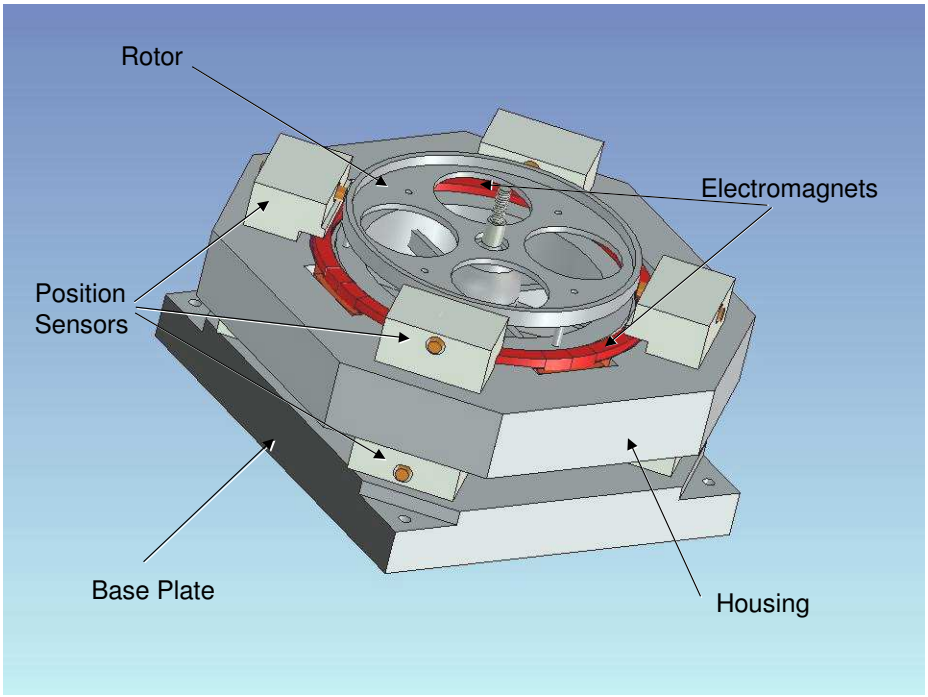

Figure 1.3: Illustration of the PREMAG magnetically suspended reaction wheel [64].

Experimental implementation of the control laws requires one to address several practical issues. The control laws are synthesized using Matlab, Simulink, the Real Time Workshop/Interface, and a dSPACE 1103 A/D control board. By selecting a sampling rate in the range of $6-10$kHz, the control laws are considered continuous and explicit discretization of the equations of motion of the system is not required. In this work, for reasons to be stated in the sequel, the flux is selected as the electrical state, however measurement of flux in the magnetic bearing is a nontrivial problem. The solution used here is to construct a flux-lookup table in terms of the measured current and position. This lookup table is the key in the implementation of the voltage-switching gcfc constraint and the generation of a flux bias via an auxiliary feedback loop. Precise implementation is ensured by proper signal conditioning. Compensation of the coil resistance is also employed. Finally, measurement of velocity is obtained through a bandwidth-limited differentiation of the position signal.

1.1 Connection to Larger Research Effort

The development of fundamental space component technology, such as the Active Magnetic Bearing (AMB), plays an important role in support of the goals of the NASA Mission plan. These goals include discovering the interactions of distant galaxies, probing the structure of the universe, and understanding the evolution of the solar system. However, the degree to which these questions can be answered depends heavily on the capabilities of the available measurement technology. Thus, investment in new technologies is essential for NASA's progress. NASA also aims to transfer their discoveries and the advanced technologies to the larger satellite communications and aerospace community. To achieve these goals, the NASA Office of Space Science (OSS) has devised a Strategic Plan [87] which identifies several *key capability* areas where improvement is needed. These areas include Advanced Power and On-Board Propulsion as well as Sensor and Instrument Component Development. Advanced energy storage techniques are required to support more capable instrumentation and longer missions. New multi-spectral sensors and improved precision instruments are required to probe the mysteries of deep space. However, the measurement capabilities of any sensors developed are limited by vibration noise transmitted to the sensor by spacecraft.

The use of AMB's in support of flywheel technology directly contributes to these two key capability areas. AMB FWBs have been proposed to *combine the functions of the attitude control and energy storage subsystems* of satellites. Such an Integrated Power and Attitude Control System (IPACS) is projected to save $30\% - 50\%$ of the satellite weight as well as double the mission lifespan [19, 67]. Furthermore, the reduced subsystem weight makes room for larger instrument payloads (larger telescopes, for instance). Moreover, the AMB's can be used to reduce or eliminate the vibration caused by spinning flywheels on the spacecraft, thus, achieving greater pointing accuracy of the scientific instruments (i.e. telescope, spectrometer, antenna,

etc.). For an introduction to flywheel batteries for space applications, see [12, 78, 65, 67, 66] and the references within.

In addition, FWBs store energy more efficiently than the current state-of-the-art chemical batteries. Chemical batteries suffer from a limited number of charge/discharge cycles and a limited discharge depth and discharge rate [5, 23]. In other words, chemical batteries are better at energy storage than power storage. Also, the "state-of-charge" of a chemical battery is not directly measurable. To compensate for these drawbacks, the chemical batteries are typically oversized at the cost of added weight. On the other hand, the high power density of AMB-enabled flywheel batteries and recent advances in power electronics have resulted in construction of compact flywheel batteries that have little external hardware, weigh less, and have less volume than the conventional Nickel Hydrogen batteries. To be competitive with the energy densities provided by chemical batteries, the flywheels must spin at very high speed (at the order of 60-100K rpm).

An additional impediment to the successful application of an IPACS system is the fact that the stator of the AMB moves with the body of the satellite. This complicates matters because the rotor tends to maintain its orientation due to its gyroscopic dynamics. If the AMB lacks the sufficient stiffness in its design, then the possibility exists for a collision of the rotor and the stator when the spacecraft changes its attitude rapidly, i.e., during a slew maneuver. However, the disturbance rejection capability and stiffness of the bearing depend on the level of the flux-bias used during operation. A larger bias level produces better bearing stiffness but at the cost of increased electrical losses in the AMB. Conceivably, the IPACS application is one which may have changing control system design requirements. During station keeping the bias should be low (maybe zero) to minimize energy losses. However during a mission critical maneuver, the bias should be increased to produce the required bearing stiffness.

The NASA Flywheel Development Program is jointly led by offices at NASA Glenn and NASA Goddard and has partners at the Air Force Research Labs (AFRL). This research is expected to culminate in a combined energy storage and attitude control ground demonstration on the ASTREX[5] experimental platform at AFRL sometime in 2004.

1.2 Current Literature on Zero- and Low-Bias Control

This brief literature review is by no means an attempt to summarize all of the literature on AMB control and instead highlights the work on zero- and low-bias nonlinear control designs. The following authors have realized the excessive power consumption with large-bias classical linear designs and have concentrated on nonlinear zero-bias designs. In particular, a comparison between linear and nonlinear functioning has been investigated by Charara et al. [7, 8] and Smith and Weldon [73]. Charara reports power consumption figures from an experimental apparatus acted on by linear large-biased and nonlinear zero-biased controllers. Nonlinear control schemes show dramatic power savings (on the order of 90%) over the linear control schemes. Zero-bias input-output linearization has been studied by several authors [7, 8, 73, 55], and [50]. Also, Lin and Knospe in [49] have studied nonlinear saturation designs based on feedback linearization and using a high gain velocity observer. Sliding mode controllers have been investigated in [8, 77] and [10]. Lévine et al. [45] developed an alternative zero-bias control method by studying the system's differential flatness properties. Yang et al. in [90] and [91] studied optimal control designs for zero-bias AMB's.

These zero-bias control laws for the AMB share a common drawback. Specifically,

[5]ASTREX is the Advanced Space Structures Technology Research EXperiment at AFRL used to investigate spacecraft dynamics.

a singularity manifesting itself as an infinite voltage command appears when the flux (or current) is zero [8], [50]. Many authors take an ad hoc approach to avoiding the singularity. For example, in [8], a small constant is added to the denominator of the control law so that a zero flux (or current) condition does not produce an infinite control effort (a divide by zero in calculation of the control law). Dawson and de Queiroz applied the integrator-backstepping method to a 2-DOF model in [15] and to a 6-DOF model in [16]. In their efforts to obtain a smooth control law, which is essentially the same as avoiding the zero-flux singularity, a small parameter was added into the control law to guarantee smoothness. The introduction of this small parameter inadvertently produced a low-bias control scheme. The smoothness of the control law and the level of the bias-current is directly related to the value of this small parameter. Using an approach based on backstepping and periodic learning control, Costic et al. in [13] have attempted to address periodic disturbance rejection.

One of the first papers to intentionally introduce a small bias into a nonlinear design to alleviate the force slew-rate limitations is [37]. In [37], Knospe and Yang developed a gain-scheduled, H_∞ control scheme by using a linear parameter varying description of the plant. In addition, Tsiotras and Velenis studied similar low-bias control of AMB's subject to saturation constraints in [81].

1.3 Contributions of this Thesis

This thesis offers *new theoretical and experimental results* to the current body of literature on low-loss AMB design. These contributions are summarized as follows:

- **Flux Feedback:** Flux-feedback in itself is not new [1], however its use in the new gcfc condition is essential. There are several advantages to using flux as the electrical state. Flux-based AMB models can accurately predict the actuator forces even when the electromagnets operate in saturation, as is often the case with the AMB. Furthermore, force/flux-based actuator models are less

susceptible to the eddy-current effects that may corrupt a force/current-based model. Along with the decision to use flux as the electrical state comes the task of measuring the flux. This thesis uses a straight forward actuator modelling technique that does not require closed-loop control to construct a lookup table that relates flux to the measured position and measured coil current. The resulting lookup table models the actuators into their saturation region, captures the effect of a changing inductance with rotor position, models the variation in flux-saturation knee with airgap, and is able to reproduce the flux, including its DC component. This enables the use of flux-feedback for control design, for flux-bias realization, and for the switching implementation of the new gcfc bias scheme.

- **A New Bias Scheme:** A flux-based model of an AMB is derived using the *new* generalized complementary flux condition (gcfc) biasing strategy. The gcfc scheme is constructed with the intent to take advantage of the power saving switching strategy of the cfc scheme, while at the same time allowing for the introduction of a flux bias into the electromagnets to increase the bearing stiffness and remove the ZB singularity. An internal flux-feedback PI control loop using voltage-mode amplifiers is employed to implement the flux bias. The practicality of the new gcfc bias scheme is evaluated on the PREMAG reaction wheel. The flux-dependent voltage switching rule which implements the gcfc condition is experimentally verified in open- and closed-loop situations. This switching rule requires relatively clean flux measurements. Consequently, significant filtering of the current and position signals is needed. Most importantly, theoretical analysis and experimental results furnish evidence that under typical operating circumstances, namely low-bias, the gcfc bias strategy is more efficient in producing the forces required for regulation than the standard constant-flux-sum (cfs) bias scheme.

- **Zero-Bias Singularity Removal:** ZB control is revisited with the goal of mitigating the ZB singularity. A new class of control laws, based in the theory of control Lyapunov functions and passivity, are proposed and are valid in both ZB and LB modes of operation. These control laws, when operating in zero-bias, are either singularity-free or have a region of singularity that is much smaller than the one using standard methods. This is experimentally verified by considering the frequency content of the control signals in ZB. It is found that control laws with larger singularity spaces produce voltage control signals with large bandwidths.

- **Flux-Bias Studies:** The trade-off between power consumption, power dissipation and bearing stiffness is experimentally illustrated for each control law as a function of the control gains and the flux bias employed. A power flow analysis illustrates the important difference between power dissipation and power consumption. The power consumption refers the total power required to operate the bearing while power dissipation is the portion of the power supplied that gets wasted as heat. For each control law, the bearing stiffness, the total rms square flux required for regulation, and consequently, the power dissipation increase with flux bias. On the other hand, the rms control flux decreases with increasing flux bias. Interestingly, there are instances in which the total power consumption is reduced by increasing the flux bias.

- **Groundwork for Time-Varying Flux-Bias Implementation:** The flux bias implementation employs flux-feedback and a simple PI control to regulate the flux bias $\Phi_0(t)$ to a desired setpoint Φ_{0des}. However, nothing in this implementation precludes the use of a time-varying desired flux reference $\Phi_{0des}(t)$. Such a flux reference may be adjusted to meet changing performance objectives as in the IPACS application or may be selected to optimize a given performance

index. For example, since there exists a tradeoff between bearing stiffness, power dissipation, and power consumption, an optimal flux bias value or trajectory may be found minimize the power consumption. Determination of such an optimal flux bias trajectory is deferred to future research, but this work provides the mechanisms for its implementation when it is found.

- **Practical Issues Addressed:** Every experiment requires the solution of several practical issues. The PREMAG reaction wheel posed several technical difficulties. The original configuration of the PREMAG reaction wheel employed NdFeB permanent magnets to implement a radial flux bias and energize the airgap for passive vertical rotor support system based on a minimum reluctance design. However, this obstructed the study of low-loss control algorithms and removal of the permanent magnets was required. A new passive magnetic bearing vertical support system was constructed. Other practical issues include the use of a bandwidth-limited differentiation scheme for velocity estimation, tuning of the IR compensation scheme to match amplifier responses, and signal conditioning.

1.4 Thesis Overview

This thesis is organized as follows. Chapter 2 presents the modelling and power analysis of the 1-DOF magnetic bearing. In particular, it is illustrated that the power dissipation mechanisms of the AMB and FWB are proportional to the square of the flux. Furthermore, the distinction between power dissipation and power consumption is made.

Chapter 3 introduces the new gcfc biasing strategy and compares it with the normal cfs biasing. A static analysis is conducted in which two AMB's implementing the gcfc and the cfs compete to produce a desired force. It is shown that under typical operating conditions, the gcfc requires less flux to generate the required force than the

cfs. That is, the gcfc is more efficient (i.e. it has less operating losses) in generating the required force than the cfs in several instances. Also, a brief discussion shows how the gcfc fits into the current family of biasing schemes used in the literature.

Chapter 4 discusses ZB and LB control designs for a 1-DOF AMB. A nondimensionalized state-space equation is defined as a matter of convenience. The goal of the control design is to find a control input u which renders the origin of the system asymptotically stable on the largest domain of definition possible. The standard techniques of feedback linearization and integrator backstepping are studied to illustrate the singularity in ZB. A control Lyapunov function (clf) based control law is developed as an improvement on the standard backstepping technique. The clf control law has a singularity space that is much smaller than that of the backstepping control law. Furthermore, several passivity-based control laws are developed which are completely nonsingular. These control designs are evaluated through simulation.

Chapter 5 introduces the PREMAG 6-DOF reaction wheel and the hardware required to operate it. The initial configuration of the PREMAG reaction wheel was unsuitable for low-loss AMB control design. Permanent magnets provided a constant radial flux bias and also provided the mmf to energize the passive vertical support system which was based on a minimum reluctance design. The permanent magnets were removed to allow for low-loss AMB studies, however, this eliminated the passive vertical support. Therefore, a new passive magnetic bearing was constructed to provide vertical support. Also discussed is the detailed operation of the Copley 412 power servo-amplifiers, the use of IR compensation, the sensor measurements, and signal conditioning.

A discussion of the competing flux measurement techniques is found in Chapter 6. The flux-current-position lookup table method is selected for the PREMAG AMB so that the DC component of the flux may be estimated. The construction of this

lookup table is presented in detail. Given the ability to measure a DC flux, a flux-feedback PI control loop is employed to implement the flux bias. The calculation of the flux bias errors, $e_b = \Phi_{0des} - \Phi_0(t)$, is critical in this technique. Finally, it is experimentally verified that a flux-dependent voltage switching rule implements the gcfc condition even in the presence of sensor noise. Furthermore, it is shown that the gcfc condition is sensitive to improper IR compensation tuning.

Chapter 7 presents the 4-DOF modelling and decentralized linear control of the PREMAG reaction wheel. In actuality, the PREMAG bearing has 6-DOF, however, the axial translation is passively controlled and the axial spin is controlled by a DC motor constructed within the hub of the rotor. The other 4-DOF are the horizontal translations and the tilting about the horizontal axes. The rotor is stabilized by regulating the translations to the $x = y = 0$ and the tilting $\theta_x = \theta_y = 0$. Equivalently, the airgaps on each side of the rotor may be regulated to the nominal airgap g_0. Two models, one based on rotor tilt and translation and the other based on rotor airgaps, are presented to gain insight into the coupling of the degrees-of-freedom of the rotor and the control axes. A decentralized control scheme is presented where the MIMO coupled system is controlled with 4 independent SISO control axes. A classical Lead+PI control scheme is employed on each axis. For time and simplicity, three of the four control axes employ linear control with amplifiers acting in current mode with a large current bias. The fourth control axis uses a voltage-mode amplifier with IR compensation and is employed as a test bed for the low-loss control designs derived in Chapter 4.

The experimental validation of the low-loss control laws is presented in Chapter 8. Aside from the standard regulation, step response, and frequency response methods used to evaluate controller performance, a "whirl" test is conducted. The "whirl" test is a situation where the rotor is regulated to a setpoint while regulating against

a persistent sinusoidal disturbance. This test allows one to measure the control performance in terms of bearing stiffness, the magnitude of the rms control signal, the rms value of the total flux, and the rms power consumption for several values of the flux bias and controller gains. It is found by comparing the passivity-based control law using the gcfc condition to a linear control law using the cfs constraint that the gcfc condition outperforms the cfs condition under typical operating circumstances.

Finally, this work is summarized and directions for future work are posed in Chapter 9. The gcfc condition implements a constant flux bias. However, the implementation of the flux bias via a flux-feedback loop allows for a time-varying reference bias. Therefore, one may choose a time-varying flux bias to meet changing system performance specifications or to optimize a performance index. For example, one may be able to select an optimal bias to minimize the power consumption. Furthermore, issues related to mutual inductance, adaptive IR compensation, nonlinear flux observer designs, MIMO control designs, and several others may be addressed in the future.

This document assumes that the reader is familiar with the basic electromagnetic definitions of inductance, reluctance, flux, etc. For readers with a limited background, a comprehensive appendix presents the basic electromagnetic concepts that apply to magnetic bearings. Furthermore, appendices on the Lorentz equation and energy analysis of magnetic circuits provide the tools required to analyze the forces generated by most magnetic actuators. Other appendices include properties of the function $x^{[q]}$ and filter construction.

CHAPTER II

1-DOF AMB MODELLING AND POWER ANALYSIS

In this work, a 1-DOF AMB refers to an opposing pair of electromagnets that actuate a rotor in a given direction. Typically, groups of 1-DOF AMBs are used to support a rotating shaft or a wheel as in Figures 1.1 and 1.2. The PREMAG 6-DOF reaction wheel shown in Figure 1.3, which is used for experimental validation, employs four 1-DOF AMBs for stabilization of the rotor horizontal translation and tilting[1]. The full dynamic modelling of this 6-DOF apparatus is presented in Chapter 5. However, the essence of the behavior is captured by the dynamics of the 1-DOF AMB. In fact, the control designs detailed in the following chapters assume that the complex MIMO, coupled behavior of the PREMAG reaction wheel may be modelled by four independent SISO, 1-DOF models. Thus, the control of the AMB begins with the study of 1-DOF AMB models.

Modelling of a 1-DOF AMB is discussed in the next section. The AMB dynamics appear in a variety in forms in the literature. The representation of the electrical dynamics, the constraints imposed on the operation of the electromagnets, and the inclusion of rotor modes produces a variety of different AMB models. The AMB model used in this work is clearly delineated. Section 2.2.1 illustrates the instantaneous power flow in the AMB FWB application. The loss mechanisms are detailed in Section 2.2.2. It is shown that the AMB power losses are minimized if the square of the flux required for stabilization is minimized.

[1]The axial translation is passively controlled and the axial spin is controlled by a motor controller amplifier.

2.1 1-DOF AMB Dynamics

Figure 2.1 shows a simple schematic of a one-degree-of-freedom AMB. This simplified

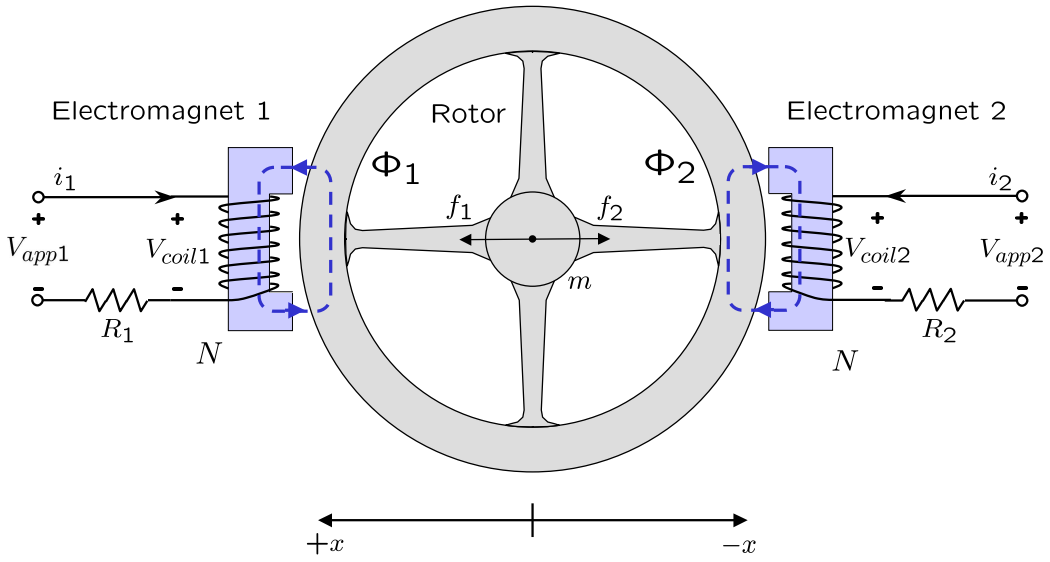

Figure 2.1: A simplified schematic of a 1-DOF AMB with gravity neglected. To regulate to $x = 0$, the electromagnet voltage inputs V_{app1} and V_{app2} or the currents i_1 and i_2 are adjusted to vary the forces f_1 and f_2 acting on the rotor. Φ_j is the total flux through the j^{th} electromagnet.

AMB model consists of two electromagnets used to move the rotor in one dimension. It is assumed that all motion occurs in the x direction. To regulate the position of the rotor to $x = 0$, the control designer adjusts the forces f_1 and f_2 acting on the rotor via the electromagnets. In the most general form, the mechanical dynamics are

$$m\ddot{x} = y_m \tag{2.1a}$$

$$\dot{x}_m = A_m x_m + B_m F \tag{2.1b}$$

$$y_m = C_m x_m + D_m F \tag{2.1c}$$

$$F = [f_1, f_2, f_{dist}]^T \tag{2.1d}$$

where the x_m subsystem is used to represent the flexible modes of the rotor. The input to the flexible mode subsystem is the force vector which consists of the electromagnet forces and a disturbance force f_{dist}. The output of the flexible mode system is the

scalar y_m and is viewed as a filtered version of the force input. When the rotor is considered rigid, as it is in this study, the mechanical dynamics simplify to

$$m\ddot{x} = f_1 - f_2 + f_{\text{dist}} \tag{2.2}$$

This equation coincides with equation (2.1) with $C_m = 0$ and $D_m = [1,\ -1,\ 1]$.

The disturbance force may be constant, synchronous with the rotor angular velocity ω, or completely general. A constant disturbance force might arise from the rotor's own weight ($f_{\text{dist}} = mg$), for example. Synchronous disturbances are due to rotor imbalance, which is typically exacerbated by large angular velocity: $f_{\text{dist}} = f_0\omega^2\sin(\omega t)$. A general disturbance force might arise from a load that changes with time, for instance. In this work, gravity is perpendicular to the active control axes and is not explicitly considered. Furthermore, since the low-loss control algorithms may be verified without spinning the rotor, imbalance disturbance is also ignored[2].

The symbols $V_{coil\,j}$, R_j, i_j, and Φ_j in Figure 2.1 represent the coil voltage, the coil resistance, the coil current, and the total flux of the j^{th} electromagnet, respectively. N is the number of turns in each coil. The applied voltage V_{appj} of the j^{th} electromagnet is typically supplied by a power servo-amplifier. These amplifiers operate in *voltage mode* or *current mode*. In voltage mode, feedback is used to ensure that $V_{\text{app}}(t)$ tracks a reference voltage $V_r(t)$. In current mode, the voltage $V_{\text{app}}(t)$ is adjusted so that $i(t)$ follows a reference current $I_r(t)$. Thus, the input signal into the electrical subsystem is arbitrary. Since more interesting control algorithms result from voltage-mode operation, the following dynamics assume that a voltage-mode servo-amplifier is employed.

The coil dynamics are derived from Faraday's and Kirchhoff's voltage laws (kvl). Note that the physical coil is modelled by an ideal coil (no resistance) in series with a resistor that represents the distributed coil resistance. Of course, this is a lumped

[2]The "whirl test", as described in Chapter 8, approximates AMB operation with rotor imbalance.

parameter model and one can not actually consider the coil without considering its resistance as well. Moreover, there is always a voltage drop across the coil resistance and consequently, the voltage V_{coil} that appears across the ideal coil must be inferred through knowledge of the applied terminal voltage V_{app} and the IR drop or by other means[3]. By kvl,

$$V_{\text{app}} = I_{\text{coil}}R + V_{\text{coil}} \tag{2.3}$$

the *ideal* coil voltage is related to the rate of change of the flux by Faraday's law, $V_{\text{coil}} = N\dot{\Phi}$. Thus, the coil dynamics are given by

$$V_{\text{app}} = I_{\text{coil}}R + N\dot{\Phi} \tag{2.4}$$

Since there is a (generally nonlinear) relationship between the current through the coil and the generated flux, one may choose the current or the flux as the electrical state and eliminate the other variable in equation (2.4). This nonlinear relationship is governed by a hysteresis curve and is discussed in detail in Appendix B.3. Note however, that in magnetic circuits with airgaps, the airgap reluctance often dominates the reluctance of the core. Consequently, the hysteresis nonlinearity is less dramatic and is well-approximated with a saturation-like, airgap-dependent function $\Phi = h(Ni, g)$: see Figures B.13 and B.14. Furthermore, if the core is not excited into its saturation region, an airgap-dependent inductance may be assumed and the linear relationship between the current and the flux may hold $N\Phi = L(g)i$. In this research, a lookup table is constructed to model the flux-current-rotor position relationship $\Phi = h(Ni, x)$: details of the construction of this lookup table are given in Chapter 6. It is important to realize that for any description of the core nonlinearity, equation (2.4) always holds true.

Since current is easily measurable, it is often used as the electrical state. However, there are several advantages of using the electromagnet flux instead of the coil current

[3]Measurement of the AC portion of the ideal coil voltage is possible with the use of a search coil. See the flux measurement discussion in Chapter 6.

to predict the forces produced by electromagnets. Example D.3 in the appendices shows that the electromagnet force[4] on a target is given by

$$f = \frac{\Phi^2}{\mu_0 A_g} \tag{2.5}$$

$$f = \mu_0 A_g N^2 \frac{i^2}{(\frac{\ell_c}{\mu_r} + 2g)^2} \tag{2.6}$$

where μ_0 is the permeability of free space, μ_r is the relative permeability of the core, A_g is the airgap cross-sectional area, ℓ_c is the length of the core, and g is the airgap length. Equation (2.6) is considered standard in the literature and often the ℓ_c/μ_r term in the denominator is neglected because μ_r is large. This equation is popular because the current i and the airgap g are easy to measure. Note that if the core nonlinearity is neglected by assuming $Ni = \mathcal{R}(x)\Phi$, these two equations are the same for the reluctance $\mathcal{R}(x)$ given in the appendix Example D.3.

In reality, the electromagnet force saturates because the core has a finite saturation flux density B_{sat} and a corresponding $\Phi_{\text{sat}} = B_{\text{sat}} A_c$. Although equation (2.6) models the force saturation with respect to g (i.e. the force is finite when $g = 0$), it does not model force saturation with respect to current. Thus, the force is represented in a more realistic manner by equation (2.5) and a description of the flux-current-position relationship $\Phi = h(Ni, x)$. This representation is convenient because the force-flux nonlinearity (Φ^2) and the nonlinear relationship between the current, rotor position, and flux $h(Ni, x)$ may be considered separately. Alternatively, one could use direct measurements of Φ in conjunction with equation (2.5), however, this often proves difficult: See the discussion on flux measurement in Chapter 6.

Further advantages of using the flux to describe the force are presented in detail by F. J. Keith in his Ph.D. thesis [32]. In that work, he maps the force-current and force-flux relationships directly on several test electromagnets. This is accomplished

[4]The negative signs have been dropped because it is known that the electromagnets always have attractive forces. Recall that magnetic force is always produced in the direction to reduce the reluctance. In the case of an electromagnet, it always pulls in the direction to reduce the airgap.

by measuring the the current directly, the force generated on a target beam by a strain gauge, and the flux via an integrating search coil[5]. He demonstrates that the force-flux relationship is unaffected by eddy currents in the EM core. In other words, the force predicted from the force-flux relationship matches the actual (measured) force when eddy currents are present, however, force-current relationship must be altered. Furthermore, since the force-current relationship of equation (2.6) implicitly assumes operation in the linear portion of the magnetization curve, it can not predict the force properly when the EM operates in saturation. The force-flux relationship can accurately model the behavior into saturation. In addition, Keith claims that the slew-rate of the force-flux model is less sensitive to hysteresis effects than the force-current model. Aside from the advantages claimed in [32], an additional advantage is that dissipativity theory, used in the closed-loop stability analysis of the magnetic bearing in Chapter 4, is directly applicable to the sector nonlinearity[6] of the force-flux equations.

In general, the saturation flux Φ_{sat} depends on the airgap as well as the material's properties: this relationship is discussed at length in Appendix B.3.3. The force-flux relationship is sometimes modified to reflect the variation of Φ_{sat} with airgap. In this case, the force is given by

$$f = \frac{\varphi_a^2}{\mu_0 A_g}$$

where φ_a is called the *airgap flux* and is related to the magnetic circuit flux φ by

$$\varphi_a = \rho(g)\varphi, \qquad \rho(g) = \frac{1}{(\rho_1 + g\rho_2)}$$

This phenomenon is sometimes called "flux-spreading". The function $\rho(g)$ typically has values in the range $\rho(g) \in [.5, .95]$ and the constants ρ_1 and ρ_2 are found empirically. In some cases, a drop in the saturation knee is modelled, but the dependence on g is neglected. In this situation, a leakage constant β_{leak} is used and $\varphi_a = \beta_{\text{leak}}\varphi$. This

[5]The use of an integrating search coil is described in Chapter 6

[6]For the pertinent sector nonlinearity definitions, see [34, 69], for example.

constant typically has a value of about 0.75. Note that in this work, a flux-current-position lookup table is constructed to represent $h(Ni, x)$. Thus, the flux-saturation knee "softening" is incorporated into the lookup table.

Chapter 5 details the operation of the power servo-amplifiers used in voltage and current mode. In current-mode operation, the feedback present in the servo-amplifier ensures that the coil current $i(t)$ follows a reference current $I_r(t)$. This is true for any I_r within the bandwidth of the current-mode amplifier. This effectively eliminates the dynamics of the coil and equation (2.4) is not needed. To generate a desired force f_{des}, the corresponding required flux Φ_{des} is generated by assigning the appropriate current. This is calculated using the flux-current-position lookup table, $I_r = h^{-1}(\Phi_{\text{des}}, x)$ and $\Phi_{\text{des}} = (\mu_0 A_g f_{\text{des}})^{1/2}$.

When the coil is driven in voltage mode, the servo-amplifier constrains $V_{\text{app}}(t)$ to follow a reference voltage $V_r(t)$. This is true for any V_r within the bandwidth of the voltage-mode amplifier. The desired force and the corresponding desired flux, are generated by controlling the $\dot{\Phi}$ through V_{app} in equation (2.4). However, $\dot{\Phi}$ is not directly assignable because of the IR drop present. The coil voltage, $V_{\text{coil}} = V_{\text{app}} - IR$, that appears across the ideal coil may be drastically different than the applied voltage V_{app}, even for a reasonably small resistance (i.e. $R = 0.5\Omega$): See the illustrations of the $RI(t)$ drop in Figure B.8. To remedy this difficulty, one may let $V_r^* = I\hat{R} + V_r$. Using this IR *compensation* approach, the coil dynamics have the form

$$N\dot{\Phi} = -IR + V_{\text{app}} = -I(R - \hat{R}) + V_r \tag{2.7}$$

where $R \gtrsim \hat{R}$. The term $I(R - \hat{R})$ is negligible when $\hat{R}$ is properly selected. Note that this approach requires a good estimate of R and that this estimate $\hat{R}$ must not be greater than R. If this was the case, then the flux could grow large even if the voltage input is turned off ($V_r = 0$). Indeed, when $R < \hat{R}$ and I is positive, then $\dot{\Phi}$ is positive even when the voltage input is grounded. Thus, care must be taken not to destabilize the voltage-mode amplifier by improper selection of $\hat{R}$: See Chapter 5 for

a detailed discussion.

In summary, the form of even a simple 1-DOF AMB model appears in great variety in the literature. Different choices for the electrical state are made by different authors. Researchers often choose the electromagnet coil current as the state in order to obtain a model with easily measurable signals. On the other hand, if one selects the electromagnet flux as the electrical state, as in this development, the structure of the nonlinearities in the model are clearly visible and the overall state equations are simpler. However, since flux is not readily measurable for AMB systems, one is implicitly agreeing to solve a state-observation problem when using flux. The dynamic equations for the 1-DOF AMB in this work are collected below:

$$m\ddot{x} = c(\Phi_1^2 - \Phi_2^2), \qquad c = \frac{1}{\mu_0 A_g} \tag{2.8a}$$

$$\begin{aligned} N\dot{\Phi}_j &= -R_j i_j + V_{appj} = -I_j(R_j - \hat{R}_j) + V_{rj} \\ &\approx V_{rj}, \qquad j = 1, 2 \end{aligned} \tag{2.8b}$$

Note that equation (2.8b) assumes that IR compensation is properly implemented. An additional source of variety in the AMB models in the literature is due to the use of different flux-bias schemes. A different equation-of-motion results each time the constraints of a particular flux-bias scheme are imposed on the electromagnet actuators. Several bias schemes are discussed in Chapter 3, but first, the AMB operating losses are studied.

2.2 AMB and FWB Power Analysis and Loss Mechanisms

As stated in Chapter 1, the flywheel battery (FWB) application of the AMB motivates one to study low-loss AMB design. In the FWB application, the frictionless nature of the AMB is exploited to levitate a spinning rotor. In such a device, the kinetic energy stored in the rotor is $W = \frac{1}{2} I\omega^2$, where I is the rotational inertia and ω is

the angular velocity. Note that angular velocity of the flywheel battery is equivalent to the "state of charge" in a chemical battery[7]. A highly efficient motor-generator is required to convert the kinetic energy to electrical energy. On first inspection, since operation in a vacuum and the frictionless nature of the AMB eliminates the mechanical losses, the state of charge of the FWB does not appear to decay. Thus, the FWB seemingly has an efficiency equal to that of the motor-generator employed. However, a loss known as an eddy-current drag (sometimes referred to as eddy-current damping or eddy-current braking) is present and is exaggerated with strong magnetic fields and at large angular velocities: recall that specifications for FWB in space applications call for rotational speeds on the order of $60 - 100$ krpm. Thus, the AMB eliminates mechanical losses, but introduces electromagnetic losses. Furthermore, the power analysis of the FWB device must consider the power required to implement the control law in addition to the energy stored in the flywheel. Since the FWB is proposed to be employed in situations where energy is limited, (on spacecraft for example) low-loss operation is vital. A full energy/power analysis of the AMB FWB application is conducted in the next section and the power dissipation mechanisms are detailed in Section 2.2.2.

2.2.1 AMB and FWB Power Analysis

Note that the power consumption and power loss (dissipation) of the AMB and the FWB are distinct quantities. The power consumption refers to the total external power supplied to the system. The power supplied to the system is converted to useful work (i.e. creating the control forces), used to increase the energy stored in the magnetic field (i.e. increases the bias), or is wasted as heat. Power loss or power dissipation refers to the wasted energy. To further clarify these concepts, a full energy/power analysis of the FWB application is warranted.

[7]Note that the state-of-charge in a chemical battery is not necessarily known because the internal resistance of the battery may change with time.

Energy analysis begins with identification of the lossless energy storage mechanisms of the process under question. At first glance, this approach seems crippled because real systems have losses. For example, a coil has a distributed coil resistance that can not physically be removed from the coil. However, a coil is often modelled by an *ideal* coil with a resistor connected at the ideal coil's terminals. Thus, identification of lossless processes is not as limiting as it sounds[8]. The energy storage elements of the FWB and AMB are the rotational inertia I_a of the rotor, the rotor mass m, and the magnetic field.

The energy stored in the flywheel battery is purely kinetic and it is supplied by a DC motor. The rotational dynamics of the FWB are

$$I_a\dot{\omega} = \tau_m - p\tau_{\text{drag}} \tag{2.9}$$

where τ_m is the supplied motor torque, τ_{drag} is the eddy-current drag torque, and p is the number of electromagnet poles[9] interacting with the rotor. Multiply the rotational dynamics by ω to find the power. Since

$$I_a\dot{\omega}\omega = \frac{d}{dt}(\frac{I_a}{2}\omega^2)$$

the left hand side of (2.9) (multiplied by ω) represents the rate of change of the kinetic energy $W_R := 1/2I\omega^2$ of the rotor. Thus, the power of the flywheel is governed by

$$\dot{W}_R = \tau_m\omega - p\tau_{\text{drag}}\omega \tag{2.10}$$

The motor supplies external mechanical power to the flywheel $\tau_m\omega$ and the power dissipated by the flywheel is due to the eddy-current drag $\tau_{\text{drag}}\omega$.

The energy related to the rotor translation is found in a similar manner. The

[8]For a further discussion of the Energy/Power analysis method, see Appendix D.
[9]$p = 8$ for the PREMAG bearing.

1-DOF equation-of-motion for the rotor is

$$\begin{aligned} m\ddot{x} &= (f_1 - f_2) - f_{\text{air}} && \text{(2.11a)} \\ &= (f_{c1} + f_{b1} - f_{c2} - f_{b2}) = (f_{c1} - f_{c_2}) + (f_{b1} - f_{b2}) - f_{\text{air}} && \text{(2.11b)} \\ &= f(\phi) + (f_{b1} - f_{b2}) - \mu_{\text{drag}} P_{air}(v) && \text{(2.11c)} \end{aligned}$$

The electromagnets operate with a flux bias: $\Phi_1 = \Phi_0 + \phi_1$ and $\Phi_2 = \Phi_0 + \phi_2$ where Φ_0 is the flux bias and ϕ_j is a control flux. The air resistance $f_{air} = \mu_{\text{drag}} P_{\text{air}}(v)$ is modelled as a drag coefficient μ_{drag} times a polynomial in the rotor velocity $P_{\text{air}}(v)$. Each actuator force f_j is decomposed into a bias term f_{bj} and a control term f_{cj}. By using a biasing scheme introduced in the next chapter, the control forces may be grouped into $f(\phi) = 2\Phi_0\phi + \phi|\phi|$ where $\phi = \phi_1 - \phi_2$. To find the translational power, multiply equation (2.11) by v. Since,

$$m\ddot{x}\dot{x} = \frac{d}{dt}(\frac{1}{2}mv^2)$$

the left hand side of (2.11 c) (multiplied by v) represents the change in translational kinetic energy of the rotor $W_T := \frac{1}{2}mv^2$. Thus, the translational power of the rotor is governed by

$$\dot{W}_T = f(\Phi_0, \phi)v + c(f_{b1} - f_{b2})v - \mu_{\text{drag}} P_{\text{air}}(v)v \qquad (2.12)$$

When the bias flux is implemented properly, $f_{b1} = f_{b2}$, the mechanical power supplied to the rotor by the bias vanishes. However, the bias does influence $f(\Phi_0, \phi)$ and therefore, affects the mechanical power flow fv into the rotor's translational kinetic energy. By operating in a vacuum ($\mu_{\text{drag}} = 0$), there is no power loss due to air damping.

The magnetic field of each electromagnet is assumed to be lossless. That is, assume that the electromagnets are ideal and there are no core losses. The resistive coil loss and the nonlinear magnetic core loss are accounted for by adding external "resistive" components to the lossless magnetic field. The energy stored in each magnetic field

is

$$W_m(x,\Phi) = \frac{1}{2}\mathcal{R}(x)\Phi^2$$

where $\mathcal{R}(x)$ is the reluctance[10]. The rate of change of the stored magnetic energy is

$$\dot{W}_m(x,\Phi) = \frac{\partial W}{\partial x}\dot{x} + \frac{\partial W}{\partial \Phi}\dot{\Phi} \tag{2.13a}$$

$$= -fv + \mathcal{R}(x)\Phi\dot{\Phi} \tag{2.13b}$$

where the definition of the force in terms of the partial derivative of the stored energy is used: see Table D.2. Equation (2.13 b) states that the mechanical power generated by the electromagnet reduces the stored energy and the second term (to be analyzed next) increases the stored energy. At this point, one may account for the core losses. The power losses in the electromagnetic core p_{core} will reduce the energy stored in the magnetic field. Thus, the power in the magnetic field is governed by

$$\dot{W}_m + fv + p_{\text{core}} = \mathcal{R}(x)\Phi\dot{\Phi}$$

Using "Ohm's law" for magnetic circuits $NI = \mathcal{R}(x)\Phi$, the above becomes

$$\dot{W}_m + fv + p_{\text{core}} = NI\dot{\Phi} \tag{2.14}$$

The power in the electrical dynamics is found by multiplying Equation (2.4) by I,

$$V_{\text{app}}I = I^2R + NI\dot{\Phi}$$

Finally, one obtains the energy dynamics of the magnetic field by plugging the above into Equation (2.14)

$$\dot{W}_m = V_{\text{app}}I - I^2R - p_{\text{core}} - fv \tag{2.15}$$

The energy stored in the magnetic field produces the mechanical power fv and is dissipated as heat in the coil resistance I^2R and the core p_{core}. External power is supplied to the magnetic field by $V_{\text{app}}I$.

[10]All of the pertinent electromagnetic definitions and energy relations may be found in the Appendix.

The power flow of the flywheel battery is illustrated in Figure 2.2. Each energy storage element is shown as a one-port or two-port network so that polarity of the inputs may be indicated. The energy storage elements (the magnetic fields and the inertia of the rotor) are shown in thick boxes. The function $h(I, x)$ is used to convert from current to flux. The power dissipation elements (resistance, core loss, and drag force) are illustrated with rounded boxes. The power supplied to each element is calculated by multiplying the variables at each terminal. For example, the power supplied to the coil is $V_{\text{app}}I$ and the power supplied to rotor is fv (translational) and $\tau_m\omega$ (rotational).

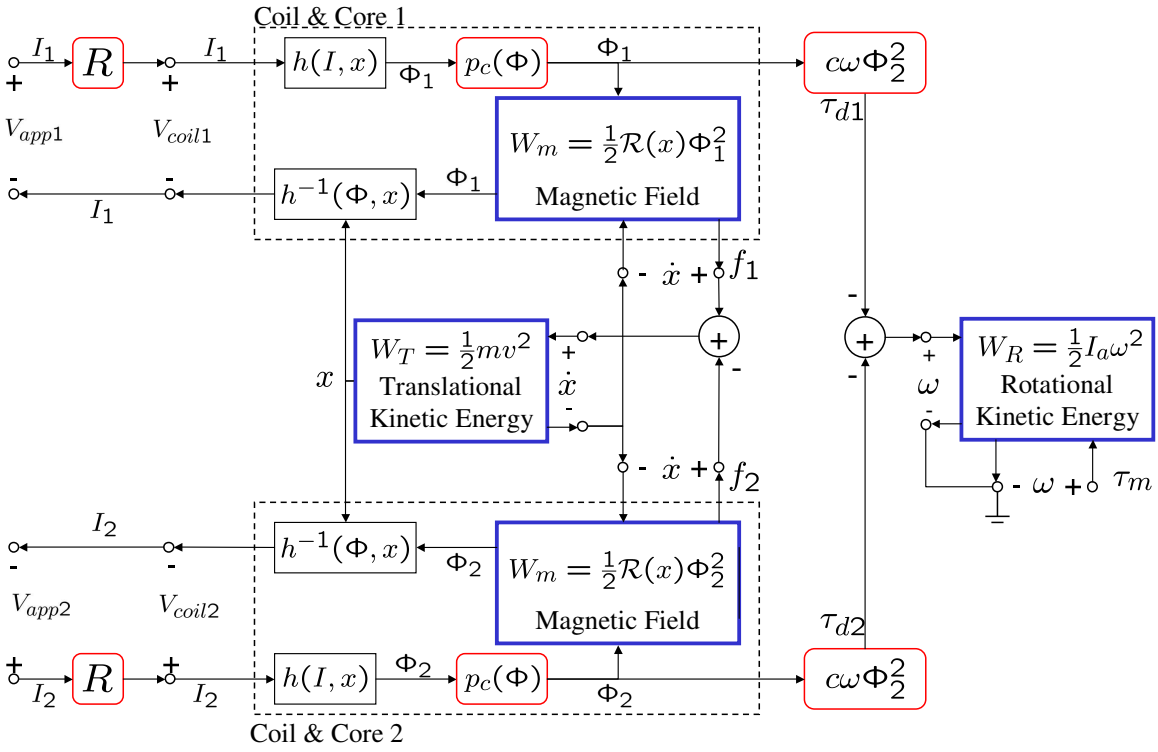

Figure 2.2: Power flow diagram of Flywheel Battery system: Energy is stored in the magnetic fields $W_m = \frac{1}{2}\mathcal{R}(x)\Phi^2$, the rotor mass $W_T = \frac{1}{2}mv^2$, and the rotor inertia $W_R = \frac{1}{2}I_a\omega^2$. Power is dissipated in the resistance I^2R, the core $p_{\text{core}}(\Phi)$, and by the drag torque $\tau_d = c\omega^2\Phi^2$ (shown in rounded boxes). Power is supplied at the terminals of each device $V_{\text{app}}I$ and $\tau_m\omega$.

The Copley 412 amplifiers acting in voltage mode with IR compensation force the applied voltage V_{app} to track V_r. This is true at least for reference signals within the

bandwidth of the voltage mode power servo-amplifiers (about 200Hz). The reference voltage applied to the amplifier is

$$V_r = V_c + V_b + I\hat{R}$$

where the terms V_c, V_b, and $I\hat{R}$ are the control, bias, and IR compensation components of the reference voltage. In this case, the power flow equation becomes

$$\dot{W}_m = V_c I + V_b I - I^2(R - \hat{R}) - p_{\text{core}} - fv \tag{2.16}$$

Thus, the reference voltage supplies the power required to implement the control and the bias, $V_c I$ and $V_b I$, respectively. Furthermore, the $I\hat{R}$ term acts to replenish the energy dissipated by the coil resistance.

In summary, the electrical power loss consists of the Ohmic power loss I^2R and the core loss p_{core}. The mechanical power loss is due to the eddy-current drag $\tau_{\text{drag}}\omega$. The external power required to operate the bearing (i.e. the power consumption) is $V_{\text{app}}I$. The next section takes a closer look at each power dissipation mechanism. It is shown that each dissipation method is related to the square of the bearing flux and that efficient operation of the AMB FWB is obtained by minimizing the bias flux Φ_0. Note however, that the value of Φ_0 that minimizes the power loss does not necessarily minimize the power consumption. These are slightly different issues. If one aims to minimize power consumption, then the total power supplied to the bearing is the quantity to be minimized by the proper choice of Φ_0. Alternatively, the goal of minimizing the power loss is to maximize the percentage of the supplied power that is employed for useful work. The first problem aims to minimize the energy required for operation while the second problem aims to increase the bearing efficiency.

2.2.2 AMB and FWB Loss Mechanisms

The AMB loss mechanisms are now discussed. As seen in Table 2.1, the AMB power loss consists of ohmic losses, electromagnetic core losses and eddy-current drag losses.

Table 2.1: Summary of AMB power losses [35].

Power Loss	Relation to flux
Ohmic loss in coil	$\propto \Phi^2,\ i^2R$
Eddy-Current loss in core	$\propto \Phi^2$
Alternating Hysteresis loss in core	$\propto \Phi_{\max}^{1.5-2.5}$
Rotational Hysteresis loss in core	$\propto \Phi$
Eddy-Current Drag loss	$\propto \Phi_{\max}^2, \omega^2$

Ohmic power loss refers to the resistive dissipation of currents flowing through the coil. The power loss is $I(t)^2R$. Since $NI = \mathcal{R}(x)\varphi(t)$, the resistive power dissipation is also proportional to the square of the flux. The resistive power dissipation can be significant, especially when a bias current or flux is introduced into the electromagnet to increase the bearing stiffness.

The electromagnetic core loss, consisting of eddy-current and hysteresis loss, is discussed in detail in Appendix B.3.2. As a consequence of Faraday's law, eddy currents are generated in the core by the AC variation of the core flux. Although the eddy-current loss is combated by a laminated core construction, large bias fluxes or currents can contribute significantly to eddy-current core loss. The eddy-current power loss under sinusoidal current excitation is determined by equation (B.18) and is repeated here

$$p_e = K_e(fB_{\max}t_\ell)^2 \qquad [W/m^3]$$

where f is the excitation frequency, $B_{\max}$ is the peak core flux density, and t_ℓ is the thickness of the laminations used to construct the core. The constant K_e depends on the conductivity of the material. The eddy-current power loss is proportional to the square of the magnitude of the flux.

Alternating hysteresis core loss refers to the standard hysteresis core loss. It arises from the fact that it takes energy to realign the magnetic domains in the core material. Equation (B.21) describes the hysteresis power loss due to a sinusoidal excitation

$$p_h = K_h f(B_{\max})^q \qquad [W/m^3]$$

where f is the excitation frequency, $B_{\max}$ is the peak flux density, K_h is a material-dependent constant, and q is an empirically determined constant usually in the range of $1.5 - 2.5$. Rotating hysteresis loss may not be significant in all types of electromagnetic machinery, but is mentioned here for completeness. This mode of hysteretic core loss is similar to alternating hysteresis, but arises from a change in the orientation of the magnetic circuit as opposed to a change in the excitation mmf. Note that manufacturers typically supply data about the total core loss $p_{\text{core}} = p_e + p_h$.

The eddy-current drag force arises from the motion of the rotor in the magnetic field. The origin of this drag force is essentially the same as the drag force produced in the linear generator of appendix Example C.3.

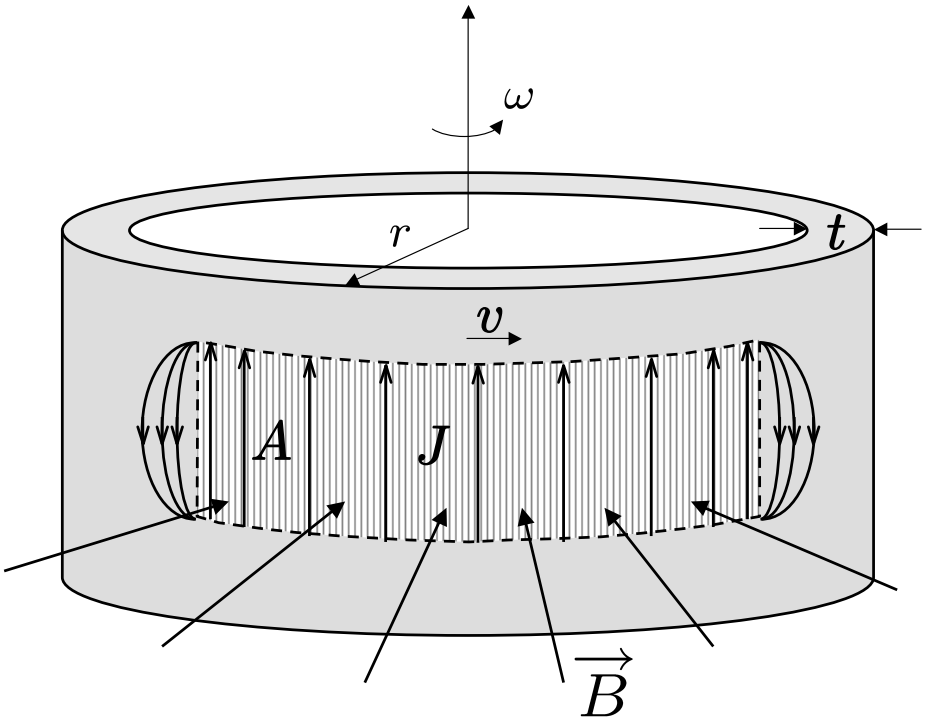

Figure 2.3: Geometry of rotor for eddy-current drag calculation.

Consider the rotor of thickness t, radius r and angular velocity ω shown in Figure 2.3. An external magnetic field B is produced by an electromagnet which has a footprint with cross-sectional area A. The B field is normal to the surface of the rotor at every point in the electromagnet shadow A. By equation (C.1), the free

charges in the rotor feel a Lorentz force upward $F_e = qv \times B$ which simplifies to qvB because v and B are always perpendicular. At every point in A, the resulting current density J points upwards. At the edges of A, the current flows downwards resulting in a roughly circular, eddy-current pattern [2, 33, 89].

The current density of the rotor is

$$J = \sigma E$$

where σ is the conductivity and E is the induced electric field. The electric field is related to the motional emf ξ by

$$E = \frac{d\xi}{dz}$$

where z represents the axial direction. To find the motional emf, proceed as in appendix Example C.3. Since voltage is the work per unit charge $\xi = W/q$, and the work required to move an electron upwards by the Lorentz force is $W = F_e z$, the differential induced emf is

$$d\xi = \frac{dW}{q} = \frac{F_e dz}{q} = \frac{qvB}{q} dz$$

Consequently, the induced electric field is $E = vB$ and the resulting current density is

$$J = \sigma v B$$

The drag force is produced from the interaction of the upward induced current density and the external magnetic field. By the right hand rule, the drag force opposes the motion of the rotor. Equation (C.6) gives the volumetric force density felt by the part of the rotor under the shadow A. Thus, the total drag force felt by the rotor is

$$f_{\text{drag}} = \text{Volume}(J \times B) = tAJB = tA\sigma B^2 v = \frac{t\sigma}{A}\Phi^2 v \tag{2.17}$$

and the drag torque is $\tau_{\text{drag}} = r f_{\text{drag}}$. Since power is $\tau\omega$, the power loss due to eddy-current drag is

$$p_{\text{drag}} = \tau_{\text{drag}}\omega = tA\sigma B^2\omega^2 = \frac{t\sigma}{A}\Phi^2\omega^2 \tag{2.18}$$

Thus, the drag force and power loss are proportional to the square of the electromagnet flux $\varphi^2 = A^2B^2$. Furthermore, the drag force and power loss increase with angular velocity. Recall from Len's law that the induced eddy currents will produce their own magnetic field B_e and this field will always oppose the applied external field B. For low-speed operation, the eddy-current produced B_e field is small. However, as the speed increases, B_e significantly counteracts the applied B field. This results in a reduced drag force as the speed increases beyond a certain critical speed ω_c. The eddy-current drag force vs. speed curve may look similar to the one shown in Figure 2.4.

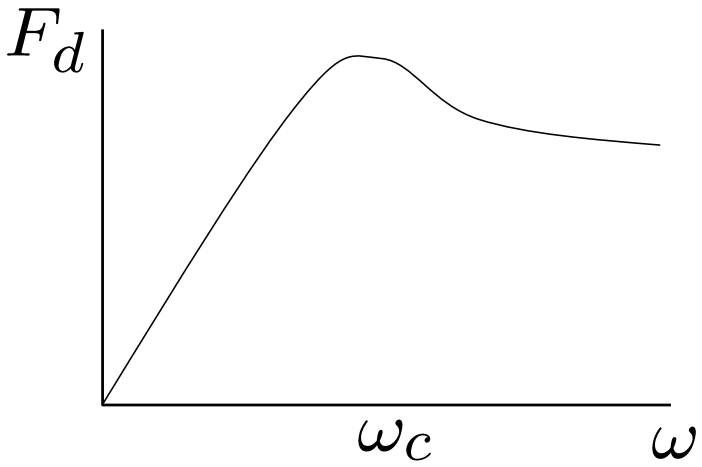

Figure 2.4: Eddy-Current drag force vs. angular velocity.

Remark 1. *(Tradeoff between bearing stiffness and efficient AMB (and FWB) operation)* In a standard AMB control design, a flux bias Φ_0 is introduced into the electromagnets to increase the bearing stiffness. Several biasing schemes are described in detail in the next chapter and the relationship between Φ_0 and the rate of change of the electromagnet force with respect to the flux (i.e. the actuator gain $\frac{df}{d\Phi}$) is outlined. A large bias design allows one to use classical linear control techniques and may lead to acceptable regulation performance and disturbance rejection properties. However, since each power loss mechanism described above is proportional to the magnitude of the flux, an efficient AMB must operate with the minimal amount of flux required

to stabilize the bearing. This implies that zero-bias techniques are desirable. However, the actuator gain $\frac{df}{d\Phi}$ is small for small Φ_0 and results in a limited slew-rate or dead-zone-like characteristic. In fact, for $\Phi_0 = 0$ the actuator gain $\frac{df}{d\Phi} = 0$, and consequently, the AMB is linearly uncontrollable in zero-bias. Thus, zero-bias ($\Phi_0 = 0$) techniques - and as a compromise between AMB stiffness and power consumption, low-bias (Φ_0 small) techniques - require nonlinear control designs. In summary, there are conflicting AMB performance objectives: large flux-bias improves bearing stiffness but at the cost of increased operating losses.

CHAPTER III

AMB FLUX-BIAS SCHEMES

In this chapter, the role of the flux bias in the AMB design is discussed, and the new *generalized complementary flux condition* (gcfc) bias scheme [82] is proposed. It is a natural extension of the zero-bias complementary flux condition (cfc) approach [83, 82]. It is shown that the gcfc technique keeps the power saving approach of the cfc technique, but allows one to introduce a bias flux to improve the bearing stiffness and slew-rate. The flux-bias level is a design parameter and does not constrain the system states, as in other biasing schemes[1]. In principle, the bias level can be time-varying to optimize some performance objectives like bearing stiffness or power dissipation. Although an evaluation of the power consumed and the total square flux required for stabilization is conducted for several bias levels in Chapter 8, optimal bias selection is beyond the scope of this thesis and is left for future investigations. The gcfc scheme is compared to the typical bias scheme used in linear control, the so-called *normal* or *constant flux sum* (cfs) bias scheme. The gcfc is shown to be more flexible than the normal bias scheme and incurs less operating losses under typical circumstances.

The basic equations of motion in (2.8) are now reconsidered under the constraints imposed by these different flux-bias schemes. This chapter assumes that a constant flux bias can be implemented. Note that the use of a constant flux bias is a bit more challenging that the use of a constant current bias because the flux depends on the airgap as well as the current. The details of the flux-bias implementation are presented in Chapters 5 and 6.

[1]For example, in the constant flux sum (cfs) scheme, the control flux ϕ is bounded by the flux bias $|\phi| < \Phi_0$.

3.1 Operation with the Constant-Flux-Sum (CFS) Bias Scheme

The constant flux sum bias scheme is introduced as a benchmark so that the benefits of the gcfc approach may be appreciated better. Consider the situation shown in Figure 2.1 where electromagnets 1 and 2 lie opposite each other on a given control axis. When using a constant flux bias, the electromagnet flux has the form

$$\Phi_j = \Phi_0 + \phi_j, \qquad j = 1, 2 \tag{3.1}$$

where Φ_j is the total flux, Φ_0 is the flux-bias, and ϕ_j is the control flux. Such a bias is typically used to setup linear control designs. The standard way of using a flux-bias for an AMB system is to impose the so-called *normal* biasing or *constant sum* [2] scheme: see [46]. In this mode of operation, an *exact* linearization of the mechanical dynamics (2.8a) is possible by enacting the additional constraint

$$\phi_1 = -\phi_2 = \phi \tag{3.2}$$

so that

$$\Phi_1 = \Phi_0 + \phi, \qquad \text{and} \qquad \Phi_2 = \Phi_0 - \phi$$

This is convenient because the two control inputs are reduced to one. In this scheme, the control flux adds to the bias-flux in one electromagnet and subtracts from the bias-flux in the opposite electromagnet to produce a net force for control. In this manner, the total flux $2\Phi_0$ is constant at all times, hence the name *constant flux sum* scheme. Since the electromagnets always produce an attractive force, the total flux Φ_i must be non-negative for proper operation. Therefore, an additional saturation constraint must be imposed on the control flux, i.e. ϕ must satisfy

$$|\phi| < \Phi_0 \tag{3.3}$$

[2] In this case, it is called the *constant flux sum* scheme because the total flux during operation is $2\Phi_0$. If current is used as the electrical state, it is referred to as a *constant current sum* scheme.

The input transformation of the cfs scheme defined by equations (3.1) and (3.2) combined with equation (2.8) gives the following *linear* equation of motion

$$\begin{aligned} m\ddot{x} &= \frac{1}{\mu_0 A_g}[\Phi_1^2 - \Phi_2^2] \\ &= \frac{1}{\mu_0 A_g}\Big[(\Phi_0 + \phi)^2 - (\Phi_0 - \phi)^2\Big] \\ &= \frac{4\Phi_0}{\mu_0 A_g}\phi \end{aligned} \tag{3.4}$$

Obviously, a linear equation of motion greatly simplifies the design allowing the control engineer to select from a wide range of classical control techniques. Observe that the flux-bias level Φ_0 directly affects the actuator gain $\frac{df}{d\phi}$. Note that in closed-loop operation when $\phi = \phi(x)$, the actuator gain $\frac{df}{d\phi}$ directly affects the AMB stiffness $\frac{df}{dx}$ where f is the net electromagnet force. Note that as Φ_0 tends towards zero, from equations (3.3) and (3.4), the size of the admissible control flux and the actuator gain become zero. Thus, the system becomes uncontrollable for zero flux bias. This is problematic because, as stated in Chapter 2, it is desirable to reduce the flux-bias to zero to minimize AMB losses.

3.2 Operation with the CFC and GCFC Constraints

The *complementary flux condition* (cfc) and the *generalized complementary flux condition* (gcfc) impose constraints on the operation of the electromagnet pair on a given control axis. Both of these schemes allow only one electromagnet at a time to accelerate the rotor along the given control axis. The main difference is that cfc is a zero-bias technique and the gcfc technique is a low-bias technique. Also, the gcfc and cfc constraints coincide as the value of the flux bias tends to zero. The cfc and gcfc conditions are introduced in Section 3.2.1 and their merits are qualitatively discussed. These constraints are physically implemented with a voltage-switching rule which requires a rigorous mathematical justification. To clarify the presentation, the mathematical derivation is presented separately in Section 3.2.2.

3.2.1 Qualitative Discussion of the CFC and GCFC Constraints

Ideally, one would like to eliminate the flux bias completely to minimize AMB losses. This is the standard approach for zero-bias designs in practice (see [83, 8, 45], for example) and is achieved by implementing the cfc[3].

To this end, define the *generalized flux* $\Phi := \Phi_1 - \Phi_2$ and introduce the following flux-dependent, voltage switching rule

$$\begin{aligned} V_{r1} = v, \quad V_{r2} = 0 \quad \text{when} \quad \Phi \geq 0 \\ V_{r1} = 0, \quad V_{r2} = -v \quad \text{when} \quad \Phi < 0 \end{aligned} \tag{3.5}$$

where v is the *generalized control voltage* such that the electrical dynamics of equation (2.8b) reduce to

$$\dot{\Phi} = \frac{v}{N} \tag{3.6}$$

It is shown in the sequel that this voltage switching rule is well defined and implements the following *complementary flux constraint*

$$\begin{aligned} \Phi_1 = \Phi, \quad \Phi_2 = 0 \quad \text{when} \quad \Phi \geq 0 \\ \Phi_1 = 0, \quad \Phi_2 = -\Phi \quad \text{when} \quad \Phi < 0 \end{aligned} \tag{3.7}$$

The fluxes Φ_j are complementary in the sense that only one flux is non-zero at any given time. This means that the electromagnets take turns applying force on the rotor during cfc operation. Note that the sign of the generalized flux Φ is recorded as a means of activating the appropriate electromagnet. Recall that the electromagnet force depends on the square of the flux, thus the sign of total fluxes Φ_j is inconsequential. However, for consistency, the actual fluxes Φ_j are implemented so that they are always non-negative.

The power saving property of the cfc constraint is illustrated by the following argument. Suppose, at some instant in time, that one wishes to apply a given net force

[3]This constraint is often implemented with the current as the electrical state. In that case, it is called the complementary current condition (ccc).

on the rotor, f_{des}. The net force on the rotor is $f_{\text{net}} = f_1 - f_2$. To achieve the desired force, let $f_1 = f_{\text{des}} + f_2$. Then, the net force is $f_{\text{net}} = f_1 - f_2 = f_{\text{des}} + f_2 - f_2 = f_{\text{des}}$. Thus, to achieve the net force, f_1 must be large enough to cancel the force from f_2 and produce the desired force. The cfc saves power because it guarantees that f_2 is zero when f_1 is non-zero, and vice versa. Therefore, the cfc scheme eliminates the unnecessary cancellation of forces.

Applying the cfc constraint (3.7) to the mechanical dynamics (2.8a) one obtains

$$\begin{aligned} m\ddot{x} &= \frac{1}{\mu_0 A_g}[\Phi_1^2 - \Phi_2^2] \\ &= \frac{1}{\mu_0 A_g}\Phi|\Phi| \end{aligned} \tag{3.8}$$

Note that the force-flux characteristic, $\Phi|\Phi|$, has a slope of zero for $\Phi = 0$. Therefore, the rate of change of the force with respect to flux, that is, the force-flux slew-rate is severely limited for small values of flux. This force-flux characteristic is similar to a dead-zone, except the dead-zone consists of one point, $\Phi = 0$, instead of an interval in Φ.

The gcfc scheme is constructed with the intent to take advantage of the power saving switching strategy of the cfc scheme, while at the same time allowing for the introduction of a flux-bias into the electromagnets to alleviate the limited force slew-rate problem. To achieve this goal, one does not impose complementarity on the *total fluxes* as in the cfc approach, but *only on the control (or perturbation) fluxes*. That is, a flux bias is introduced into the electromagnets with the same form as in equation (3.1): $\Phi_i = \Phi_0 + \phi_i$ for $i = 1, 2$ where Φ_i is the total flux, Φ_0 is the flux-bias and ϕ_i is the control flux. However, the following *generalized complementary flux condition* is imposed on the control flux ϕ_i (as opposed to the total flux Φ_i). The gcfc and cfc schemes are implemented in a similar manner.

Define the *generalized control flux* $\phi := \phi_1 - \phi_2$ and introduce the following

flux-dependent, voltage-switching rule

$$\begin{aligned} V_{r1} &= v, \quad V_{r2} = 0 \quad \text{when} \quad \phi \geq 0 \\ V_{r1} &= 0, \quad V_{r2} = -v \quad \text{when} \quad \phi < 0 \end{aligned} \tag{3.9}$$

where v is again the *generalized control voltage* such that the electrical dynamics of equation (2.8b) reduce to

$$\dot{\phi} = \frac{v}{N} \tag{3.10}$$

It is shown in the sequel that this voltage switching rule is well defined and implements the following *generalized complementary flux constraint*

$$\begin{aligned} \phi_1 &= \phi, \quad \phi_2 = 0 \quad \text{when} \quad \phi \geq 0 \\ \phi_1 &= 0, \quad \phi_2 = -\phi \quad \text{when} \quad \phi < 0 \end{aligned} \tag{3.11}$$

This constraint dictates that the *control flux* ϕ is generated by only one electromagnet at a time, depending on the direction of the force that is required. That is, the electromagnets take turns applying a *net* force on the rotor during gcfc operation. As in the cfc technique, the sign of ϕ is recorded as a means to trigger the voltage switching and the control fluxes ϕ_j are non-negative. Note that at all times, both electromagnets are excited with the flux bias Φ_0 and consequently, both electromagnets always produce a bias force of $F_{min} = \Phi_0^2/\mu_0 A_g$. When the generalized control flux ϕ is positive, extra flux is commanded from electromagnet 1, and when ϕ is negative, extra flux is commanded from electromagnet 2. Thus, one may view the control flux ϕ as the "excess" flux that needs to be commanded in order to obtain a given desired net force.

Imposing this constraint on the mechanical dynamics, (2.8a) one obtains

$$\begin{aligned} m\ddot{x} &= \frac{1}{\mu_0 A_g}(\Phi_1^2 - \Phi_2^2) \\ &= \frac{1}{\kappa}[\phi_1^2 - \phi_2^2 + 2\Phi_0(\phi_1 - \phi_2)] \\ &= \frac{1}{\mu_0 A_g}(2\Phi_0\phi + \phi|\phi|) \end{aligned} \tag{3.12}$$

Note that the equation of motion for the gcfc scheme (3.12) reduces to that of cfc scheme (3.8) as Φ_0 reduces to zero. This is due to the fact that the gcfc constraint coincides with the cfc constraint as $\Phi_0 \to 0$.

The gcfc scheme is markedly different than the constant flux sum and cfc control schemes. Contrary to what is customary in practice, it is not assumed that the bias Φ_0 is large. That is, $|\Phi_0| \ll |\phi_i|$ is allowed. This is possible because the magnitude of the bias flux Φ_0 in the gcfc scheme does not impose a constraint on the control flux ϕ as it does in the normal bias scheme (as in equation (3.3)). Since it is assumed that the flux bias is small, perhaps on the order of the control flux, the quadratic term in equation (3.12) is significant. Furthermore, the cfc condition imposes constraints on the total flux whereas the gcfc is imposed only on the "extra" control flux. In addition, the gcfc approach has the ability to partially alleviate the force slew-rate limit problem of the zero-bias cfc model. The available force slew-rate is controlled by

$$\frac{df}{dt} = \frac{df}{d\Phi}\frac{d\Phi}{dt} \tag{3.13}$$

where the ability to change f is determined by $\frac{df}{d\Phi}$[4]. The force as a function of the control flux is shown in Figure 3.1 in zero- and low-bias modes. Observe that the cfc ($\Phi_0 = 0$) slew-rate is zero at the origin while the slew-rate for the gcfc ($\Phi_0 > 0$) at the origin is non-zero. In fact, at the origin $\frac{dF}{d\Phi} = 2\Phi_0$. One expects that such an improvement will lead to greater bearing stiffness and disturbance rejection capability. Note however, that AMB losses increase as the slew-rate is compensated by a larger flux bias.

[4]It is assumed that the ability to change the flux Φ is independent of the flux biasing scheme. This is a realistic assumption if the same amplifiers are used to drive the coils of the AMB in each case.

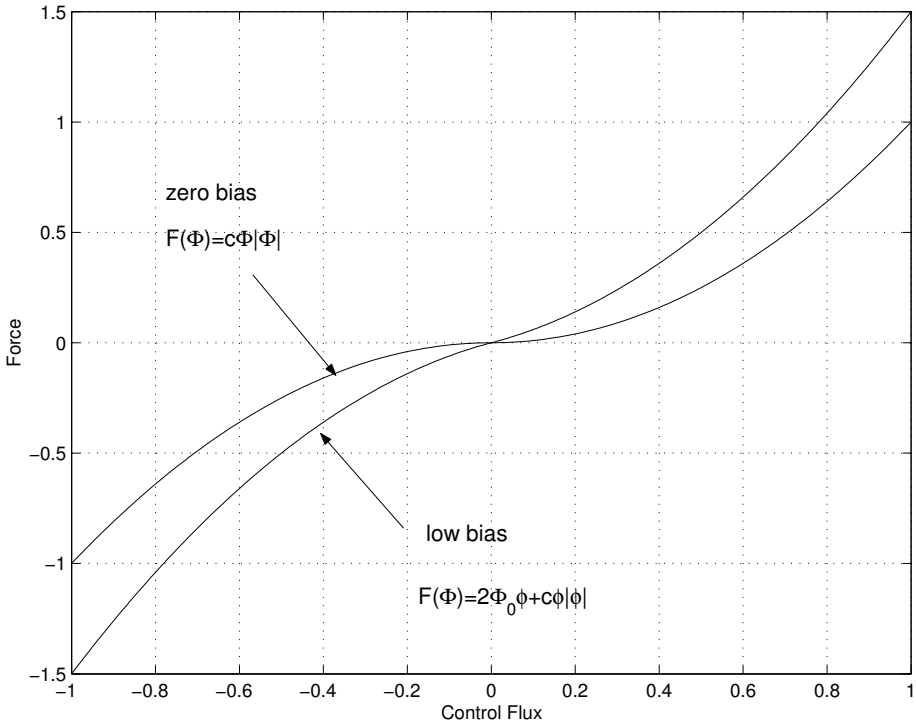

Figure 3.1: The electromagnet force vs. control flux in ZB and LB. For ZB ($\Phi_0 = 0$), the force-flux function is flat at the origin. This is the source of the slew-rate limitation in ZB mode. Note $\frac{df}{d\phi}|_{\phi=0} = 2\Phi_0$.

3.2.2 Mathematical Justification for the GCFC Bias Scheme

Since the gcfc incorporates the cfc scheme, one only needs to show that the gcfc voltage-switching scheme in equation (3.9) with $\dot{\phi} = \frac{v}{N}$ and $\phi = \phi_1 - \phi_2$ implements the gcfc condition in equation (3.11). Furthermore, the control flux $\phi_j(t) \geq 0$ for all $t > 0$ given any positive initial conditions $\phi_j(0) \geq 0$.

Figure 3.2 illustrates the argument. The total flux is $\Phi_j(t) = \Phi_0 + \phi_j(t)$. Suppose without loss of generality, that $\phi_1(0) \geq \phi_2(0) \geq 0$. In this case, $\phi \geq 0$ and the control voltage v is distributed to electromagnet 1. Thus, $\dot{\phi}_1 = \frac{v}{N}$, $\dot{\phi}_2 = 0$, and ϕ_2 remains constant at $\phi_2(0)$. This mode of operation continues until $\phi < 0$ at time t_1 when $\phi_1(t_1) = \phi_2(0)$. At this point, $\dot{\phi}_1 = 0$ and $\dot{\phi}_2 = \frac{-v}{N}$. Consequently, $\phi_1(t) = \phi_2(0)$ for $t > t_1$ until another switching occurs at t_2. Thus, given initial control fluxes $\phi_j(0) \geq 0$, the gcfc condition holds with the caveat that the implemented bias flux is slightly

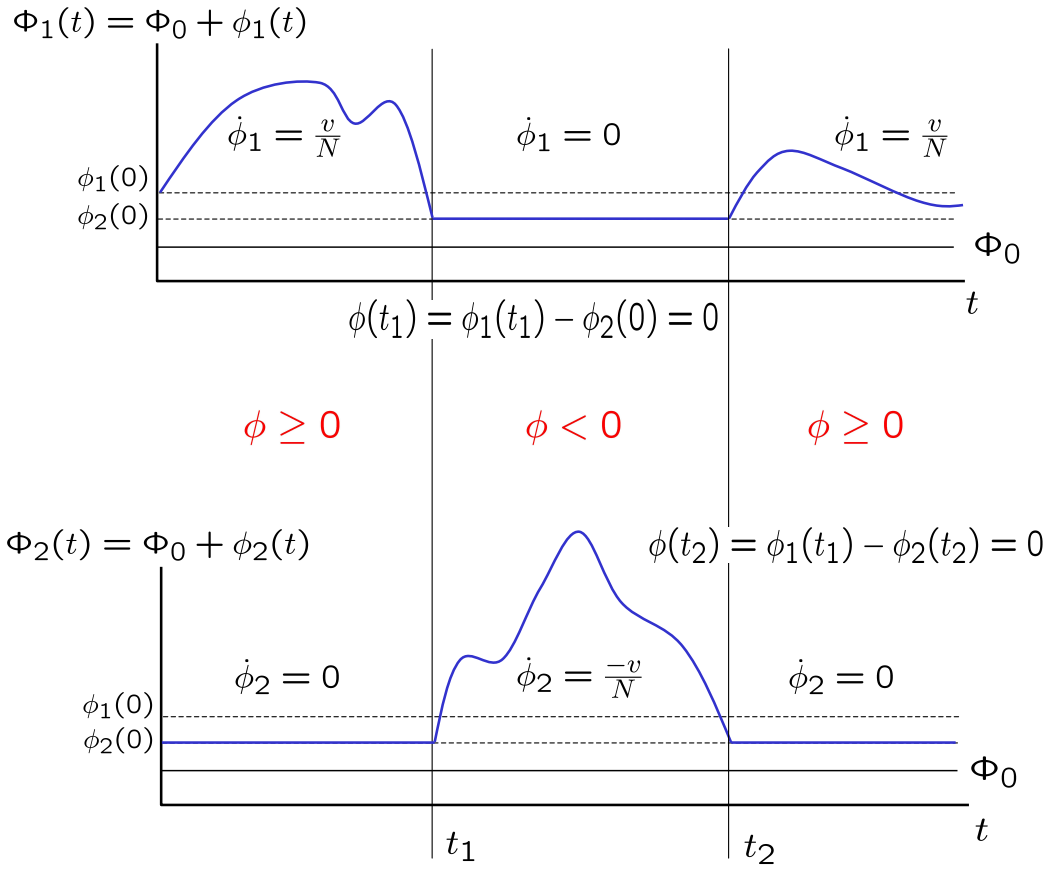

Figure 3.2: Implementation of the voltage-switching rule (3.9) and the gcfc constraint with time.

perturbed $\overline{\Phi}_0 = \Phi_0 + \min\{\phi_1(0), \phi_2(0)\}$. Consequences of this minor complication are discussed below.

Using the above argument, the mechanical dynamics in equation (2.8a) may be manipulated as follows.

$$\begin{aligned}
\ddot{x} &= \frac{1}{\kappa}(\Phi_1^2 - \Phi_2^2) \\
&= \frac{1}{\kappa}((\Phi_0 + \phi_1)^2 - (\Phi_0 + \phi_2)^2) \\
&= \frac{1}{\kappa}(2\Phi_0(\phi_1 - \phi_2) + \phi_1^2 - \phi_2^2) \\
&= \frac{1}{\kappa}(2\Phi_0 + \phi_1 + \phi_2)\phi
\end{aligned} \tag{3.14}$$

where $\kappa = m\mu_0 A_g$. Assume without loss of generality that $\phi_1(0) \geq \phi_2(0)$. Then $\phi(0) \geq 0$ and by (3.9) and (3.10), it follows that for $t \geq 0$, $\phi_2 = \phi_2(0)$, and $\phi_1 =$

$\phi + \phi_2(0)$. Subsequently, (3.14) can be written as

$$\ddot{x} = \frac{1}{\kappa}(2\Phi_0 + 2\phi_2(0) + \phi)\phi, \qquad (\phi \geq 0)$$

If at some point $t_1 > 0$ a switching occurs, then $\phi_1(t_1) = \phi_2(t_1) = \phi_2(0)$. Moreover, from (3.5) and (3.10) and for $t \geq t_1$ one concludes that $\phi_1 = \phi_2(0)$ and $\phi_2 = \phi_2(0) - \phi$. Subsequently, (3.14) can be written in this case as

$$\ddot{x} = \frac{1}{\kappa}(2\Phi_0 + 2\phi_2(0) - \phi)\phi, \qquad (\phi < 0) \tag{3.15}$$

The same arguments can be used if another switching occurs and so on.

From the previous analysis it follows that the equation of motion (3.14) under the switching strategy (3.9) and (3.10) takes the form

$$\ddot{x} \;\; = \;\; \frac{1}{\kappa}(2\bar{\Phi}_0\phi + \phi|\phi|) \tag{3.16}$$

where $\bar{\Phi}_0 := \Phi_0 + \min\{\phi_1(0), \phi_2(0)\}$. As previously mentioned, physical considerations allow one to restrict the set of all realizable trajectories of system (3.14) inside the set $\mathcal{S} := \{(x, \dot{x}, \phi_1, \phi_2) \in \mathbb{R}^4 : \phi_i \geq 0,\ i = 1, 2\}$. The following proposition states that the switching scheme (3.9) is well-defined.

Proposition 1. *The set $\mathcal{S}$ is invariant under the switching scheme (3.9).*

Proof. Let $c(t) := \min\{\phi_1(t), \phi_2(t)\}$. Now notice that if $\phi_1 \geq \phi_2$ then $c = \phi_2$ and (3.9) and (3.10) imply $\dot{\phi}_2 = \dot{c} = 0$. Similarly, if $\phi_2 \geq \phi_1$ then $c = \phi_1$ and (3.9) and (3.10) imply that $\dot{\phi}_1 = \dot{c} = 0$. Therefore $\dot{c} \equiv 0$. It follows that if $c(0) \geq 0$ then $c(t) \geq 0$ for all $t \geq 0$. □

An immediate consequence of the previous result is that the flux for each electromagnet is never reduced below $\bar{\Phi}_0$ and hence the minimum force generated by each electromagnet is $F_{\min} = \bar{\Phi}_0^2/\mu_0 A_g$.

The introduction of the switching scheme in (3.9) is motivated from the desire to minimize the control fluxes ϕ_1 and ϕ_2 to minimize AMB losses. It was previously

stated that the electromagnets under the gcfc constraint take turns applying a net force to the rotor. However, proposition 1 shows that it is possible for the control fluxes ϕ_j to have a nonzero constant component, $c = \min\{\phi_1(0), \phi_2(0)\}$. This fact seems to imply that the control fluxes ϕ_1 and ϕ_2 are in actuality *not* complementary when c is non-zero. However, as seen in equation (3.16) and as illustrated in Figure 3.2, this constant c can be grouped into the bias flux $\bar{\Phi}_0$. As a result, the value of the actual flux bias $\bar{\Phi}_0$ differs from the value of the desired flux bias Φ_0 by the amount c. This means that complementarity may in fact be imposed on ϕ_1 and ϕ_2, but the implementation of the flux bias Φ_0 will be perturbed by $c = \min\{\phi_1(0), \phi_2(0)\}$.

In particular, if at the initial time at least one of the control fluxes is zero, i.e., $\phi_1(0)\phi_2(0) = 0$ (as will be typically the case in practice when operation starts from rest), then at every instant of time at least one of the electromagnets is inactive (its control flux ϕ_j is zero). In other words, if either one of the initial control fluxes is zero, then the gcfc condition may be implemented with perfect implementation of the bias flux: $\bar{\Phi}_0 = \Phi_0$. The following result as an immediate consequence of Proposition 1.

Proposition 2. *The set* $\mathcal{S}_0 := \{(x, \dot{x}, \phi_1, \phi_2) \in \mathcal{S} : \phi_1\phi_2 = 0\}$ *is invariant under the switching scheme (3.10)-(3.9).*

Proof. If $(x(0), \dot{x}(0), \phi_1(0), \phi_2(0)) \in \mathcal{S}_0$ then $\min\{\phi_1(0), \phi_2(0)\} = 0$. The claim follows from the fact that $\min\{\phi_1(0), \phi_2(0)\} = \min\{\phi_1(t), \phi_2(t)\}$ for all $t \geq 0$. □

It is evident from Proposition 2 that for all initial conditions in $\mathcal{S}_0$ the voltage-switching logic (3.10)-(3.9) reduces to the gcfc condition of equation (3.11).

In this work, the primarily interest lies in the stabilization of the AMB mechanical states $(x, \dot{x})$ under low-bias (LB) operation, i.e., when $\bar{\Phi}_0$ is small. As a special case, one obtains a zero-bias (ZB) model by setting $\bar{\Phi}_0 = 0$ in (3.16). For the subsequent control derivations presented in Chapter 4, model (3.10)-(3.16) is used for designing the control law v. Once v is constructed, the voltage is distributed to the actual

control inputs V_{r1} and V_{r2} by activating each electromagnet according to (3.9). Note that since operation at some non-zero bias is acceptable in this context, typically only *asymptotic* stability is required with respect to the states x and $\dot{x}$ of the system (2.8)[5].

The following result clarifies the relation between equations (3.10)-(3.16) and the original AMB model, given by equation (2.8) .

Theorem 1. *Any control law that renders the system (3.10)-(3.16) globally asymptotically stable, ensures that:*

(i) For all initial conditions in $\mathcal{S}$ the system (2.8) is stable.

(ii) For all initial conditions in $\mathcal{S}$, the system (2.8) is asymptotically stable with respect to the states $(x, \dot{x})$. Moreover, the fluxes ϕ_1 and ϕ_2 remain bounded and, in addition, $\lim_{t\to\infty} \phi_1(t) = \lim_{t\to\infty} \phi_2(t) = \min\{\phi_1(0), \phi_2(0)\}$.

(iii) For all initial conditions in $\mathcal{S}_0$ the system (2.8) is asymptotically stable.

Proof. (i) Choose $\varepsilon > 0$. From the stability of the system (3.10) and (3.16), it follows that there exists $\bar{\delta} = \bar{\delta}(\varepsilon) > 0$ such that if $|(x(0), \dot{x}(0))| + |\phi(0)| < \bar{\delta}$ then $|(x(t), \dot{x}(t))| + |\phi(t)| < \varepsilon/2$ for all $t \geq 0$. Consider now all initial conditions in $\mathcal{S}$ such that $|(x(0), \dot{x}(0))| + |\phi(0)| < \bar{\delta}$ and $2\min\{\phi_1(0), \phi_2(0)\} < \varepsilon/2$. Choose $\delta(\varepsilon) := \min\{\bar{\delta}(\varepsilon), \varepsilon/2\}$ and notice that the switching scheme (3.10)-(3.9) implies that $\phi_1 = \max\{\phi, 0\} + \bar{c}$ and $\phi_2 = -\min\{\phi, 0\} + \bar{c}$ where $\bar{c} := \min\{\phi_1(0), \phi_2(0)\}$. Hence, for all initial conditions such that $|(x(0), \dot{x}(0))| + |\phi_1(0)| + |\phi_2(0)| = |(x(0), \dot{x}(0))| + |\phi(0)| + 2\min\{\phi_1(0), \phi_2(0)\} < \delta$, then $|(x(t), \dot{x}(t))| + |\phi(t)| < \varepsilon/2$ holds and thus, $|(x(t), \dot{x}(t))| + |\phi_1(t)| + |\phi_2(t)| = |(x(t), \dot{x}(t))| + |\phi(t)| + 2\min\{\phi_1(0), \phi_2(0)\} < \varepsilon/2 + \varepsilon/2 = \varepsilon$ for all $t \geq 0$. Hence (i) follows.

[5]This type of stability is also known as partial stability. For the relevant definitions and major results see, for example, [9, 86].

(ii) For all initial conditions in $\mathcal{S}$ asymptotic stability with respect to $(x, \dot{x})$ follows directly from Proposition 1 and the fact that $(x, \dot{x}) \to 0$. Using the fact that $\phi_1 = \max\{\phi, 0\} + \bar{c}$ and $\phi_2 = -\min\{\phi, 0\} + \bar{c}$ and since ϕ is bounded, it follows that both ϕ_1 and ϕ_2 remain bounded. Moreover, since $\phi \to 0$, then $\lim_{t\to\infty} \phi_i(t) = \bar{c}$, for $i = 1, 2$.

(iii) First, recall from Proposition 2 that the set $\mathcal{S}_0$ is invariant. Moreover, for all initial conditions in $\mathcal{S}_0$, $\bar{c} = 0$ and the states ϕ_1 and ϕ_2 are related to ϕ via $\phi_1 = \max\{\phi, 0\}$ and $\phi_2 = -\min\{\phi, 0\}$. Since $\phi \to 0$ it follows that $\lim_{t\to\infty} \phi_i(t) = 0$, for $i = 1, 2$. □

3.3 CFS vs. GCFC: Total Square Flux Comparison

Recall that the motivation of using the gcfc scheme is to minimize the power losses of the AMB while allowing for some minimal amount of bearing stiffness. On the other hand, the normal biasing scheme typically provides plenty of stiffness but has excessive losses. Since the losses of an AMB are in direct relation to the total amount of squared flux required (see Table 2.1), the total square flux, and thus the flux bias, should be minimized during operation.

To compare the normal and gcfc biasing schemes, consider two bearings, one operated using the gcfc constraint with a flux bias Φ_{0g} and control flux ϕ_g, and the other AMB operated using normal biasing with a bias flux of Φ_{0n} and a control flux of ϕ_n. Furthermore, to make a "fair" comparison, suppose that a certain level of positive force F_{0des} is required by both bearings, i.e., $F_g = F_n = F_{0des}$ where

$$F_n = \frac{1}{\kappa} 4\Phi_{0n}\phi_n, \qquad \text{and} \qquad F_g = \frac{1}{\kappa}(2\Phi_{0g}\phi_g + \phi_g^2) \tag{3.17}$$

The total square flux for normal biasing is

$$T_n = (\Phi_{0n} + \phi_n)^2 + (\Phi_{0n} - \phi_n)^2 \tag{3.18}$$

whereas the total square flux for the gcfc is

$$T_g = (\Phi_{0g} + \phi_g)^2 + \Phi_{0g}^2 \tag{3.19}$$

Now, one may compare the ratio of T_n/T_g subject to the constraint $F_n = F_g$. To this end, note that (3.17) implies that

$$\phi_n = \frac{2\Phi_{0g}\phi_g + \phi_g^2}{4\Phi_{0n}} \tag{3.20}$$

Furthermore, let $\alpha = \Phi_{0n}/\Phi_{0g}$ and $\beta = \phi_g/\Phi_{0g}$. Forming the total flux ratio, one obtains

$$\frac{T_n}{T_g} = \frac{4\alpha^2 + \beta^2(1+\beta/2)^2}{2\alpha^2(2+\beta^2+2\beta)} \tag{3.21}$$

The plot of this ratio as a function of β for several values of α are shown in Figure 3.3. From this Figure 3.3, one may investigate the relative flux (or force) production

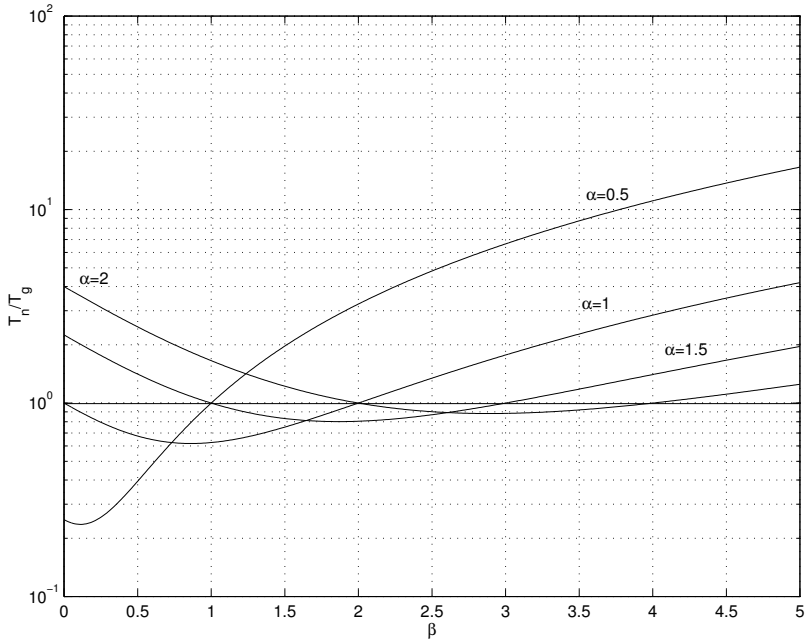

Figure 3.3: Total square flux ratio T_n/T_g. Note logarithmic scale on vertical axis.

capability of the above schemes. The parameter $\alpha = \Phi_{0n}/\Phi_{0g}$ measures the relative size of the bias fluxes used in either scheme. Larger α is typical of the gcfc scheme. The parameter $\beta = \phi_g/\Phi_{0g}$ measures only the relative size of the control flux to the

bias flux of the gcfc scheme. First, if both bearings are biased with the same flux ($\alpha = 1$), then the normal biasing scheme is better than the gcfc scheme, $T_n/T_g < 1$ (i.e. less flux is required to produce the desired force), if $\beta < 2$. For low-bias designs, it is typical that $\beta > 2$. Any line segment that lies above 10^0 in Figure 3.3 indicates where the gcfc scheme has a smaller total square flux requirement than the normal scheme. In these instances, the AMB requires less flux to generate the required force and consequently, should have less operating losses using the gcfc scheme. Thus, in low-bias with ($\beta > 2$), the gcfc is preferable over normal biasing. By reducing the flux bias level Φ_{0g} as compared to Φ_{0n} ($\alpha > 1$), the gcfc performs increasingly better ($T_n/T_g > 1$) over a wide range of control fluxes. Note that using the gcfc scheme, the bias may be reduced to zero, however, controllability is lost in the normal scheme when $\Phi_{0n} = 0$. Note that even in the case of the normal bias Φ_{0n} smaller than that of the gcfc ($\alpha < 1$), the gcfc scheme performs better for large perturbation flux ($\beta > 1$).

Since α and β are not defined in zero-bias, one may re-parameterize the T_n/T_g ratio. The total square flux for the cfs constraint is

$$T_n = 2\Phi_{0n}^2 + 2\phi_n^2$$

The total square flux for the gcfc condition is $T_g = \phi_g^2$. Let $\overline{\beta} = \frac{\phi_g}{\Phi_n}$. Using the force constraint,

$$\phi_n = \frac{\phi_g^2}{4\Phi_n}$$

the total square flux ratio in terms of $\overline{\beta}$ is

$$\frac{T_n}{T_g} = \frac{2}{\overline{\beta}^2} + \frac{\overline{\beta}^2}{8} \tag{3.22}$$

Note that for the cfs to be implemented properly $|\phi_n| < \Phi_n$. This constraint translates into $\overline{\beta} < 2$. The flux ratio is plotted in Figure 3.4. In zero bias, the gcfc always operates with less loss than the cfs because $T_n/T_g > 1$ for $\beta < 2$. (For $\beta > 2$, the cfs is not properly defined.) In summary, this analysis shows that the gcfc has the

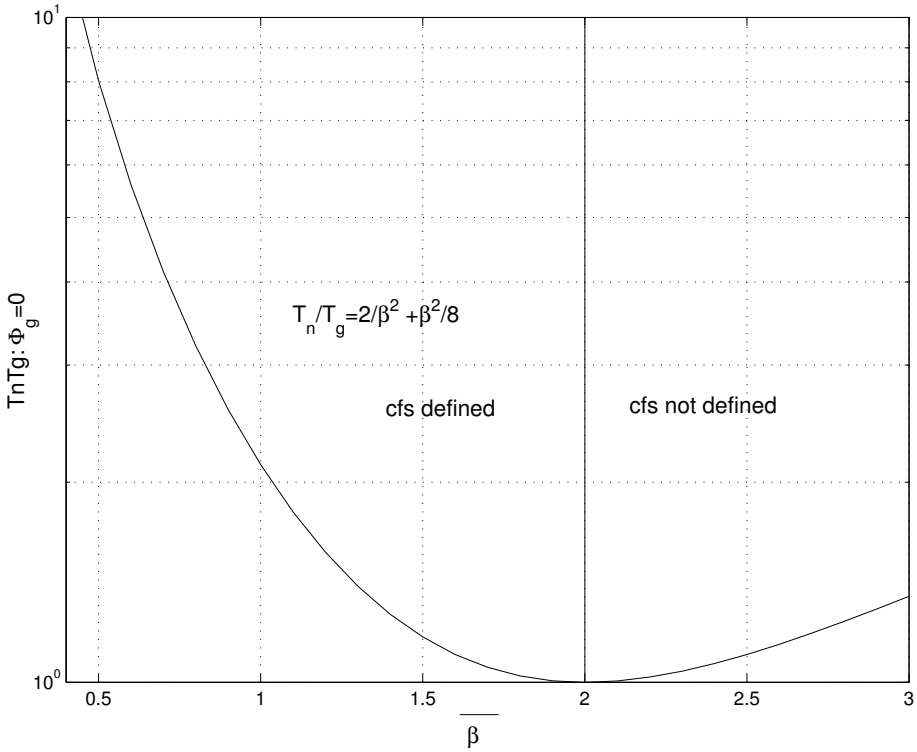

Figure 3.4: Total square flux ratio T_n/T_g for zero bias. $\overline{\beta} = \phi_g/\Phi_n$. The cfs condition is not defined for $\overline{\beta} > 2$.

ability to produce force more efficiently than the cfs in a several instances.

Note that the analysis in this section is limited by the fact that it is conducted in a static sense. It asks the question, "For a given constant desired force $F_{0\text{des}}$, which bias scheme requires the least amount of flux to deliver $F_{0\text{des}}$ and under what conditions?" The square of the flux relates to the instantaneous power loss, however, the total energy loss of the system may depend on the state history. In Chapter 8, the total square flux and rms power consumption of the bearing are measured under a testing scenario in which the rotor is regulated to a setpoint in the presence of a persistent sinusoidal disturbance. The above analysis and the results in Chapter 8 show that the gcfc scheme can outperform the cfs scheme in several situations.

3.4 Contribution of the GCFC Bias Scheme to the-State-of-the-Art

The constraints of a given bias scheme are often plotted in the $\Phi_1 - \Phi_2$ plane. Figure 3.5 clearly illustrates the differences between the constant flux sum (cfs), constant flux product (cfp) [1], the cfc and the gcfc bias schemes. The cfs scheme is shown

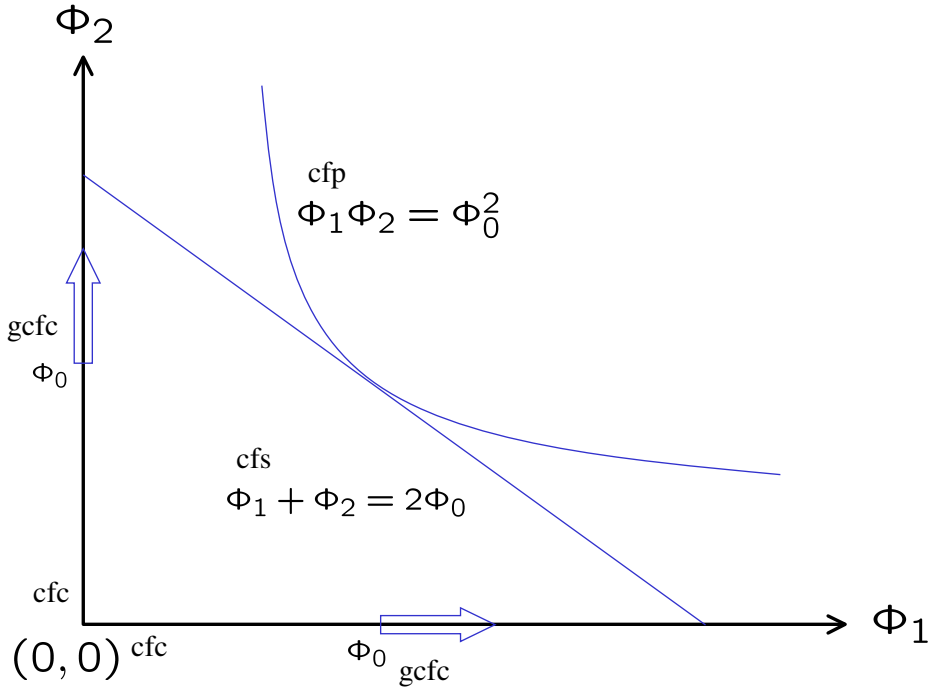

Figure 3.5: The cfc, gcfc, cfs, and cfp [1] bias constraints shown in the $\Phi_1 - \Phi_2$ plane.

as a straight line with axis intercepts at $2\Phi_0$. Recall that the control flux is limited by $|\phi| < \Phi_0$. This was an implementation constraint so that the flux would remain positive. However, it a also limits the load capacity (i.e. the maximum force) that can be generated by the bearing. An approximation to the cfs piecewise continuous constraint is the constant flux product (cfp) constraint $\Phi_1\Phi_2 = \Phi_0^2$. The cfp does not allow for negative flux but also does not artificially limit the load capacity. That is, the maximum force is not determined by the bias flux, only by the limits of the actuator (B_{sat} and I_{max}). The cfp scheme has the rather complex flux dynamics $\dot{\Phi}_1 = \frac{\Phi_2}{\Phi_2}\dot{\Phi}_2$. Compare this to the flux dynamics of the cfs, $\dot{\Phi}_1 = -\dot{\Phi}_2$. The cfp

scheme is posed in conjunction with the feedback linearization scheme in [1]. It is conveniently implemented by defining an additional output $h_2 = \Phi_1\Phi_2$ and regulating this output to the constant $h_2 = \Phi_0^2$. It can also implement the cfs scheme by letting the auxiliary output $h_2 = \Phi_1 + \Phi_2$ and regulating to the constant $h_2 = 2\Phi_0$.

The cfc and gcfc schemes operate only on the positive Φ_1 and Φ_2 axis. Note that the gcfc scheme operates on the subsets of the Φ_1 and Φ_2 axis where $\Phi_j \geq \Phi_0$. The cfc and gcfc scheme may be thought of as a cfp scheme. Specifically, the cfc is equivalent to the cfp scheme with $\Phi_1\Phi_2 = 0$ and the gcfc scheme is similar to the cfp scheme with $\phi_1\phi_2 = 0$.

The gcfc scheme has several advantages over the conventional cfs and cfc bias schemes. When using the gcfc scheme, the selection of the value of the bias flux Φ_0 does not impact the magnitude of the control flux ϕ in any way. Recall that proper implementation of the cfs scheme requires that $|\phi| < \Phi_0$ and typically, $|\phi| << \Phi_0$. The gcfc scheme, on the other hand, allows for small flux bias levels. In conventional low-bias operation, $\Phi_0 << |\phi|$. In fact, Φ_0 can be reduced all the way to zero to save power. In this case, the gcfc scheme coincides with the cfc scheme and the term $\phi|\phi|$ provides nonlinear controllability in zero-bias operation. However, the cfs scheme looses controllability as Φ_0 goes to zero.

The cfc scheme saves power losses as compared to the gcfc scheme, but at the cost of a limited slew-rate capacity in for small levels of flux. The gcfc scheme is capable of mitigating the slew-rate limitation by introducing a bias flux and imposing the complementarity condition on the control fluxes as opposed to the total electromagnet fluxes. This is achieved at the cost of decreased AMB efficiency, but the gcfc scheme shows potential for greater efficiency than the cfs biasing mode in low-bias operation. These advantages make the gcfc scheme one worth of study.

CHAPTER IV

ZERO- AND LOW-BIAS CONTROL DESIGN FOR THE 1-DOF AMB

Recall that the 4-DOF PREMAG reaction wheel is controlled by 4 independent 1-DOF control algorithms. To save time, three of the control axes are implemented with standard, large-bias, classical control techniques while the fourth axis is used as the nonlinear zero-bias (ZB) and low-bias (LB) control law test bed. This chapter presents several control designs for the 1-DOF AMB. Since this thesis is primarily concerned with low-loss AMB control design, the focus is on ZB and LB control algorithms[1]. However, to better appreciate the contributions of the new ZB and LB control laws, they are compared to standard nonlinear techniques.

In the sequel, the control laws are developed on a state model that is operating under the gcfc constraint with voltage-mode amplifiers. Thus, the resulting control laws contain a ZB implementation as a limiting case of the more general LB implementation as the bias flux Φ_0 is reduced to zero. Section 4.1 presents a non-dimensionalized state model for a 1-DOF AMB using the gcfc condition and clearly states the control objectives. Section 4.2 presents a brief discussion of the standard feedback linearization (FBL) and integrator backstepping (IB) nonlinear control techniques. These control laws suffer from a singularity in ZB when the control flux is zero which manifests itself as an infinite voltage command. Section 4.3 introduces a *new* control law based on the theory of control Lyapunov functions (clf). This control law also suffers from a singularity in ZB mode, however its domain of definition is

[1]These control algorithms were first reported by Tsiotras and Wilson in [83, 82].

much larger than that of the standard nonlinear FBL and IB approaches. Section 4.4 presents an additional *new* passivity-based control law which is completely nonsingular in ZB. Note that each of the above control laws are nonsingular in LB. This chapter restricts itself to a control law performance comparison through simulation: Chapter 8 completes the evaluation with experimental testing on the PREMAG reaction wheel. Finally, Section 4.5 closes the chapter with numerical simulations to illustrate the characteristics of each control law.

4.1 Nondimensionalized State Equations and Control Objectives

The low-loss 1-DOF AMB control designs in this work assume that the system is using voltage-mode amplifiers and the switching rule of equation (3.9) to implement the gcfc constraint in equation (3.11). This assumption results in the mechanical and electrical dynamics of equations (3.12) and (3.10). To minimize the number of system parameters, a non-dimensionalized state-space version of the equations of motion is used. This results in a normalization of several of the state variables and conveniently avoids problematic simulation issues such as "stiffness". Furthermore, conclusions made about the control law performance based on non-dimensionalized simulation results apply to AMBs in general and are not restricted to a particular AMB defined by a specific choice of system parameters.

To this end, define the non-dimensionalized state and control variables

$$x_1 = \frac{x}{g_0}, \qquad x_2 = \frac{\dot{x}}{\Phi_{sat}\sqrt{g_0/\kappa}}, \qquad x_3 = \frac{\phi}{\Phi_{sat}}, \qquad u = \frac{v\sqrt{g_0\kappa}}{N\Phi_{sat}^2} \tag{4.1}$$

along with the non-dimensionalized time

$$\tau = t\frac{\Phi_{sat}}{\sqrt{g_0\kappa}} \tag{4.2}$$

where g_0 is the nominal air-gap and Φ_{sat} is the value of the saturation (maximum) flux which is calculated from the electromagnet cross-sectional area and the saturation

flux density B_{sat}. The resulting non-dimensionalized state-space equations are

$$x_1' = x_2 \tag{4.3a}$$

$$x_2' = \epsilon x_3 + x_3|x_3| := f_2(x_3) \tag{4.3b}$$

$$x_3' = u \tag{4.3c}$$

where $\epsilon = 2\Phi_0/\Phi_{sat}$ and where the prime denotes differentiation with respect to τ. Notice that $\epsilon \geq 0$ for all initial conditions in $\mathcal{S}$ (defined in Section 3.2.2). LB operation in this context therefore implies that $\epsilon \ll 1$, while ZB implies that $\epsilon = 0$.

With a slight abuse of notation, redefine the use of dot in (4.3) to denote differentiation with respect to the non-dimensionalized time. Also, re-write the state equation (4.3) and define the output λ equation with the following control-affine form

$$\dot{x} = f(x) + g(x)u \tag{4.4a}$$

$$\lambda = h(x) \tag{4.4b}$$

with vector fields $f : \mathbb{R}^3 \to \mathbb{R}^3$, $g : \mathbb{R}^3 \to \mathbb{R}^3$, and output function $h : \mathbb{R}^3 \to \mathbb{R}$ given by

$$f(x) := \begin{bmatrix} x_2 \\ \epsilon x_3 + x_3^{[2]} \\ 0 \end{bmatrix}, \qquad g(x) := \begin{bmatrix} 0 \\ 0 \\ 1 \end{bmatrix}, \qquad h(x) = x_1 \tag{4.5}$$

and where the notation $x_3^{[2]} := \text{sgn}(x_3)x_3^2 = x_3|x_3|$ has been adopted[2].

The control objective may be stated as follows: find a control law $u : \mathcal{D} \subseteq \mathbb{R}^3 \to \mathbb{R}$ such that

(i) the closed-loop system $\dot{x} = \tilde{f}(x) := f(x) + g(x)u(x)$ has an isolated equilibrium at the origin

(ii) the origin is asymptotically stable for all $x(0) \in \mathcal{D}$

[2]The properties of this function are listed in Appendix A.

(iii) the domain of definition $\mathcal{D} \subseteq \mathbb{R}^3$ of the control law $u(x)$ is as large as possible

According to the discussion in the previous chapter, in order to reduce the power losses one would like, ideally, to set $\epsilon = 0$. However, this approach introduces several difficulties. First, from (4.3) it is seen that for $\epsilon = 0$ the system is linearly uncontrollable. Second, for zero-bias, the AMB has no force-slew rate capability when the flux is zero [46, 47, 53, 4, 71]. The force vs. flux curve has a zero slope at $\phi = 0$ and the AMB cannot respond fast enough to force commands. As a result, most control design techniques for zero-bias AMBs will command a very high (even infinite) voltage when the flux is zero. The ZB control design for a voltage-controlled AMB is therefore far from trivial. The following discussion revisits the ZB control design for a 1-DOF AMB with the purpose of mitigating the ZB singularity and proposes a new class of control laws which are valid both for LB and ZB operation.

4.2 Standard Nonlinear Techniques: Feedback Linearization and Integrator Backstepping

The techniques of feedback linearization (FBL) and integrator-backstepping (IB) have grown into maturity in the mid 1980's and early 1990's. Feedback linearization employs the theory of differential geometry to construct a feedback transformation to make the controllable and observable part of a nonlinear system behave with linear dynamics. A full exposition of this theory may be found in the well-known texts by Isidori [28, 29] and Vidyasagar [57], however, it is only briefly introduced in Section 4.2.1. IB is applicable to systems which have a strict-feedback or cascaded form [43]. It is an iterative design process which defines intermediate control variables and control laws for subsystems to construct a composite control law for the entire system. This type of design approach is introduced in section 4.2.2 and is well documented, for example, in [43, 34, 69].

4.2.1 Feedback Linearization Design

The feedback linearization technique employs a nonlinear coordinate transformation and preliminary feedback law to decompose the n-dimensional nonlinear system in equation (4.4) into a controllable linear subsystem of dimension $r(\leq n)$ and an uncontrollable, unobservable nonlinear subsystem of dimension $n - r$. The FBL technique is limited to systems where the decomposition results in a nonlinear subsystem that is stable under certain conditions stated below. The integer r is called the *relative degree* and gives information about the controllability of the output λ with respect to the input u.

The Lie (directional) derivative is used frequently to formulate the feedback linearization technique. If given a vector field f and a scalar function h as defined above, then the Lie derivative of h with respect to f at x is the scalar function

$$L_f h(x) =< \nabla_x h(x), f(x) >$$

Furthermore, the higher-order or iterated Lie derivative is defined as

$$L_f^k h(x) =< \nabla_x L_f^{k-1} h(x), f(x) >$$

By virtue of the dot product, the Lie derivative of h calculates the projection of the gradient of h in the direction of the vector f. When the vector field f defines the flow of the state x, $\dot{x} = f(x)$, then the Lie derivative calculates the change in h as x evolves along the state-trajectory: $\dot{h}(x) = \nabla_x h(x)\dot{x} := L_f h(x)$.

In the controlled system of equation (4.4), the trajectory of x flows in the direction determined by the drift vector field $f(x)$ and the control input channel $g(x)$. In this case, the Lie derivative can give information about the controllability of the output λ with respect to u. The dynamics of the output are governed by

$$\dot{\lambda} = \dot{h}(x) = \nabla_x h(x)\dot{x} = \nabla_x h(x) f(x) + \nabla_x h(x) g(x) u = L_f h(x) + L_g h(x) u$$

Thus, the velocity of λ is considered controllable if the function $L_g h(x)$ is nonzero for all $x \in \mathcal{D}$. Suppose however that $L_g h(x)$ was identically zero for all $x \in \mathcal{D}$. That is, the control input channel $g(x)$ does not directly affect the velocity of λ. Then, one may investigate the acceleration of λ.

$$\ddot{\lambda} = \frac{d}{dt}(L_f h(x) + 0u) =< \nabla_x L_f h(x), \dot{x} >$$
$$=< \nabla_x L_f h(x), f(x) > + < \nabla_x L_f h(x), g(x) > u = L_f^2 h(x) + L_g L_f h(x) u$$

If $L_g L_f h(x)$ is not identically zero on $\mathcal{D}$, then one concludes that u directly influences the acceleration of λ. Every time the function multiplying the control input u is found to be identically zero, the next higher-order derivative of λ is computed. The q^{th} order derivative is given by

$$\lambda^{(q)} = L_f^q h(x) + L_g L_f^{q-1} h(x) u \tag{4.6}$$

The *relative degree* r is defined as the value of the integer q in equation (4.6) such that $L_g L_f^{q-1} h(x)$ is not identically zero on $\mathcal{D}$. In this sense, the relative degree is the number of times one must differentiate the output to obtain an explicit dependence on the control input u. This concept of relative degree coincides with the linear system interpretation that $r = P - Z$, where P is the number of system poles and Z the number of system zeros. The formal definition of the relative degree is given below.

Definition 1. *(Relative Degree)*
The SISO system given in equation (4.4), is said to have relative degree r on the set $\mathcal{D}$ if

1. $L_g L_f^k h(x) = 0 \ \forall x \in \mathcal{D}, \ \forall k < r - 1$
2. $L_g L_f^{r-1} h(x) \neq 0 \ \forall x \in \mathcal{D}$

The computations needed for the relative degree calculation for system (4.5) are given below.

$$h(x) = x_1, \qquad L_g h(x) = 0, \qquad L_f h(x) = x_2, \qquad L_g L_f h(x) = 0$$

$$L_f^2 h(x) = x_3|x_3| + \epsilon x_3, \qquad L_g L_f^2 h(x) = 2|x_3| + \epsilon, \qquad L_f^3 h(x) = 0$$

From the above calculations, *in low-bias mode* $\epsilon \neq 0$, the relative degree is $r = 3$ for all $x \in \mathbb{R}^3$. However, *in zero-bias mode* $\epsilon = 0$, the relative degree is 3 away from the plane $x_3 = 0$. Thus, the set of definition for the control law is $\mathcal{D}_1 = \{x \in \mathbb{R}^3 | x_3 \neq 0\}$. Consequences of this are discussed below.

Since the relative degree is equal to the dimension of the system $r = 3$, the nonlinear state equation defined by (4.5) may be transformed into a third order linear system[3]. This is fortunate because if r was less than three, say $r = 2$ for example, then the system could only be decomposed into a *second-order linear subsystem* and a first-order *unobservable and uncontrollable nonlinear* subsystem. Furthermore, even if the control objective is met, that is, λ is regulated to zero, the nonlinear subsystem may still be unstable. Thus, the dynamics of the remaining nonlinear subsystem when the output is held at zero, i.e. the *zero dynamics* , must be proven stable. Systems that are known to have stable zero dynamics are said to be minimum phase.

To see the underlying linear structure of this system, one defines the following nonlinear change of variables. The new state variable ξ is a smooth function of the old state variable x. Specifically,

$$\xi := \Psi(x) = \begin{bmatrix} h(x) \\ L_f h(x) \\ L_f^2 h(x) \end{bmatrix} \tag{4.7}$$

Differentiating ξ to find the new dynamics,

$$\begin{aligned} \dot{\xi}_1 &= \xi_2 \\ \dot{\xi}_2 &= \xi_3 \\ \dot{\xi}_3 &= L_f^3 h(x)|_{x=\Psi^{-1}(\xi)} + L_g L_f^2 h(x)|_{x=\Psi^{-1}(\xi)} u \end{aligned} \tag{4.8}$$

[3]This system does not have zero dynamics.

Select the control input u

$$u = \frac{1}{L_g L_f^2 h(x)}(\nu - L_f^3 h(x)), \tag{4.9}$$

to linearize (4.8) in the ξ coordinates.

$$\dot{\xi}_1 = \xi_2 \tag{4.10a}$$

$$\dot{\xi}_2 = \xi_3 \tag{4.10b}$$

$$\dot{\xi}_3 = \nu := -k_0\xi_1 - k_1\xi_2 - k_2\xi_3 \tag{4.10c}$$

The auxiliary control input ν is used to place the poles of this new linearized system with the appropriate choice of k_0, k_1 and k_2. Equation (4.10c), if written in terms of the output λ,

$$\dddot{\lambda} + k_2\ddot{\lambda} + k_1\dot{\lambda} + k_0\lambda = 0 \tag{4.11}$$

asserts that the λ dynamics may be assigned by the designer to follow any desired linear behavior. This is possible as long as the feedback linearizing control u in equation (4.9) is well defined, that is, if the relative degree is well defined.

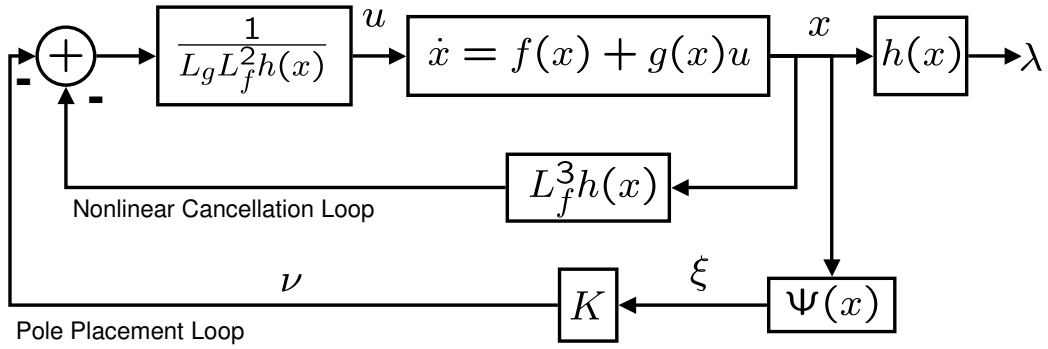

Figure 4.1: Schematic of feedback linearization technique.

In summary, the feedback linearization technique uses an inner feedback loop (4.9) to cancel the nonlinear dynamics and replaces them with the linear dynamics implemented by an outer pole-placement loop in equation (4.10c): see Figure 4.1.

Using f, g and h in equation (4.5), the control law given in (4.9) and (4.10c) is

$$u = \frac{-k_0x_1 - k_1x_2 - k_2(x_3|x_3| + \epsilon x_3)}{2|x_3| + \epsilon} \tag{4.12}$$

This control is singular in ZB ($\epsilon = 0$) on the plane $x_3 = 0$. This is precisely where the relative degree is undefined. As a result, an infinite voltage command is requested in ZB mode when the flux passes through $x_3 = 0$.

4.2.2 Integrator Backstepping Design

Notice that the system of equations (4.4)-(4.5) has the simple cascaded structure below

$$\dot{z} = f_0(z, y) \tag{4.13a}$$

$$\dot{y} = u \tag{4.13b}$$

where the state variables x_1, x_2, and x_3 are partitioned into the mechanical subsystem variables $z = [z_1, z_2]^T := [x_1, x_2]^T$ and the electrical subsystem variables $y = x_3$. With these definitions, $f_0(z, y) := [z_2,\ f_2(y)]^T$ and $f_2(y) = \epsilon y + y^{[2]}$. In the backstepping approach, one views the state-variable y as the "*virtual*" control input to the $f_0(z, y)$ subsystem and assigns the y dynamics via the integrator (4.13b). To this end, first note that if one chooses y such that

$$f_2(y) = \sigma(z) := -k_1 z_1 - k_2 z_2 \tag{4.14}$$

the z-subsystem is feedback linearized and asymptotically stable for $k_1 > 0$ and $k_2 > 0$. In this case, the z-subsystem is given by $\dot{z} = Az$ where

$$A := \begin{bmatrix} 0 & 1 \\ -k_1 & -k_2 \end{bmatrix} \tag{4.15}$$

For $k_1 > 0$ and $k_2 > 0$ the matrix A is Hurwitz. The function σ is often called the *stabilizing* function. Now, introduce the function $u_0 : \mathbb{R}^2 \to \mathbb{R}$ such that $f_2(u_0(z)) = \sigma(z)$ for all $z \in \mathbb{R}^2$. It can be easily verified that

$$u_0(z) := -\tfrac{1}{2}\mathrm{sgn}(\sigma(z))(\epsilon - \sqrt{\epsilon^2 + 4|\sigma(z)|}) \tag{4.16}$$

For $\epsilon = 0$ this function reduces to

$$u_0(z) = \text{sgn}(\sigma)|\sigma|^{\frac{1}{2}} \tag{4.17}$$

If one now tries to implement the *virtual control law* $u_0(z)$ via (4.13b) one immediately faces the problem of the non-Lipschitz continuity of the inverse of the function $f_2(y)$ at the origin when $\epsilon = 0$. If, for instance, the typical error variable $\eta = f_2(y) - \sigma(z)$ is defined, one obtains the backstepping control law

$$u(z,y) = \left(\frac{\partial f_2}{\partial y}\right)^{-1}\Big[\frac{\partial \sigma}{\partial z}(Az + b\eta) - 2b^T Pz - \gamma\eta\Big], \quad \gamma > 0 \tag{4.18}$$

where $b^T = [0,1]$ and $P > 0$ satisfies the matrix inequality (such a P always exists since A is Hurwitz)

$$A^T P + PA < 0 \tag{4.19}$$

Using the Lyapunov function

$$V(z,y) = z^T Pz + \tfrac{1}{2}\eta^2 \tag{4.20}$$

it can be shown easily that the control law in equation (4.18) globally asymptotically stabilizes (GAS) the complete, cascaded system of equation (4.13). However, the control law (4.18) is singular at $y = 0$ for $\epsilon = 0$. Indeed, since

$$\left(\frac{\partial f_2}{\partial y}\right)^{-1} = \frac{1}{2|y| + \epsilon} \tag{4.21}$$

the control law (4.18) is not defined at $x_3 = y = 0$ for the case of zero-bias flux. This is the same singularity space as in the feedback linearization design and consequently, an infinite voltage is requested in ZB when $x_3 = 0$. The domain of definition for the control law (4.18) is $\mathcal{D}_1 = \{x \in \mathbb{R}^3 | x_3 \neq 0\}$.

It should come as no surprise that the singularity is still present even if one introduces an alternative definition for the error. For example, let $\eta = y - u_0(z)$. Then, the z-subsystem can be written as

$$\dot{z} = Az + b(z,y)\eta \tag{4.22}$$

where $b(z,y) = [0,\ \pi(z,y)]^T$, and where $\pi(z,y) \in \mathcal{C}^0$ satisfies $f_2(y) = f_2(u_0(z)) + \pi(z,y)\eta$. For example, one may choose[4]

$$\pi(z,y) := \frac{f_2(y) - f_2(u_0(z))}{y - u_0(z)} \tag{4.23}$$

Using the same Lyapunov function candidate as in (4.20) it can be shown that the choice of the control law

$$\begin{aligned} u(z,y) =& \frac{1}{\sqrt{\epsilon^2 + 4|\sigma(z)|}} \left(\frac{\partial \sigma}{\partial z}\right) \Big(Az + b(z,y)\eta\Big) \\ & - 2b^T(z,y)Pz - \gamma\eta, \qquad \gamma > 0 \end{aligned} \tag{4.24}$$

results in a GAS closed-loop system for all $\epsilon \geq 0$. The control law (4.24) is bounded for all $\epsilon > 0$. For $\epsilon = 0$ this control law exhibits a singularity when $\sigma(z) = 0$. The singularity space consists of a plane in $\mathbb{R}^3$. An infinite voltage is requested on this plane when operating in ZB. The domain of definition for the control law (4.24) is $\mathcal{D}_2 = \{x \in \mathbb{R}^3 | k_1 x_1 + k_2 x_2 \neq 0\}$.

The issue of singularity with the standard FBL and IB control design approaches are well-known in the literature. Several ad hoc methods to remedy this situation have been proposed. In [8] and [50][5], for instance, for the ZB case the authors replace $1/2|y|$ with $1/(2|y| + \delta)$ where $\delta > 0$ is a very small number in the calculation of the denominator of (4.12). A similar small bias term has been added when calculating $(\partial f_2/\partial y)^{-1}$ in the backstepping designs of [15] and [16] to avoid this singularity.

4.3 CLF's for Cascaded Systems

In the sequel, ideas from the theory of control Lyapunov functions (clf's) and the extended integrator backstepping techniques of [63] are used to design a stabilizing control law for (4.3). The clf is defined below.

[4]Notice that $\pi(z,y) \in \mathcal{C}^0$ for all $\epsilon \geq 0$ since $f_2 \in \mathcal{C}^1$.

[5]In these references the current is used instead of the flux as a state variable. However, the approach is essentially the same.

Definition 2. *(Control Lyapunov Function)*

A function $V : \mathbb{R}^n \to \mathbb{R}_+$ is a control Lyapunov function (clf) for the system $\dot{x} = f(x) + g(x)u$ if it satisfies the following properties:

(i) V is positive definite

(ii) $V \in \mathcal{C}^1$

(iii) V is radially unbounded, and

(iv) $L_f V(x) < 0$ for all $x \neq 0$ such that $L_g V(x) = 0$

The stability proof of the control-affine system is obtained by showing that

$$\dot{V}(x) = \nabla_x \dot{x} = L_f V(x) + L_g V(x) u < 0 \tag{4.25}$$

The control input u is selected to dominate $L_f V(x)$ so that $\dot{V} < 0$, however, this is not possible when $L_g V(x) = 0$ because the controllability is lost. Property (iv) of definition 2 guarantees that $\dot{V} < 0$ in equation (4.25) even when $L_g V(x) = 0$.

Control Lyapunov functions have been instrumental for global stabilization of nonlinear systems (see, for instance, [43] and [69]). Generally speaking, if a system has a clf, then there exists a control law (with certain smoothness properties) that renders the system asymptotically stable. Sontag [74] has proposed an explicit expression for such a control law that stabilizes a system using its clf. Sontag's formula is

$$u = \begin{cases} 0, & L_g V(x) = 0 \\ -\dfrac{L_f V + \sqrt{L_f V^2 + L_g V^4}}{L_g V}, & \text{otherwise} \end{cases} \tag{4.26}$$

This control law is smooth in $\mathbb{R}^n \backslash \{0\}$ and it is continuous at the origin if and only if the clf satisfies the *small control property* [43, 74, 83].

The main drawback of the clf approach is that, generally, it is difficult to determine if a system possesses a clf. However, for systems that have a cascaded structure, there exist constructive algorithms to find clf's. To this end, consider a cascade system of

the form as in (4.13) with $z \in \mathbb{R}^{n-1}$ and $y \in \mathbb{R}$. Assume that there exists a control law $u_0(z)$ with corresponding Lyapunov function $V_0(z)$, so that $z = 0$ is a GAS equilibrium of the closed-loop system $\dot{z} = f_0(z, u_0(z))$. Under some mild hypotheses, the function

$$V(z, y) = \tfrac{1}{2}(y - u_0(z))^2 + V_0(z) \tag{4.27}$$

is then a clf for the cascade system [43]. This construction may not work if the stabilizing control law $u_0(z)$ for the z-dynamics is not smooth enough, since in this case the function V may not be $\mathcal{C}^1$; see property (ii) of Definition 2. Notice that this is precisely the situation with the control $u_0(z)$ in (4.17) for the case of an AMB in ZB operation.

To remedy this difficulty, the results of extended backstepping design of Praly et al [63] are employed. According to [63], one introduces a "desingularizing" function $\psi(z, y) \in \mathcal{C}^0$ so that V has the required smoothness properties. The function $\psi(z, y)$ is chosen such that $\psi(z, y) = 0$ implies $y = u_0(z)$. Related to the function $\psi(z, y)$ is the function $\Psi \in \mathcal{C}^1$ defined by

$$\Psi(z, y) := \int_0^y \psi(z, q)dq \tag{4.28}$$

where, for all $z \in \mathbb{R}^{n-1}$, $\Psi(z, y) \to \infty$ as $|y| \to \infty$. The form of the clf is then given by

$$V(z, y) = \Psi(z, y) - \Psi(z, u_0(z)) + \beta V_0(z)^\alpha, \quad \beta > 0 \tag{4.29}$$

where α is such that $V_0(z)^\alpha \in \mathcal{C}^1$.

Assuming a Lyapunov function $V_0(z)$ for the z-subsystem in (4.13a) is known, the problem of finding a clf for (4.13) is reduced to one of finding a desingularizing function ψ. Once the clf is known, one may use Sontag's formula (4.26) to construct a controller. Alternatively, one may use the control law in the following lemma.

Lemma 1. *(Control of Cascade System (4.13) given clf in (4.29) [63])*

Given a system as in (4.13), assume that $u_0(z)$ is a control law that asymptotically

stabilizes (4.13a) and $V_0(z)$ is the corresponding Lyapunov function. Consider the positive definite function $V(z,y)$ given in (4.29). This function is a proper clf for (4.13) and the following choice of the control law will globally asymptotically stabilize (4.13)

$$\begin{aligned} u(z,y) = &\left(\frac{\partial \Psi}{\partial y}(z,y)\right)^{-1} \left\{ \left(\frac{\partial \Psi}{\partial z}(z,u_o(z)) - \frac{\partial \Psi}{\partial z}(z,y)\right) f_0(z,y) \right. \\ &\left. + \alpha\beta V_0(z)^{\alpha-1}\Big(L_{f_0(z,u_0(z))}V_0(z) - L_{f_0(z,y)}V_0(z)\Big)\right\} \\ &- \Theta(z,y) \end{aligned} \tag{4.30}$$

where $\Theta(z,y) \in \mathcal{C}^0$ and has the same sign as $\psi(z,y)$.

4.3.1 CLF Design for the 1-DOF AMB

Next, Lemma 1 is applied in order to find a stabilizing control law for (4.3). The first step is to find a stabilizing controller u_0 and a Lyapunov function V_0 for the z-dynamics. Select u_0 as in (4.16) and $V_0 = z^T P z$ with P as in (4.19). With $u_0(z)$ and $V_0(z)$ in hand, one needs to determine the desingularizing function. Since $u_0(z)^{[2p]} \in \mathcal{C}^1$ for $p \geq 1$ and for all $\epsilon \geq 0$, the following desingularizing function is proposed

$$\psi(z,y) = \epsilon\,(y - u_0(z)) + y^{[2p]} - u_0(z)^{[2p]}, \qquad p \geq 1 \tag{4.31}$$

It can be shown that ψ is continuous and that $\psi(z,y) = 0$ implies that $y = u_0(z)$. The function $\psi(z,y)$ is integrated with respect to y to obtain $\Psi(z,y)$ and $\Psi(z,u_0(z))$. A simple calculation shows that

$$\Psi(z,y) = \int_0^y \psi(z,q)\,dq = \frac{\epsilon}{2}y^2 - \epsilon y u_0(z) + \frac{y^{[2p+1]}}{2p+1} - y u_0(z)^{[2p]} \tag{4.32}$$

and

$$\Psi(z,u_0(z)) = -\frac{\epsilon}{2}u_0(z)^2 - \frac{2p}{2p+1}u_0(z)^{[2p+1]} \tag{4.33}$$

Inserting equations (4.32) and (4.33) into (4.29), one obtains the clf

$$\begin{aligned} V(z,y) = &\frac{\epsilon}{2}\,(y - u_0(z))^2 + \frac{y^{[2p+1]}}{2p+1} - y u_0(z)^{[2p]} \\ &+ \frac{2p}{2p+1}u_0(z)^{[2p+1]} + \beta V_0(z)^{\alpha} \end{aligned} \tag{4.34}$$

with $p \geq 1$, $\beta > 0$, and $\alpha > \frac{1}{2}$, is an appropriate clf for the system (4.3). The value of $\alpha > \frac{1}{2}$ ensures that $V_0(z)^\alpha \in \mathcal{C}^1$. Given the clf in (4.34), one applies Lemma 1 to obtain the following control law for (4.3).

Proposition 3. *(Application of Lemma 1)*

Let $k_1 > 0$ and $k_2 > 0$ and let P be a positive definite matrix such that $A^T P + PA < 0$. Let $V_0 = z^T P z$ and consider the control law

$$\begin{aligned} u = &\Big(\epsilon x_3 + x_3^{[2p]} - \epsilon u_0 - u_0^{[2p]}\Big)^{-1} \\ &\times \Big\{ \frac{p\,(\epsilon - \sqrt{\epsilon^2 + 4|\sigma|})^{2p-1} - 2^{2p-2}\epsilon}{2^{2p-2}\sqrt{\epsilon^2 + 4|\sigma|}} \\ &\times (x_3 - u_0)\Big(k_1 x_2 + k_2 f_2(x_3)\Big) \\ &+ \alpha\beta V_0^{\alpha-1} \frac{\partial V_0}{\partial x_2}\Big(f_2(u_0(z)) - f_2(x_3)\Big)\Big\} - \Theta(x) \end{aligned} \tag{4.35}$$

where $p \geq 1$, $\beta > 0$, $\alpha > \frac{1}{2}$, and where $\Theta(x)$ has the same sign as $\epsilon(x_3 - u_0) + x_3^{[2p]} - u_0^{[2p]}$ with $u_0(\sigma(z))$ and $\sigma(z)$ defined in (4.16) and (4.14), respectively. This control law globally asymptotically stabilizes system (4.3).

Proof. The proposition follows from Lemma 1 by noticing that

$$\begin{aligned} \frac{\partial \Psi(z,y)}{\partial z} &= -y\frac{\partial u_0(z)^{[2p]}}{\partial z} - \epsilon y \frac{\partial u_0(z)}{\partial z} \\ \frac{\partial \Psi(z,u_0(z))}{\partial z} &= -\frac{2p}{2p+1}\frac{\partial u_0(z)^{[2p+1]}}{\partial z} - \epsilon u_0 \frac{\partial u_0(z)}{\partial z} \end{aligned}$$

A straightforward calculation shows that

$$\frac{\partial u_0}{\partial z} = \frac{1}{\sqrt{\epsilon^2 + 4|\sigma|}}\frac{\partial \sigma}{\partial z}$$

Moreover, since

$$\frac{\partial}{\partial z} u_0^{[2p]} = -p\,\frac{(\epsilon - \sqrt{\epsilon^2 + 4|\sigma|})^{2p-1}}{2^{2p-2}\sqrt{\epsilon^2 + 4|\sigma|}}\frac{\partial \sigma}{\partial z}$$

$$\frac{\partial}{\partial z} u_0^{[2p+1]} = \frac{2p+1}{2}\mathrm{sgn}(\sigma)\frac{(\epsilon - \sqrt{\epsilon^2 + 4|\sigma|})^{2p}}{2^{2p-1}\sqrt{\epsilon^2 + 4|\sigma|}}\frac{\partial \sigma}{\partial z}$$

one obtains,

$$\frac{\partial \Psi(z,u_0(z))}{\partial z} - \frac{\partial \Psi(z,y)}{\partial z} = \left(-\frac{p\,(\epsilon - \sqrt{\epsilon^2+4|\sigma|})^{2p-1}}{2^{2p-2}\sqrt{\epsilon^2+4|\sigma|}} + \frac{\epsilon}{\sqrt{\epsilon^2+4|\sigma|}} \right)(y-u_0)\,\frac{\partial \sigma}{\partial z}$$

Furthermore, the difference between the Lie derivative terms in (4.30) can be written as

$$L_{f_0(z,u_0(z))}V_0(z) - L_{f_0(z,y)}V_0(z) = \frac{\partial V_0(z)}{\partial z_2}(f_2(u_0(\sigma)) - f_2(y))$$

Inserting the last two equations into (4.30) one obtains (4.35). □

Since the function $x^{[2p]}$ is odd and one-to-one, a simple choice for Θ that satisfies the requirements of the previous proposition is

$$\Theta(x) = \gamma(x_3 - u_0(z)), \qquad \gamma > 0 \tag{4.36}$$

The control law in (4.35) simplifies to the one reported in [83] for zero-bias mode. Setting $\epsilon = 0$ in (4.35) one obtains

$$\begin{aligned} u = &-(u_0^{[2p]} - x_3^{[2p]})^{-1}\Big\{p\,u_0^{2p-2}(u_0 - x_3)(k_1x_2 + k_2x_3^{[2]}) \\ &+ \alpha\beta V_0^{\alpha-1}\frac{\partial V_0}{\partial x_2}(u_0^{[2]} - x_3^{[2]})\Big\} - \Theta(x) \end{aligned} \tag{4.37}$$

with u_0 as in (4.17). Recall that once the clf (4.34) is known, one can also use (4.26) to construct a stabilizing control law. The added benefit of using (4.37) instead, is that one can ensure that the closed-loop system is homogeneous of degree zero with respect to the dilation[6] $\Delta_\lambda(x) = (\lambda^2 x_1, \lambda^2 x_2, \lambda x_3)$ when $\alpha = (2p+1)/4$ and for all $p \geq 1$. Moreover, the larger the p, the smoother the control law on $\mathbb{R}^n\backslash\{0\}$. Thus, p can be used as a "tuning" parameter to smooth the control law away from the origin.

Remark 2. *(Singularity Spaces of Control Laws)*
The control law in (4.37) is defined on the set $\mathcal{D}_3 := \{x \in \mathbb{R}^3 |\ x_3 \neq 0\ \&\ u_0(z) \neq 0\}$. By

[6]For the relevant definitions on homogeneous vector fields and dilation operators, as well as their properties, see [83] and the references therein.

comparison, the standard feedback linearization (4.12) and backstepping controllers (4.18) and (4.24) are defined on the sets $\mathcal{D}_1 := \{x \in \mathbb{R}^3 | \ x_3 \neq 0\}$ and $\mathcal{D}_2 := \{x \in \mathbb{R}^3 | \ u_0(z) \neq 0\}$, respectively. Thus, the domain of definition of the proposed control (4.37) is much larger than that of a typical backstepping and feedback linearization designs. In fact, the singularity[7] sets $\overline{\mathcal{D}}_1$ and $\overline{\mathcal{D}}_2$ are planes in $\mathbb{R}^3$ while $\overline{\mathcal{D}}_3 = \overline{\mathcal{D}}_1 \cap \overline{\mathcal{D}}_2$ is a line in $\mathbb{R}^3$. Note, however, that in LB mode the control law in (4.35) is always well-defined and $\mathcal{D} = \mathbb{R}^3$.

The next section shows that one may use passivity arguments to design ZB control laws that are nonsingular everywhere.

4.4 Passivity-Based Control Design

In this section it is shown that the simple virtual control law

$$u_0(z) = -k_1 z_1 - k_2 z_2 \tag{4.38}$$

where $k_1 > 0$, $k_2 > 0$, globally asymptotically stabilizes (4.13a) via the virtual input y. Since the control law in (4.38) is linear, it can be implemented directly via (4.13b) using standard backstepping. In order to show that (4.38) is a stabilizing control law for (4.13b), ideas from the theory of dissipative/passive systems [69, 60, 51] are used. The basic concepts are now briefly introduced.

Given a system as in (4.4) with input $u \in \mathbb{R}^m$ and output $\lambda \in \mathbb{R}^m$, define a locally integrable[8] function $w : \mathbb{R}^m \times \mathbb{R}^m \to \mathbb{R}$ called the *supply rate*. For system (4.5), $m = 1$. The supply rate is customarily defined for square systems ($\dim(\mathrm{u}) = \dim(\lambda)$). Physically, this function measures the net power supplied to the system by the input and output channels. The system is called *dissipative* if there exist a function $S(x)$

[7] The singularity set is the complement of the set of definition.

[8] Locally integrable means that $\int_{t_0}^{t_1} |w(u(t), \lambda(t))| dt < \infty$ for all $t_0 < t_1$.

which satisfies $S(0) = 0$, $S(x) \geq 0$, and

$$S(x(T)) - S(x(0)) \leq \int_0^T w(u(t), \lambda(t))dt \tag{4.39}$$

for all bounded u and all $T \geq 0$. If the above *dissipation inequality* holds, then S is called a storage function. Intuition hints that the storage function is similar to the stored energy. The dissipation inequality is interpreted as follows. The change in energy stored in a system (LHS of (4.39)) is less than the net energy supplied. Since the energy stored is less than the supplied energy, some of the supplied energy must have been dissipated by the "resistive" elements of the system. When (4.39) holds with equality, the system is called *lossless*. When the supply rate has the particular form $w(u, \lambda) = u^T\lambda$, the system is called *passive*. Note that if S is differentiable, it is typically easier to evaluate the following differential dissipation inequality

$$\dot{S}(x) \leq w(u, \lambda)$$

The usefulness of the passivity techniques stems from the fact that the passivity properties of dissipative systems are preserved under certain cascade and feedback interconnections. This allows for the study of dissipative subsystems and the construction of composite storage functions as summations of the individual subsystem storage functions. Furthermore, a large class of passive systems may be asymptotically stabilized by output feedback. For example, suppose that $\lambda = 0$ implies that $x = 0$. Then, the storage function $S(x)$ may be used as a Lyapunov function to prove stability. Indeed, $\dot{S}(x) \leq u^T\lambda = -\lambda^T\lambda < 0$ with negative output feedback. Via LaSalle, $x = 0$ is asymptotically stable because $\lambda = 0$ implies that $x = 0$. These ideas are at the heart of the passivity-based control law constructions below.

4.4.1 Stabilization of the Mechanical Subsystem

First, the stabilization of the mechanical subsystem dynamics of the AMB, which is described by the equations,

$$\dot{z}_1 = z_2 \tag{4.40a}$$

$$\dot{z}_2 = f_2(y) = \epsilon y + y^{[2]} \tag{4.40b}$$

is obtained. Then stabilization of the full cascaded system of (4.13) is undertaken in Section 4.4.2.

Lemma 2. *(Dissipativity of $f_2(y)$ nonlinearity)*

Consider the z_2-equation of the mechanical subsystem dynamics (4.40b) with

$$y = -k_2 z_2 + r_1, \qquad k_2 > 0 \tag{4.41}$$

This system is dissipative with input r_1 and output z_2 with respect to the supply rate $w_1(r_1, z_2) = z_2 f_2(r_1)$. Equivalently, it is passive from input $f_2(r_1)$ to output z_2.

Proof. Consider the storage function $S_1(z_2) = \frac{1}{2} z_2^2$. Calculating its time derivative one obtains $\dot{S}_1 = z_2 \dot{z}_2 = z_2 f_2(r_1 - k_2 z_2)$. If $z_2 = 0$ then $\dot{S}_1 = 0$ and the system is trivially dissipative. If $z_2 \neq 0$ (assume without loss of generality that $z_2 < 0$), by the Mean Value Theorem [3] there exists $\xi \in (r_1, r_1 - k_2 z_2)$ such that $f_2(r_1 - k_2 z_2) = f_2(r_1) - k_2 f_2'(\xi) z_2$. Let $\delta(\xi) := f_2'(\xi) = \epsilon + 2|\xi|$. If $\epsilon > 0$ then $\delta(\xi) \geq \epsilon > 0$ for all $\xi \in \mathbb{R}$. For the zero-bias case, $\epsilon = 0$ and $\delta(\xi) = 2|\xi| \geq 0$. Moreover, if $z_2 \neq 0$ then necessarily $\xi \neq 0$ and hence $\delta(\xi) > 0$. To see this, assume instead that $\xi = 0$. Then $f_2(r_1 - k_2 z_2) = f_2(r_1)$ and since the function f_2 is one-to-one, this implies that $r_1 - k_2 z_2 = r_1$ or that $z_2 = 0$, a contradiction.

Hence, the above arguments have shown that

$$\begin{aligned} \dot{S}_1 &= z_2(f_2(r_1) - k_2 \delta(\xi) z_2) \\ &= z_2 f_2(r_1) - k_2 \delta(\xi) z_2^2 \leq z_2 f_2(r_1) \end{aligned}$$

for all r_1 and z_2. Therefore the system (4.40b)-(4.41) is dissipative from input r_1 to output z_2 or passive from input $f_2(r_1)$ to output z_2. □

The integrator (4.40a) is clearly dissipative (in fact, lossless) from z_2 to z_1 with respect to the supply rate $w(z_1, z_2) = z_1 z_2$ and the storage function $S = \frac{1}{2} z_1^2$. The next lemma shows that dissipativity still holds if one chooses a slightly different supply rate.

Lemma 3. *(Dissipativity of Integrator)*

The system (4.40a) from input z_2 to output z_1 is dissipative (lossless) with respect to the supply rate $w(z_1, z_2) = f_2(k_1 z_1) z_2$. Equivalently, it is passive from input z_2 to output $f_2(k_1 z_1)$.

Proof. Let the storage function

$$S_2(z_1) = \frac{1}{k_1} \int_0^{k_1 z_1} f_2(\tau)\, d\tau$$

This is positive definite since f_2 is an odd function. Calculating its derivative yields

$$\dot{S}_2 = f_2(k_1 z_1) \dot{z}_1 = f_2(k_1 z_1) z_2$$

which gives the desired result. □

Lemmas 2 and 3 motivate one to choose the following expression for the input r_1 in (4.41)

$$r_1 = -k_1 z_1, \qquad k_1 > 0 \tag{4.42}$$

The previous choice for r_1 results in a negative feedback interconnection of a dissipative system with a lossless one. The overall feedback interconnection is shown in Fig. 4.2. Under some mild assumptions, it is expected that this interconnection will be GAS. This is indeed true as shown in the next proposition.

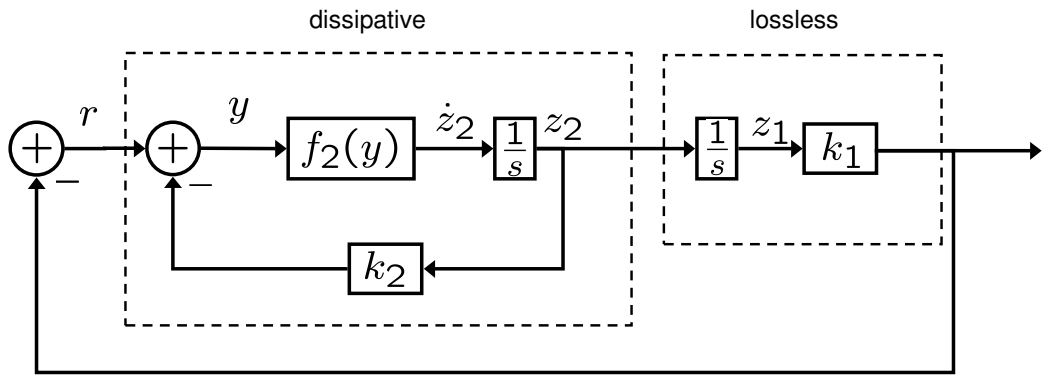

Figure 4.2: Overall feedback interconnection.

Proposition 4. *(Mechanical Subsystem Stabilization)*

The system (4.40) with the control law

$$y = u_0(z) = -k_1 z_1 - k_2 z_2 \tag{4.43}$$

where $k_1 > 0$ and $k_2 > 0$ is GAS.

Proof. Consider the Lyapunov function candidate

$$V_1 = S_1(z_2) + S_2(z_1) = \frac{1}{2} z_2^2 + \frac{1}{k_1} \int_0^{k_1 z_1} f_2(\tau)\, d\tau \tag{4.44}$$

Clearly, this is a positive definite function. Calculating the time derivative of V_1 along the trajectories of (4.40) and following similar arguments as in the proof of Lemma 2, one obtains,

$$\begin{aligned} \dot{V}_1 &= -z_2 f_2(k_1 z_1 + k_2 z_2) + \frac{1}{k_1} f_2(k_1 z_1) k_1 z_2 \\ &= -z_2 f_2(k_1 z_1) - \delta(\xi) k_2 z_2^2 + z_2 f_2(k_1 z_1) \\ &= -\delta(\xi) k_2 z_2^2 \leq 0 \end{aligned}$$

Recall that $\delta(\xi) \geq 0$ and $\delta(\xi) = 0$ if and only if $\epsilon = 0$ and $z_2 = 0$. If $z_2 = 0$ identically then $\dot{z}_2 = 0$. It follows that $f_2(k_1 z_1) = 0$ and hence $z_1 = 0$. Thus, the only invariant set of the system (4.40)-(4.43) is $z_1 = z_2 = 0$. Since V_1 is radially unbounded and $\dot{V}_1 \leq 0$, all system trajectories are bounded. Using LaSalle's Theorem [34], it follows that the system is GAS. □

Energy considerations lead to the following alternative proof of stability of the system (4.40) with control law (4.43).

Proposition 5. *(Mechanical Subsystem Stabilization (Alternate Lyapunov function))* *The following positive-definite, radially unbounded function*

$$V_2 = \frac{k_1}{2} z_2^2 + \int_0^{u_0(z)} f_2(\tau)\, d\tau \tag{4.45}$$

with $u_0(z)$ as in (4.43) is a Lyapunov function[9] *for system (4.40). The first term is similar to the kinetic energy ($\frac{1}{2}mv^2$) of the rotor and the second term is a kin to the work done on the rotor by the electromagnet force.*

Proof. Calculating the time derivative of V_2 along the trajectories of (4.40) one obtains,

$$\begin{aligned} \dot{V}_2 &= k_1 z_2 f_2(u_0(z)) + f_2(u_0(z))(-k_1 z_2 - k_2 f_2(u_0(z))) \\ &= -k_2 f_2^2(u_0(z)) \leq 0 \end{aligned}$$

Since V_2 is radially unbounded all solutions are bounded. If $u_0(z) = 0$ identically, then $\dot{u}_0(z) = 0$. The last condition implies that $\dot{u}_0(z) = -k_1 \dot{z}_1 - k_2 \dot{z}_2 = -k_1 z_2 - k_2 f_2(u_0(z)) = 0$ which together with $u_0(z) = 0$ implies that $z_2 = 0$. Hence also $z_1 = 0$ and the origin is the only invariant subset inside the set $\{ z \in \mathbb{R}^2 : \dot{V}_2 = 0 \}$. Global asymptotic stability follows immediately from LaSalle's Theorem. □

4.4.2 Stabilization of the Cascade

To complete the stabilization of the overall system it suffices to implement the flux command (4.43) via the integrator (4.13b). To this end, let the new state variable

[9] *This Lyapunov function was suggested by A. Teel and M. Arcak [75].*

$\eta = y - u_0(z)$ and rewrite the system dynamics as follows

$$\dot{z}_1 = z_2 \tag{4.46a}$$

$$\dot{z}_2 = f_2(\eta + u_0(z)) \tag{4.46b}$$

$$\dot{\eta} = u + k_1 z_2 + k_2 f_2(y) \tag{4.46c}$$

Proposition 6. *(Local Asymptotic Stability via Input to State Stability)*
Consider the system (4.46) and let the control law

$$u = -k_1 z_2 - k_2 f_2(y) - \gamma\eta \tag{4.47}$$

where k_1, k_2 and γ are some positive constants. Then the closed-loop system is locally asymptotically stable.

Proof. Using (4.47) the closed-loop system takes the form

$$\dot{z}_1 = z_2 \tag{4.48a}$$

$$\dot{z}_2 = f_2(u_0(z)) + \tilde{\pi}(z, \eta)\eta \tag{4.48b}$$

$$\dot{\eta} = -\gamma\,\eta \tag{4.48c}$$

where $\tilde{\pi}(z, \eta) = \pi(z, \eta + u_0(z))$ and $\pi(z, y)$ as in (4.23). The result follows directly by linearizing the closed-loop system (4.46)-(4.47) and showing that the linearized system matrix is Hurwitz. □

Global asymptotic stability cannot be ensured with the control law (4.47) without extra conditions. For example, if one could show that the system (4.48a)-(4.48b) is (Globally) Input-to-State Stable[10] (ISS) from input η to the state z then global asymptotic stability would follow as a result of a cascade interconnection of the globally exponentially stable system $\dot{\eta} = -\gamma\,\eta$ with an ISS system [69].

[10]One may easily show that system (4.48a)-(4.48b) from input η to state z is *Locally* ISS. Thus, only local asymptotic stability of the local ISS system cascaded with the exponentially stable η subsystem may be concluded at this time. For the pertinent definitions, see [69], [34].

Global asymptotic stability can still be ensured if one chooses a slightly different control law and uses the Lyapunov function from Proposition 4.

Proposition 7. *(GAS via Prop. 4)*

The system (4.46) with the control law

$$u = -k_1 z_2 - k_2 f_2(y) - z_2 \pi(z, y) - \gamma\eta \tag{4.49}$$

where k_1, k_2, γ are positive constants, is GAS.

Proof. Consider the Lyapunov function $V = V_1 + \frac{1}{2}\eta^2$ where V_1 as in equation (4.44). The derivative of V is

$$\begin{aligned}
\dot{V} &= z_2 f_2(y) + f_2(k_1 z_1) z_2 + \eta\dot{\eta} \\
&= z_2 f_2(u_0(z)) + z_2 \pi(z, y)\eta + f_2(k_1 z_1) z_2 \\
&\quad +\eta(u + k_1 z_2 + k_2 f_2(y)) \\
&= -\delta(\xi) k_2 z_2^2 + \eta(u + k_1 z_2 + k_2 f_2(y) + z_2 \pi(z, y))
\end{aligned}$$

where $\xi \in (-k_1 z_1, -k_1 z_1 - k_2 z_2)$. Using the control law (4.49) the last equality yields,

$$\dot{V} = -\delta(\xi) k_2 z_2^2 - \gamma\eta^2 \tag{4.50}$$

Recall that $\delta(\xi) = f_2'(\xi) \geq 0$ and that $\delta(\xi) > 0$ for all $\xi \in \mathbb{R}$ if $\epsilon > 0$. In case $\epsilon = 0$ then $\delta(\xi) = 0$ if and only if $z_2 = 0$. In either case, (4.50) implies that the origin is a stable equilibrium point and that all trajectories are bounded. To show asymptotic stability, assume that $\eta = 0$ and that $z_2 = 0$ over a non-trivial interval of time. Then $\dot{z}_2 = 0$ as well, and from (4.46b) it follows that $u_0(z) = 0$. This, along with $z_2 = 0$ implies that $z_1 = 0$. Therefore, the only invariant subset inside the set $\{(z_1, z_2, \eta) \in \mathbb{R}^3 : \dot{V} = 0\}$ is the origin. From LaSalle, it follows that the origin is asymptotically stable. GAS follows from the radial unboundedness of V. □

Alternatively, global asymptotic stability is ensured via the Lyapunov function from Proposition 5.

Proposition 8. *(GAS via Prop. 5)*

The system (4.46) with the control law

$$u = -k_1 z_2 - k_2 f_2(y) - \pi(z,y)(k_1 z_2 - k_2 f_2(u_0(z))) - \gamma\eta \tag{4.51}$$

where k_1, k_2, γ are positive constants, is GAS.

Proof. Let $V = V_2 + \frac{1}{2}\eta^2$ where V_2 as in (4.45). Calculating the derivative of V, yields

$$\begin{aligned}
\dot{V} &= k_1 z_2 f_2(y) - f_2(u_0(z))(k_1 z_2 + k_2 f_2(y)) + \eta\dot{\eta} \\
&= k_1 z_2 (f_2(u_0(z)) + \eta\pi(z,y)) - k_1 z_2 f_2(u_0(z)) \\
&\quad -k_2 f_2(u_0(z))(f_2(u_0(z)) + \eta\pi(z,y)) + \eta\dot{\eta} \\
&= -k_2 f_2^2(u_0(z)) + \eta\Big(u + k_1 z_2 + k_2 f_2(y) \\
&\quad +\pi(z,y)(k_1 z_2 - k_2 f_2(u_0(z)))\Big)
\end{aligned}$$

Letting u as in (4.51) yields $\dot{V} = -k_2 f_2^2(u_0(z)) - \gamma\eta^2 \leq 0$. It follows that the origin is stable in the sense of Lyapunov and that all trajectories are bounded. Global asymptotic stability follows using a standard LaSalle argument. □

In summary, two control laws, (4.49) and (4.51), were derived from Lyapunov functions based on energy considerations and a third (4.47) was constructed from input to state stability arguments. Each of these control laws are nonsingular in ZB. The virtual control law u_0 of (4.38) is implemented through the integrator in equation (4.13b). In contrast to the FBL and IB designs of Section 4.2, the mechanical subsystem (4.40) is *not linearized* by the passivity-based virtual control law u_0 of (4.38). This is advantageous because linearization of (4.40) requires the inverse of the f_2 nonlinearity which is non-Lipschitz continuous and is the source of the infinite voltage commands in the standard ZB nonlinear techniques. In fact, the passivity arguments take advantage of the sector nonlinearity form of the f_2 nonlinearity to prove stability of the mechanical subsystem. A sector nonlinearity is one which exists

in the first and third quadrants: see [34] and [69], for example, for the appropriate definitions. Furthermore, since the f_2 nonlinearity retains its sector properties for any $\epsilon \geq 0$, the passivity based control design gracefully incorporates both the ZB and LB modes of operation.

4.5 Numerical Examples

This section serves several purposes. First, the numerical simulations (via Simulink) allow one to illustrate the performance of the above control laws on the voltage-mode gcfc model of (4.3) with respect to their control parameters. Second, the simulations illustrate the implementation of the gcfc (and cfc) constraint of (3.11) via the state-dependent voltage switching rule (3.9). Assumed in the gcfc condition is the use of a flux bias, however the implementation of this bias has not been addressed. These simulations show that a flux bias may be established in the coils in accordance with the gcfc condition with voltage-mode amplifiers by using a extra feedback loop. This feedback loop has flux measurements available during simulation. For application of this technique on the PREMAG AMB, flux measurements are provided via a static lookup table: see Chapter 6 for a further discussion on flux measurements.

In addition to the simple simulations above, a high fidelity 1-DOF AMB Simulink model is available from Knospe [35]. This model is highly tuned from an experimental apparatus and incorporates several nonlinear dynamics such as flux-spreading (see Section B.3.3), a flux-current-position lookup table for each electromagnet, coil resistance, voltage saturation, and some flexible modes of a rotor. This model was used to test the control laws for robustness to unmodelled dynamics before the PREMAG experimental apparatus was available.

4.5.1 Control Law Verification

This section illustrates the performance of the above control laws when applied to a specific AMB as modelled in (4.3). The specifications for this AMB are shown in

Table 4.1. The constant g_0 is the distance from each electromagnet to the rotor when the rotor is centered at $x = 0$: see Fig. 2.1. These specifications were taken from [35].

Table 4.1: AMB specifications for the numerical examples [35].

Symbols	**Meaning**
$N = 321$	♯ of turns in coil
$m = 4.5$ kg	effective mass of rotor
$\Phi_{\text{sat}} = 200\ \mu$Wb	saturation flux
$A_g = 137$ mm^2	electromagnet pole area
$g_0 = 0.33$ mm (13 mils)	nominal width of airgap (when $x = 0$)
$x_{\max} = 0.254$ mm (10 mils)	maximum displacement

Numerical simulations were conducted for various combinations of the control parameters. The initial conditions for all the simulations are $(x(0), \dot{x}(0), \phi(0)) = (x_{\max}, 0, 0)$. In all simulations it was assumed that both electromagnets start from rest and thus $\phi_1(0) = \phi_2(0) = 0$. This allows for testing the performance of the control laws in zero bias mode by setting $\bar{\Phi}_0 = \Phi_0 = 0$.

Figure 4.3 shows the results for the ZB control law in equation (4.37) for several values of γ. In addition to γ, the control law depends on the parameters p and the gains k_1, k_2, β. The gains k_1 and k_2 were selected as $k_1 = 1$ and $k_2 = 2$. This choice places both poles of the mechanical subsystem (the eigenvalues of the matrix A) at -1. The parameter p in the control law (4.37) governs the degree of smoothness of the function $u_0(z)^{[2p]}$, hence also of the Lyapunov function itself. The states and control histories become smoother with increasing p. The parameter p can thus be used to control the smoothness and "aggressiveness" of the control law. The value of α in all simulations was chosen as $\alpha = (2p + 1)/4$ in order to make the clf homogenous[11] (of degree $2p + 1$) with respect to the dilation $\Delta_\lambda(x) = (\lambda^2 x_1, \lambda^2 x_2, \lambda x_3)$. In all simulations, the parameter p was chosen as $p = 1$. From the figures, one concludes

[11] Homogeneity properties of the zero-bias control law (4.37) are discussed in [83] and the references therein.

that larger values of γ lead to smaller settling times. Similarly, although not explicitly shown, if the gains k_1 and k_2 are selected so that the poles of the matrix A in (4.15) become more negative, the settling time also decreases.

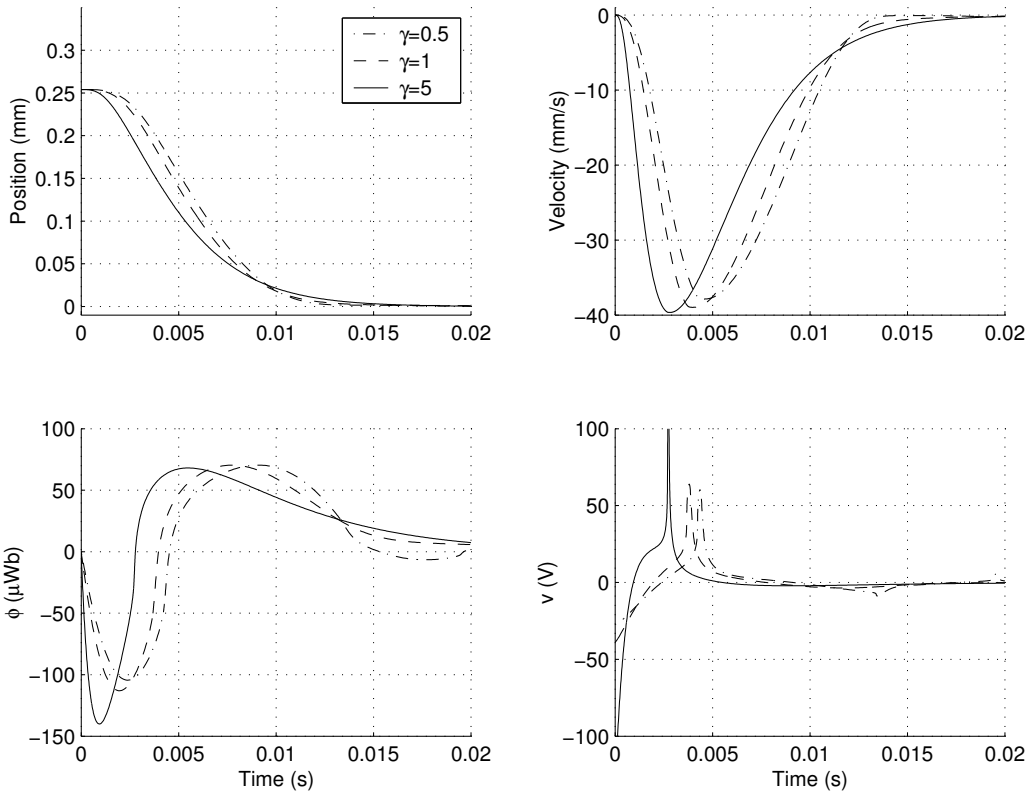

Figure 4.3: ZB operation with control law (4.37) for $\beta = 1, p = 1, k_1 = 1, k_2 = 2$, and $\gamma = 0.5, 1, 5$.

Figure 4.4 compares zero- and low-bias regulation using (4.35) for several values of the bias flux. Specifically, simulations for $\Phi_0 = 0,\ 20$ and 100 μWb are shown. The gains for the first two cases were chosen as $k_1 = 1$ and $k_2 = 2$, whereas in the third case they were chosen as $k_1 = 1.69$ and $k_2 = 2.6$. This ensures that controllers use approximately the same energy (same area under control voltage signals). The results show that a larger bias results in smaller voltages and shorter settling times, as expected. The effect of the parameters γ, p, k_1, and k_2 in low-bias mode were similar to those for the zero-bias mode and hence the results of these simulations are omitted.

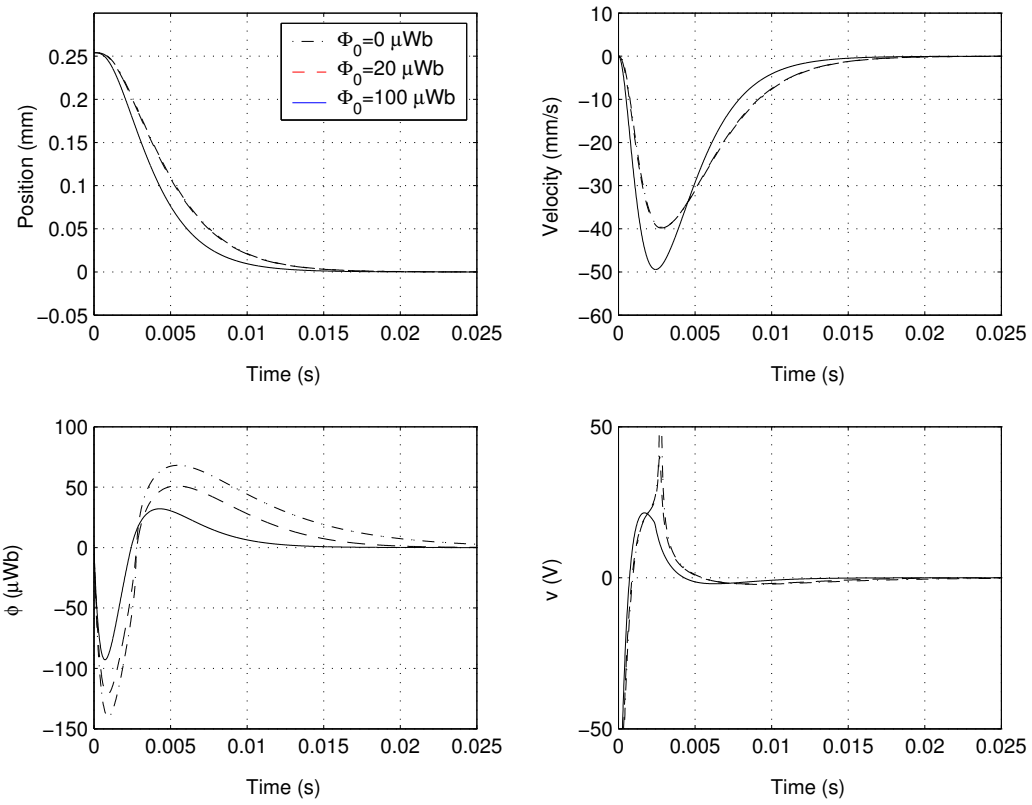

Figure 4.4: ZB and LB operation with control law (4.35) for $\beta = 1, \gamma = 5$ and $p = 1$. $\Phi_0 = 0, 20$, and 100 μWb. Gains k_1 and k_2 are chosen so that each case has similar control.

For Comparison, Figure 4.5 shows the simulation results for the ZB backstepping control law in equation (4.18). The results are shown for several values of γ with $k_1 = 1$ and $k_2 = 2$. Note the presence of the large control spikes as the control flux ϕ passes through zero despite the fact that this simulation was implemented with a nonzero value for $\epsilon = 10^{-3}$ in (4.18).

Several simulations with the passivity-based controllers (4.47), (4.49), and (4.51) were also performed. Since the responses with control laws (4.47), (4.49), and (4.51) were similar, only the results with the control law (4.47) are shown here for illustration. Figure 4.6 shows the dependence of the system trajectories and the control input on the control gain γ for ZB operation. The control gains are chosen as $k_1 = 1$ and $k_2 = 2$. As observed in Fig. 4.6, and similarly to Fig. 4.3, the settling time

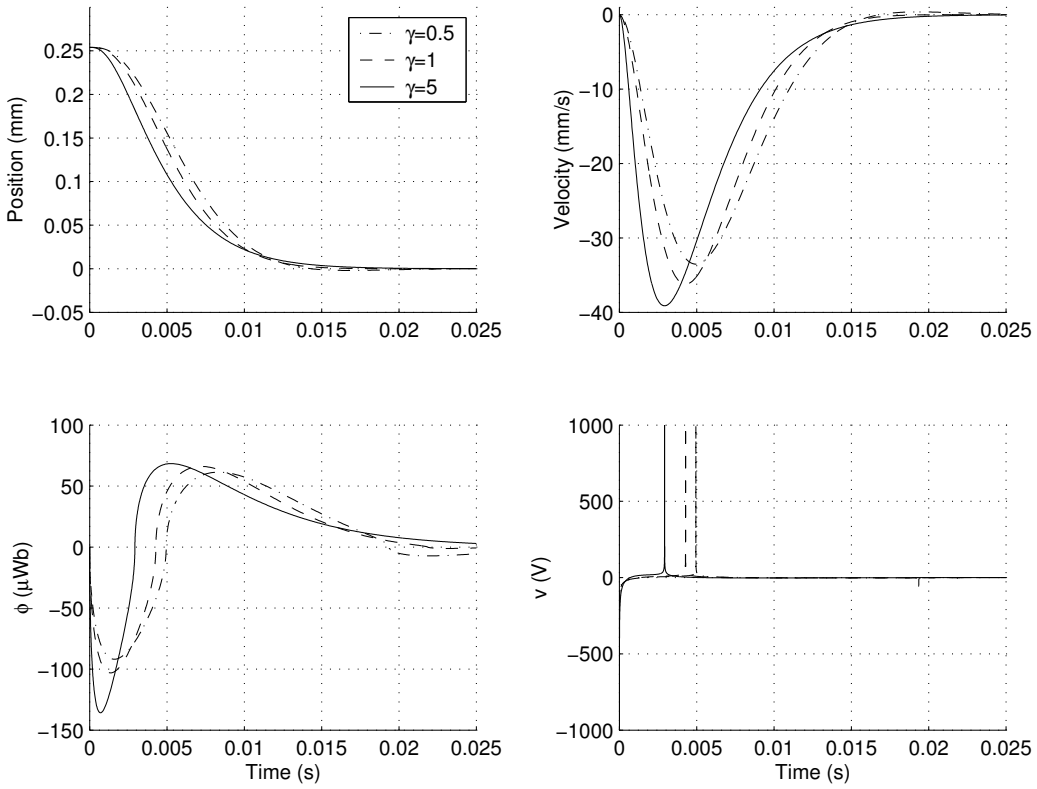

Figure 4.5: ZB operation with backstepping control law (4.18) for $\gamma = 0.5, 1, 5$, $k_1 = 1$, and $k_2 = 2$, and $\gamma = 0.5, 1, 5$. Note the presence of the large control spikes as ϕ passes through zero.

decreases as γ increases. This is achieved at the expense of higher voltage commands. Although not explicitly shown, larger values of k_1 result in faster state convergence rates and larger values of k_2 result in more damped responses.

4.5.2 GCFC Implementation Issues

To implement the gcfc condition in simulation, one must apply the voltage switching rule of (3.9) and implement a flux bias. These are tasks discussed below.

4.5.2.1 The gcfc voltage-switching rule

Care should be taken in interpreting the equation $\dot{\phi} = v/N$ between the generalized control flux and the generalized control voltage. It is reminded that the generalized control voltage v is a fictitious control variable used to simplify the control design.

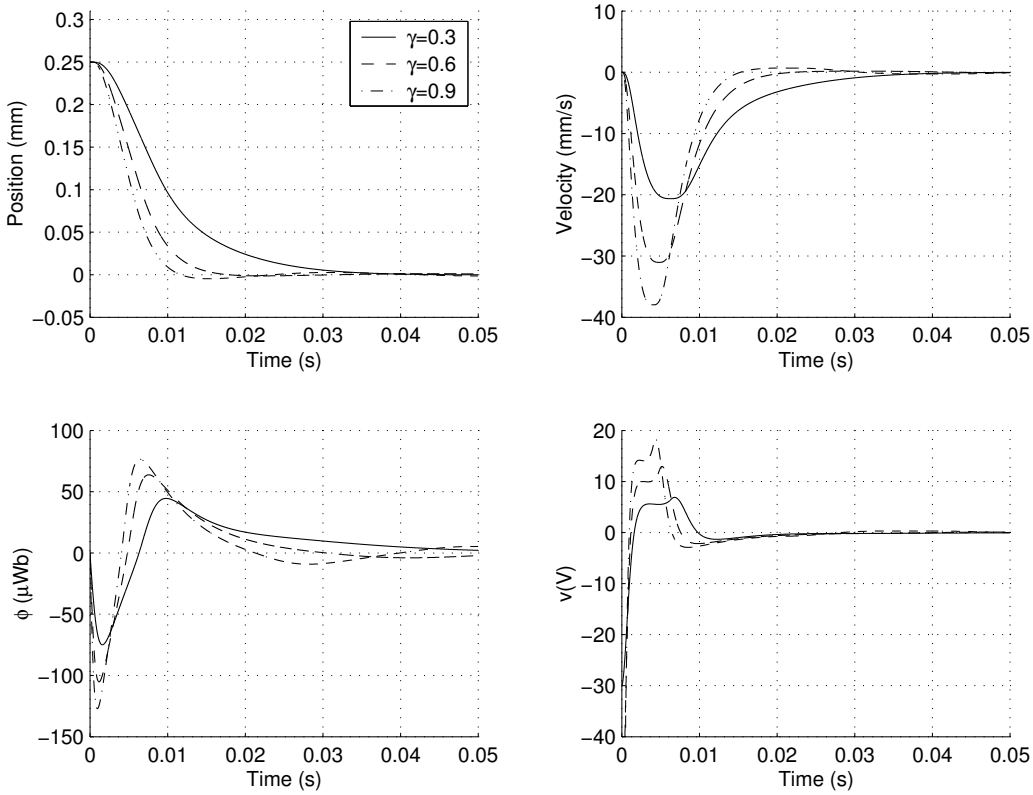

Figure 4.6: ZB operation with control law (4.47) for $k_1 = k_2 = 5$ and $\gamma = 0.3, 0.6, 0.9$.

The actual voltages applied to each electromagnet V_i should be commanded according to the state-dependent switching (3.9). As shown in Theorem 1, at steady-state the bearing will operate at a bias level which is determined by the sum of the actual bias Φ_0 and the minimum of the initial values of the control fluxes. Although typically the latter term will be very small (at least when starting the AMB operation from rest) spurious fluxes may still persist. Normally, these remaining spurious control fluxes will help improve the bearing force-slew rate characteristics. In cases where the elimination of these spurious steady-state fluxes is imperative one has several options:

(i) apply any control law to reduce the control flux in at least one of the electromagnets to zero and thus bring the state into the set $\mathcal{S}_0$. For, example,

using

$$V_1 = \quad v - \lambda\phi_2, \quad V_2 = -\lambda\phi_2 \quad \text{when} \quad \phi \geq 0$$

$$V_2 = -v - \lambda\phi_1, \quad V_1 = -\lambda\phi_1 \quad \text{when} \quad \phi < 0$$

with $\lambda > 0$ instead of (3.9) one obtains system (3.16) with $\bar{\Phi}_0(t) := \Phi_0 + \mathrm{e}^{-\lambda t}\min\{\phi_1(0), \phi_2(0)\}$. A deadbeat controller may also be used to drive the trajectories to the set $\mathcal{S}_0$ in finite time.

(ii) Do nothing. In this case, as shown in Theorem 1 the states $(x, \dot{x}) \to 0$ while $\phi_i(t) \to \min\{\phi_1(0), \phi_2(0)\}$. So, stability of the mechanical states of AMB is still ensured, albeit the AMB will operate at a small additional bias. Nonetheless, in practice due to the coil resistance and the resulting dissipation of fluxes even at zero voltage, the AMB states will drift to the set $\mathcal{S}_0$. In that respect, the proposed gcfc switching scheme is forgiving in the presence of nonzero spurious fluxes. Furthermore, in a real AMB system, measurement noise will corrupt the flux measurement. It is quite possible that the spurious initial flux is smaller than the precision in which the flux can be measured. Thus, it seems as if elimination of the spurious flux is more of a theoretical than practical concern.

For the numerical simulations of the previous section, the switching strategy (3.9) was implemented using SIMULINK without any difficulty. Figure 4.7 shows the control voltages and fluxes for the simulation shown in Figure 4.3. It illustrates how the switching of the generalized control input v according to (3.9) implements the cfc on the total fluxes Φ_2 and Φ_1 (recall that the gcfc strategy (3.9) and the cfc strategy (3.5) coincide in this case). In Figure 4.7 the flux Φ_1 and the negative of Φ_2 are shown for clarity. For comparison, Figure 4.9 shows a simulation with a nonzero bias $\Phi_0 = 20\mu\text{Wb}$ ($\epsilon = 0.2$) using the high-fidelity model previously mentioned (more on this later). Figure 4.9 shows the total fluxes and the corresponding control voltages. It demonstrates how switching of the control input v in accordance with (3.9) imposes

the gcfc constraints on the control fluxes ϕ_1 and ϕ_2. One may verify that both electromagnets are biased, however, only one electromagnet is used at a time to produce a net control force on the rotor.

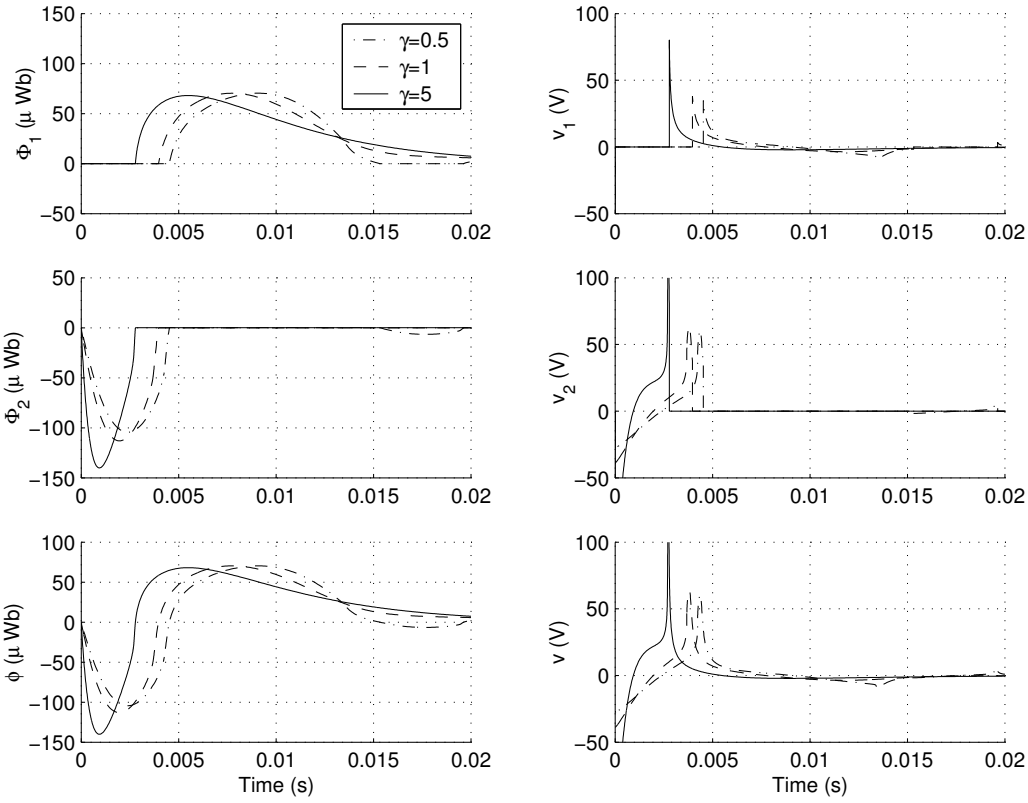

Figure 4.7: ZB operation with control law (4.37) for $p = 1, k_1 = 1, k_2 = 2$, and $\gamma = 5, 10, 15$. Illustration of how the voltage switching rule (3.5) imposes the cfc constraint on the total fluxes.

4.5.2.2 Flux-Bias Implementation

The gcfc condition of equation (3.11) assumes voltage-mode amplifiers and the use of a flux bias, however, the realization of the flux bias has not yet been addressed. With the power amplifiers operating in voltage mode a flux-feedback inner loop can be used to regulate the bias flux at Φ_0. That is, one may modify the voltage reference V_r as follows.

$$V_{rj} = V_{bj} + V_{cj} \qquad j = 1, 2$$

where V_r is the voltage reference signal applied to the amplifiers, V_b is the flux bias control signal and V_c is the control signal generated by any of the control laws in Sections 4.2, 4.3 and 4.4 above.

In Figures 4.8 and 4.9 use a flux-feedback PI inner loop to generate the bias flux control signal V_b. Figure 4.8, in particular, shows the results of the simulations using the high-fidelity AMB model of [35] (voltage saturation level set to $V_{\text{sat}} = 10$ V). In the figures, the dashed line is the simulation results when the control law of (4.35) acts on the ideal model, i.e., when the plant's flexible modes, coil resistance, flux leakage and voltage saturation are neglected. The solid line is the response of controller (4.35) with $p = 1$, $\epsilon = 0.2$ ($\Phi_0 = 20$ μWb) using the high-fidelity AMB model. This simulation presents a situation where the control is acting on a system with additional un-modelled dynamics. The "ripples" in the voltage input are due to the rotor flexible modes. Despite the additional effects of the high-fidelity model, the qualitative behavior of the system is similar as in the ideal model case. The discrepancy (mainly delay) in the state trajectories of the actual system in Figure 4.8 can be traced to the voltage saturation through simulation. The effects of voltage saturation during LB operation are dealt with in [80]. From Figure 4.9, one also sees that the implementation of the flux bias via a PI flux-feedback inner loop works well. Observe that a bias of 20μWb is quickly established in both electromagnets. The voltage v is the voltage generated from the control law (4.35). This voltage command is distributed to the two electromagnets as V_{c1} and V_{c2} where it is added to the flux bias voltage commands V_{b1} and V_{b2}. The voltages V_1 and V_2 shown represent the total voltage request, that is, $V_{rj} = V_{bj} + V_{cj}$ for $j = 1, 2$.

4.6 Chapter Summary

This chapter presents the designs of several ZB and LB control laws for a 1-DOF AMB that is working with voltage-mode amplifiers and constrained by the gcfc condition.

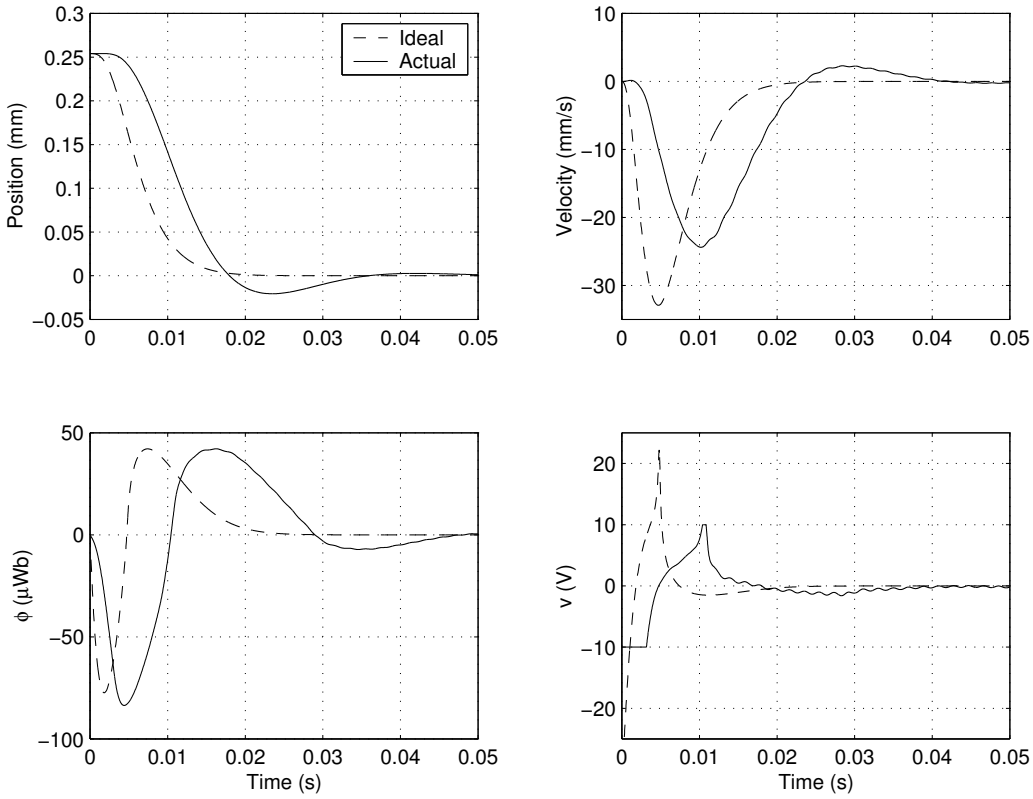

Figure 4.8: Comparison of response between ideal and high-fidelity AMB models with control law (4.35).

The assumed plant model is given in equation (4.3) and is parameterized by the bias constant $\epsilon \geq 0$. ZB is implemented when $\epsilon = 0$ and LB operation occurs with $\epsilon > 0$. These new control laws stem from the theory of control Lyapunov functions and dissipativity and are valid for both ZB and LB operation. Due to the form of the plant model, each LB control law contains a ZB control implementation as $\epsilon \to 0$. The control laws developed in Sections 4.3 and 4.4 are better behaved than the standard feedback linearization and integrator backstepping control laws described in Section 4.2. In particular, as the bias reduces to zero, the FBL and IB laws are singular on a plane in $\mathbb{R}^3$, the clf control law is singular on a line in $\mathbb{R}^3$ and the passivity-based control laws are nonsingular on $\mathbb{R}^3$.

The feasibility of the gcfc constraint was shown through simulation. The state-dependent voltage switching law of (3.9) imposes the complementarity condition on

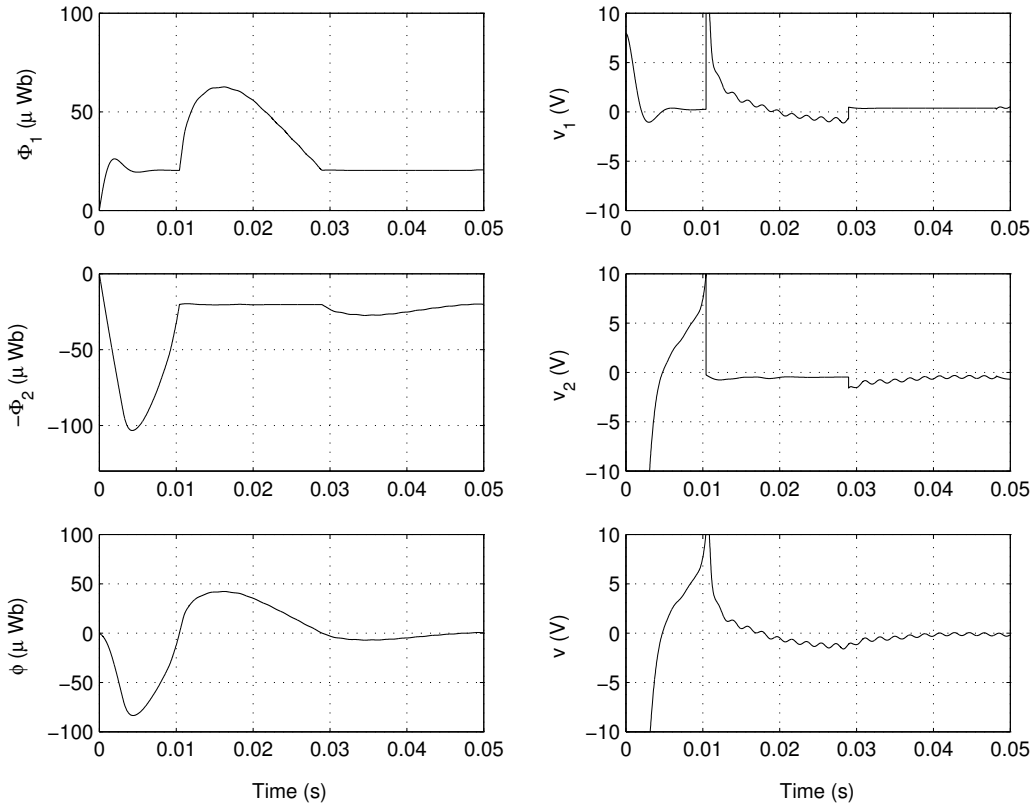

Figure 4.9: Illustration of gcfc scheme for the high-fidelity AMB model with control law (4.35). The total fluxes Φ_1 and Φ_2, the control flux ϕ, and the corresponding control voltages are shown. The bias flux is set to $\Phi_0 = 20\mu$Wb by an extra flux-bias feedback loop. The signals v_1 and v_2 include the voltages used to set this bias.

the control fluxes ϕ_1 and ϕ_2: See Figure 4.9. Furthermore, a voltage-mode flux-bias feedback-control loop may be used to set up a flux bias in the electromagnets. In the simulation, flux measurements are assumed to be available. In addition, simulations with a high-fidelity AMB model show that the control laws have some degree of robustness to un-modelled dynamics.

CHAPTER V

EXPERIMENTAL SETUP

5.1 Overview of Experimental Investigations

Although the simulation results in the previous chapter suggest that the gcfc technique and the new control laws of Sections 4.3 and 4.4 are valid, several practical and theoretical questions must be posed. There are practical concerns about the implementation of the flux bias, the gcfc technique, and the control laws because each one depends on flux measurements. However, measurement of the flux is not trivial. Furthermore, since the voltage-switching rule is triggered when the flux passes through zero, it is unclear if flux measurement noise will interfere with the realization of the gcfc condition. Also, it has been assumed that IR compensation is possible on a real system. However, this may be a challenging proposition because the resistance may change with coil temperature. In addition, each control law uses the rotor velocity as a state. In general, velocity estimation in the presence of measurement noise can be problematic.

The simulations and control laws from the previous chapter also pose several theoretical questions. The reduction of the singularity space for the control laws operating in ZB in the previous chapter was of great concern. The control designs progressed from the backstepping controller, singular on a plane in $\mathbb{R}^3$, to the clf-based controller, singular on a line in $\mathbb{R}^3$, to the completely non-singular passivity-based control laws. At this point, it is unclear whether the effort to reduce the singularity space is of practical value or if it is just a theoretical exercise. Also, it is suggested that there is a trade-off between the AMB stiffness, power consumption, and FWB efficiency as the flux bias changes. How large should the bias be before any significant

change in the stiffness is seen? How small can the bias become before the singularities of the ZB control laws produce large voltage spikes? Will the limited bandwidth and voltage saturation of the voltage mode amplifiers lead to instability in ZB or just to a reduction in performance? These questions can only be answered by verifying the above control laws and gcfc conditions on a real AMB system such as the PREMAG reaction wheel.

This and the next several chapters describe the experimental setup for testing of the nonlinear control laws on the PREMAG reaction wheel and the experimental results. This chapter focuses on the setup of the experimental hardware and its operation. Chapter 6 continues to answer the practical questions concerning flux measurement, the implementation of the flux bias and the gcfc condition. Chapter 7 derives the 4 degree-of-freedom state space model of the PREMAG reaction wheel and the approach to its control. As a preliminary step to the investigation of the nonlinear control laws, the reaction wheel is first stabilized with 4 independent, SISO, Lead+PI linear control laws with the amplifiers using a large bias while acting in current mode. Once the reaction wheel is stabilized, one of the control axes is converted to a test bed for the nonlinear low-loss controllers by using the amplifier in voltage mode with IR compensation. Chapter 8 presents the experimental results for the low-loss nonlinear controllers. In particular, the modifications to the control laws so that they can eliminate steady state errors due to disturbances is presented. Also, their regulation performance as a function of the flux bias is investigated in several testing situations. The trade-off between stiffness, power consumption, total square flux requirements, and operation near ZB singularities is presented.

5.2 Experimental Hardware and Configuration

This chapter describes geometry and operation of the 6-DOF reaction wheel illustrated in Figure 1.3 and the supporting control hardware. The reaction wheel was

provided to the author by the Air Force Research Labs (AFRL) for experimental testing of the low-loss control algorithms designed in Chapter 4. AFRL originally commissioned Precision Magnetic Bearing Systems, Inc. (PREMAG) to construct the lightweight, magnetically-suspended reaction wheel for use on a small satellite.

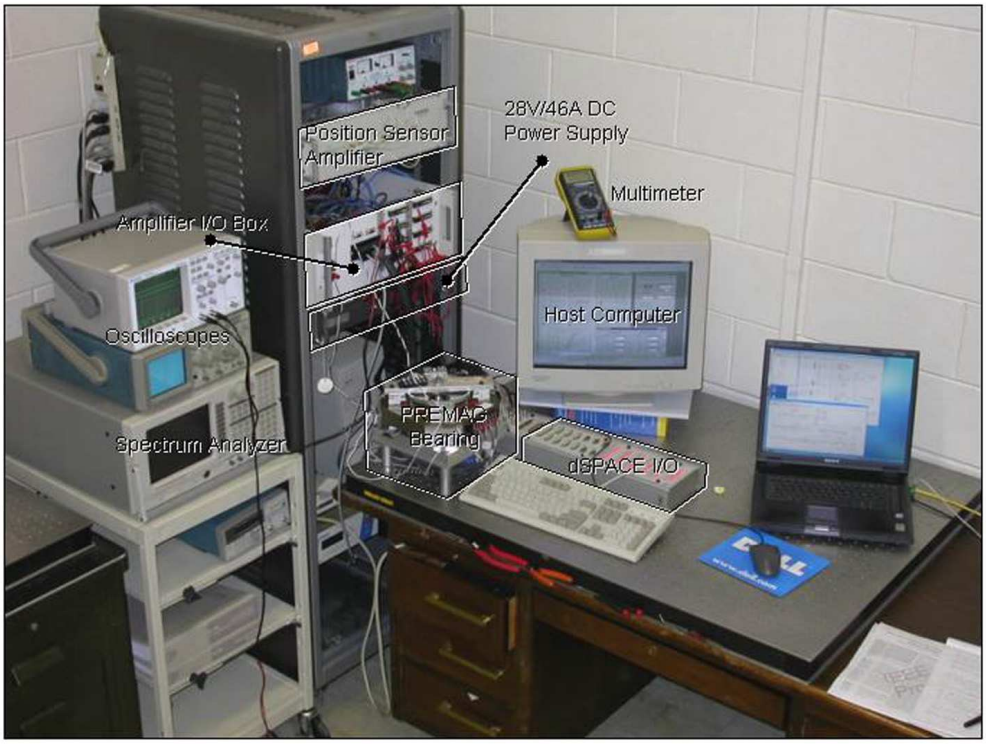

Figure 5.1: Dynamics & Control Systems Laboratory (DCSL) at Georgia Tech Aerospace Engineering Department.

Figure 5.1 presents a photo of the Dynamics and Control Systems Laboratory (DCSL) of the Aerospace Engineering department at Georgia Tech. The reaction wheel assembly occupies about one cubic foot in volume and is mounted on a standard optics bench. Since the low-loss control algorithms may be verified with the rotor spinning at low (or even zero) angular velocity, a cost-prohibitive containment

system is not deemed necessary[1]. Standard laboratory equipment including a spectrum analyzer, several oscilloscopes, a multimeter, and a bench power supply are shown.

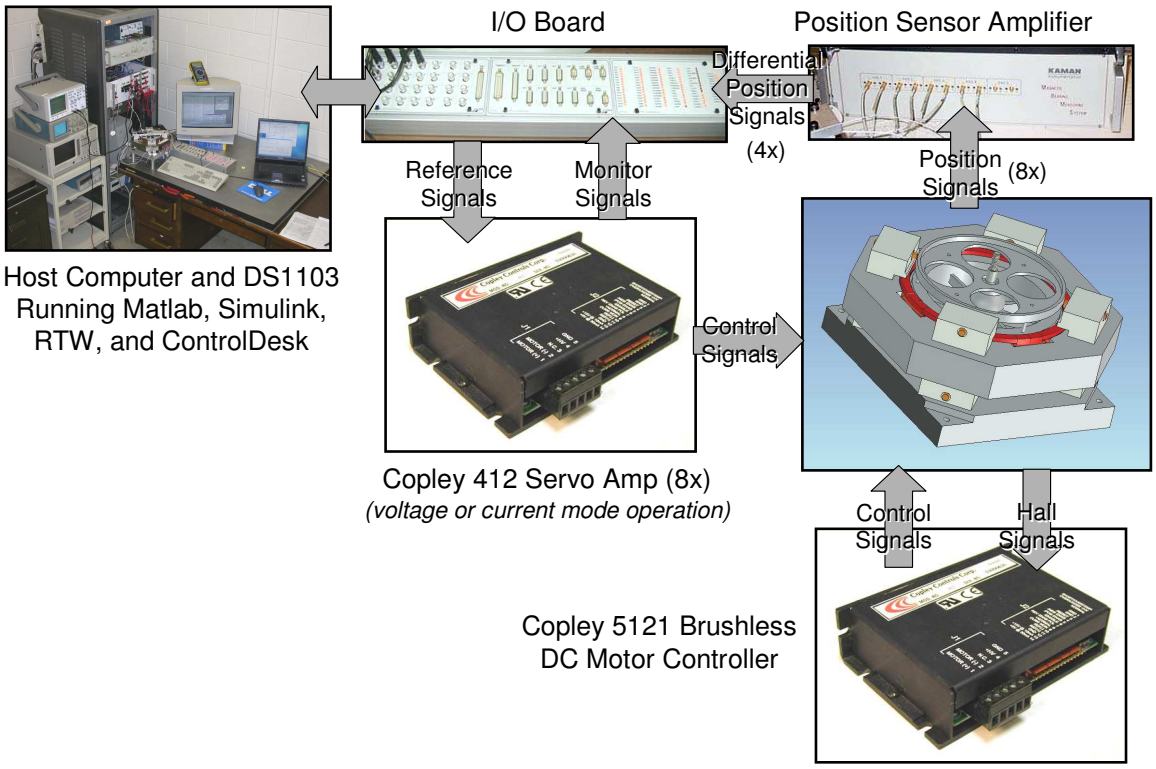

Figure 5.2: Hardware feedback loop.

Figure 5.2 shows a graphic of the hardware feedback loop. The components are listed below. Each component is described in detail in the following sections.

- **PREMAG Reaction Wheel:** The PREMAG reaction wheel assembly consists of a highly-balanced rotor, eight electromagnets, brushless 3-phase DC motor mounted in rotor hub and necessary hall position sensors, and eight eddy-current proximity sensors. Neodymium-Iron-Boron (Neo) radially poled permanent magnets provide a flux bias for bearing stiffness and passive vertical rotor levitation.

[1]At this time, reaction wheel spin tests are not conducted because the reaction wheel spin motor is in need of repair. Since the control laws may be verified without spinning, repair of the reaction wheel motor was deemed low priority.

- **Position Sensor Amplifier:** The Kaman Instrumentation Measurement Systems Inc. eight-channel preamplifier provides the driver electronics for the eddy-current proximity sensors and produces eight voltage signals (and four differential voltage signals) that are proportional to the airgaps on each side of the rotor.

- **Eight Power Servo-Amplifiers:** [**84, 85**] Eight Copley Controls Inc. model 412 power servo-amplifiers are selected to drive the eight electromagnet coils. The amplifier uses a high-power H-Bridge PWM output stage and employs internal feedback to operate in *current* mode, *voltage mode* or *voltage mode with IR compensation.* Note that the Copley Controls model 5121 Brushless DC motor controller is available for driving the DC motor constructed within rotor hub. However, since the spin motor was not used in this investigation, the presentation of this hardware is omitted.

- **Anti-Aliasing and Signal Conditioning Filters:** Several active and passive low-pass and notch filters are implemented for anti-aliasing and PWM noise rejection on each A/D and D/A channel.

- **dSPACE 1103 Data Acquisition System:** The dSPACE Inc. model 1103 data acquisition system is selected for digital implementation of the control algorithms. The hardware has 20 analog inputs, 8 analog outputs, multiple digital I/O channels. The system is designed around a Motorola $400MHz$ power PC processor and has a convenient I/O interface board. The dSPACE board seamlessly interfaces with Matlab and Simulink and makes control implementation a one mouse-click procedure.

5.3 PREMAG AMB Geometry and Operation

The geometry of the AMB is now described. Figure 5.3 shows an exploded view of the AMB. Eight electromagnets and eddy-current proximity sensors are mounted into the housing which is bolted to the base plate. The rotor shaft fits through the center hole of the base plate and is held securely in place by a nut. A nominal airgap g_0 of about 20 mils exists between the electromagnets and the rotor. Define an inertial coordinate frame centered at the geometric center of the housing with the X and Y axes aligned with the axes of the position sensors: see Figure 5.3. The inertial Z axis lies along the rotor shaft.

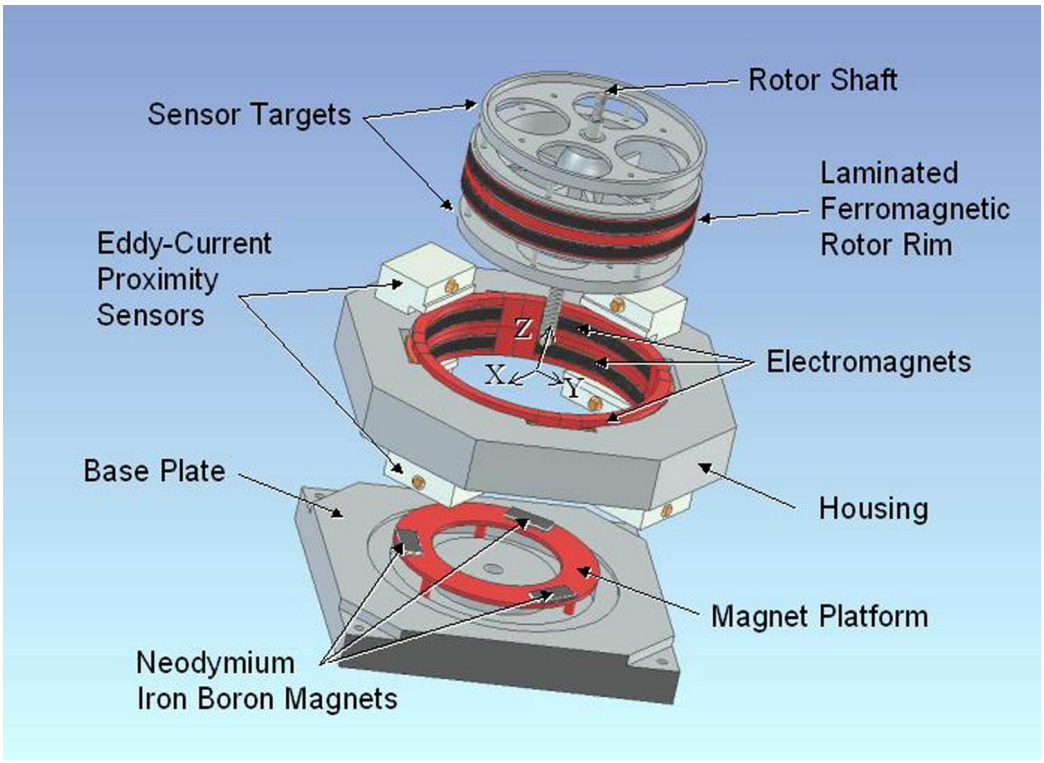

Figure 5.3: Exploded view of PREMAG reaction wheel. Note that some position sensors are hidden for clarity.

The rotor is composed of the hub, the spokes, the laminated ferromagnetic rim, the two circular Aluminium sensor targets, and the rotor shaft. Most of the mass of the rotor is concentrated in the rim to increase the rotational inertia. This rotor

has been spin balance tested by PREMAG up to 28,000 rpm. As illustrated in Figure 5.4, a brushless DC permanent magnet motor constructed within the rotor hub provides the spin about the Z axis. Note that the stator windings of this DC motor are mounted on the stationary rotor shaft and the motor permanent magnets are mounted on the interior of the rotor hub. This motor is driven by the Copley 5121 Motor controller. The rotor is only *loosely connected* to the stationary rotor shaft. A horizontal and vertical clearance between the rotor hub and the rotor shaft allows for 6-DOF of movement of the rotor. The backup or catcher ball-bearings limit the range of motion to ± 18 mil horizontally and ± 5 mil vertically. The axial motion is passively stabilized.

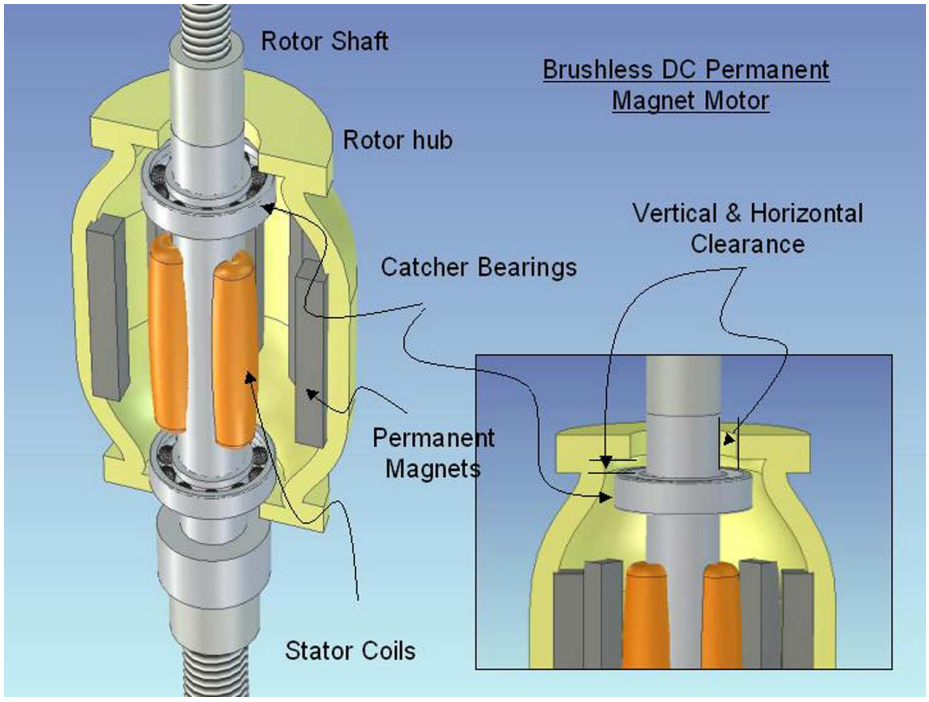

Figure 5.4: Detail of the brushless DC permanent magnet motor.

Four degrees-of-freedom of the rotor are actively stabilized via feedback control. The proximity sensors measure the airgap between the sensor face and the sensor targets. The rotor position and orientation is determined from these measurements. The goal of the control law is to regulate the rotor position and orientation to $X =$

$Y = 0$ and $\theta_X = \theta_Y = 0$, respectively. Equivalently, one may regulate each of the eight airgap lengths to g_0. In this case, the four degrees-of-freedom are the horizontal positions of the center of the top and bottom of the rotor. These control axes are represented by X_t, Y_t, X_b, and Y_b. In this work, strict performance specifications on the rotor regulation are not stated. This work serves only as a control law feasibility study, and a control law will be deemed successful if the rotor avoids contact with the electromagnets and the rotor shaft in the presence of disturbances. Stabilization of the rotor is of primary concern. The 4-DOF modelling and stabilization of the rotor by 4 independent SISO linear control laws is presented in Chapter 7. Once the rotor is stabilized, the X_b control axis is used as the test bed for the nonlinear low-loss control techniques of Chapter 4.

5.3.1 Passive Axial Stabilization

Figure 5.5 shows a closeup of the AMB airgap and a cross-section of the rotor, the housing, and the electromagnet (EM) cores (the electromagnets that fit around them have been suppressed for clarity). In the original configuration of the PREMAG bearing, a radial flux bias was established with radially poled Neodymium-Iron-Boron (Neo) magnets. They were oriented so that flux would flow through the top EM core, down through the rotor, into the bottom EM core and complete the loop in the housing. This flux bias served two purposes. First, the radial bearing stiffness is increased: recall that the bearing stiffness depends directly on the bias flux, see equation 3.4. This is an inexpensive way to provide a constant bias flux and has the added benefit of requiring no electrical power. Second, the flux bias is required energize the airgap for the passive stabilization of the rotor in the axial Z direction. Table D.2 in Appendix D.2 states that the force generated by a magnetic field always acts in the direction to minimize the reluctance of the airgap. The clever tooth-like design of the rotor and EM faces results in an airgap reluctance that is minimum when

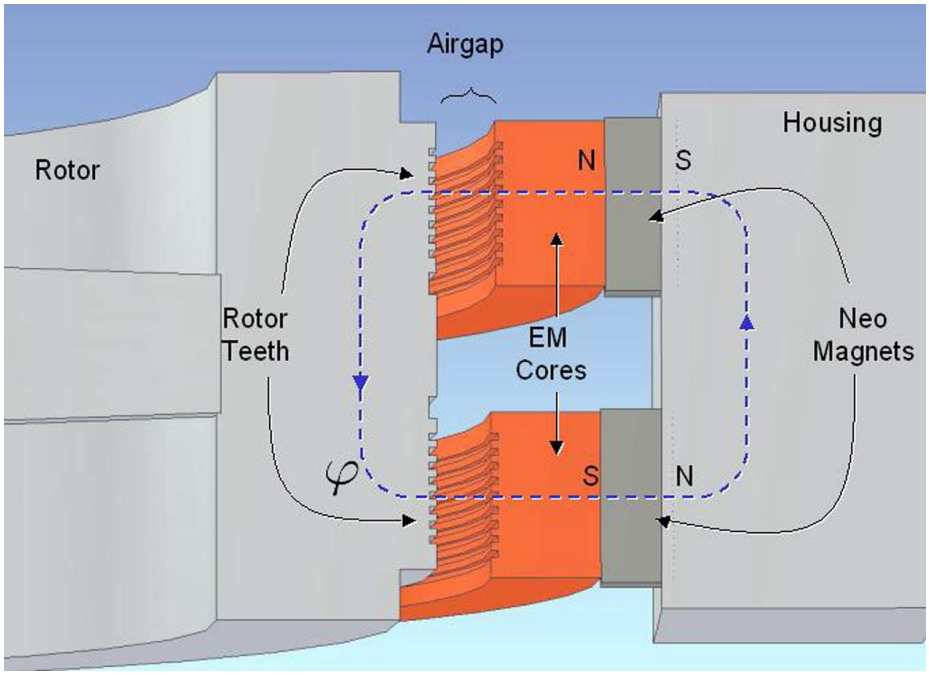

Figure 5.5: Original permanent magnet flux bias and passive Z magnetic bearing .

the teeth are aligned. When the rotor moves in the axial Z direction, the reluctance increases and consequently the force generated by the magnetic field reacts to reduce the reluctance. This results in a passive axial magnetic bearing. The alignment of the rotor and electromagnets shown in Figure 5.5 is the minimum reluctance $Z = 0$ equilibrium point.

This approach to passive vertical stabilization of the rotor is advantageous for low angular velocity, linearly controlled AMBs. The constant flux bias is provided with no electrical power and it only requires proper shaping of the bearing components and some inexpensive Neo magnets. However, this configuration presents a problem *for low-loss AMB studies*. The problems of a large flux bias for low-loss bearing design are stated in Section 2.2.2. Operation with low or zero flux bias is desired. In principle, one could bias the electromagnet coils to lower or even remove the flux bias, however this is a tricky proposition. The extraordinarily strong field and very high coercivity of Neo magnets may require large bias currents leading to coil heating, changing coil resistances, core heating, etc. Furthermore, if one is successful in eliminating

the radial flux bias for ZB control studies, then one has also eliminated the vertical support for the rotor. A new vertical support system must be constructed that is independent of the radial bias flux.

To solve this problem, the radially poled permanent magnets are removed and a new passive magnetic bearing is constructed. As shown in Figure 5.6, twelve axially poled Neo magnets are attached to the bottom of the lower sensor target with industrial strength epoxy. No analysis has been done to calculate the maximum angular rotor velocity that will stress the epoxy to failure. This presents a potentially hazardous situation and high-speed rotor testing with this configuration is not recommended. Fortunately, the low-loss AMB control feasibility studies may be conducted with the rotor at low (even zero) angular velocities. The twelve magnets mounted on

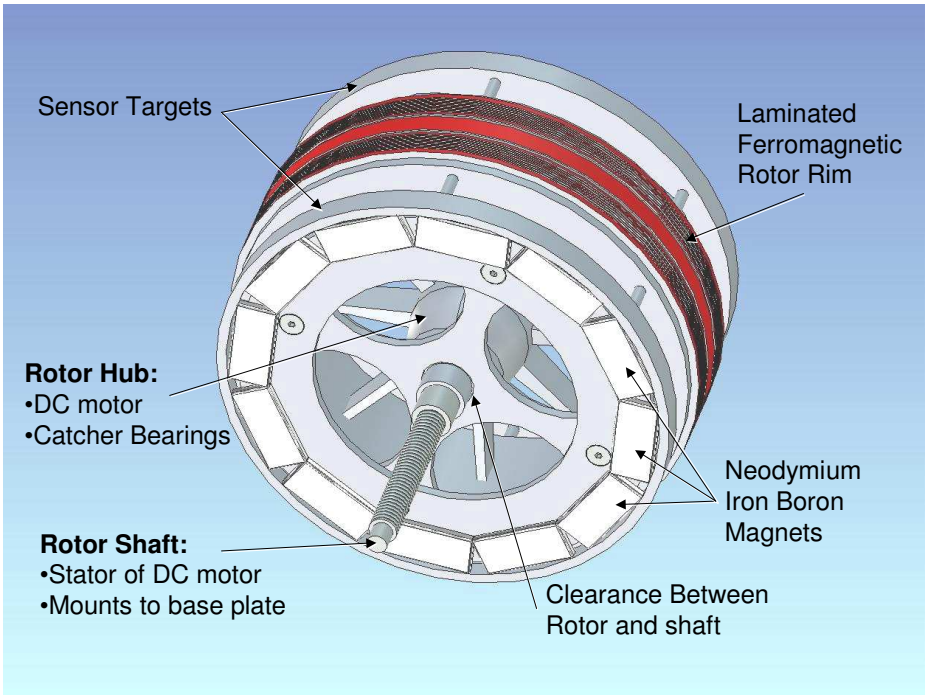

Figure 5.6: Bottom view of rotor.

the rotor repel the three Neo magnets mounted on the base magnet platform shown in Figure 5.3. Thus, the rotor floats on a magnetic cushion and is passively supported against its own weight in the Z direction.

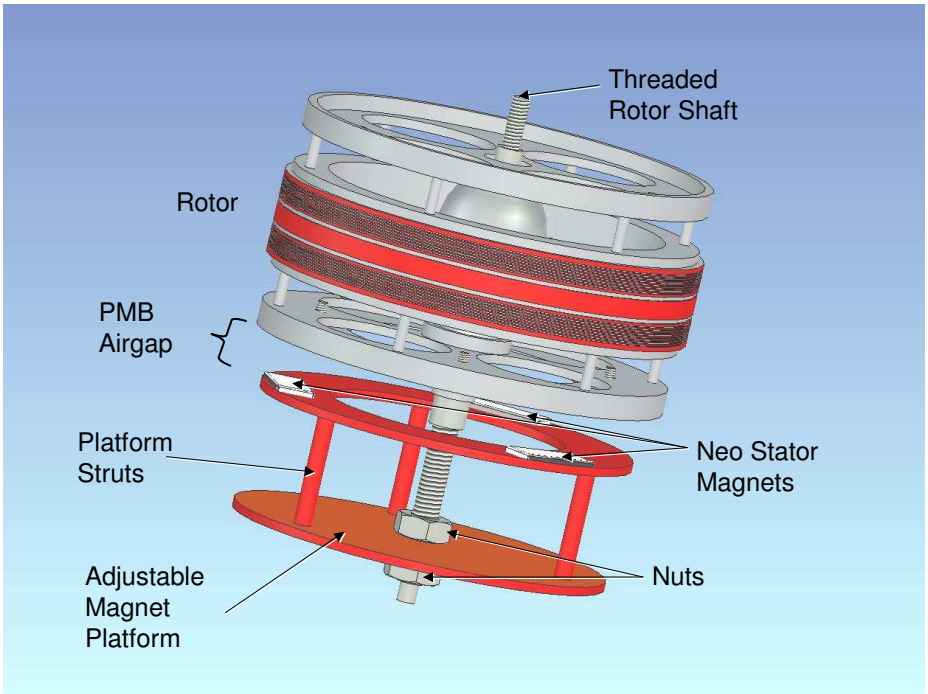

Figure 5.7: Rotor axial support system.

The design of this passive magnetic bearing (PMB) was conducted by trial and error. To make the mechanical design flexible, the stator mounting platform's axial position is adjustable. As seen in Figure 5.7, the mounting platform is connected to the threaded rotor shaft by a two nuts and the platform struts fit through holes bored into the base plate. Adjustment of the nuts allows one to precisely set the PMB airgap. To tune the PMB, use the following procedure. First, regulate the rotor position with feedback control so that the rotor is not touching the electromagnets or the catcher bearings in the radial direction. Next, check to see if the rotor is rubbing against the catcher bearings in the Z direction by spinning the rotor. The rotor comes to a stop within a few revolutions when there is contact with the catcher bearings. Now adjust the nuts to eliminate any contact between the rotor and the catcher bearings and continue with the radial control design testing.

Note that the PMB does not have the best damping characteristics and some minor oscillation along the Z axis during a quick rotor transient is possible. Also, proper

design of the shape of the PMB field is required to avoid some "bouncing" of the rotor along the Z direction when the rotor spins. To have a perfectly symmetric PMB field, one would ideally construct a continuous, axially poled Neo ring and mount it to the sensor target in place of the 12 Neo magnets. However, this would most likely require the services of a subcontractor to construct. The cheaper 12 discrete Neo magnet solution is an approximation to this ideal situation. The magnetic flux density of the Neo magnet is strongest at the center of the magnet and degrades quickly near the edges. Thus, there is a variation in the B field in the Z direction as one traverses the discrete 12 magnet ring. If this variation in the axial B field is too dramatic, the net axial magnetic force created by the interaction of the PMB rotor and stator magnets may be a function of the rotor spin angle. As a result, the rotor may "bounce" in the Z direction when the rotor spins if the axial B field variation is extreme.

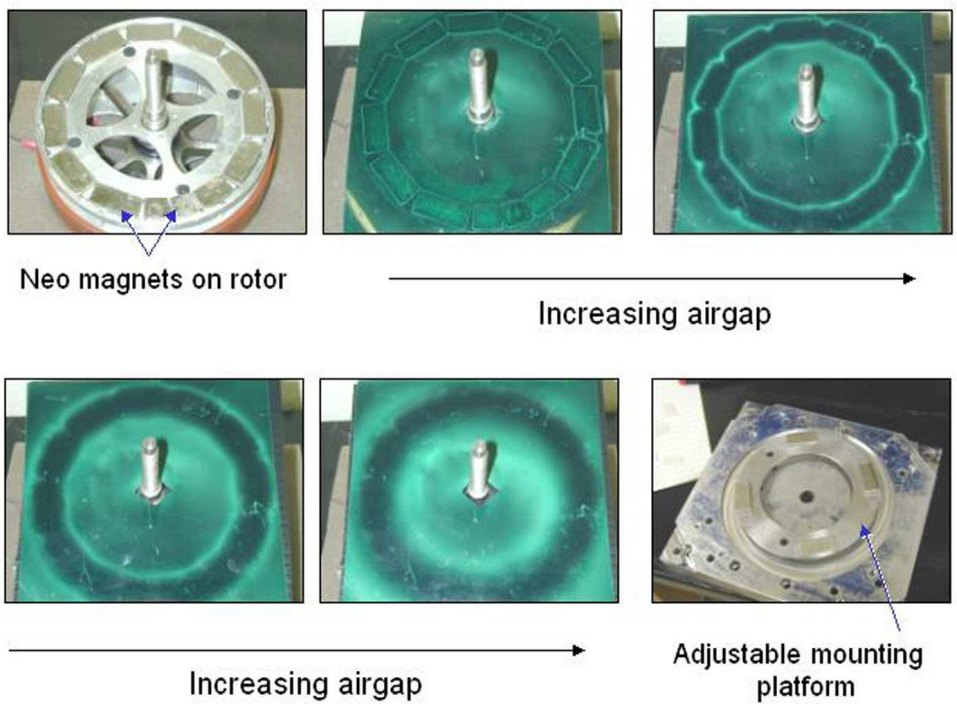

Figure 5.8: Magnetic field of the 12 Neodymium-Iron-Boron PMB rotor magnets as a function of axial Z direction. The ferromagnetic celluloid sheet reveals a slice of the magnetic field. Note that the fields tend to blend together as the axial distance from the surface of the rotor increases.

To reveal the shape of the magnetic field without resorting to finite element computer simulations, a cellulose sheet coated with a ferromagnetic colloidal substance is used. When in the presence of a magnetic field, the iron particles suspended in the celluloid sheet change their orientation and consequently change the luminosity/reflectivity of the sheet. When used near a magnet, the sheet reveals a slice of the magnetic field. Figure 5.8 shows several slices of the magnetic flux density of the 12 Neo magnet ring at increasing distances from the face of the rotor. As illustrated, the variation of the B field is dramatic close to the surface of the rotor. However, as the PMB airgap increases, the fields of the individual magnets blend together and lead to a relatively smooth and symmetric B field. At an airgap of about 1 cm, the bounce of the rotor in the Z direction is minimal.

5.3.2 Electromagnet Core Design

Figure 5.9 shows the housing with the upper and lower electromagnet ring cores installed. The 60-turn 22-gage wire electromagnets are painted with a red insulating enamel to avoid short circuits between coils and the rotor. Eight coils fit into the two ring-shaped electromagnet cores. The cores are built up from 4 mil thick laminations of SuperPerm49 (49% Nickel non-oriented electrical steel) to reduce eddy-current losses in the core. The core has a saturation flux density of $B_{\text{sat}} = 1.2T$ and a cross-sectional area of $10.7cm^2$.

For ease of construction and installation, four electromagnets share one ring-shaped core. In general, when several coils share a common core a transformer results. That is, the flux passing through one coil is shared by all of the coils. The flux in one coil is highly dependent on the currents in the other coils. This concept of mutual inductance is introduced in Appendix D.3. This makes for a terrible actuator since current through one coil will excite all the coils and produce forces on the rotor in several directions. The laminated ring-shaped cores used in the PREMAG bearing

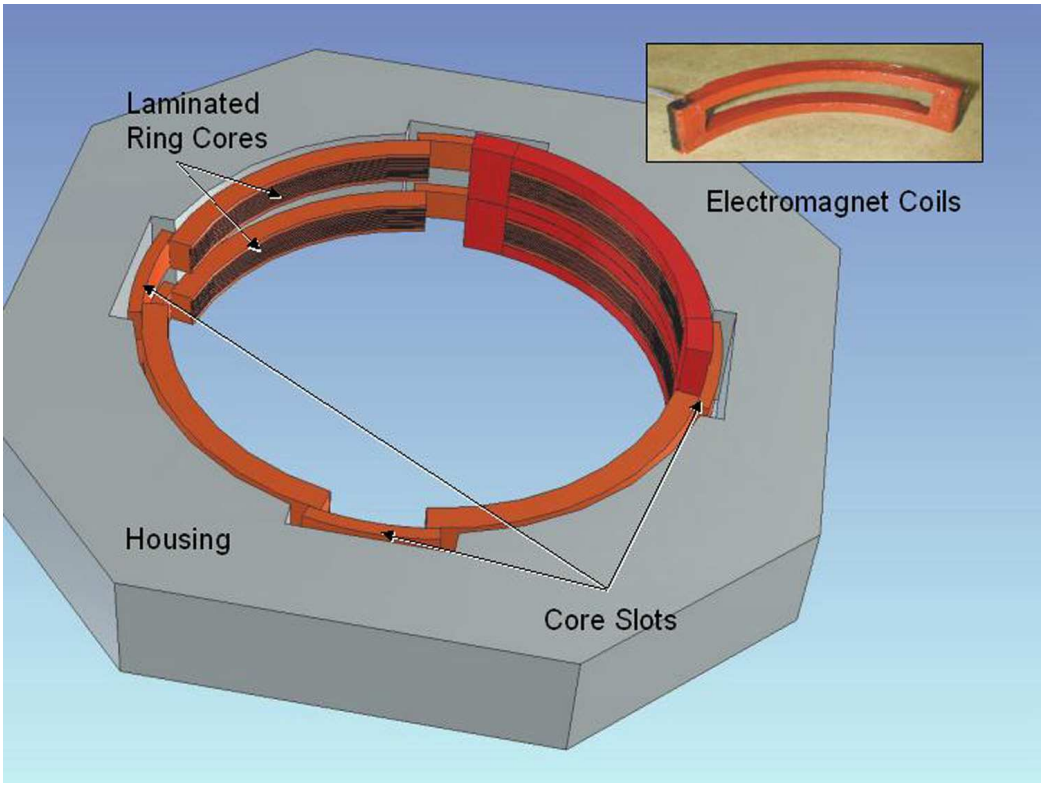

Figure 5.9: Geometry of the electromagnets and electromagnet cores.

have a special shape which reduces the coupling between the coils to an acceptable level. Looking closely at Figure 5.9, one notes that each ring-shaped core has four notches. The flux produced by one electromagnet tends to flow through the core in the radial direction to produce a force and also *around* the core to be shared by the other electromagnets. These notches increase the reluctance of the core along its perimeter so that most of the flux of the electromagnet will flow in the radial direction. That is, the mutual inductance between the coils is reduced to a small level by the notches. The resulting structure is a set of four essentially decoupled electromagnets that have a mechanically firm base.

5.4 Sensor Measurements

The proper placement and choice of sensors in a system can often be a critical issue in control design. For example, as shown in Chapter 7, the natural choice of variables

for derivation of the dynamics of the rotor is the horizontal position of the rotor in the XY plane and the tilt θ_X and θ_Y about the X and Y axes. With these states, one may regulate the rotor to $(X, Y, \theta_X, \theta_Y) = (0, 0, 0, 0)$. However, the positioning of the sensors allows for direct measurement of the airgaps. One obtains an easier control design by independently regulating each airgap length to g_0.

The eddy-current based proximity sensors are mounted on the AMB housing along each control axis: See Figure 1.3. Note that there are two sensors per control axis, giving a total of eight. The sensor produces a voltage that is a *nonlinear* function of the distance between the face of the sensor and the circular aluminium targets mounted on the rotor. This nonlinear function has a roughly sigmoidal shape, perhaps $V = a \arctan(bx) + c$, for $a, b, c \in \mathbb{R}$. Thus, over a small range in x, the output voltage is approximately linear with an offset bias. These eight voltages are amplified and reproduced by the Kaman Instrumentation Measurement Systems preamplifier/sensor driver.

Notice that the airgaps on opposite sides of the rotor are *not* independent. If the length of the airgaps are g_0 when the rotor is centered, then for any given rotor position, the airgaps on opposite sides of the rotor will always add to $2g_0$. Thus, four of the eight airgap sensor measurements are redundant. However, the Kaman Instrumentation Systems preamplifier puts these redundant signals to use by producing a differential voltage output. The differential voltage V_d is the difference between the airgap voltages on opposite sides of the rotor. For example, if g_1 and g_3 are the gap lengths on opposite sides of the rotor, and the sensors measure $V_1(g_1)$ and $V_3(g_3)$, respectively, then $V_d(g_3 - g_1) = V_3(g_3) - V_1(g_1) := V_{\text{Ytop}}$. It is shown in the sequel that $g_3 - g_1$ gives the position of the center of the top of the rotor in the Y direction and is zero when the rotor is centered. The voltage V_{Ytop} is also sigmoidal, but has greater position sensitivity and a larger linear range. The greater position sensitivity is achieved by a sensitive circuit design and matching of the sensor characteristics on

each control axis. For simplicity of the feedback law, a linear characteristic is fit to this nonlinear voltage/airgap signal and compensation for any voltage offset bias is implemented with software. This results in direct measurement of the center of the top and bottom of the rotor. The linearized position sensor maps are shown in Figure 5.10.

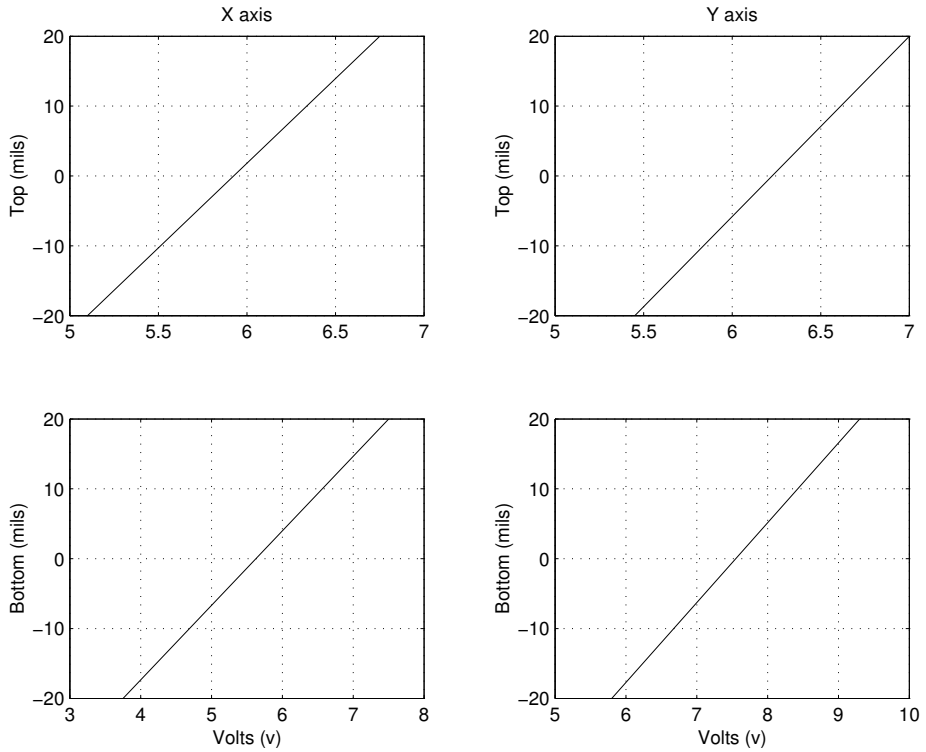

Figure 5.10: Voltage-Position sensor maps.

In addition to measurement of airgap lengths, the coil currents, and the applied coil voltage measurements are available for feedback control. Note that direct measurement of the ideal coil voltage via a *search coil*[2] is used to construct a flux-current-position lookup table, but the search coil measurements are not used for feedback control. The coil current and applied voltage measurements are outputs of the Copley Controls, model 412 power servo-amplifiers. In this work, the coil current is measured in current-mode operation and both the applied voltage and coil current are measured

[2]See Chapter 6.

in voltage-mode operation.

5.5 Copley 412 Power Servo-Amplifiers

The electromagnet coils are driven by the Copley Controls model 412 Power Servo-Amplifiers. These amplifiers are capable of providing 10 Amps continuous and 20 Amps peak current when operating from a 24-90 Volt DC power supply. Note that an internal component header allows for adjustment of the peak and continuous current levels. To simulate a spacecraft bus, a 28 volt, 1200 watt (46 A max @40°C-31 A max @70°C) regulated DC power supply is used.

Note that these amplifiers are servo amplifiers as opposed to power amplifiers. A power amplifier only boosts the signal level of the control signal to one that can drive the coils. A servo amplifier utilizes internal feedback as well as power amplification. The Copley 412 amplifiers use a PWM output stage for efficient power amplification. There are two modes of operation: voltage mode and current mode. Recall that the coil dynamics have the form

$$V_{\text{app}} = I_c R + N L(x) \frac{dI_c}{dt} + I_c \frac{dL(x)}{dx} \dot{x} \tag{5.1a}$$

$$= I_c R + N \dot{\varphi} \tag{5.1b}$$

When operating in current mode, current feedback is used to drive the error between the coil current I_c and a reference current I_r to zero. That is, the actual coil current is regulated to the desired current, even in the presence of a changing inductance. In this way, the electrical dynamics of equation (5.1a) are effectively eliminated (at least for reference signals within the bandwidth of the current loop). Depending on the choice of components, the bandwidth of this control loop is approximately $1 - 3$ kHz.

When operating in voltage mode, the applied voltage V_{app} is regulated to V_r. This essentially gives the coil dynamics as $N\dot{\phi} = V_r - IR$. That is, the reference voltage

assigns the derivative of the flux, minus the IR voltage drop. As discussed in Section 2.1, IR compensation may also be used at this point so that the reference voltage can directly assign the rate of change of the coil flux. The reported control bandwidth of the voltage loop in the Copley data sheet is approximately 200Hz.

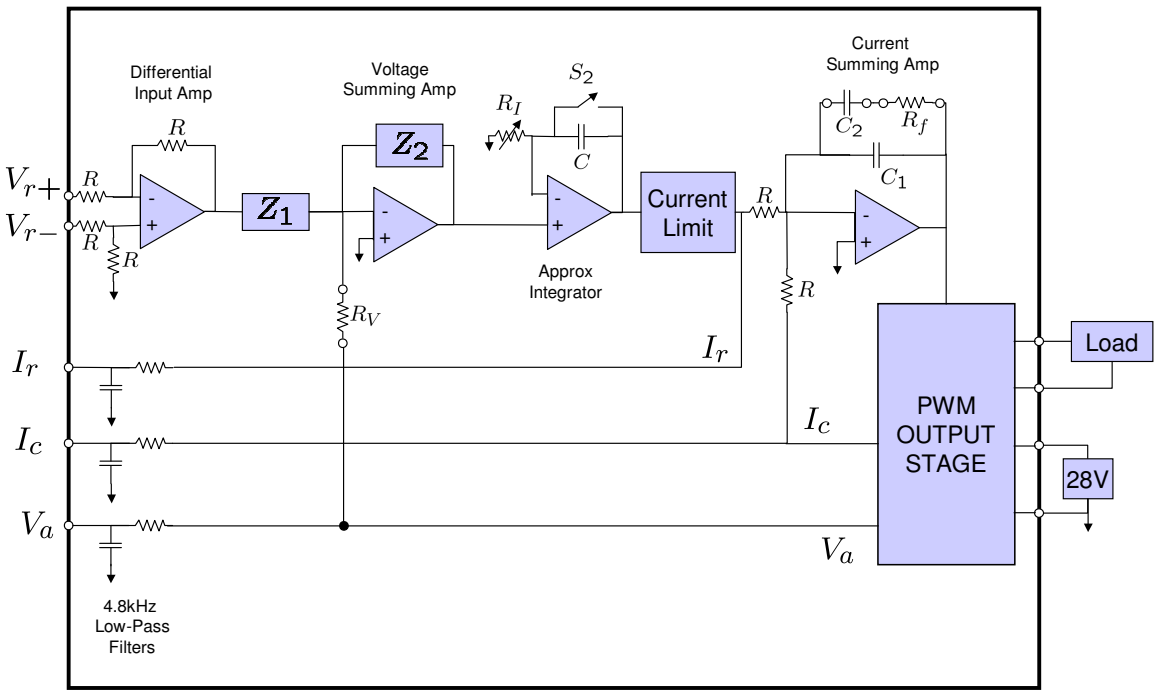

Figure 5.11: A functional schematic diagram of the Copley Controls 412 Servo Amplifier.

To better understand the operation of the amplifiers, a functional schematic is shown in Figure 5.11. The load and 28 V power supply are connected to the PWM output stage. This subcircuit monitors the voltage applied across the coil V_{app} and the current through the coil I_c. These signals are provided at output terminals for user access.

To setup the amplifier in current mode, the resistor R_v is removed and the switch S_2 is closed. A unity-gain differential opamp is used as the input stage of the Copley 412. This produces a voltage $V_r = V_{r+} - V_{r-}$. One has the option of using the voltage summing amplifier as an input filter stage with the proper selection of components for Z_1 and Z_2. The opamp integrator stage simplifies into a voltage buffer when S_2 is

closed. If desired, one may select header resistors to set current limits. In this work, the current limits are left at the default values of 10 A continuous and 20 A peak. The resulting current reference I_r is a possibly scaled version of the externally applied V_r. The current reference is also available for monitoring. The current summing opamp forms the feedback loop and uses a compensation network to boost the bandwidth of the coil. One can monitor the performance of the current loop by comparing I_r and I_c.

When the amplifier is used in voltage mode, S_2 is opened so that the integrator is active. Instead of implementing a true integrator, the integral is approximated by a low-pass filter with a very low break frequency. The break frequency can be adjusted by tuning R_I. To form the voltage feedback loop, the resistor R_V is inserted into the component header. The voltage loop basically wraps an outer PI control loop around the inner current feedback loop. These control loops are better illustrated in the block diagram form shown in Figure 5.12.

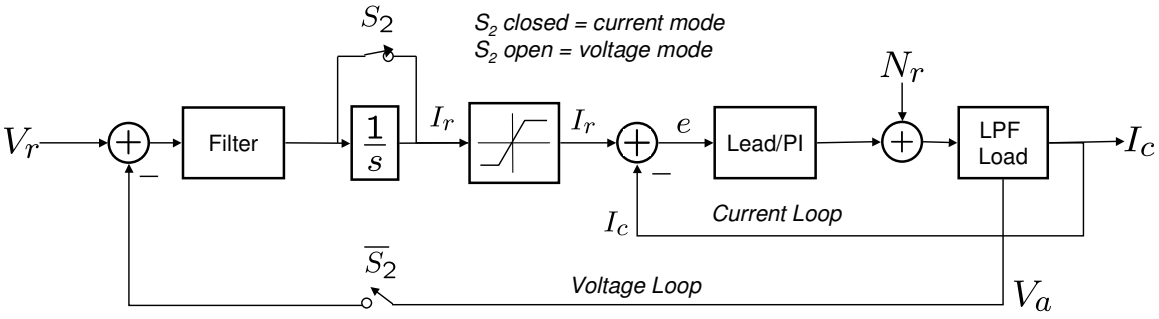

Figure 5.12: Feedback loops used in the Copley 412 amplifier.

5.5.1 Amplifier PWM Output Stage

The output stage employs a power MOSFET H-Bridge configuration to produce positive and negative coil currents from the single polarity $28V$ power supply. Figure 5.13 shows a *simplified*[3] schematic of a typical PWM output stage. The n-channel

[3]A well designed H-bridge circuit has several extra features such as over-voltage and short circuit protection for the transistors.

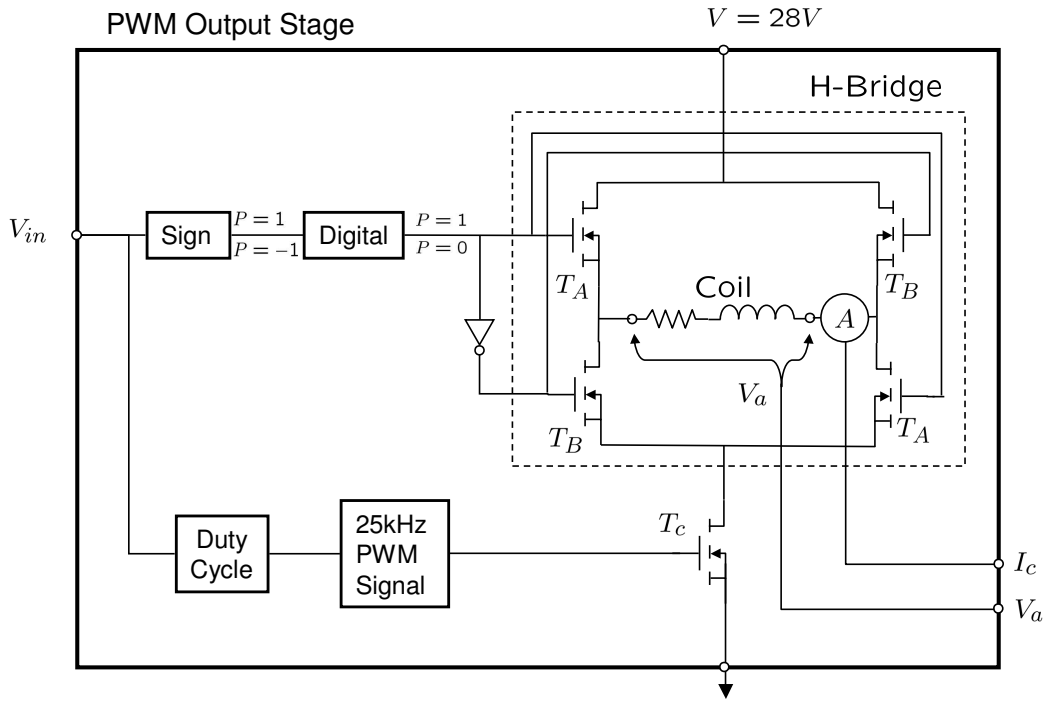

Figure 5.13: A typical configuration of a PWM amplifier.

enhancement MOSFET transistors shown are operated as normally-open switches. When the gate voltage is zero, the transistor is off (an open circuit). When the gate voltage is above a certain threshold voltage, the transistors are fully on (basically a short circuit). To illustrate the operation of the H-Bridge, assume that transistor T_c is on. The digital logic and connection of the transistor gates ensures that the transistors marked T_A are on and T_B are off when $V_{in} > 0$. In this case, current flows from the power supply, through the top T_A transistor, through the coil, through the bottom T_A transistor and finally to ground through T_c. The full $28V$ is allowed to drop across the coil. Likewise, when $V_{in} < 0$, the transistors marked T_A are off and T_B are on. A negative $-28V$ is applied across the coil and the current flows in the opposite direction. When T_c is turned off, no current flows.

A variable duty-cycle or pulse width modulated (PWM) digital signal is applied to the gate of T_c. This PWM signal is a periodic 25 kHz square wave with duty cycle proportional to V_{in}. As a result, a 0 to 28 V or 0 to -28 V (depending on the sign of

V_{in}) PWM voltage is applied across the coil. The resulting coil current I_c is a filtered version of the PWM voltage signal. This is due to the inductive, low-pass nature of the coil. To see this, model the load as a series winding resistance R_s and a series inductance $L(x)$. The load is governed by

$$V_{\text{app}} = R_s I_c + L(x)\frac{dI_c}{dt}$$

The transfer function from the voltage applied across the coil to the current through the coil is

$$\frac{I_c(s)}{V_c(s)} = \frac{1}{R_s + Ls} = \frac{1}{R_s}\frac{1}{1 + \frac{s}{\omega_c}} := P(s)$$

where $\omega_c = R_s/L(x)$. Since this transfer function is a low-pass filter, the current passing through the coil has a DC value with some ripple noise at multiples of the 25kHz switching frequency. The DC value is roughly the average value of the square wave over one period and varies with the duty cycle of the PWM signal.

The switching noise, or ripple, can often be a significant source of noise in PWM systems. The amount of ripple noise that appears in the coil current depends on the closed loop bandwidth of the current loop. Also, this noise tends to bleed into other electronic subsystems and can be problematic. Additional filtering of the measured signals is often required: see Section 5.6 for further discussion.

5.5.2 Inner Current-Loop Inductance Compensation

The following numerical example of the Lead/PI compensation in the inner current loop illustrates tradeoffs between a large closed-loop current bandwidth and ripple noise rejection.

When used in open-loop, the amount of ripple is determined by the inductance of the coil. Since the corner-frequency ω_c decreases with increasing inductance, larger inductances produce more filtering of the 25kHz noise. The series resistances are in the range of 0.5Ω. The average value of the coil inductance is about 4mH and changes by about 20% with the rotor position.

Using these values, a typical transfer function of the load may look like that in Figure 5.14. The beak frequency is at $53Hz$ and the noise attenuation at 25kHz is about $55dB$. This is very good noise attenuation, but the corner frequency is quite low. This low corner-frequency leads to relatively clean coil currents, but makes for a pretty terrible servo-amplifier.

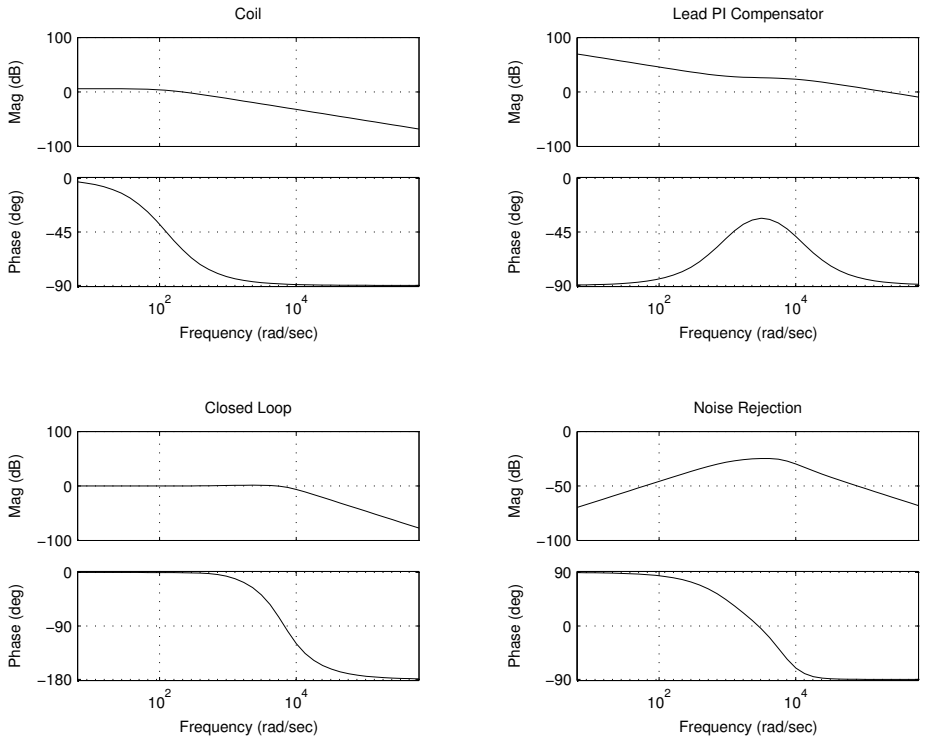

Figure 5.14: Copley Lead/PI inner current-loop bode design: **(a)** Coil $\frac{I_c}{V_{\text{app}}}$, **(b)** Lead/PI Compensator $C(s)$, **(c)** Closed-Loop TF $\frac{I_c}{I_r}$, **(d)** Disturbance TF $\frac{I_c}{N_r}$

One can determine that the current error summing amplifier implements a Lead/PI compensator with the following transfer function

$$C(s) = k\frac{1+\frac{s}{\omega_1}}{s(1+\frac{s}{\omega_2})}$$

where

$$k = \frac{1}{R_f(C_2+C_1)}, \qquad \omega_1 = \frac{1}{R_fC_2}, \qquad \omega_2 = \frac{1}{R_fC_2} + \frac{1}{R_fC_1}$$

The Copley 412 data sheet [84] has suggested values for the header components C_2

and R_f given the 4mH coil inductance. This gives

$$C_2 = 4.7\text{nF}, \qquad R_f = 220k\Omega, \qquad R = 10k\Omega, \qquad C_1 = 470\text{pF}$$

Using Figure 5.12 as a guide, the closed-loop I_c/I_r and I_c/N_r transfer function is

$$I_c(s) = \frac{P(s)C(s)}{1 + P(s)C(s)} I_r(s) + \frac{P(s)}{1 + P(s)C(s)} N_r(s)$$

The resulting compensator and closed loop frequency response is shown in Figure

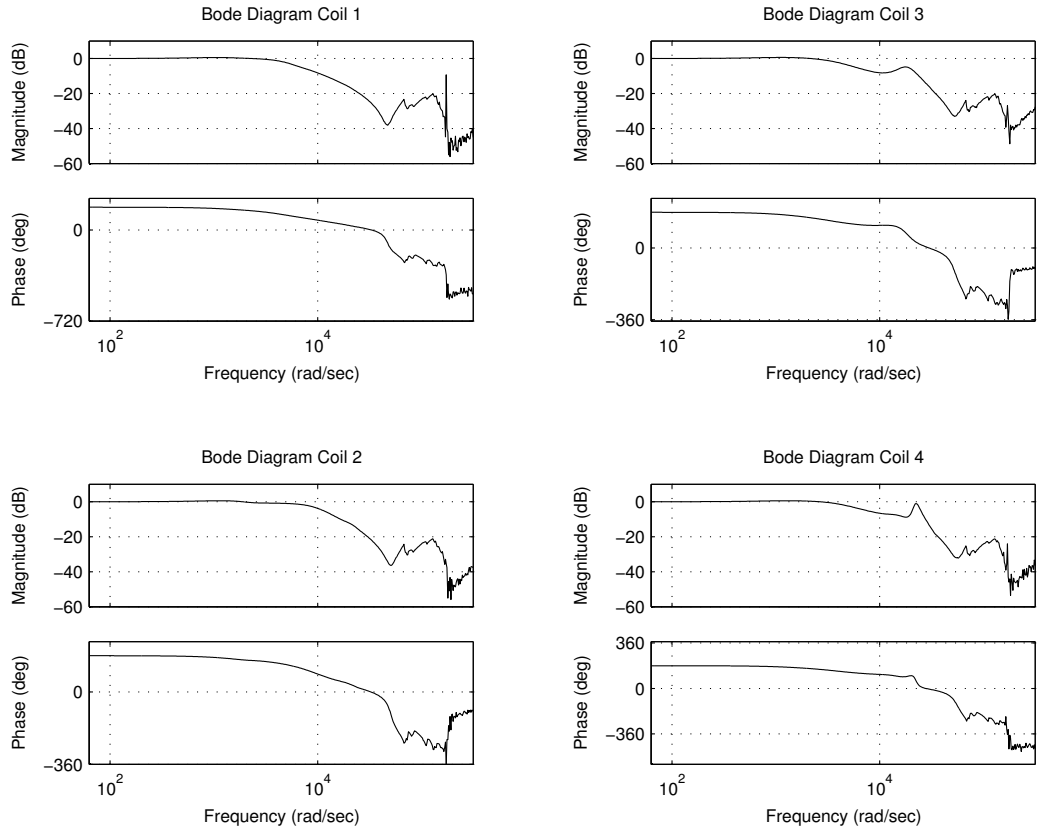

Figure 5.15: Closed-loop I_c/I_r Frequency response of top coils.

5.14. For the above component values, the compensator pushes the closed-loop bandwidth out to about 1.3kHz. Potentiometers which determine the system gains may be adjusted to tune the current-loop step response. The noise rejection at 25kHz is about 55dB, however it is seen from the experiments that there is still a significant amount of noise in the coil current.

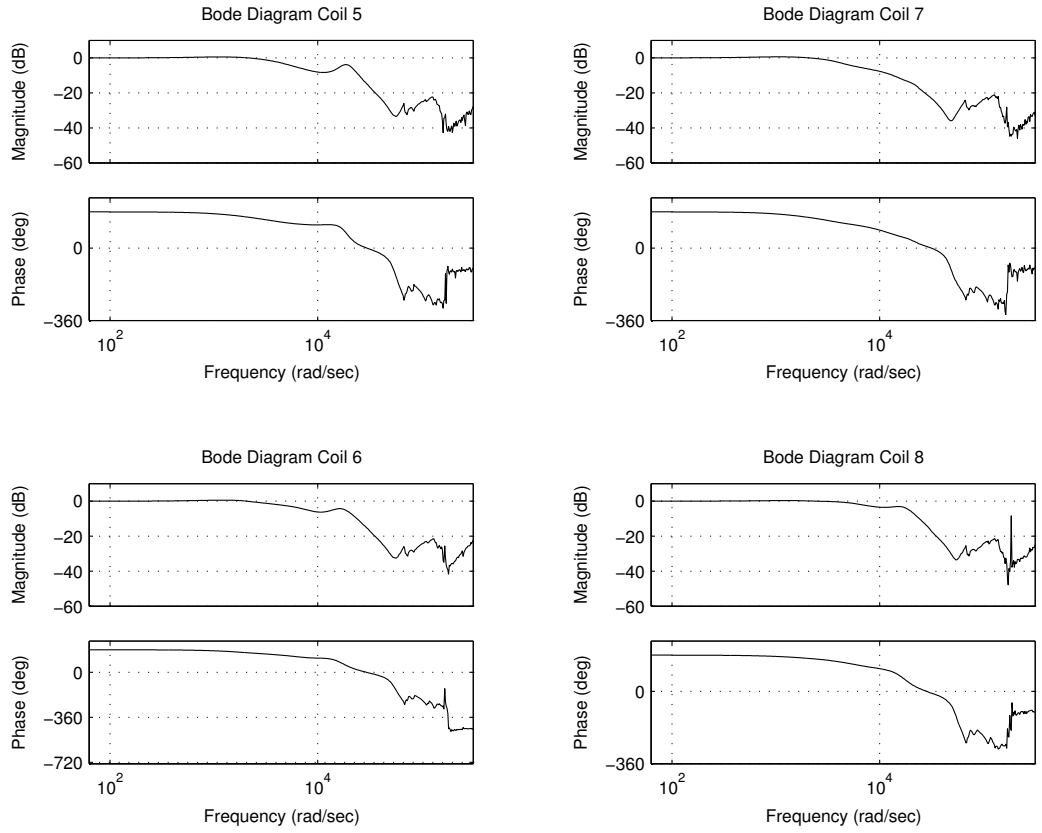

Figure 5.16: Closed-loop I_c/I_r Frequency response of bottom coils.

The above design is used in each of the current-mode amplifier channels. Figures 5.15 and 5.16 show the closed-loop I_c/I_r frequency response as measured on a spectrum analyzer for the top set and bottom set of coils. Each closed-loop bandwidth is about 1kHz.

5.5.3 Voltage-Mode Operation with IR Compensation

The setup procedure for voltage mode operation is similar to current mode operation. Recall that an outer-PI voltage loop is wrapped around the inner current-loop. This is similarly tuned by varying the gain potentiometers while inspecting the voltage step response. The balance potentiometer is used to trim the output current to zero when the voltage input is zero. The closed-loop voltage mode frequency response of the coils on the bottom x-axis are shown in Figure 5.17. Recall that only this axis is

used for nonlinear control verification. The −3dB bandwidth is about 200Hz.

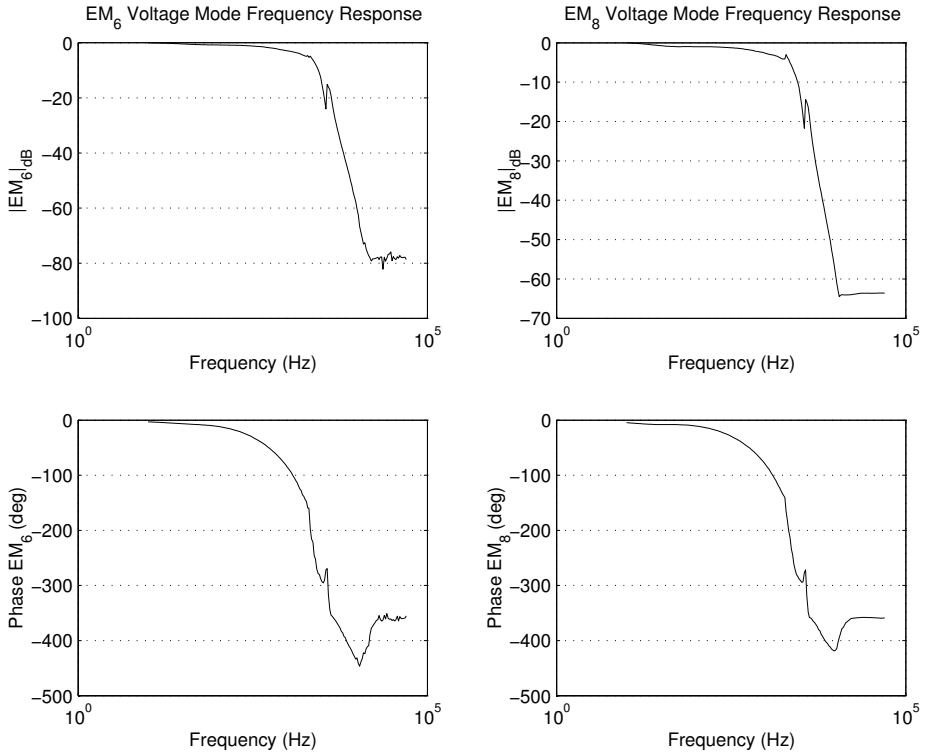

Figure 5.17: Closed-loop V_{app}/V_r frequency response of bottom coils.

Figure 5.18 illustrates the voltage mode operation. Note that the applied coil voltage V_{app6} equals reference voltage V_{r6}. The applied voltage V_{app6}, the coil current I_{c6} and the ideal coil voltage V_{c6} are related to each other by equation (5.1). The ideal coil voltage and flux are related by Faraday's law, $N\dot{\Phi}_6 = V_{c6}$. Flux measurement techniques are discussed in Chapter 6.

IR compensation was introduced in Section 2.1. With this approach, the reference voltage is increased by the amount $I\hat{R}$ so that the coil dynamics (5.1b) simplify to

$$V_r = I_c(R - \hat{R}) + N\dot{\varphi}$$

where the term $R - \hat{R}$ is small and $\hat{R}$ is an estimate of the coil resistance. When this term is small, the reference voltage controls the rate of change of the coil flux. The Copley 412 Amplifier has the ability to implement IR compensation in hardware,

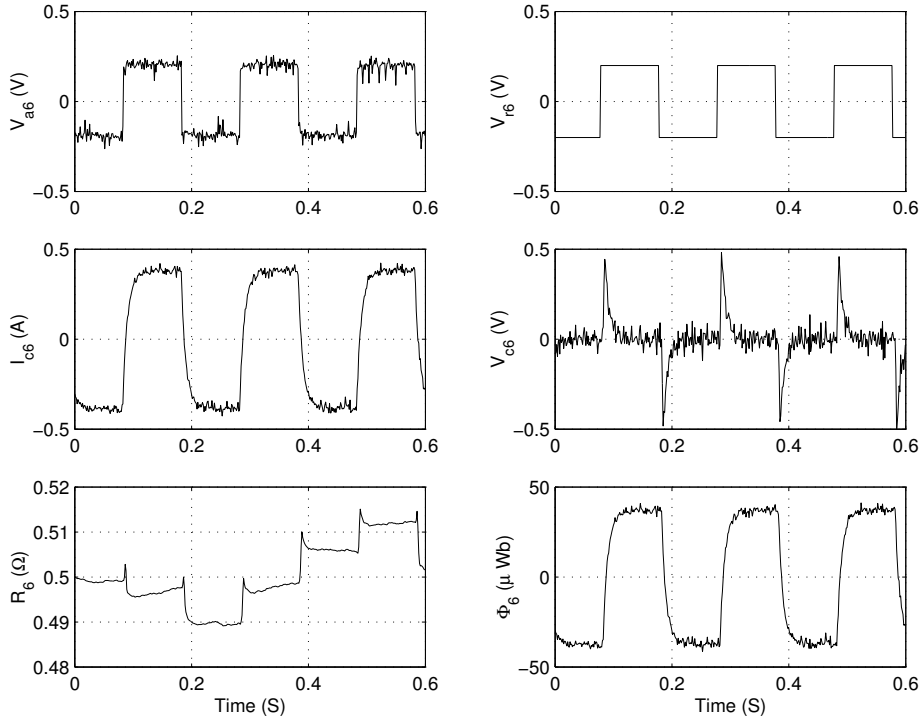

Figure 5.18: Voltage-mode operation without IR compensation. The applied voltage V_{app6} matches square wave reference signal V_{r6}. The ideal coil voltage V_{coil} is spike-like for the square wave reference signal.

however, one has more flexibility when implementing it in software. Note that a good estimate of the resistance must be known for $R - \hat{R}$ to be small. This can be challenging because the coil resistance may change significantly with temperature.

Equation (5.1) may be solved for R to obtain an online estimate.

$$R = \frac{V_{\text{app}} - V_{\text{coil}}}{I_c}$$

Observe however that this estimate is infinite whenever the coil current passes through zero. A heavily low-pass filtered version of this signal is shown in Figures 5.18 through 5.20. On average the resistance is about 0.5Ω for coil 6 and 0.6Ω for coil 8 (not shown). Although this online resistance estimate is useful for these simple tests, it proves unreliable for online, closed-loop control with automatic IR compensation. In this work, a constant value of the resistance estimate is used. The IR compensation tuning procedure is outlined in Chapter 6. Figure 5.19 shows the amplifier operating

in voltage mode with IR compensation ($\hat{R} = 0.5\Omega$). In this case, V_{coil} as opposed to V_{app} tracks the reference signal. Although there is quite a bit of overshoot in the V_{coil} signal, the performance is deemed adequate because a square reference voltage is producing a roughly triangular flux signal.

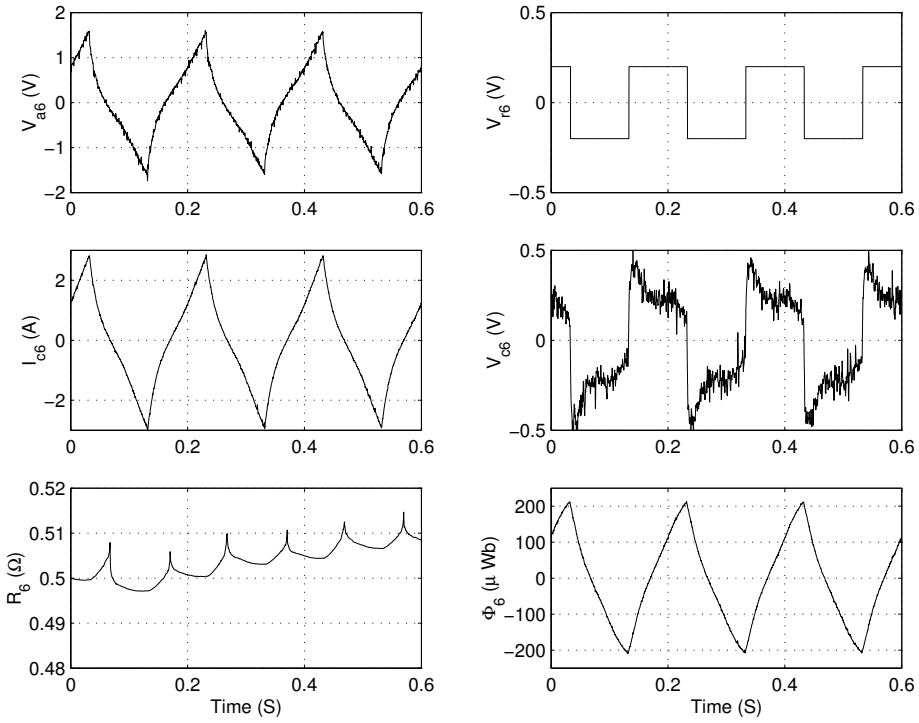

Figure 5.19: Voltage-mode operation with IR compensation ($\hat{R} = 0.5\Omega$). V_{coil} tracks the reference signal with significant overshoot. $N\dot{\phi} = V_{\text{coil}}$ and ϕ is approximately triangular.

When using IR compensation, $\hat{R}$ must be less than R. If $\hat{R} > R$, then $(R - \hat{R})$ is negative and may cause the flux to increase even when the voltage input is zero. Figure 5.20 shows the amplifier working in voltage mode with IR compensation. The ideal coil voltage tracks the sinusoidal reference voltage until 3 seconds, at which time the coil estimate $\hat{R}$ is increased from 0.5Ω to 0.55Ω. This results in an uncontrolled increase in the coil current and flux.

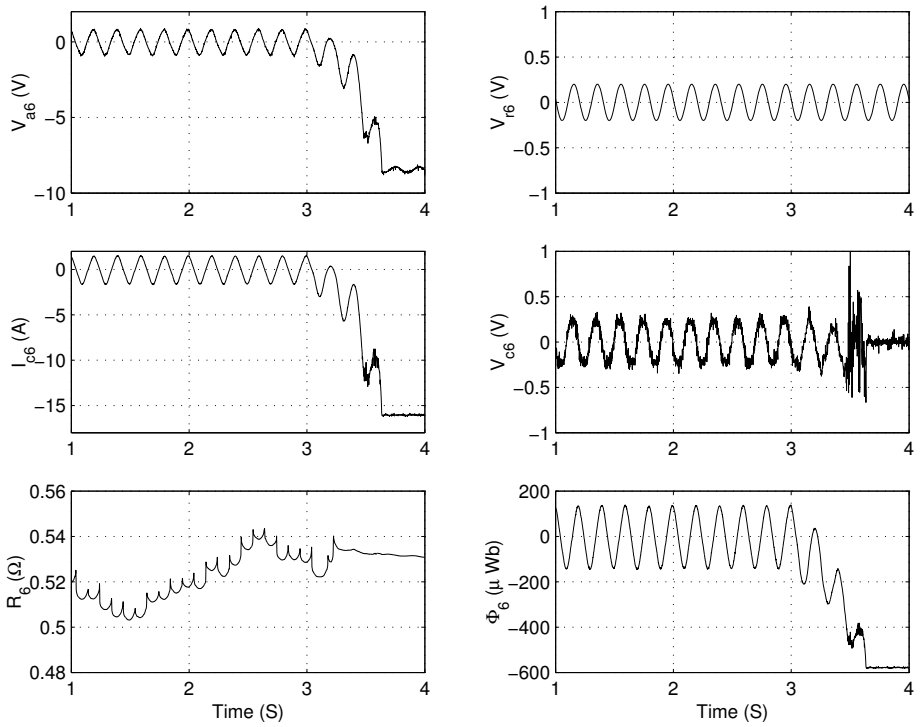

Figure 5.20: Voltage-mode operation with IR compensation ($\hat{R} = 0.5\Omega$). At 3 seconds, $\hat{R}$ changes from 0.5Ω to 0.55Ω

5.5.4 Mutual Inductance

Section 5.3.2 states that the core has been designed so that the mutual inductance between the coils is reduced to an acceptably small level, however, it isn't completely eliminated. Figure 5.21 illustrates the mutual inductance by exciting coil 6 with a large sinusoidal current and keeping the current in coil 8 zero. The coil 6 is excited to about 400μWb and the mutual inductance also excites coil 8 to about 50μWb. Note that the flux is saturated indicating that this is a worst case scenario.

In general, the inductance is modelled by a matrix

$$\begin{bmatrix} N\varphi_6 \\ N\varphi_8 \end{bmatrix} = \begin{bmatrix} L_6(x) & M(x) \\ M(x) & L_8(x) \end{bmatrix} \begin{bmatrix} I_6 \\ I_8 \end{bmatrix} \tag{5.2}$$

The inductance is related to the slope of flux vs. current curve: see Chapter 6 and Appendix B.3 for details. Figure 5.22 shows a matrix of flux vs. current curves with sinusoidal excitation currents for the rotor held at a particular position. The entries

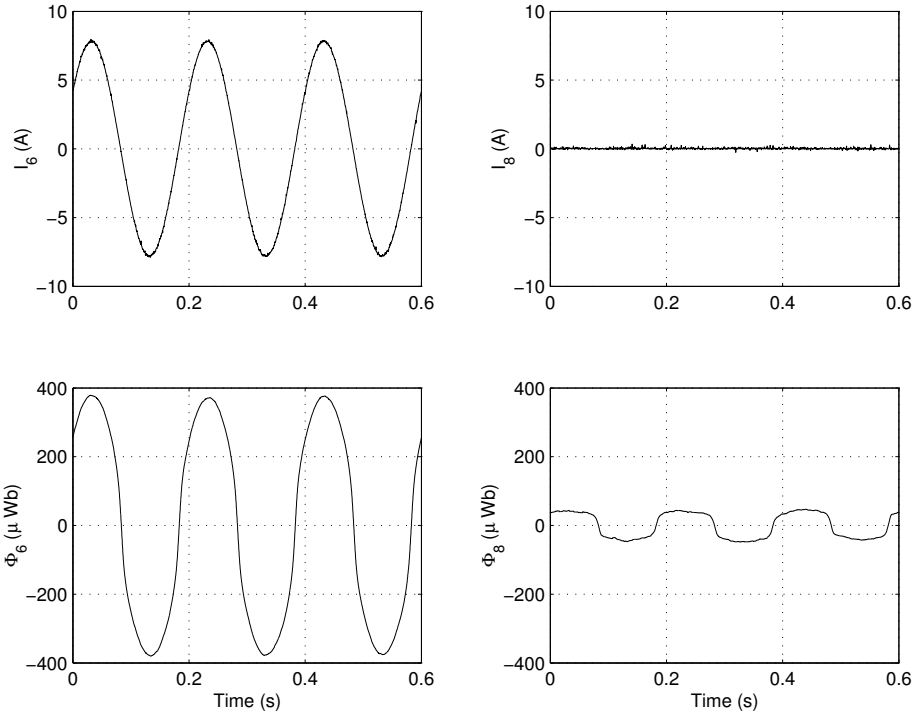

Figure 5.21: Flux excitation of coils 6 and 8 by the current excitation of coil 6.

in this matrix further illustrate the magnitude of the flux created by the mutual inductance terms. Note that this graph is generated in two steps: first $I_6 = 8\sin(\omega t)$ is sinusoidal while $I_8 = 0$ and then vice versa.

The magnitude of the flux generated by the mutual inductance shown in Figures 5.21 and 5.22 suggests that the mutual inductance may, in fact, be significant. However, in this study, it is ignored. Efforts may be undertaken in the future to address this issue: see Chapter 9. Nonetheless, the presence of this mutual inductance does not seem to significantly interfere with the ability to assign the rate of change of the coil flux. Figure 5.23 shows the amplifiers working in voltage mode with IR compensation ($\hat{R}_6 = 0.5\Omega$ and $\hat{R}_8 = 0.63\Omega$) while applying a square wave reference to both amplifiers. The ideal coil voltage from each amplifier follows its square wave reference and the resulting flux is roughly triangular in both amplifiers, in spite of the mutual inductance.

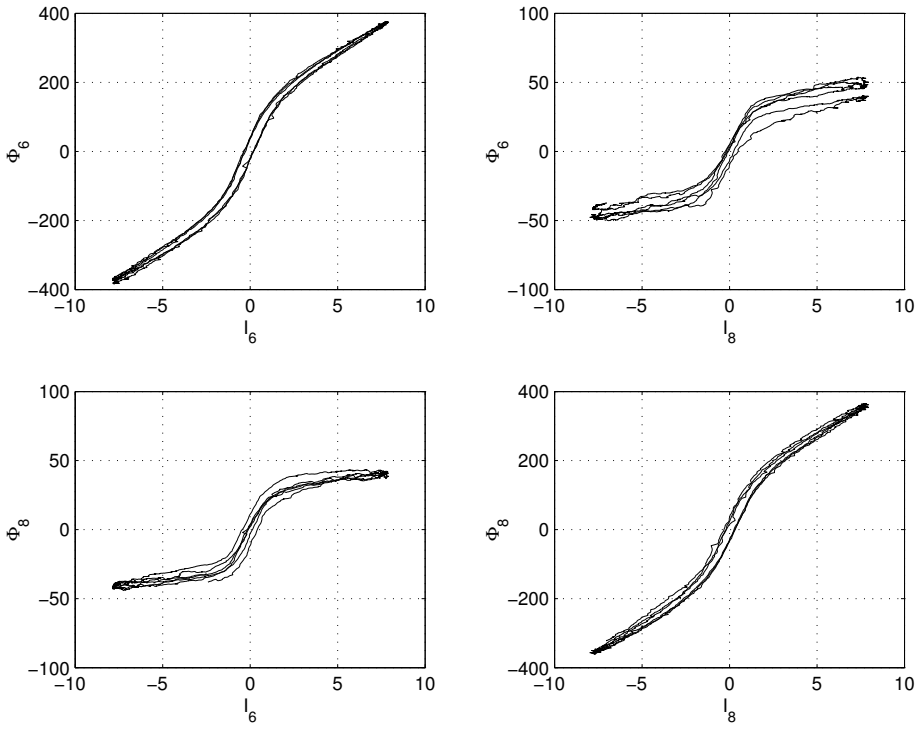

Figure 5.22: Flux vs. current curves for sinusoidal current excitations.

5.6 Amplifier Noise and Signal Conditioning

In any practical electronics application, the noise in the system must be managed by proper filtering. However, the classification of noise in a system is somewhat subjective. The main source of noise in this experiment is the PWM 25kHz switching or ripple noise. This noise is often neglected in systems that employ PWM amplifiers because the $25kHz$ (and higher harmonic) noise is typically much larger than the bandwidth of the system being designed. For example, the linear control design presented in Chapter 7, which uses the amplifiers in current mode, has a bandwidth on the order of $20-50$Hz. Thus, the switching noise present in the current control signal which actuates the rotor does not significantly affect the performance of the positioning control system. In fact, there is no detectable difference in the performance of the linear control designs conducted in this work when current filtering is employed. The only effect of the ripple noise is to make the currents "messy" when viewing.

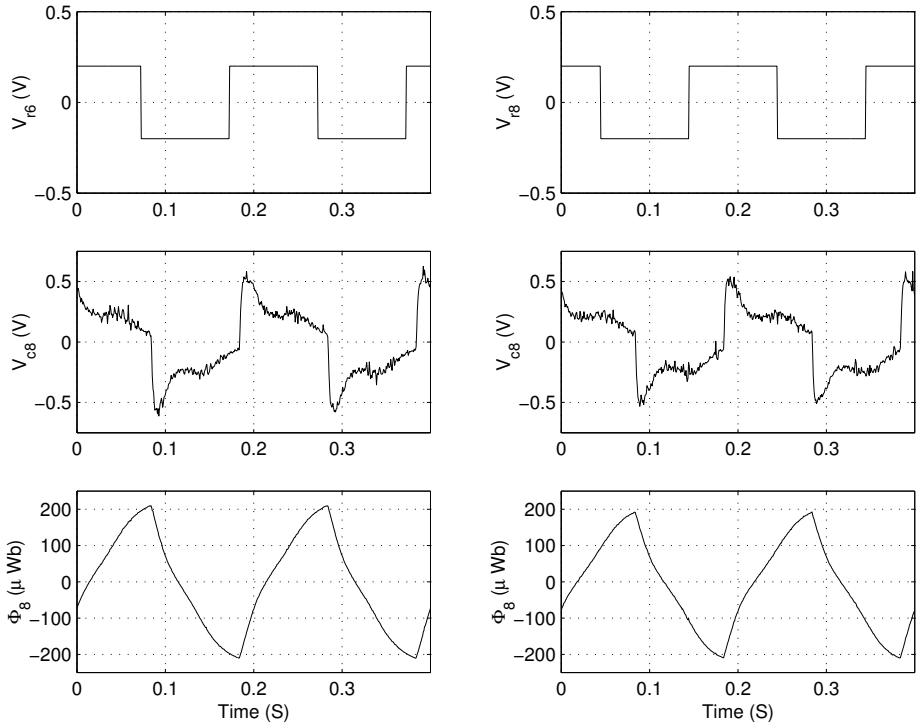

Figure 5.23: Voltage-mode amplifier operation for coils 6 and 8 with IR compensation ($\hat{R}_6 = 0.5\Omega$ and $\hat{R}_8 = 0.63\Omega$). V_{rj} is the reference signal, V_{cj} is the ideal coil voltage, and Φ_j is the resulting coil flux for $j = 6, 8$. Note that both fluxes are roughly triangular even in the presence of the mutual inductance.

Thus, filtering of the coil current does not seem necessary. However, as discussed in Chapter 6, the measurement of the flux depends on the coil current and the position. To obtain clean flux measurements, filtering of the coil current and rotor position is necessary. Furthermore, to properly implement the data acquisition, anti-aliasing low-pass filters are required.

Figure 5.24 illustrates the noise sources and the noise reduction components (shown in gray). One source of noise is the quantization noise from the D/A converter. This is easily eliminated with the use of low-pass reconstruction filters. A passive, first-order RC filter with a break frequency of 1kHz is utilized. Note that the Lead+PI filter in the current error amplifier is shown as a noise reduction component because some of the PWM noise is filtered in this control loop. However, the design of the current control loop prioritizes closed-loop bandwidth over PWM noise rejection.

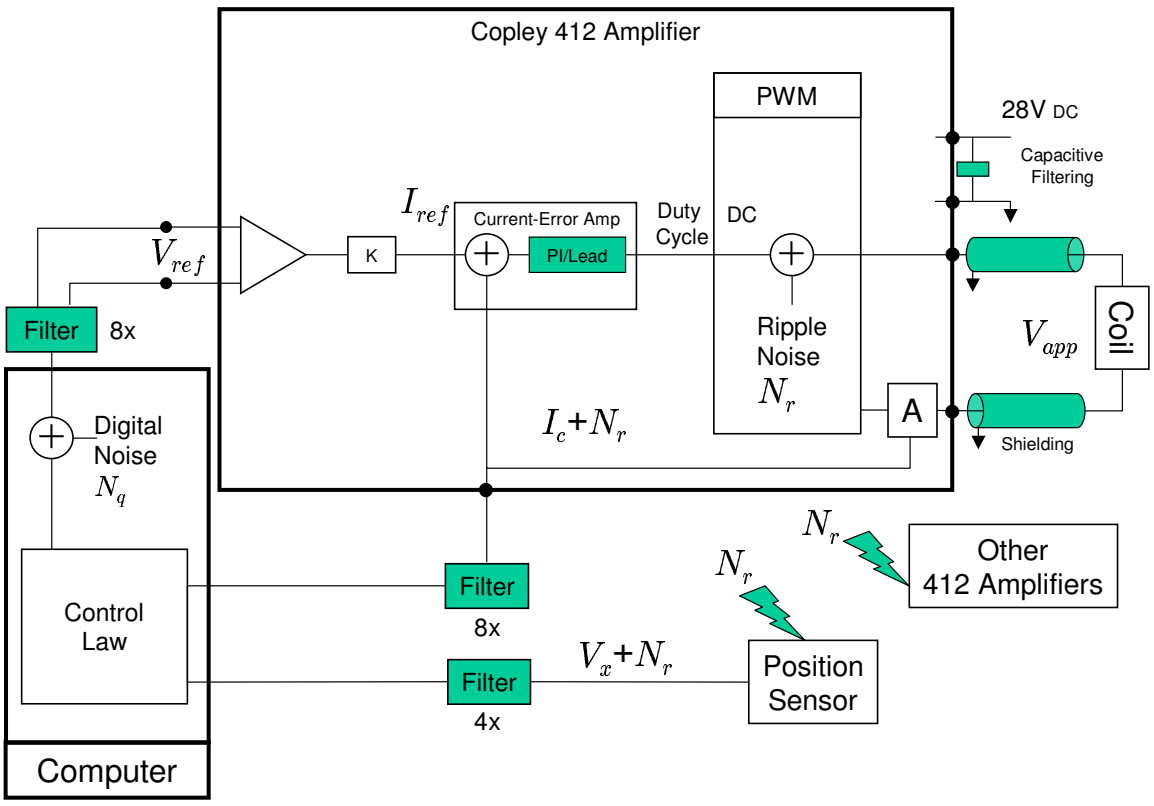

Figure 5.24: Illustration of noise reduction components.

The PWM signal is modelled by a DC signal with additive ripple noise N_r. Besides appearing in the Copley 412 amplifier shown, the ripple noise can feed into the other amplifiers and position sensors through two channels. One way is through the power and ground connections and the other way is by noise radiated through the coils themselves (a coil is basically a crude antenna). To protect against amplifiers coupling through the power supply, 680μF bypass capacitors are employed at each power connection terminal. A bypass capacitor acts as a high frequency short to ground. Also, the amplifiers are connected in a "star-point" ground to minimize ground currents. Twisted-shielded cables are used to connect the amplifiers to each coil to combat the radiated noise. As is standard in shielding practice, the end of the shield closest to the amplifier is grounded and the other end near the coils is floating.

The tweleve filters monitoring the coil current and position sensor voltages have

two purposes. The first is to act as anti-aliasing filters for the A/D conversion process. Ideal Nyquist theory says that the anti-aliasing low-pass filter corner frequency should be at least half of the sampling frequency. In practice however, it a more practical value is closer to $1/10^{th}$ the sampling rate. The sampling rate in this work is determined somewhat arbitrarily. The sampling rate depends on the complexity of each control law, however, rates in the range of 6.8kHz to 8kHz are used. Thus, the bandwidth of the anti-aliasing filters are placed at about 750Hz. The second is to eliminate the PWM noise from the measurements. One could use extra low-pass filtering to eliminate the 25kHz noise, however, since it has a specific frequency, a notch filter is employed.

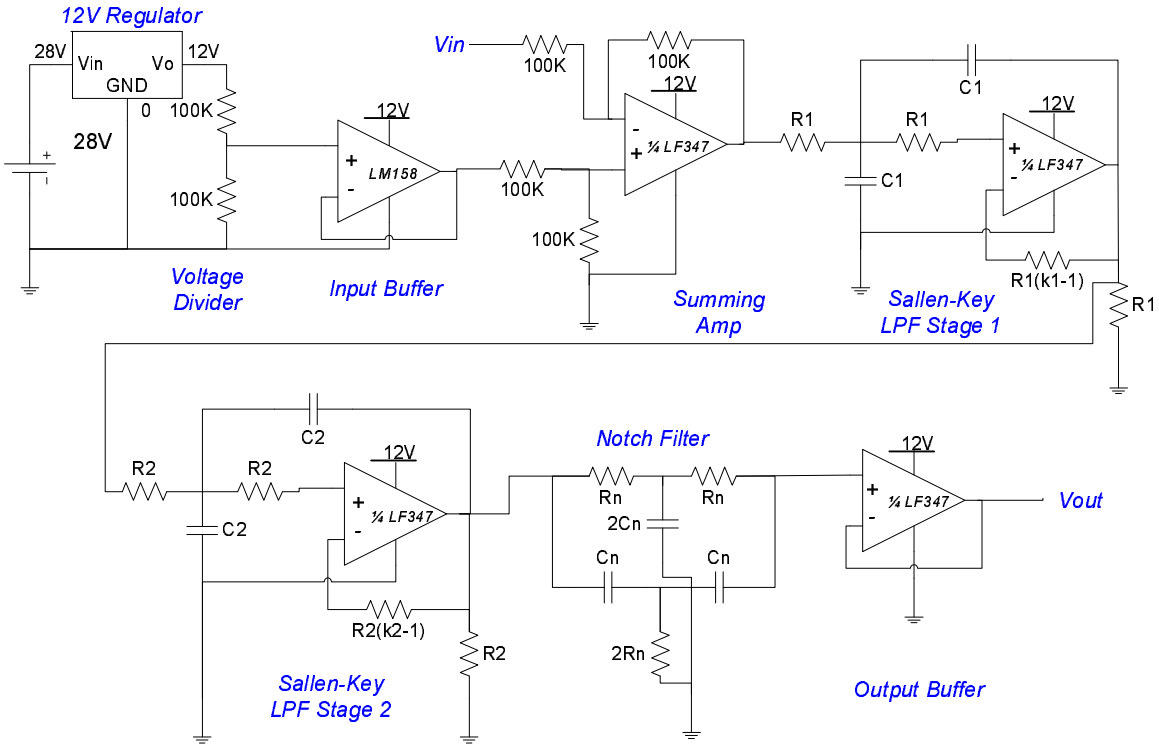

Figure 5.25: Filter Implementation.

The circuit design is shown in Figure 5.25. To implement the filter with a single polarity power supply, the opamps are powered by a 12 V regulator and the input voltage is biased. The maximum voltage swing of the position sensors is $\pm 4V$. A

simple voltage divider is used to bias the input signal at $6V$ so that the output voltage is with in the ± 10 V range expected by the A/D converter. The input signal is added to the bias with a simple unity-gain summing amplifier. A two stage anti-aliasing filter with a Fourth-Order Chebyshev response is designed for 0.5dB ripple in the pass-band and a break frequency of $f_c = 1.3$kHz [4]. This is implemented with a Sallen-Key filter configuration. The RC constants are determined by $RC = \frac{1}{2\pi f_n f_c}$ where f_c is the desired break frequency and f_n is a normalization factor for each stage. The normalization factors and gains k_1 and k_2 for each stage are shown in Table 5.6. One may find the transfer functions and Chebyshev designs in any standard filter handbook [25, 88].

Table 5.1: Chebyshev LPF fourth order (0.5dB ripple) filter parameters.

Parameter	**Value**
f_{n1}	0.597
k_1	1.582
f_{n2}	1.031
k_2	2.66

The notch filter is implemented with the Twin-T configuration. The RC ratio is set by $RC = \frac{1}{2\pi f_0}$ where f_0 is the desired notch frequency. The output of the notch filter is buffered to avoid loading any problems. The filter component values are listed in Table 5.6. Appendix E gives an overview of the filter construction.

Table 5.2: Filter component values.

Component	**Value**	**Component**	**Value**
R_1	$1k\Omega$	C_1	100nF
R_2	$1.2k\Omega$	C_2	100nF
$R1(k_1 - 1)$	$1.2k\Omega$	$R2(k_2 - 1)$	$2.7k\Omega$
R_n	$6.2k\Omega$	C_n	1nF

Figure 5.26 shows the frequency response of the filter as measured on a spectrum analyzer. The magnitude roll off is acceptable and has a steep notch at 25kHz. The

[4] Typically, the break frequency tends to be lower than the designed frequency f_c. This choice of f_c results in an implemented 3dB bandwidth of 750Hz.

corner frequency is at 750Hz as desired. The phase shift is less than 10° for frequencies less than about 100Hz. Since the closed-loop position bandwidth is in the $20 - 50$Hz range, this amount of phase shift should not significantly degrade the designed phase margins.

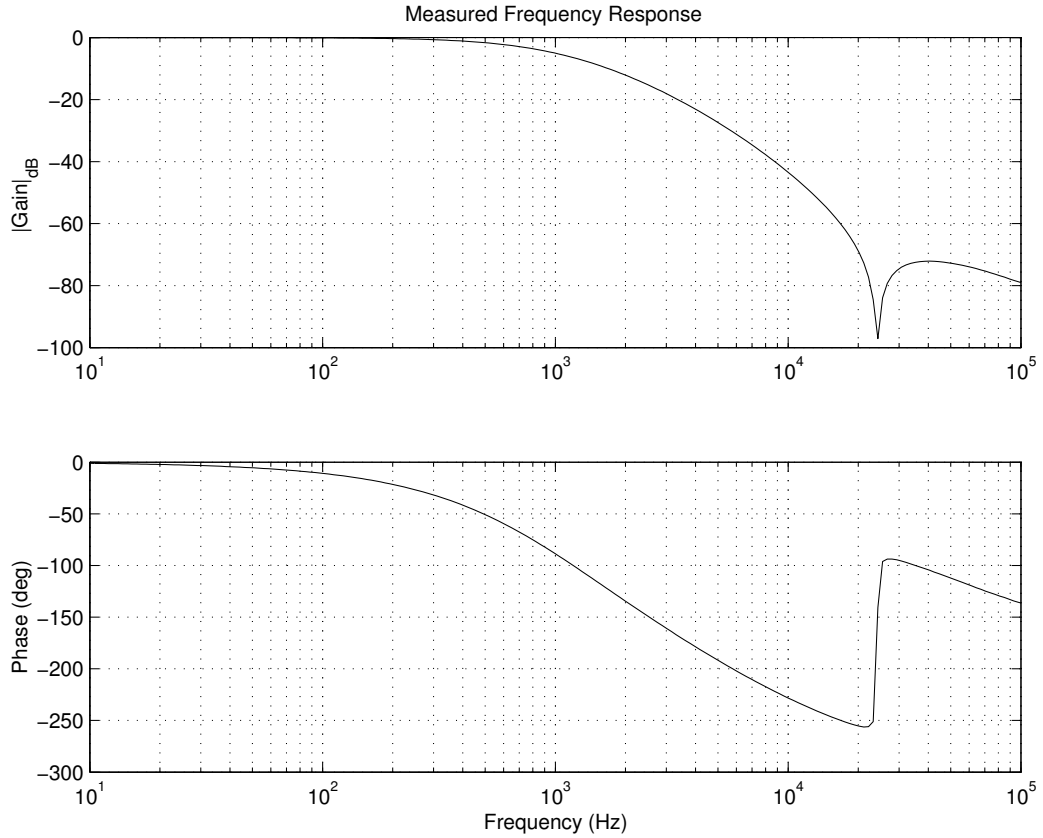

Figure 5.26: Bode Plot of LPF as measured by spectrum analyzer.

5.7 Control Implementation Hardware and Software

Control of the reaction wheel is implemented with the dSPACE Inc. DS1103 PPC controller board. This hardware uses the Motorola Power PC 604e processor running at 400MHz for real-time simulation. Integrated onto the controller board are several A/D and D/A converter channels. Four ADC units with four 16-bit multiplexed channels each (16 channels total) operate with a $4\mu s$ sampling time. In addition,

there are an additional 4 ADC 12-bit channels that operate with an 800ns sampling time. Note that these sampling times correspond to 250kHz and 1.25MHz sampling rates, respectively. However, these sampling rates consider only the hardware capabilities and do not include the calculation time required to implement the control algorithms. The actual maximum sampling rate attainable for control synthesis depends on the complexity of the control algorithm, however, sampling rates on the order of $6-10$kHz are attainable for the control algorithms used in this work. In this assumes that the sampling rate is fast enough so that the digital implementation of the control algorithm approximates the continuous-time control law. Thus, explicit discreteization of the control laws and dynamics is not considered. Eight 14-bit D/A channels with 5μs settling time are available for interfacing with the eight Copley 412 controls amplifiers. In addition, the DS1103 has four 8-bit programmable digital I/O channels. There are also several PWM generators, incremental encoders, a serial interface and a slave DSP board on the DS1103, but these are not used in this experiment.

The DS1103 works with MATLAB®, Simulink® and the Real-Time Workshop® from The Mathworks Inc. to make a easy to use control synthesis procedure. First, a controller model is created in Simulink®. A Simulink® block library allows one to access each feature of the DS1103. After selecting a fixed sampling time in the Simulink® solver parameters window and one click of the build button on the Real-Time Workshop® parameters page, the Real-Time Interface® converts the Simulink® model to C code, complies it, downloads it to the DS1103, and automatically starts the real-time simulation. The dSPACE ControlDesk® software lets the user create virtual instruments for data collection and experiment management. Furthermore, one has the ability to change any of the controller parameters in real-time and automatically run parameter studies. Figure 5.27 shows an example of the virtual instruments used in this experiment.

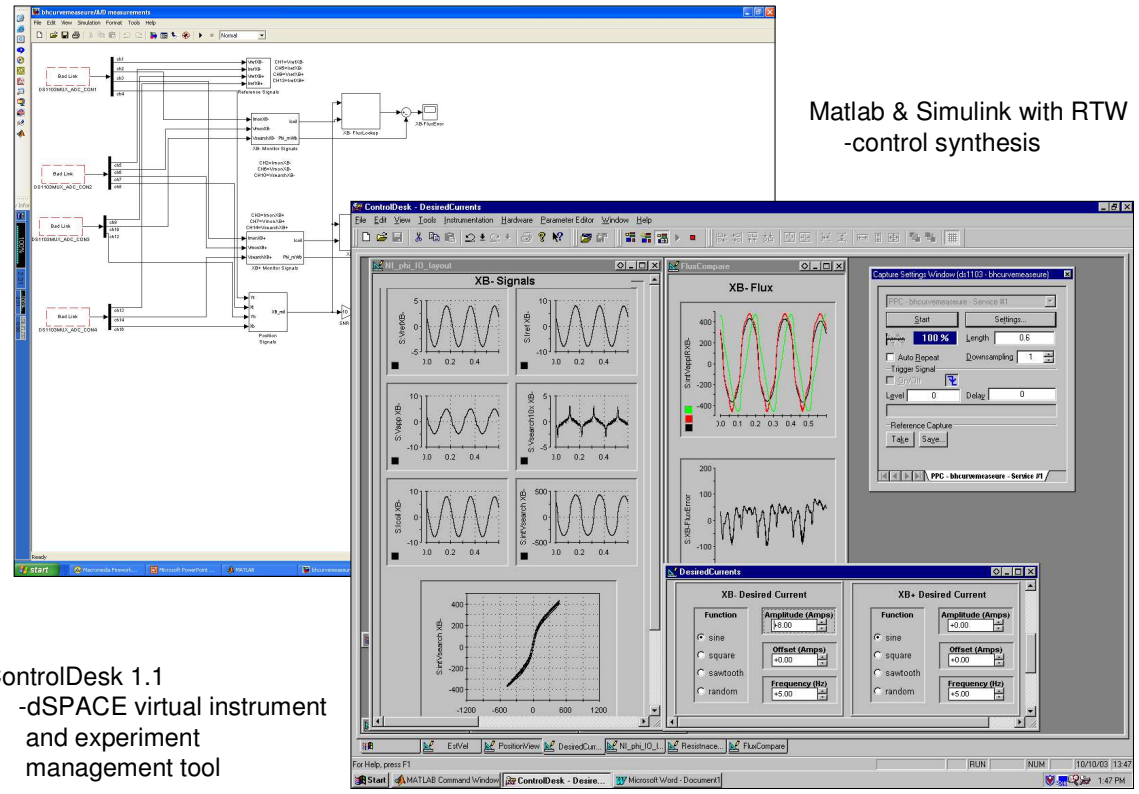

Figure 5.27: Use of Simulink and ControlDesk to take data and control the real-time simulation with virtual instruments. The virtual instrument shows a real-time readout of the voltage, currents, and $\phi - I$ curve of an electromagnet coil.

CHAPTER VI

FLUX MEASUREMENT AND IMPLEMENTATION OF THE GCFC CONSTRAINT

In this work, the magnetic flux is used to represent the electrical state as opposed to the typical choice of the easily-measurable coil current. Chapter 2 outlines some of the advantages of using the flux as opposed to the current to predict the electromagnet force. The assumption that flux is measurable was implicit in the development of the gcfc in Chapter 3 and the control laws in Chapter 4, however, this problem is not trivial. Section 6.1 compares several different techniques for measuring the flux. The pros and cons of each technique depends on the particular application. For the PREMAG AMB, a lookup table relating the flux, current, and position is constructed in Section 6.2.

The implementation of the gcfc condition depends not only on the measurement of flux, but also on the ability to introduce a flux bias into the electromagnets. This requires the use of a feedback loop to automatically adjust for the change in inductance as the airgap changes. The implementation of the flux bias on the PREMAG AMB is illustrated in Section 6.3. Furthermore, the flux-dependent voltage-switching rule of equation (3.9) that implements the gcfc condition is experimentally verified in Section 6.4.

6.1 Flux Measurement Techniques

Several methods of flux measurement are now discussed. The method of choice depends on the specific application.

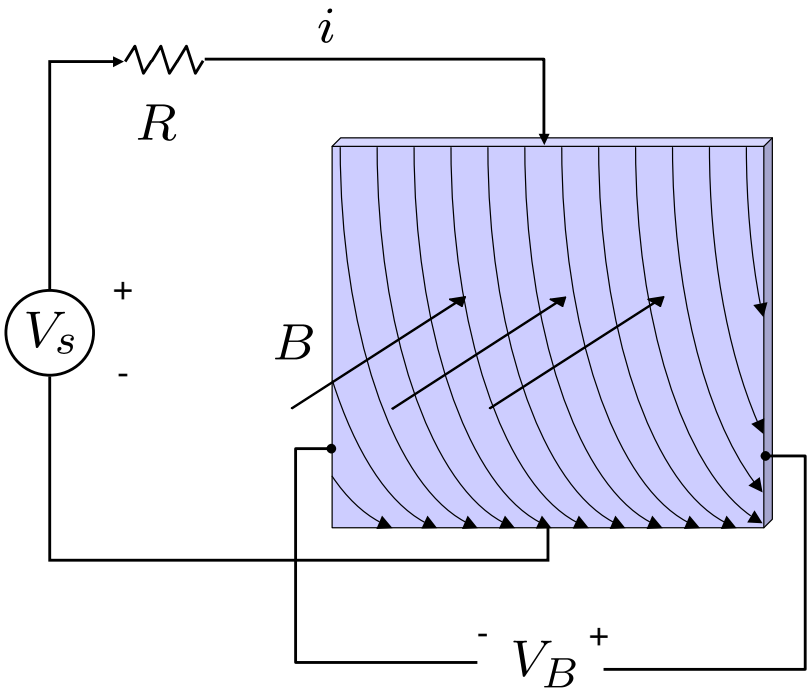

Figure 6.1: Hall-effect sensor. The magnetic field B is perpendicular to the face of the semiconductor.

Direct, real-time measurement of flux is possible via a Hall-effect sensor shown in Figure 6.1. A thin current-carrying semiconductor is inserted into the path of the magnetic field with flux density B. A downward current is established in the semiconductor by an external circuit. Via the Lorentz equation (Appendix C), the magnetic field deflects the downward current to the right inducing a voltage across the semiconductor. The voltage V_B generated is proportional to the magnetic flux density B. Flux is calculated by multiplying by the cross-sectional area. Although direct flux measurement is an attractive feature, these sensors are usually too large to be inserted into the airgap of a magnetic bearing. The nominal airgap for the PREMAG bearing is curved and about the thickness of 5 sheets paper, $g_0 = 20$ mils. This airgap is much too small for most of the available sensors. Furthermore, they

are often expensive and fragile.

Another technique uses a closed-loop position control law, for example, a PI controller with servo-amplifier acting in current mode, to create a force-current-position lookup table. Since the force is $f = c\varphi^2$, the flux can be calculated from the measured force. This technique as been successfully applied in [35]. The apparatus used in [35] is illustrated in Figure 6.2. In this technique, the beam is regulated to a setpoint

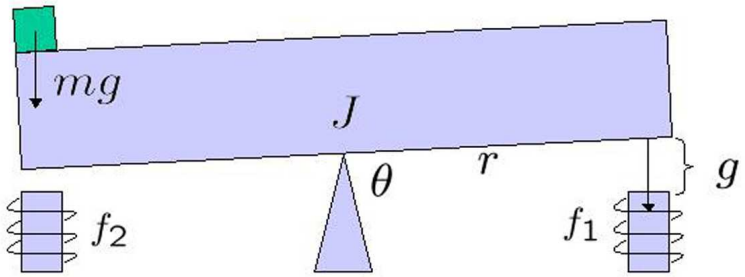

Figure 6.2: Illustration of Knospe's apparatus of [35]. The dynamics $J\ddot{\theta} = r(f_1 - f_2)$ implement a physical simulation of the 1-DOF AMB dynamics $m\ddot{x} = f_1 - f_2$.

using feedback control while a known weight is applied to one end of the beam. Since the rotor is regulated to a constant position, f_1 must be equal and opposite to the known applied force. The current required for regulation is measured. From these quantities, a lookup table between the flux ($\varphi = \sqrt{mg}/c$), current, and position may be constructed. However, this technique depends on the ability to consistently apply a known force. In a multi-degree of freedom apparatus like the PREMAG bearing, it is quite difficult to apply an external force in a given direction.

It is possible, but typically difficult, to reconstruct the velocity and flux from the measured signals (position and current) with the use of a nonlinear observer. Since the Separation Principle [34] does not hold for nonlinear systems, the closed-loop stability depends on the observer dynamics as well as the system dynamics. Consequently, each

of the previously obtained stabilizing control laws discussed in Chapter 4 must be re-designed with the observer in the loop. While this is a worthwhile task[1], it is deferred to future research while a simpler solution is pursued.

A classic technique for measuring the flux is to use a search coil. In this method, an additional coil of very thin magnet wire is wrapped around the actuator coil so that the coils share the same flux. If the terminals of the search coil are connected to an opamp differential amplifier (so that the amplifier has a magnificently large input impedance), no search coil current will flow and the open-circuit voltage is successfully monitored. Using Faraday's law, $V_s = N_s\dot{\varphi}$, the open-circuit voltage V_s generated across the search coil is integrated to obtain the flux. Since the coils are bound to pick up noise and have a small DC offset voltage from the opamp, true integration of the coil voltage is impractical. A DC-gain limited integration scheme must be used. Furthermore, the search coil can not detect a constant flux bias, because in this situation, the voltage generated across the search coil is zero. Thus, search coils are a good way to reconstruct AC portion the flux. This is insufficient for the PREMAG bearing because measurement of the DC flux bias is required.

Each of the above methods for flux measurement are deficient in terms of their practicality or their ability to measure a DC flux. A straightforward method for constructing a flux-current-position lookup table is selected for the PREMAG AMB. It is created with the use of a search coil and curve fitting, can measure the DC flux component, and is calculated off-line without the use of closed-loop control. This method is described next.

[1]Some progress has been made in this area. Acrak and Tsiotras have developed a reduced order nonlinear flux observer for the gcfc operated magnetic bearing that uses only velocity measurements [80].

6.2 Construction of the Flux-Current-Position Lookup Table

From the available flux measurement techniques previously discussed, the flux-current-position lookup table approach is selected. With the use of an integrating search coil and a sinusoidal excitation current, a family of $\varphi - I$ curves for several fixed rotor positions is generated: see Appendix B.3.1. Approximating these curves with their corresponding DC magnetization curves, a set of curves similar to those shown in Figure B.14 is obtained and a lookup table is constructed. The lookup table is able to detect the flux, including its DC component, from measurements of the current and position. Since the nonlinear-control test bed is implemented on only one control axis, only two lookup tables are required.

The DC magnetization curve is desirable because one may correlate a DC flux bias with the corresponding current bias and rotor position. One may be tempted to think that the following procedure is used to construct a DC magnetization curve: (1) fix the rotor position (2) set a DC current (3) measure the resulting DC flux. However, a *search coil can only sense a changing flux*. Thus, the DC magnetization curve is obtained by first generating a $\varphi - I$ curve and then fitting a curve to this AC data.

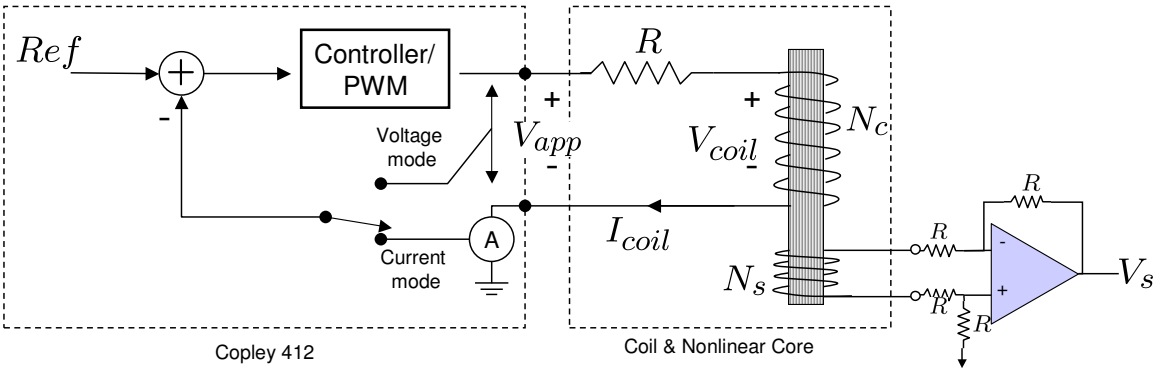

Figure 6.3: Configuration of Copley 412 amplifier, electromagnet, search coil, and differential amplifier.

The lookup table for each electromagnet is constructed from several $\varphi - I$ curves. The extra equipment required for the $\varphi - I$ curve generation is a search coil, a differential amplifier, and a Copley 412 servo-power amplifier. The Copley 412 is set to operate in current mode with a sinusoidal current reference. The search coil is used to obtain the flux and the $\varphi - I$ curve is generated as described in Appendix B.3.1. The measured $\varphi - I$ curves have the shape similar to those in Figure B.9. The configuration for one half of a control axis is shown in Figure 6.3.

The search coil is made from 36 gage copper magnet wire and has 10 turns ($N_s = 10$). It is wrapped tightly around the 60 turn actuator coil ($N_c = 60$) so that the search coil and the actuator coil share approximately the same flux. Since $V_{coil} = N_c\dot{\varphi}$ and $V_s = N_s\dot{\varphi}$,

$$V_{coil} = \frac{N_c}{N_s} V_s \tag{6.1}$$

The unity-gain, high-input impedance, differential opamp does not allow current to flow in the search coil. Consequently, the open-circuit voltage V_s is is produced at the output of the opamp. This allows direct measurement of the coil voltage *without* knowledge of the coil resistance. Since the Copley 412 monitors V_{app} and I_{coil}, one could calculate $V_{coil} = V_{app} - IR$ if a good estimate of the resistance is known. However, this method is very sensitive to the estimate of the coil resistance. This is further complicated by the fact that large operating currents may result in coil heating and changing resistance.

The search coil voltage is sampled and integrated in software to obtain the flux.

$$\varphi = \frac{N_c}{N_s} \int V_s dt$$

or in the frequency domain,

$$\varphi(s) = \frac{N_c}{N_s} \frac{V_s(s)}{s}$$

The output of the differential amplifier is bound to have some small DC offset voltage. Since the DC gain of the ideal integrator is infinite, this small offset voltage will cause

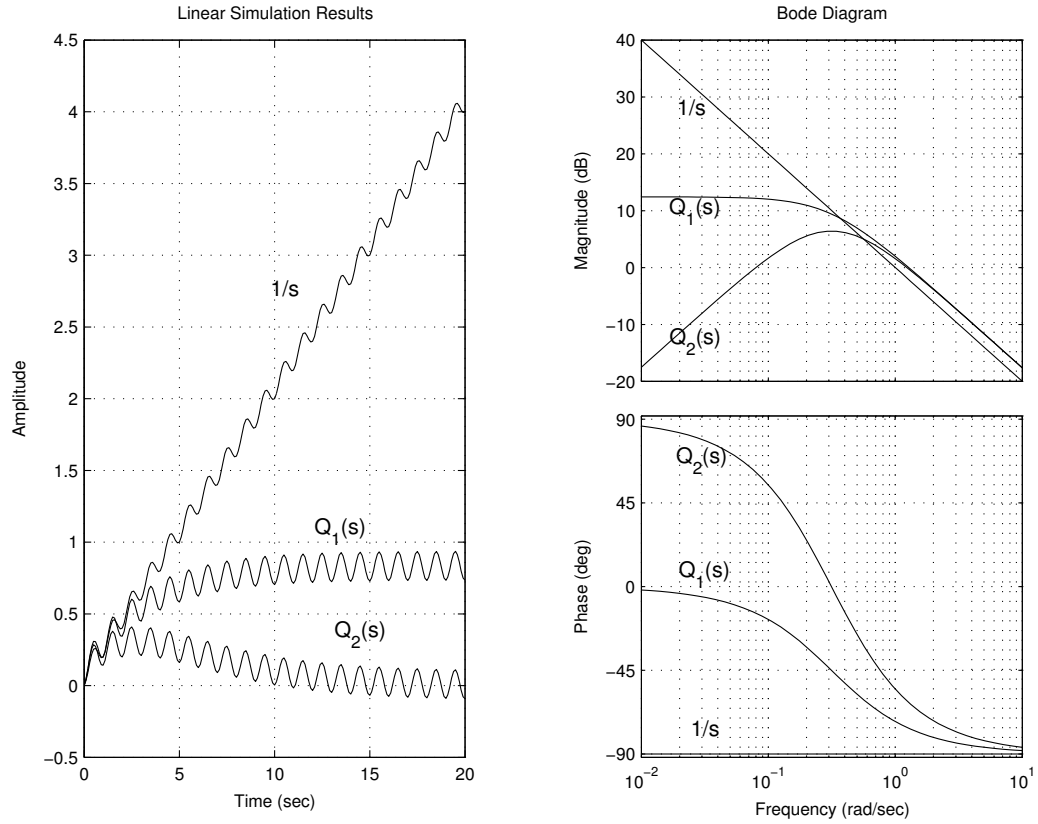

Figure 6.4: Comparison of the integrators $Q_2(s)$, $Q_1(s)$ ($a = 2\pi(50mHz)$) and $1/s$: **(a)** time response of $1/s$, $Q_1(s)$ and $Q_2(s)$ to input $V_s = .5\sin(2\pi t) + .2$ **(b)** frequency response of $1/s$, $Q_1(s)$ and $Q_2(s)$

the output of a true integrator to become unbounded. A limited, but high DC-gain low-pass filter can approximate the transfer function of the integrator down to a low frequency. For example,

$$Q_1(s) = \frac{1+a}{s+a}, \qquad \varphi(s) = \frac{N_c}{N_s} Q_1(s) V_s(s)$$

The low-frequency pole is set to $a = 2\pi(50\times10^{-3})$ so that $Q_1(s)$ emulates an integrator down to $50mHz$ and has a finite DC-gain: see Figure 6.4. At the output of the approximate integrator, one observes the integrated version of the periodic signal V_s superimposed on the step response of $Q_1(s)$ to the small DC offset. The steady-state value of this signal may be easily subtracted out after the settling time is reached.

Alternatively, Q_1 may be modified so that the DC gain is zero. For example, let

$$Q_2(s) = \frac{s}{(s+a)} Q_1(s) = \frac{(1+a)s}{(s+a)^2}$$

This transfer function has zero gain at DC and approximates the integral down to $50mHz$. After the transient response of $Q_2(s)$, the integral of the periodic component of V_s is available. A comparison of $Q_2(s)$, $Q_1(s)$ and $1/s$ is shown in Figure 6.4. The input signal for the simulation is $V_s = .5\sin(2\pi t) + .2$.

Since nonlinear control is used only on the bottom x axis of the PREMAG bearing, only two $\varphi - I - x$ lookup tables (one for the positive and negative x axis) are required. Several experiments are conducted to model the electromagnets. An experiment consists of fixing the rotor position with shims, setting a sinusoidal electromagnet current of a given frequency and amplitude and then recoding the coil current I_c, coil voltage V_s, applied voltage V_{app}, the rotor position x, and the flux in each electromagnet Φ_1 and Φ_2. The flux and current are plotted against each other to obtain the $\varphi - I$ curve. The entire set of collected data is summarized by the following piece of pseudo-code.

```
for x=[-16:2:16] % Step through the entire range of rotor positions
    for f=[5 10 20] % use 3 excitation frequencies
        for A=[1 3 8] % use 3 excitation amplitudes
            set I1 = Asin(2πft), I2 = 0;
            measure x, Ic, Vs, Vapp and φ for both electromagnets;
            set I1 = 0, I2 = Asin(2πft);
            measure x, Ic, Vs, Vapp and φ for both electromagnets;
        end
    end
end
```

In the above experimental test procedure, about 80% of the range of motion is traversed in two mil steps. This allows one map the variation of the inductance with

position. At each position, three excitation frequencies are used to investigate the effects of eddy-currents. Recall that eddy-current effects increase with frequency: see Appendix B.3.2. Three excitation amplitudes are used: one that keeps the core well below saturation (1 Amp), one that is just beginning to saturate the core (3 Amps), and one that is well into saturation (8 Amps). For each position, frequency, and amplitude, one electromagnet is excited while the other is open-circuited. However, the voltage signals are recorded in *both* electromagnets to check for mutual inductance between the coils. The above test procedure creates 288 data sets.

Figure 6.5 shows the signals collected for an excitation frequency of $5Hz$, and an amplitude of 1 Amp. This amplitude and frequency avoids driving the core into saturation and has minor eddy-current effects. Observe that the coil current I_{coil}, the applied voltage V_{app}, and the flux φ are roughly sinusoidal. The coil voltage V_{coil} (shown in tens of millivolts) is very noisy but is still approximately sinusoidal.

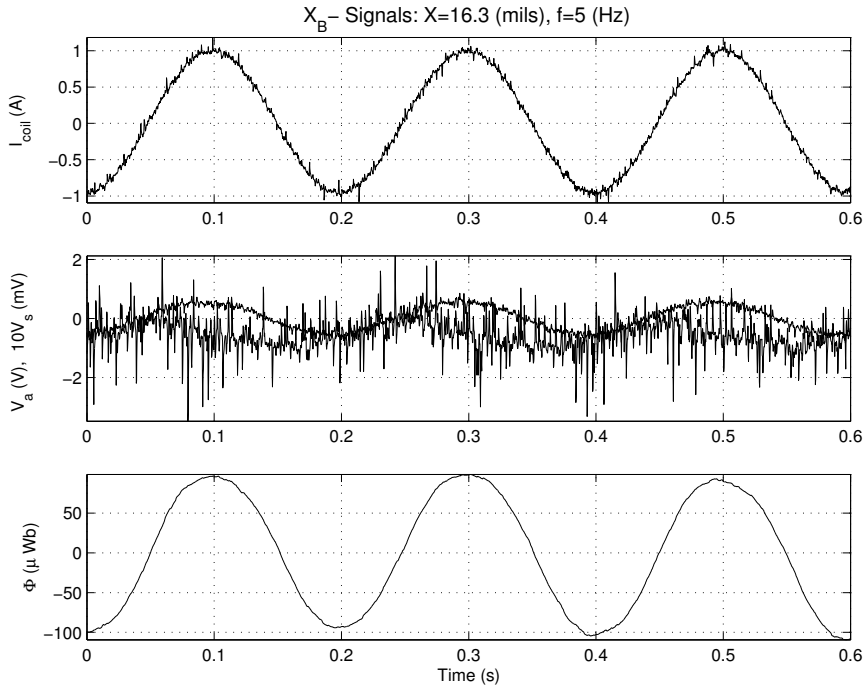

Figure 6.5: Electromagnet signals for $I_1 = \sin(10\pi t)$ (A): **Top:** coil current I_c (A) **Middle:** applied voltage V_{app} (V) and coil voltage $10V_{coil}$ (mV) **Bottom:** electromagnet flux $\varphi = \int V_{coil}$ (μWb).

Figure 6.6 shows the electromagnet signals for $I_1 = 8\sin(10\pi t)$ Amps. This excitation frequency avoids major eddy-current effects and the large amplitude drives the core into saturation. Observe the current I_{coil} and applied voltage V_{app} are sinusoidal. As expected, the flux is slightly distorted and coil voltage V_{coil} (shown in tens of millivolts) is very noisy and is highly distorted.

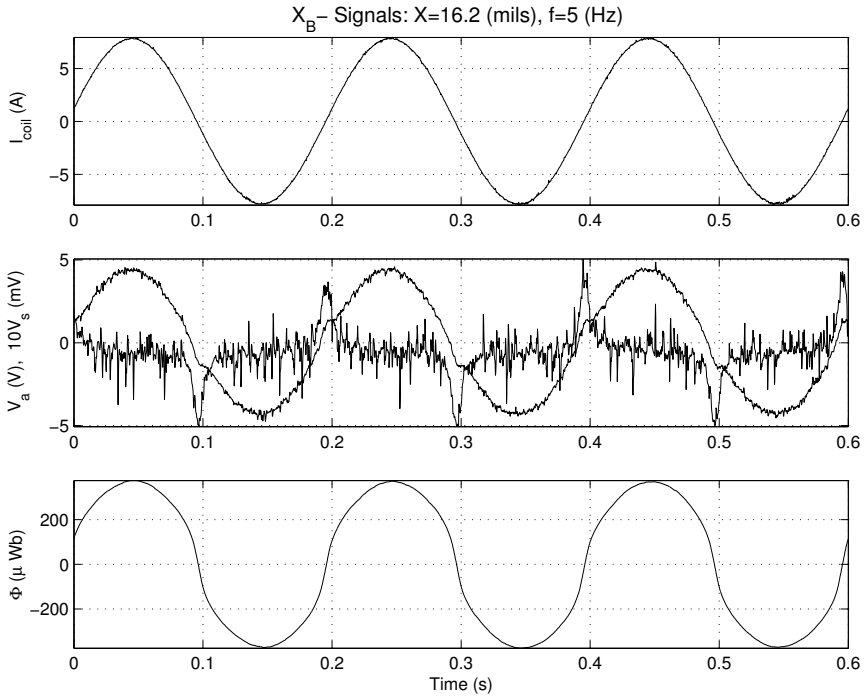

Figure 6.6: Electromagnet signals for $I_1 = 8\sin(10\pi t)$ (A): **Top:** coil current I_c **Middle:** applied voltage V_{app} (V) and coil voltage $10V_{coil}$ (mV) **Bottom:** electromagnet flux $\varphi = \int V_{coil}$ (μWb).

Figure 6.7 shows the $\varphi - I$ curve for each set of data in Figure 6.5 and 6.6. The first data set is clearly unsaturated while the second data set operates the core well into saturation. Note that the saturation is not as dramatic as in Figure B.9. The unsaturated curve is easily approximated by a straight line[2].

There is some "thickness" to this $\varphi - I$ curve in Figure 6.7, but it difficult to

[2]The slope of this line is $\frac{N}{\mathcal{R}(x)}$. If φ vs NI was plotted, the slope would be the inverse of the reluctance.

determine if this is due to hysteresis or eddy-current effects. In any case, this hysteresis effect is relatively minor. Recall that the main problem posed by hysteresis when trying to estimate the flux from current measurements is that the flux and the current are *not necessarily in phase*: see Section B.3.1. In general, the current and flux peak together but do not share common zero-crossings. However, one may investigate Figure 6.5 and 6.6 to find that the zero-crossings of the flux and current are so close that they may be considered equal. For example, checking the data set in Figure 6.6, the current has a zero crossing at $t = .0857s$ and the flux has a zero crossing at $t = .0871s$. Since the position controller bandwidth will only be on the order of $100Hz$, this slight difference in zero crossings should pose no serious problems.

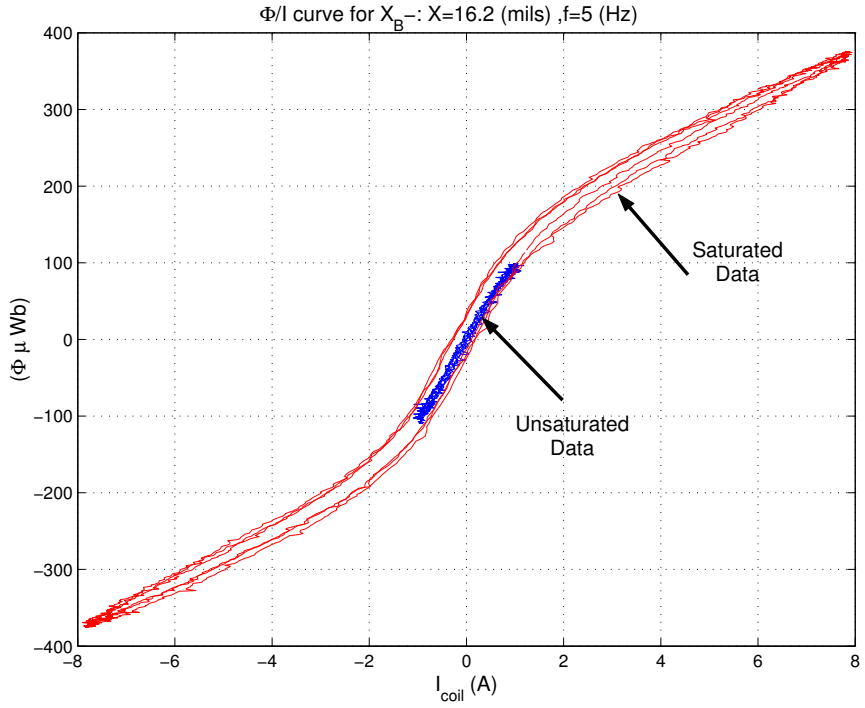

Figure 6.7: Two $\varphi - I$ curves for the data in Figures 6.5 and 6.6. For this position ($x = 16.2$ mil), the electromagnet starts to saturate for currents larger than about 1.5 Amps. The unsaturated portion of the curve ($I_{coil} < 1.5$ Amp) is well-approximated by a straight line.

Figure 6.8 shows the effect of eddy-currents. Recall that eddy-current core losses increase with frequency. The figure shows the $\varphi - I$ curves for an excitation signal

that saturates the core and has excitation frequencies of $5Hz$, $10Hz$, and $20Hz$. As expected, the area enclosed by the $\varphi - I$ curve increases with frequency.

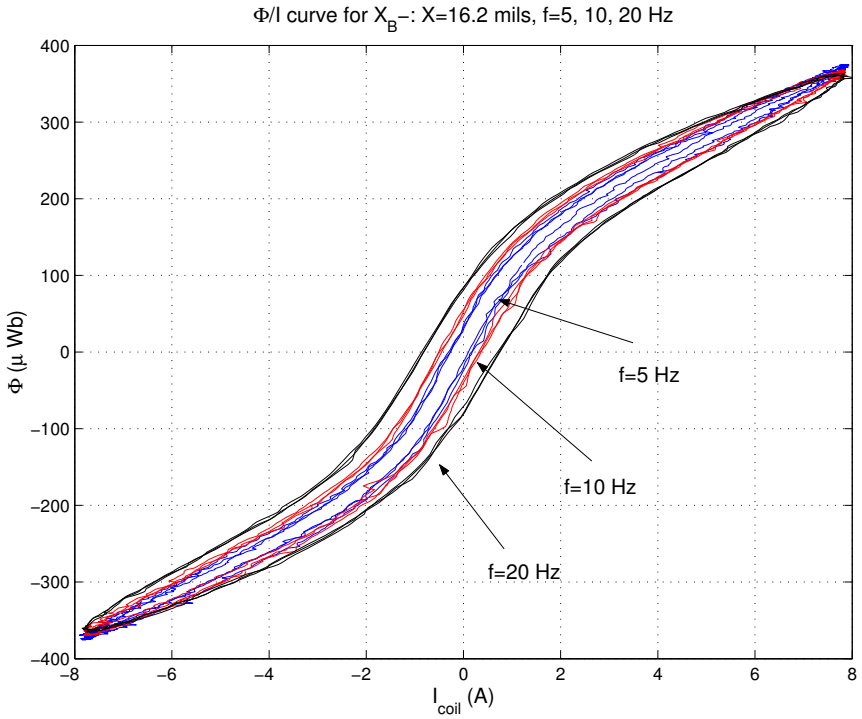

Figure 6.8: Electromagnet signals for $I_1 = 8\sin(2\pi ft)\ (A)$. $f = 5, 10, 20\ Hz$. Eddy-current distortion is worse as f increases.

Note that sinusoidal currents of "low" frequency are used to construct the sample $\varphi - I$ curves shown in Figure 6.7. However, the DC magnetization curve is desired: see Appendix B.3.1. One may consider the $\varphi - I$ curves as "perturbed" or "corrupted" away from the DC magnetization curve by eddy-current effects and hysteresis. A polynomial fit to this data serves as a good approximation to the DC magnetization curve. From the slope of the unsaturated data in Figure 6.7, the inductance is found $4.3mH$[3]. A ninth-order polynomial (not shown in Figure 6.7) is fit to the saturated data.

A family of the above polynomial approximations to the DC magnetization curve

[3]The slope, which corresponds to $N/\mathcal{R}(x)$, on the $\varphi - I$ curve is 71 $\mu H/turn$. To calculate the inductance, $L(x) = N \times slope \times 1e-6$.

parameterized by the rotor position is used to construct the $\varphi - I - x$ lookup table. The lookup table for the bottom negative x axis (X_B-) is shown in Figure 6.9 (only shown for $I_c \geq 0$). The lookup table for X_B+ is similar. The airgap for X_B- is $g = g_0 + x$. As the rotor position increases, the airgap for the X_B- electromagnet increases. From the graph, observe that as the airgap increases, the inductance (slope) decreases. This is consistent with the discussion in Appendix B.3.3. A $3D$ visualization of this lookup tables is shown in Figure 6.10.

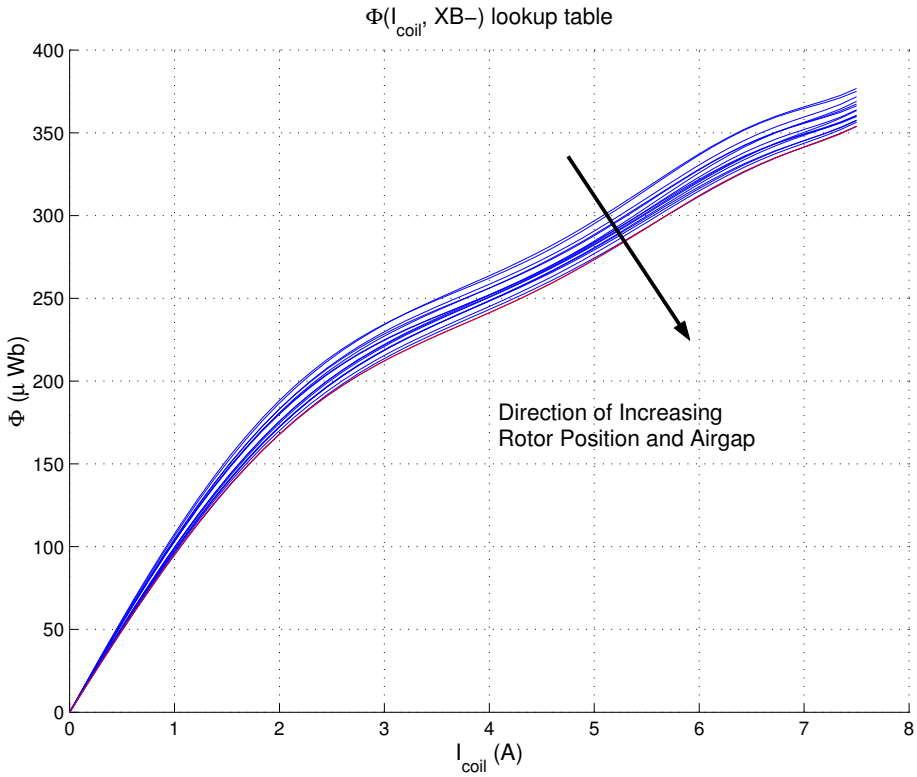

Figure 6.9: $2D$ $\varphi - I - x$ lookup table for the x_b- axis constructed from ninth-order polynomial approximations to the DC magnetization curves for several rotor positions.

To illustrate the fit of the x_B- lookup table, the measured search coil flux is compared to the output of the lookup table which is driven by the measured coil data for the position $x_B- = 0.137$ mils. The comparison is shown in Figure 6.11. The lookup table successfully reproduces the flux as measured by the search coils. Also shown is the flux as calculated by $\int V_{app} - I_c \hat{R}$ where $\hat{R}$ is a resistance estimate. In

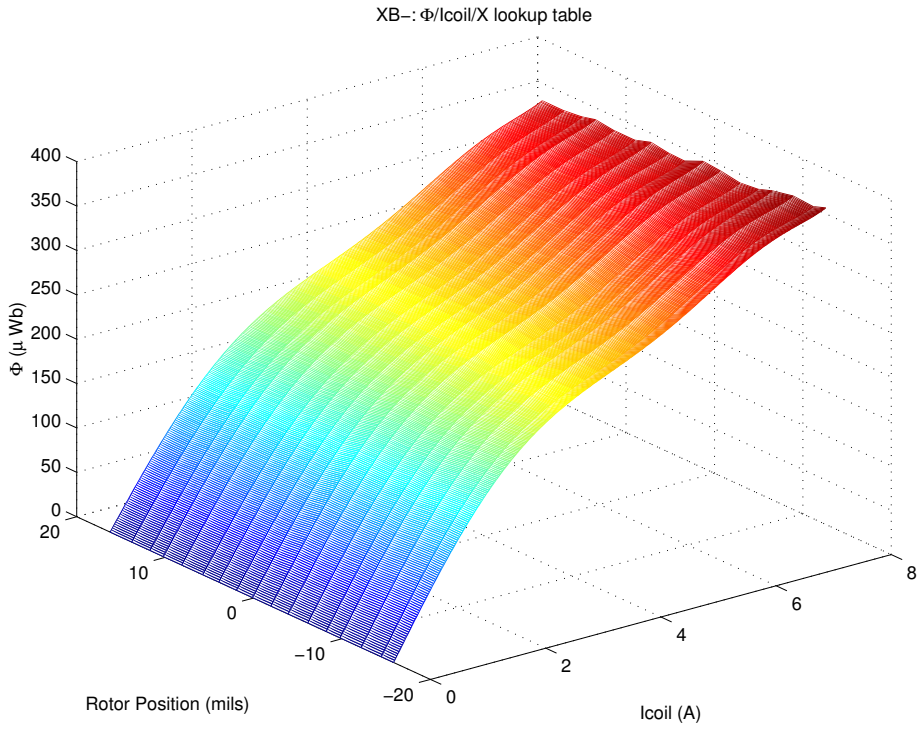

Figure 6.10: $3D$ visualization of the $\varphi - I - x$ lookup table for the x_b- axis.

the figure, $\hat{R} = 0.45\Omega$ is used, however, the true resistance value of the coil is about 0.5Ω. Although the difference $R - \hat{R}$ is very small, the estimation of the flux with $\int V_{app} - I_c\hat{R}$ is poor. Thus, use of the coil resistance for reconstruction of the flux is probably too sensitive with respect to $\hat{R}$ to be of any practical use.

6.3 Flux-Bias Implementation

In the gcfc method, a flux bias is introduced into the electromagnet to increase the bearing stiffness. While this subject has been discussed previously, the implementation of a bias has not.

A current bias is typically easy to implement. It is a trivial matter with a servo-amplifier acting in current-mode (add a constant to the reference signal). The implementation of a flux bias requires a little more work. If one has a lookup

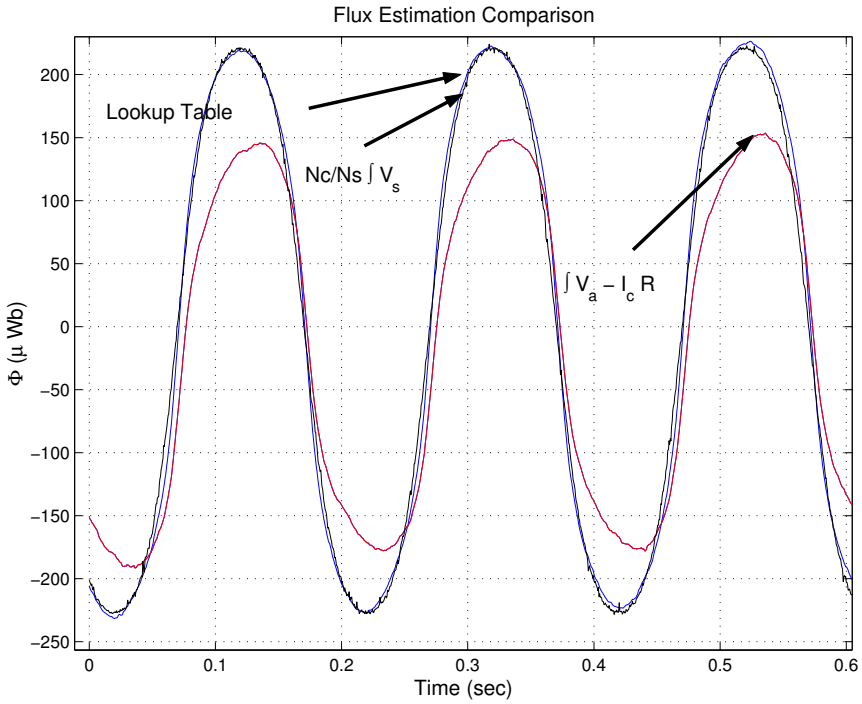

Figure 6.11: Flux estimation using the search coil ($\frac{N_c}{N_s}\int V_s$), the x_b- lookup table, and the resistance ($\int V_{app} - I_c\hat{R}$). Note $\hat{R} = 0.45\Omega$, $R = 0.5\Omega$, and $x_B- = 0.137$ mils.

table relating flux, current, and position $\varphi = h(I, x)$ and a servo-amplifier operating in current mode, then the setting of a flux bias only requires the calculation of the inverse of the lookup table. By selecting $I_{ref} = h^{-1}(\Phi_{0des}, x)$ so that $\Phi = h(I_{ref}, x) = h(h^{-1}(\Phi_{0des}, x), x) = \Phi_{0des}$ the desired bias is implemented.

When operating in voltage mode, as in the case of the nonlinear control axes in the PREMAG bearing, a feedback loop is required. The coil dynamics in voltage-mode are

$$\begin{aligned} N\dot{\Phi} &= -RI + V_{app} = -Rh^{-1}(\Phi, x) + V_{app} \\ &\approx -\frac{R}{NL(x)}\Phi + V_{app} \end{aligned}$$

where V_{app} is regulated to V_r by the servo-amplifier and the $\approx$ sign is used with the approximation $N\varphi = L(x)I$. Rewriting,

$$\dot{\Phi} = -\frac{R}{N^2L(x)}\Phi + V_r = -R\mathcal{R}(x)\Phi + V_r$$

When the inputs into the coil dynamics are viewed as the voltage V_{app} and x with Φ as the state, the system is nonlinear due to the product of $\mathcal{R}(x)$ and Φ. However, for constant x, the system is completely linear. This allows one to use a superposition-like approach to implement $\Phi_j(t) = \Phi_{j0}(t) + \phi_j(t)$ by setting

$$V_{jr} = V_{jb} + V_{jc}, \qquad j = 1, 2 \tag{6.2}$$

V_{jc} is generated from one of the control laws of Chapter 4 and the voltage switching rule of (3.9) to implement ϕ_j. V_{jb} is produced from a simple PI controller used to regulate $\Phi_{j0}(t)$ to the constant Φ_{0des}. Specifically, $V_{jb} = (k_p + \frac{k_i}{s})e_{jb}$ where the bias error is defined as $e_{jb}(t) := \Phi_{0des} - \Phi_{j0}(t)$.

Section 3.2.2 shows that the voltage switching rule (3.9) implements the gcfc. Repeated here for convenience, the voltage switching rule

$$\begin{aligned} V_{c1} = v, \quad V_{c2} = 0 \quad \text{when} \quad \phi \geq 0 \\ V_{c1} = 0, \quad V_{c2} = -v \quad \text{when} \quad \phi < 0 \end{aligned}$$

implements the gcfc condition

$$\begin{aligned} \phi_1 = \phi, \quad \phi_2 = 0 \quad \text{when} \quad \phi \geq 0 \\ \phi_1 = 0, \quad \phi_2 = -\phi \quad \text{when} \quad \phi < 0 \end{aligned}$$

Under this condition, the control fluxes may be written as

$$\phi_1(t) \quad = \phi_+(t) := \max(\phi(t), 0) \tag{6.3a}$$

$$\phi_2(t) \quad = \phi_-(t) := \max(-\phi(t), 0) \tag{6.3b}$$

where

$$\phi(t) := \Phi_1(t) - \Phi_2(t) \tag{6.4}$$

Consequently,

$$\Phi_1(t) \quad = \Phi_{10}(t) + \phi_+(t) \tag{6.5a}$$

$$\Phi_2(t) \quad = \Phi_{20}(t) + \phi_-(t) \tag{6.5b}$$

Using (6.5), the bias errors $e_{jb} = \Phi_{0des} - \Phi_{j0}$ may be calculated as

$$e_{b1} = \Phi_{0des} - \Phi_1(t) + \phi_+(t) \tag{6.6a}$$

$$e_{b2} = \Phi_{0des} - \Phi_2(t) + \phi_-(t) \tag{6.6b}$$

The signals Φ_j are the total fluxes of each electromagnet and are calculated from $\Phi_j = h_j(I_j, x)$ where I_j is the measured electromagnet current. The signals $\phi_\pm(t)$ are calculated from (6.3) and (6.4).

Figure 6.12 shows the performance of the PI control as it regulates the flux bias on the X_B axis to $\Phi_0 = 50\mu Wb$ in the presence of rotor motion (due to an external force). The control voltage $V_c = 0$ so that $\phi = 0$. The bias errors e_{bj}, the bias control voltages V_{bj}, and the total fluxes Φ_j for $j = 6, 8$ are shown. For clarity, the error signals and bias voltages have been low-pass filtered to remove some of the PWM switching noise. Specifically, the bias control voltages are $V_{bj} = (1 \times 10^{-3})(30 + \frac{1}{s})e_{jb}$ for $j = 6, 8$. Observe that the bias voltages automatically adjust for changes in the rotor position so that the flux bias is regulated to $50\mu Wb$ in both electromagnets.

6.4 Open-Loop Verification of the GCFC

This section presents the experimental results which verify that implementation of the flux bias via an extra PI control loop as discussed in Section 6.3 and the voltage-switching rule of (3.9) impose the gcfc on the coil dynamics. This is shown in a simple test that does not require a closed-loop position controller. The gcfc implementation is further demonstrated in Chapter 8 where the experimental validation of the control laws in Chapter 4 is presented.

To clarify the implementation of the gcfc condition, Figure 8.1 shows the block diagram of the plant and required feedback to implement the gcfc. The Copley 412 amplifiers regulate the voltage applied to coils V_{app} to the reference voltage V_r. When IR compensation is employed, the amplifiers regulate the ideal coil voltage V_{coil} to

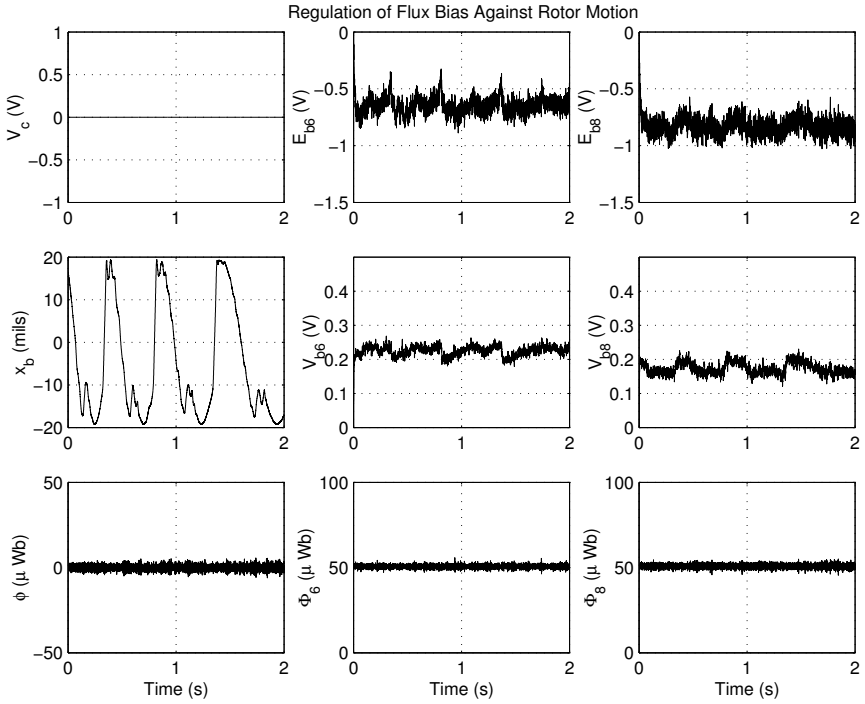

Figure 6.12: Regulation of flux bias on the x_b axis to $\Phi_0 = 50\mu Wb$ against rotor motion: $k_p = 30 \times 10^{-3}$, $k_i = 1 \times 10^{-3}$.

V_r so that $N_c\dot{\Phi}_j = V_{rj}$. The measured current I_6, I_8 and the measured rotor position x in conjunction with the flux lookup tables are used to produce flux measurements Φ_6 and Φ_8 and the generalized flux ϕ. The flux bias control block uses these signals to generate voltage commands V_{bj} to regulate the flux bias. The gcfc block uses the generalized flux ϕ to distribute the control voltage V_c according to the voltage switching rule. The control voltage V_c is typically generated by a control law from Chapter 4, however, it is set to a reference signal in this open-loop actuator test. The total reference voltage V_{rj} is the sum of a bias component V_{bj} and a control component V_{cj}.

Recall that when the flux bias is set to zero, the gcfc corresponds with the cfc. Figure 6.14 shows the experimental data for the X_B control axis. The sinusoidal control voltage V_c is used as a reference in this open-loop actuator test. Depending on the sign of the generalized flux Φ, the control voltage V_c is distributed to the

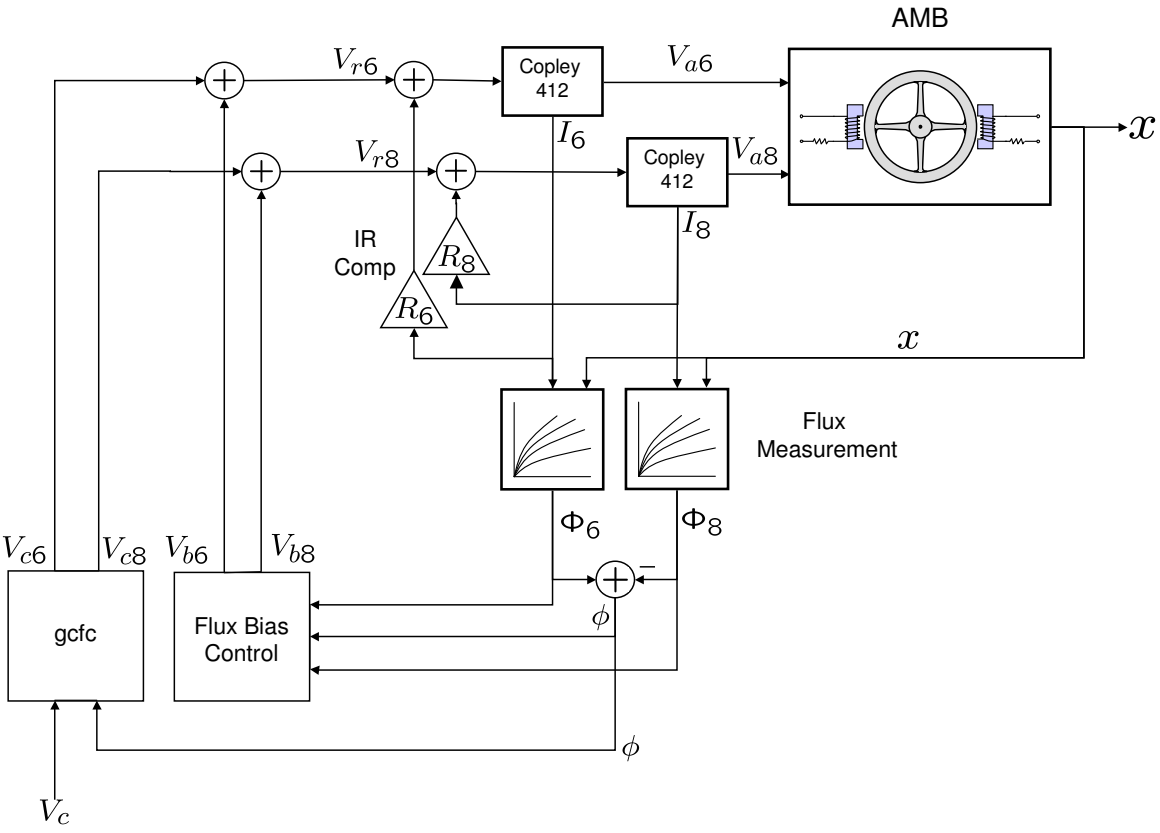

Figure 6.13: Block diagram of gcfc implementation for the x_b actuator axis. Copley 412 amplifiers working in voltage mode with software IR compensation.

appropriate coils V_{c6} and V_{c8}. Note that V_{cj} may be positive and negative while the total fluxes $\Phi_j \geq 0$ (and total currents $I_{cj} \geq 0$) for $j = 6, 8$. The rotor position x_B is fixed in this test. The resulting flux Φ_6 and Φ_8 are complementary and the generalized control flux $\Phi = \Phi_6 - \Phi_8$.

Figure 6.15 shows a similar test, however a $100\mu Wb$ flux bias is implemented and the rotor is free to move. The total coil currents I_{cj} and total fluxes Φ_j for $j = 6, 8$ are shown. The bias control voltages V_{jB} are not shown, but regulate the flux bias to $100\mu Wb$ even in the presence of the time varying rotor position. One may verify that $\Phi_6 = \Phi_0 + \phi_+(t)$, $\Phi_8 = \Phi_0 + \phi_-(t)$, and $\phi = \Phi_6 - \Phi_8 = \phi_6 - \phi_8$.

Figure 6.16 shows a similar gcfc test, however a square wave voltage reference is used. Again one may verify that gcfc condition and the $100\mu Wb$ flux bias are properly implemented. Furthermore, the IR compensation with $\hat{R}_6 = 0.5\Omega$ and $\hat{R}_8 = 0.63\Omega$

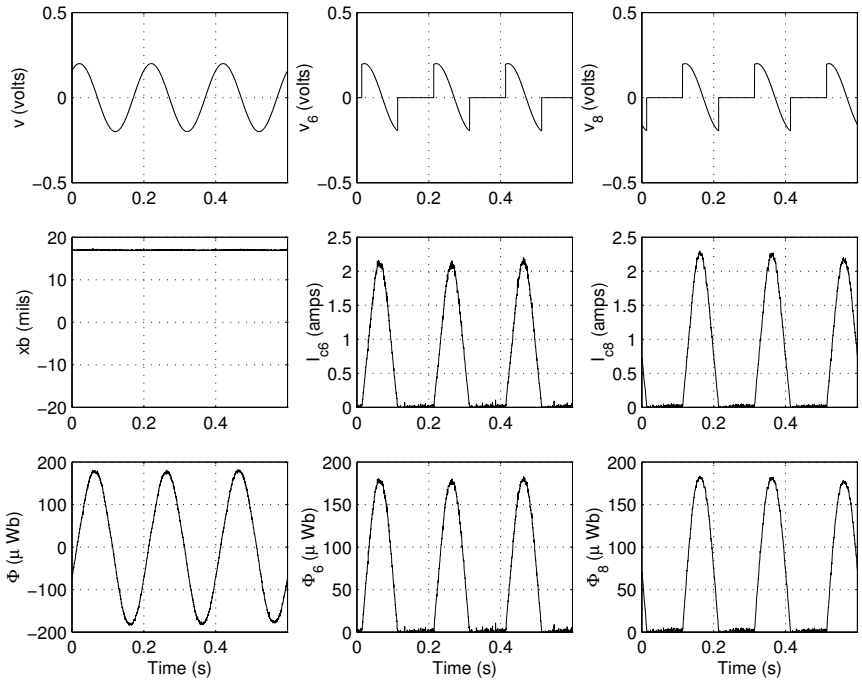

Figure 6.14: Open-loop ZB cfc test using IR compensation ($\hat{R}_6 = 0.5\Omega$, $\hat{R}_8 = 0.63\Omega$).

is illustrated. Since the IR compensation roughly implements $N_c\dot{\phi} = V_{cr}$, a square wave voltage reference generates a roughly triangular generalized flux ϕ signal.

Note that the current measurements are significantly filtered to remove much of the ripple noise generated by the PWM amplifiers: see Chapter 5 for details. Any noise in the current measurement appears in the flux signal. The magnitude of the flux noise is on the order of $\pm 3\mu Wb$. According to the gcfc switching rule, V_{c1} is active when $\phi \geq 0$ and V_{c2} is active when $\phi < 0$. Thus, a noisy ϕ may result in several undesirable switchings or chattering. To prevent this, one may introduce a switching boundary layer of $\pm B$ into the voltage switching rule. In this way, if V_{c1} is active, then it does not deactivate until $\phi < -B$, at which point, V_{c2} activates. When V_{c2} is active, it does not deactivate until $\phi > B$, at which point V_{c1} reactivates. This switching technique is equivalent to an electronic comparator with hysteresis or a relay. It is easily implemented in Simulink with the relay block from the nonlinear block library.

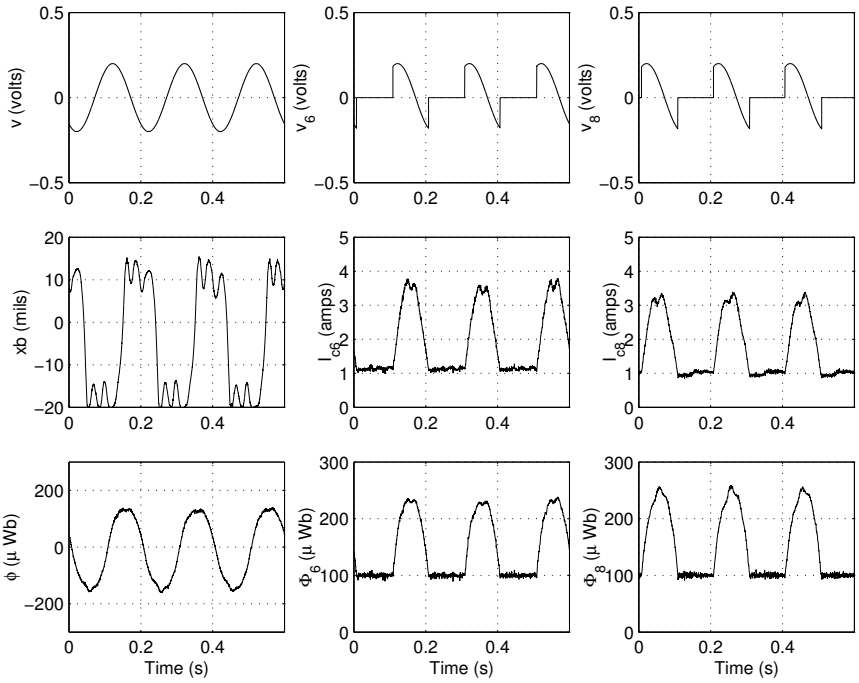

Figure 6.15: Open-loop LB gcfc test using IR compensation ($\hat{R}_6 = 0.5\Omega$, $\hat{R}_8 = 0.63\Omega$) with flux bias set to $100\mu Wb$.

The gcfc condition assumes that the coils and amplifiers used on opposing ends of a control axis are identical. Of course, the coils in practice are not identical. The resistances are unequal. When using IR compensation, the coil resistance is effectively changed to $R - \hat{R}$ in each coil. This new effective resistance is made small by selecting $\hat{R}$ so that the ideal coil voltage V_{coil} tracks the reference voltage. However, efforts must also be made to make sure the $R_6 - \hat{R}_6 \approx R_8 - \hat{R}_8$ so that the amplifiers are "matched". To match the amplifiers, one adjusts the $\hat{R}$ estimates while monitoring V_{coil} in each amplifier. For example, when applying a square wave reference to each amplifier, the V_{coil} response in both amplifiers will be very similar when the IR compensation is tuned properly. Figure 5.23 shows an example of IR compensation where the amplifiers are matched. Figure 6.17 shows a open-loop gcfc test with IR compensation $\hat{R}_6 = 0.5\Omega$ and $\hat{R}_8 = 0.52\Omega$. In this case, the amplifiers are unmatched because the ideal coil voltages do not have a similar shape. As a result, the reconstructed generalized flux in an open-loop gcfc test will be asymmetric. Observe

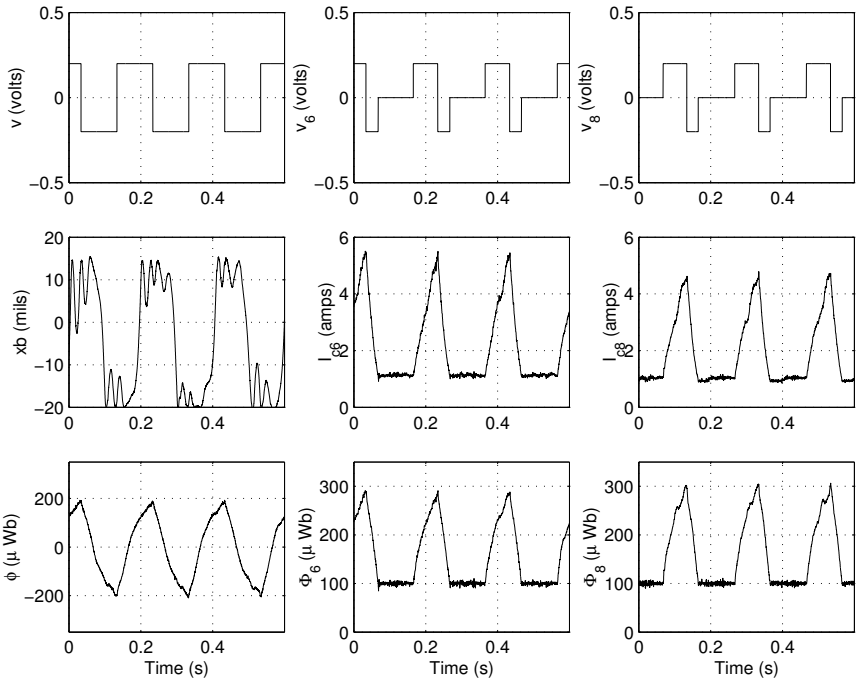

Figure 6.16: Open-loop LB gcfc test using IR compensation ($\hat{R}_6 = 0.5\Omega$, $\hat{R}_8 = 0.63\Omega$) with flux bias set to $100\mu Wb$. Square wave reference signal.

in Figure 6.18 that the reconstructed generalized flux has a positive amplitude of about $175\mu Wb$ and a negative amplitude of about $125\mu Wb$.

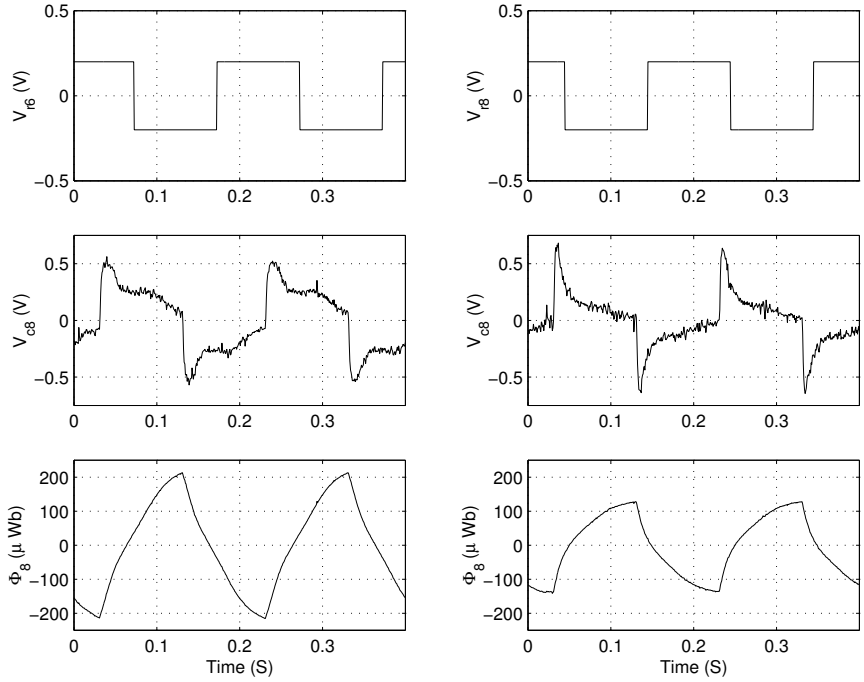

Figure 6.17: IR compensation test: $\hat{R}_6 = 0.5\Omega$, $\hat{R}_8 = 0.52\Omega$. Amplifiers are "unmatched".

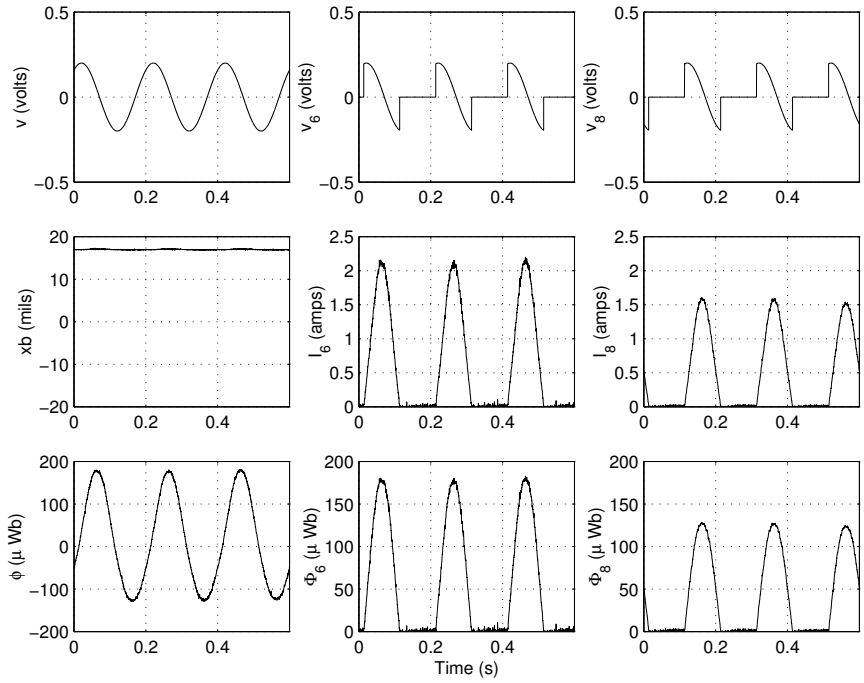

Figure 6.18: Open-Loop gcfc test using IR compensation ($\hat{R}_6 = 0.5\Omega$, $\hat{R}_8 = 0.52\Omega$) with "unmatched" amplifiers. The resulting generalized flux ϕ is asymmetric.

CHAPTER VII

4-DOF PREMAG BEARING MODELLING AND LINEAR CONTROL

This chapter presents the 4-DOF modelling and linear control of the PREMAG reaction wheel. Although 4 independent SISO current-mode control laws are used in a decentralized control approach to stabilize the reaction wheel, modelling of the full 4-DOF AMB dynamics gives insight into the coupling of the input channels and how the current biasing effects the open-loop stiffness for each degree-of-freedom. In Section 7.1, the dynamics are naturally derived by modelling the horizontal translation of the rotor's center of gravity and the tilt of the rotor about the horizontal axes. However, since airgap measurements are available and regulation of each airgap to g_0 is equivalent to regulation of the rotor tilt and translation, the dynamics in terms of the measured airgaps are also presented. Note that the rotor's axial spin and translation are considered constant in this derivation. The linearization of each model, presented in Section 7.2, gives slightly different insights into the open-loop characteristics.

A decentralized control approach is used to stabilize the reaction wheel. In this technique, it is assumed that the four DOF of the reaction wheel may be controlled independently. The linear control design used on each degree-of-freedom is presented in Section 7.3. Since a decentralized PID-like control ignores the coupling between the degrees-of-freedom, it is not guaranteed in general that this approach will stabilize a MIMO system. However, *local* asymptotic stability of the MIMO coupled system using decentralized control is verified by checking the eigenvalues of a closed-loop system matrix. This is analysis presented in Section 7.4. Global asymptotic stability

is predicted by simulation of the decentralized linear control scheme on the nonlinear model in Section 7.5, however, only local asymptotic stability is verified by the experimental results presented in Section 8.6.

Recall that in the interests of time and simplicity, the verification of the low-loss nonlinear control laws developed in Chapter 4 is only conducted on one degree-of-freedom of the AMB: see Chapter 8. The linear control presented in this chapter is used on the remaining three axes.

7.1 AMB Dynamic Modelling

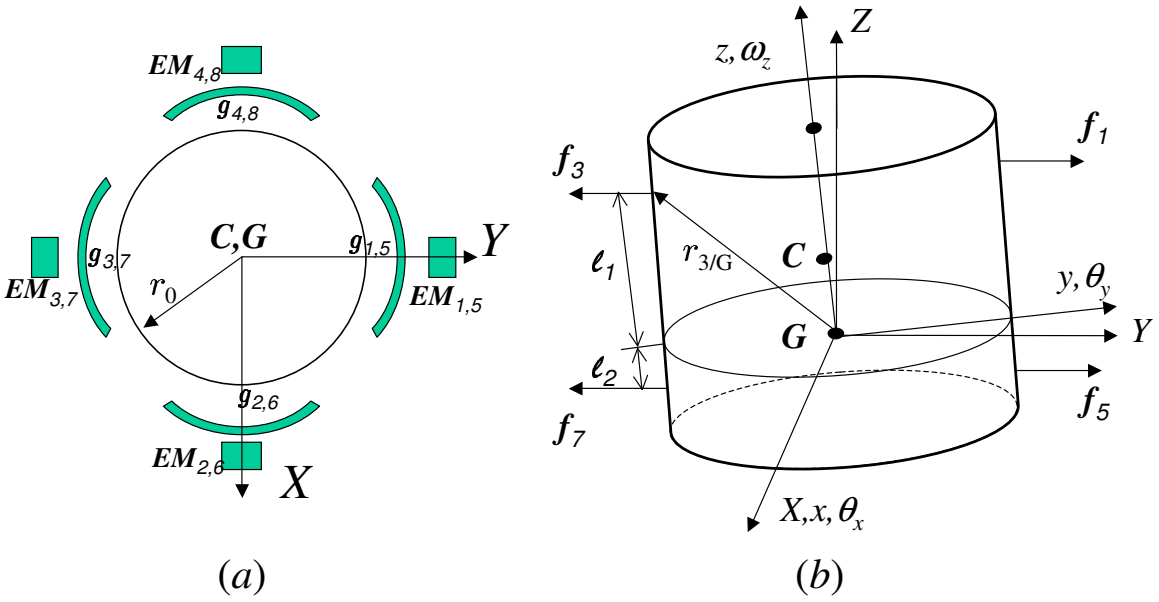

Figure 7.1: Schematics and free-body diagram of rotor. Forces in the XZ plane are hidden for clarity.

Figure 7.1a shows a top-view of the AMB illustrating the numbering scheme for the electromagnets, sensor blocks, and airgaps. The labels EM_j and g_j indicate the position of the j^{th} electromagnet, sensor, and airgap. The variables corresponding to the top stack of actuators and sensors have subscripts $j = 1, ..., 4$, while the lower stack is denoted with subscripts $j = 5, ..., 8$. Note that the even and odd subscripts correspond to the inertial horizontal X and Y directions, respectively. Note that the

rotor is said to be "centered" when all of the airgaps g_j have the same length, g_0. The rotor has radius r_0.

Figure 7.1*b* shows the free-body diagram of the rotor. First, note that the rotor center of mass G is located directly below the rotor geometric center C. That is, the rotor is modelled as initially being perfectly balanced and the addition of the PMB magnets acts only to shift the center of gravity downward. Actual rotor imbalance may cause the rotor to whirl during high speed operation, however, this is considered a disturbance effect instead of modelling it directly. Since the translation of the rotor along its axial direction is neglected, assume that the rotor center of mass G translates only in the inertial XY plane. The inertial frame is denoted XYZ (with unit vectors $\hat{I}, \hat{J}, \hat{K}$) and is fixed in space at G when the rotor is centered. A body-fixed frame xyz (with unit vectors $\hat{i}, \hat{j}, \hat{k}$) is also defined to describe rotations of the rotor about the x and y axes. Positive rotations θ_x and θ_y are taken in accordance with the right hand rule. The angular velocity ω_z along the body-fixed z axis is assumed to be constant. The electromagnet forces, acting at moment arms ℓ_1 and ℓ_2 measured along the z axis, produce torques on the rotor[1]. A sample moment arm $r_{3/G}$ of the force f_3 as measured from G is also shown. Note that the electromagnet forces always point in the same direction in inertial space.

7.1.1 Modelling Assumptions

The assumptions used in the derivation of the dynamics are now stated. The translation about Z axis is neglected. It is implicit that the PMB supplies a positive Z force to just cancel the weight of the rotor. In actuality, the PMB magnets also supply reaction torques that help to compensate for the rotor tilt. These reaction forces are neglected in the analysis. In addition, the angular velocity about the z axis is considered constant. Furthermore, since the amplifiers are operating in current-mode for

[1]Forces in the XZ plane in Figure 7.1 have been hidden for clarity.

the linear control, the electrical dynamics are neglected. This is a realistic assumption because the current-loop bandwidth of the Copley 412 is is much faster than the bandwidth of the position control loop.

It is sensible to presume that the small airgap assumption holds for the PREMAG AMB. When the radius of the rotor r_0 is much larger than the nominal airgap g_0, the small airgap assumption is valid. In this machine, the ratio of $r_0/g_0 = 150$. The small airgap restricts the rotations, θ_x and θ_y, and translations, X and Y, to be very small. This has significant consequences on the derivation of the dynamics.

Assume that the X and Y electromagnet forces act only to accelerate the rotor in X and Y directions, respectively[2]. Furthermore, the forces in the XZ and YZ planes only produce rotations about the Y and X axes, respectively. In addition, many authors have shown that the expression of an airgap in the XZ plane *predominately* depends on the translation of G along the X axis and the rotation θ_y [54, 56, 72]. That is, a gap in the XZ plane is a *very weak* function of θ_x and Y[3]. Similar statements can be made about the airgaps in the YZ plane.

The gap lengths under the small-airgap assumption are

$$g_1 = g_0 - Y + \theta_x \ell_1, \qquad g_3 = g_0 + Y - \theta_x \ell_1 \tag{7.1a}$$

$$g_5 = g_0 - Y - \theta_x \ell_2, \qquad g_7 = g_0 + Y + \theta_x \ell_2 \tag{7.1b}$$

$$g_2 = g_0 - X - \theta_y \ell_1, \qquad g_4 = g_0 + X + \theta_y \ell_1 \tag{7.1c}$$

$$g_6 = g_0 - X + \theta_y \ell_2, \qquad g_8 = g_0 + X - \theta_y \ell_2 \tag{7.1d}$$

where g_0 is the nominal airgap length. Note that only four of the airgaps are independent because gaps on opposite sides of the rotor add to $2g_0$.

The expression for the torque on the rotor is also significantly simplified due to

[2]This is not necessarily true in a large airgap machine.

[3]Since the radius of the rotor is so much larger than the airgap, the curvature of the rotor does not contribute significantly to a change in the airgap on a given vertical plane when you rotate or translate in a direction perpendicular to that plane.

the small airgap assumption. Consider Figure 7.1b and the torque produced on the rotor about G by f_3. In general, the torque is given by $\tau = r \times f$, where the vectors r and f are expressed in the same frame. The force is known in the inertial (I) frame, $(F_3)_I = -f_3\hat{J}$, and the moment arm $(r_{3/G})_B = -r_0\hat{j} + \ell_1\hat{k}$ in the body (B) frame. To calculate the torque in the body frame, one rotates the inertial force into the body frame, $(F_3)_B = R_x(\theta_x)(F_3)_I$, where $R_x(\theta_x)$ is the standard rotation matrix. Thus, the torque in the body frame $\tau = r_{3/G} \times (F_3)_B$ generally depends on the rotation angle θ_x. However, since θ_x is small, one approximates the torque magnitude by using the perpendicular moment arm, $|\tau_3| = \ell_1 f_3$, and the direction via the right hand rule.

7.1.2 Dynamics

The motion of any rigid body can be described by independently considering translation of the center of gravity and the rotation about the center of gravity. The motion of the center of mass G is given by Newton's law and the rotation about G is given by Euler's equation

$$\Sigma_j \overrightarrow{F}_j = m\overrightarrow{a}_G \tag{7.2}$$

$$\Sigma_j \overrightarrow{M}_{j,G} = \dot{\overrightarrow{H}}_G \tag{7.3}$$

where the subscript G means "of G" or "with respect to G". Equation (7.2) states that the acceleration of the center of mass G is equal to the sum of the external forces. Equation (7.3) states that the sum of the external moments (torque) $\overrightarrow{M}_{j,G}$ computed about G is equal to the rate of change of angular momentum H_G calculated about G.

Equation (7.3) is well known and is most often considered in its scalar component form. When the body-frame coincides with the principle axes of inertia, equation

(7.3) has a particularly simple form.

$$M_x = I_x\dot{\omega}_x + (I_z - I_y)\omega_y\omega_z \tag{7.4a}$$

$$M_y = I_y\dot{\omega}_y + (I_x - I_z)\omega_x\omega_z \tag{7.4b}$$

$$M_z = I_z\dot{\omega}_z + (I_x - I_y)\omega_y\omega_x \tag{7.4c}$$

where I_x,I_y, and I_z are the principle moments of inertia, ω_x, ω_y and ω_z are the components of the angular velocity in the body frame, and the moments M_x, M_y, and M_z are the net moments about the body-fixed axes.

The symmetry of the rotor implies that $I_x = I_y = I_r$ and $I_z = I_a$ where I_r and I_a are the radial and axial moments of inertial, respectively. Thus, the last term in equation (7.4c) drops out. This equation states that the torque from the DC motor in the rotor hub controls the angular velocity ω_z. However, in these considerations, it is assumed that $\dot{\omega}_z = 0$ and ω_z given.

The translational dynamics are given by

$$m\ddot{X} = f_2 - f_4 + f_6 - f_8 \tag{7.5a}$$

$$m\ddot{Y} = f_1 - f_3 + f_5 - f_7 \tag{7.5b}$$

With $\ddot{\theta}_y = \dot{\omega}_y$ and $\ddot{\theta}_x = \dot{\omega}_x$, the rotational dynamics become

$$\ddot{\theta_x} = (1 - I_a/I_r)\omega_y\omega_z + \Sigma M_x/I_r \tag{7.6a}$$

$$\ddot{\theta_y} = -(1 - I_a/I_r)\omega_x\omega_z + \Sigma M_y/I_r \tag{7.6b}$$

The total moments on the rotor are

$$M_x = -\ell_1(f_1 - f_3) + \ell_2(f_5 - f_7) \tag{7.7a}$$

$$M_y = \ell_1(f_2 - f_4) - \ell_2(f_6 - f_8) \tag{7.7b}$$

and the magnitude of magnetic force in terms of the current as derived in Appendix B is given by

$$f_j = c\frac{i_j^2}{g_j^2} \tag{7.8}$$

where i_j are the current inputs and g_j are given in equation (7.1). The electromagnet constant c is

$$c = \frac{\beta_{\text{leak}} \mu_0 A_p N^2}{4}$$

where $\beta_{\text{leak}} \in (0, 1]$ is a flux-leakage derating factor[4], A_p is the cross-sectional area of a pole face, N is the number of turns of a coil, and μ_0 is the permeability. Note that μ_0, A_p, and N are known with good precision, however, β_{leak} is only roughly known.

7.1.3 State Equation based on Rotor Translation and Tilt

The derivation of the dynamics of the system is naturally carried out on the physical variables that are related by Newton's and Euler's differential equations. However, the sensor output variables often motivate the selection of state variables. In this section, the states are selected as the two translation and tilting degrees of freedom (as well as their velocities). In Section 7.1.4, the position sensor outputs (and their derivatives) are taken as the states. Each model gives slightly different insights into the coupling of the AMB and the stiffness properties.

Let the states be $x = [x_1,\ x_2, \cdots, x_8]$ where

$$x_1 = Y, \qquad x_2 = X, \qquad x_3 = \theta_x, \qquad x_4 = \theta_y \tag{7.9a}$$

$$x_5 = \dot{Y}, \qquad x_6 = \dot{X}, \qquad x_7 = \dot{\theta}_x, \qquad x_8 = \dot{\theta}_y \tag{7.9b}$$

[4]There is a significant amount of flux leakage in the PREMAG AMB. This is apparent during operation because a nearby computer monitor flickers with variation in the coil currents. The PREMAG final report [64] gives figures of $\beta_{\text{leak}} = 0.3 - 0.5$, but these figures have not been verified. This is a source of parameter uncertainty. It is shown below that the open-loop pole positions of the AMB depend on this parameter.

Then the state equation for the system, neglecting the electrical dynamics, is

$$\dot{x}_1 = x_5 \tag{7.10a}$$

$$\dot{x}_2 = x_6 \tag{7.10b}$$

$$\dot{x}_3 = x_7 \tag{7.10c}$$

$$\dot{x}_4 = x_8 \tag{7.10d}$$

$$\dot{x}_5 = (f_1 - f_3 + f_5 - f_7)/m \tag{7.10e}$$

$$\dot{x}_6 = (f_2 - f_4 + f_6 - f_8)/m \tag{7.10f}$$

$$\dot{x}_7 = (1 - I_a/I_r)x_8\omega_z - \tfrac{\ell_1}{I_r}(f_1 - f_3) + \tfrac{\ell_2}{I_r}(f_5 - f_7) \tag{7.10g}$$

$$\dot{x}_8 = -(1 - I_a/I_r)x_7\omega_z + \tfrac{\ell_1}{I_r}(f_2 - f_4) - \tfrac{\ell_2}{I_r}(f_6 - f_8) \tag{7.10h}$$

The inputs to the system are taken as the eight coil currents. Using equation (7.1), a vector of the airgaps is calculated from the state by

$$\mathbf{Y}_{\text{gap}} = g_0\mathbf{1}_{8\times 1} + C_g x$$

with

$$C_g = \begin{bmatrix} C_{g1} & \mathbf{0}_{8\times 4} \end{bmatrix}, \qquad C_{g1} = \begin{bmatrix} -1 & 0 & \ell_1 & 0 \\ 0 & -1 & 0 & -\ell_1 \\ 1 & 0 & -\ell_1 & 0 \\ 0 & 1 & 0 & \ell_1 \\ -1 & 0 & -\ell_2 & 0 \\ 0 & -1 & 0 & \ell_2 \\ 1 & 0 & \ell_2 & 0 \\ 0 & 1 & 0 & -\ell_2 \end{bmatrix}$$

The description of the system is incomplete without the output equation. The differential output voltages of the Kaman preamplifier are used to determine the position and orientation of the rotor. Recall that the differential outputs are a function of the difference of the airgaps on opposite sides of the rotor. The system outputs are

thus defined as $(g_{j+2} - g_j)/2$ for $j = 1, 2, 5, 6$. More explicitly, using equation (7.1), the outputs are

$$Y_1 = Y - \theta_x \ell_1 := Y_t \tag{7.11a}$$

$$Y_2 = X + \theta_y \ell_1 := X_t \tag{7.11b}$$

$$Y_3 = Y + \theta_x \ell_2 := Y_b \tag{7.11c}$$

$$Y_4 = X - \theta_y \ell_2 := X_b \tag{7.11d}$$

The output vector is the horizontal displacement of center of the top and bottom of the rotor. Note that this output is zero if and only if the state is zero. Defining

$$C_y = \frac{1}{2}\begin{bmatrix} -1 & 0 & 1 & 0 & 0 & 0 & 0 & 0 \\ 0 & -1 & 0 & 1 & 0 & 0 & 0 & 0 \\ 0 & 0 & 0 & 0 & -1 & 0 & 1 & 0 \\ 0 & 0 & 0 & 0 & 0 & -1 & 0 & 1 \end{bmatrix}$$

the system output equation is

$$\mathbf{Y} = C_y Y_{\text{gap}} = C_y g_0 \mathbf{1}_{8\times 1} + C_y C_g x = C_y C_g x \tag{7.12}$$

7.1.4 State Equation Based on Airgap Dynamics

Since the position sensors give the outputs in equation (7.11), the dynamics may be explicitly written in terms of the center positions of the top and bottom of the rotor. From equation (7.11), the angles θ_x and θ_y in terms of the sensor variables are

$$\theta_x = \frac{Y_b - Y_t}{\ell_1 + \ell_2}, \qquad \theta_y = \frac{X_t - X_b}{\ell_1 + \ell_2} \tag{7.13}$$

Using equation (7.11a),

$$\begin{aligned} \ddot{Y}_t &= \ddot{Y} - \ell_1 \ddot{\theta}_x \\ &= \frac{1}{m}(f_1 - f_3 + f_5 - f_7) - \frac{\ell_1}{I_r}(-\ell_1(f_1 - f_3) + \ell_2(f_5 - f_7)) - \ell_1 \omega_z (1 - \frac{I_a}{I_r})\dot{\theta}_y \\ &= \Big[\frac{1}{m} + \frac{\ell_1^2}{I_r}\Big](f_1 - f_3) + \Big[\frac{1}{m} - \frac{\ell_1 \ell_2}{I_r}\Big](f_5 - f_7) - \ell_1 \omega_z (1 - \frac{I_a}{I_r})\frac{\dot{X}_t - \dot{X}_b}{\ell_1 + \ell_2} \end{aligned}$$

Likewise,

$$\ddot{X}_t = \Big[\frac{1}{m} + \frac{\ell_1^2}{I_r}\Big](f_2 - f_4) + \Big[\frac{1}{m} - \frac{\ell_1\ell_2}{I_r}\Big](f_6 - f_8) - \frac{\ell_1}{\ell_1+\ell_2}\omega_z(1 - \frac{I_a}{I_r})(\dot{Y}_b - \dot{Y}_t)$$
$$\ddot{Y}_b = \Big[\frac{1}{m} - \frac{\ell_1\ell_2}{I_r}\Big](f_1 - f_3) + \Big[\frac{1}{m} + \frac{\ell_2^2}{I_r}\Big](f_5 - f_7) + \frac{\ell_2}{\ell_1+\ell_2}\omega_z(1 - \frac{I_a}{I_r})(\dot{X}_t - \dot{X}_b)$$
$$\ddot{X}_b = \Big[\frac{1}{m} - \frac{\ell_1\ell_2}{I_r}\Big](f_2 - f_4) + \Big[\frac{1}{m} + \frac{\ell_2^2}{I_r}\Big](f_6 - f_8) + \frac{\ell_2}{\ell_1+\ell_2}\omega_z(1 - \frac{I_a}{I_r})(\dot{Y}_b - \dot{Y}_t)$$

For convenience, let

$$\begin{aligned} m_1 &= \Big(\tfrac{1}{m} + \tfrac{\ell_1^2}{I_r}\Big)^{-1}, \quad m_2 = \Big(\tfrac{1}{m} + \tfrac{\ell_2^2}{I_r}\Big)^{-1} \\ m_3 &= \Big(\tfrac{1}{m} - \tfrac{\ell_1\ell_2}{I_r}\Big)^{-1}, \quad \lambda = \tfrac{\omega_z}{\ell_1+\ell_2}(1 - \tfrac{I_a}{I_r}) \end{aligned} \tag{7.14}$$

$$\begin{aligned} F_{yt} &= (f_1 - f_3), \quad F_{xt} = (f_2 - f_4) \\ F_{yb} &= (f_5 - f_7), \quad F_{xb} = (f_6 - f_8) \end{aligned} \tag{7.15}$$

Using the above,

$$\ddot{Y}_t = -\ell_1\lambda(\dot{X}_t - \dot{X}_b) + \tfrac{F_{yt}}{m_1} + \tfrac{F_{yb}}{m_3} \tag{7.16a}$$
$$\ddot{X}_t = -\ell_1\lambda(\dot{Y}_b - \dot{Y}_t) + \tfrac{F_{xt}}{m_1} + \tfrac{F_{xb}}{m_3} \tag{7.16b}$$
$$\ddot{Y}_b = \ell_2\lambda(\dot{X}_t - \dot{X}_b) + \tfrac{F_{yt}}{m_3} + \tfrac{F_{yb}}{m_2} \tag{7.16c}$$
$$\ddot{X}_b = \ell_2\lambda(\dot{Y}_b - \dot{Y}_t) + \tfrac{F_{xt}}{m_3} + \tfrac{F_{xb}}{m_2} \tag{7.16d}$$

Defining the state as $x = [x_1,\ x_2, \cdots, x_8]$ where

$$x_1 = Y_t, \qquad x_2 = X_t, \qquad x_3 = Y_b, \qquad x_4 = X_b \tag{7.17a}$$
$$\dot{x}_5 = \dot{Y}_t, \qquad \dot{x}_6 = \dot{X}_t, \qquad \dot{x}_7 = \dot{Y}_b, \qquad \dot{x}_8 = \dot{X}_b \tag{7.17b}$$

and $F = [F_{yt}, F_{xt}, F_{yb}, F_{xb}]^T$, the state equation has the form

$$\dot{x} = A_1 x + [\mathbf{0}_{4\times4}, B_1]^T F(x, i) \tag{7.18}$$

with

$$A_1 = \begin{bmatrix} \mathbf{0}_{4\times4} & I_4 \\ \mathbf{0}_{4\times4} & A_\omega \end{bmatrix}, \qquad A_\omega = \lambda \begin{bmatrix} 0 & -\ell_1 & 0 & \ell_1 \\ \ell_1 & 0 & -\ell_1 & 0 \\ 0 & \ell_2 & 0 & -\ell_2 \\ -\ell_2 & 0 & \ell_2 & 0 \end{bmatrix}, \qquad B_1 = \begin{bmatrix} \frac{1}{m_1} & 0 & \frac{1}{m_3} & 0 \\ 0 & \frac{1}{m_1} & 0 & \frac{1}{m_3} \\ \frac{1}{m_3} & 0 & \frac{1}{m_2} & 0 \\ 0 & \frac{1}{m_3} & 0 & \frac{1}{m_2} \end{bmatrix} \tag{7.19}$$

and the force in terms of the state is

$$F(x,i) = c \begin{bmatrix} \frac{i_1^2}{(g_0-x_1)^2} - \frac{i_3^2}{(g_0+x_1)^2} \\ \frac{i_2^2}{(g_0-x_2)^2} - \frac{i_4^2}{(g_0+x_2)^2} \\ \frac{i_5^2}{(g_0-x_3)^2} - \frac{i_7^2}{(g_0+x_3)^2} \\ \frac{i_6^2}{(g_0-x_4)^2} - \frac{i_8^2}{(g_0+x_4)^2} \end{bmatrix} \tag{7.20}$$

Since F depends nonlinearly on the current and the airgaps, the state equation is *not* linear. Observe that the A_w angular velocity coupling matrix vanishes when $\omega_z = 0$. The B matrix illustrates the redundancy (or over-actuation) in the control forces. The output equation for our system is $Y = [I_4, \mathbf{0}_{4\times4}]x$.

7.2 Linearized AMB Dynamics

In this section the two MIMO state space models from the previous section are linearized for the purposes of linear control. The coefficients of these linear models are interpreted in terms of their effect on the open-loop AMB stiffness and the coupling between the control inputs. The two different state space models give slightly different interpretations of how these parameters are effected by the selection of the bias currents. For comparison, the linearization of a 1-DOF AMB for use in the decentralized Lead+PI control scheme is first presented.

7.2.1 1-DOF Linearized AMB Dynamics

Recall that in the interest of time and simplicity, only one of the four control axes on the PREMAG bearing is used as a nonlinear voltage-mode test bed. The other three

control axes are implemented with a standard, large-bias linear current-mode control design. The constant-current-sum (ccs) biasing scheme introduced in Chapter 3 is easily implemented in software. Recall that in this scheme, the two current inputs i_1 and i_2 are reduced to one control input by the following input transformation.

$$i_1 = I_b + i_c, \qquad i_2 = I_b - i_c$$

where I_b is the current bias and i_c is the new control current. This results in the following dynamic equation for the 1-DOF AMB in current-mode with ccs biasing.

$$m\ddot{x} = c\frac{(I_b + i_c)^2}{(g_0 - x)^2} - c\frac{(I_b - i_c)^2}{(g_0 + x)^2} \tag{7.21}$$

with $c = \beta_{\text{leak}}\mu_0 A_g N^2/4$ and β_{leak} is a flux-leakage factor. Linearizing (7.21) about $x = i_c = 0$ gives

$$m\ddot{x} = K_x x + K_i i_c$$

where

$$K_x = \frac{4cI_b^2}{g_0^3}, \qquad K_i = \frac{4cI_b}{g_0^2} \tag{7.22}$$

The transfer function from current input to position output is

$$\frac{X(s)}{I_c(s)} = \frac{K_i/m}{s^2 - K_x/m} := P(s) \tag{7.23}$$

which has two real poles symmetric about the $j\omega$ axis. Clearly, this is unstable and the pole magnitude depends on the position stiffness. Furthermore, the DC gain of the transfer function depends on the ratio of current to position stiffness. From equation (7.22), the pole positions also depend directly on the bias I_b and leakage coefficient β_{leak}.

7.2.2 MIMO Linear Model 1

The nonlinear state-space model of Section 7.1.3 is now linearized about an operating point for application of linear control. The constant-current-sum bias is easily

implemented with software

$$i_1 = I_{b13} + i_{c13}, \qquad i_3 = I_{b13} - i_{c13} \tag{7.24a}$$

$$i_2 = I_{b24} + i_{c24}, \qquad i_4 = I_{b24} - i_{c24} \tag{7.24b}$$

$$i_5 = I_{b57} + i_{c57}, \qquad i_7 = I_{b57} - i_{c57} \tag{7.24c}$$

$$i_6 = I_{b68} + i_{c68}, \qquad i_8 = I_{b68} - i_{c68} \tag{7.24d}$$

where I_{bj} is the current bias and i_{cj} is the new input control current. This effectively reduces the eight current inputs to four. Let $u = [i_{c13}, i_{c24}, i_{c57}, i_{c68}]^T$. The state equation (7.10) modified by (7.24) is linearized about $x = u = 0$ to give a model of the form $\dot{x} = Ax + Bu$. The output equation for the linearized system is the same as that in equation (7.12), $Y = C_y C_g x$. The A and B matrices are given below in terms of their corresponding stiffness and input gain matrices.

$$A = \begin{bmatrix} 0_{4\times4} & I_{4\times4} \\ A_F & 0_{2\times4} \\ A_\tau & A_\omega \end{bmatrix}, \qquad B = \begin{bmatrix} 0_{4\times4} \\ \beta \\ \Gamma \end{bmatrix} \tag{7.25}$$

The force stiffness matrix A_F and torque stiffness matrix A_τ are

$$A_F = \frac{1}{m}\begin{bmatrix} a_1 & 0 & a_3 & 0 \\ 0 & a_2 & 0 & a_4 \end{bmatrix}, \qquad A_\tau = \frac{1}{I_r}\begin{bmatrix} a_3 & 0 & a_5 & 0 \\ 0 & a_4 & 0 & a_6 \end{bmatrix} \tag{7.26}$$

with

$$a_1 = \frac{4c}{g_0^3}(I_{b13}^2 + I_{b57}^2), \qquad a_2 = \tfrac{4c}{g_0^3}(I_{b24}^2 + I_{b68}^2) \tag{7.27a}$$

$$a_3 = \frac{4c}{g_0^3}(I_{b57}^2\ell_2 - I_{b13}^2\ell_1), \qquad a_4 = \tfrac{4c}{g_0^3}(I_{b24}^2\ell_1 - I_{b68}^2\ell_2) \tag{7.27b}$$

$$a_5 = \frac{4c}{g_0^3}(I_{b57}^2\ell_2^2 + I_{b13}^2\ell_1^2), \qquad a_6 = \tfrac{4c}{g_0^3}(I_{b68}^2\ell_2^2 + I_{b24}^2\ell_1^2) \tag{7.27c}$$

The terms equation (7.27a) represent the sensitivity of the translational forces acting on the center of gravity G with respect to the rotor translation. The translational stiffness terms in equation (7.27a) are similar to the stiffness term in the 1-DOF case,

equation (7.22). Observe that the translational stiffness is the sum of the individual translational stiffness terms from the bottom and top bearing.

The stiffness terms, $\partial F/\partial\theta$, in equation (7.27b) represent a coupling between the translation of G and tilt of the rotor about G. In a perfectly balanced rotor ($\ell_1 = \ell_2$), this coupling is introduced when the top and bottom bias levels are unequal. In the case of the modified PERMAG AMB where the rotor's center of gravity does not coincide with the geometric center, this coupling term depends on the difference between the top and bottom bias levels, weighted by the imbalance lengths. Equation (7.27b) suggests that one may adjust the top and bottom bias levels to eliminate the coupling. Indeed, if $I_{btop}^2\ell_1 = I_{bbottom}^2\ell_2$, the coupling stiffness terms a_3 and a_4 vanish[5]. To achieve this, the ratio of the top bias to the bottom bias level should be set to

$$\frac{I_{b57}}{I_{b13}} = \sqrt{\frac{\ell_2}{\ell_1}} \tag{7.28}$$

The ratio for the PREMAG AMB is about 1/2. Thus, to avoid coupling between the translational and rotational motion, the bottom bias level should set to about twice the top bias level. This agrees with the intuition in that the bottom bearing must be stiffer to compensate for the "bottom-heaviness" of the rotor. Although this is theoretically possible, it may be impractical. For example, the region of convergence of the closed-loop locally asymptotically stable nonlinear system acted on by the linear controller depends on the current bias. To have a reasonably large region of attraction, the bias in the top bearing may be set at 2-3 amps, for example. Thus, the bottom bearing would require a bias of 4-6 amps which is prohibitively large. Such a large bias dissipates much power and leads to overheating of the coils and rotor.

The torque stiffness matrix A_τ is defined by the terms in equations (7.27b) and (7.27c). The rotational torque stiffness terms in equation (7.27c) represent the change in torque τ about G with respect to the rotor tilt about G. Observe that the rotational

[5]Note that all coupling is not eliminated. There is still coupling between the input channels via the B matrix.

stiffness is a sum of the top and bottom translational stiffness terms weighted by the imbalance lengths. Again the a_3 and a_4 coupling stiffness terms appear. In this equation, they represent the sensitivity of the torque about G produced by the EM forces to a translation of G. As seen previously, proper selection of the ratio of the biases in the top and bottom axes can eliminate the dependence of the torque on rotor translation.

The A_ω damping matrix is

$$A_\omega = \omega_z(1 - \frac{I_a}{I_z}) \begin{bmatrix} 0 & 0 & 0 & 1 \\ 0 & 0 & -1 & 0 \end{bmatrix} \tag{7.29}$$

and represents the coupling between the angular acceleration $\ddot{\theta}_x$ and $\ddot{\theta}_y$. This coupling disappears when $\omega_z = 0$.

The matrices of the input gain matrix are

$$\beta = \frac{4c}{g_0^2 m} \begin{bmatrix} I_{b13} & 0 & I_{b57} & 0 \\ 0 & I_{b24} & 0 & I_{b68} \end{bmatrix} \tag{7.30}$$

and

$$\Gamma = \frac{4c}{g_0^2 I_r} \begin{bmatrix} -\ell_1 I_{b13} & 0 & \ell_2 I_{b57} & 0 \\ 0 & \ell_1 I_{b24} & 0 & -\ell_2 I_{b68} \end{bmatrix} \tag{7.31}$$

β and Γ represent the input current gains of the force and torque, respectively.

7.2.3 MIMO Linear Model 2

The MIMO nonlinear model of Section 7.1.4 is now linearized for application of linear control. Using the previous ccc bias scheme and control input, (7.18) is linearized about $x = u = 0$ to obtain $\dot{x} = Ax + Bu$. Starting with

$$\dot{x} = A_1 x + [\mathbf{0}_{4\times4}\ B_1]^T F(x, u)$$

the A and B matrices are

$$A = \begin{bmatrix} \mathbf{0}_{4\times4} & I_4 \\ B_1 \frac{\partial F}{\partial x}\Big|_{(0,0)} & A_\omega \end{bmatrix}, \qquad B = \begin{bmatrix} \mathbf{0}_{4\times4} \\ B_1 \frac{\partial F}{\partial I_c}\Big|_{(0,0)} \end{bmatrix} \tag{7.32}$$

Specifically,

$$\left.\frac{\partial F}{\partial x}\right|_{(0,0)} = \frac{4c}{g_0^3}[\mathrm{diag}(I_{b13}^2, I_{b24}^2, I_{b57}^2, I_{b68}^2), \mathbf{0}_{4\times 4}] \tag{7.33a}$$

$$\left.\frac{\partial F}{\partial I_c}\right|_{(0,0)} = \frac{4c}{g_0^2}\mathrm{diag}(I_{b13}, I_{b24}, I_{b57}, I_{b68}) \tag{7.33b}$$

$$B_1\left.\frac{\partial F}{\partial x}\right|_{(0,0)} = \frac{4c}{g_0^3}\begin{bmatrix} \frac{I_{b13}^2}{m_1} & 0 & \frac{I_{b57}^2}{m_3} & 0 \\ 0 & \frac{I_{b24}^2}{m_1} & 0 & \frac{I_{b68}^2}{m_3} \\ \frac{I_{b13}^2}{m_3} & 0 & \frac{I_{b57}^2}{m_2} & 0 \\ 0 & \frac{I_{b24}^2}{m_3} & 0 & \frac{I_{b68}^2}{m_2} \end{bmatrix} \tag{7.33c}$$

$$B_1\left.\frac{\partial F}{\partial I_c}\right|_{(0,0)} = \frac{4c}{g_0^2}\begin{bmatrix} \frac{I_{b13}}{m_1} & 0 & \frac{I_{b57}}{m_3} & 0 \\ 0 & \frac{I_{b24}}{m_1} & 0 & \frac{I_{b68}}{m_3} \\ \frac{I_{b13}}{m_3} & 0 & \frac{I_{b57}}{m_2} & 0 \\ 0 & \frac{I_{b24}}{m_3} & 0 & \frac{I_{b68}}{m_2} \end{bmatrix} \tag{7.33d}$$

As in the previous model, $A_\omega \to 0$ as $\omega \to 0$: see equation (7.19). It is clear that the coupling between the input channels is introduced by the B_1 matrix. The effect of the axial imbalance is a little less clear in this model. No interpretation about a bias level ratio here is obvious. The stiffness terms and current gains only depend on the local bias current. That is, $\frac{\partial F}{\partial x}$ and $\frac{\partial F}{\partial I_c}$ are diagonal.

7.3 1-DOF Lead+PI Linear Control

A Lead+PI linear control design is applied to the 1-DOF AMB model of Section 7.2.1. Data collected from the PREMAG final report [64] suggests that $\beta_{\text{leak}} \approx 0.5$, but is not known exactly. For preliminary design purposes, let $\beta_{\text{leak}} = 0.5$ and $I_b = 3A$: the resulting open-loop pole positions are at ± 350. These values are used to illustrate the design, however, since the real open-loop pole positions are not known, some trial and error is required when implementing this Lead+PI design on the PREMAG bearing.

The root locus of the open-loop system results in a locus that converges along the real axis to the origin and then breaks away along the $j\omega$ axis: See top row of Figure

7.2. This indicates that one can only hope to achieve marginal stability with pure gain feedback. Due to the symmetry of the poles, the transfer function is purely real. The phase is -180° ($PM = 0$) over the entire frequency range.

A lead controller pulls the root locus into the left half plane, while at the same time, contributes positive phase to increase the phase margin to a non-zero value. To fully specify a lead controller with transfer function as in equation (7.34),

$$L(s) = K_p \frac{(s+z)}{(s+\gamma z)} \tag{7.34}$$

one needs to select the zero, pole, and gain values. There are a multitude of zero/pole/gain selections that will make the root locus pass through a particular set of desired closed-loop pole locations. However, Bode design asserts that to achieve a decent phase contribution from the lead, one should place the pole of the lead 6-10 times further in the LHP than the zero. That is, choose $\gamma \in [6, 10]$ in equation (7.34). With this design choice, one selects the zero position and gain to achieve a reasonable phase margin. The second row of Figure 7.2 analyzes the loop gain of the plant and lead controller. Let $\gamma = 10$, $z = 150$, and $k_p = 8 \times 10^4$. This choice of γ places the lead pole 10 times further out in the LHP than the zero. The lead controller forces most of the root locus is into the LHP. For increasing values of gain K_p, the open-loop unstable RHP pole moves towards the zero of the lead[6]. A phase margin of $PM = 50^\circ$ is achieved for the above values of z and k_p.

While this design may lead to a good transient response and relative stability, the steady state error to a step input is large because the DC gain is only about 4dB. There are two ways to compensate for this. The simplest way is to re-scale the reference input to so that the DC gain of the closed-loop plant/lead controller is unity. Note that the proper scaling value is easily determined by experiment and

[6]Note that this value of k_p assumes that x is in meters. If the position is expressed in mils, $k_{\text{pmils}} = k_p \times 2.54 \times 10^{-5} \frac{m}{mil} = 2.03$

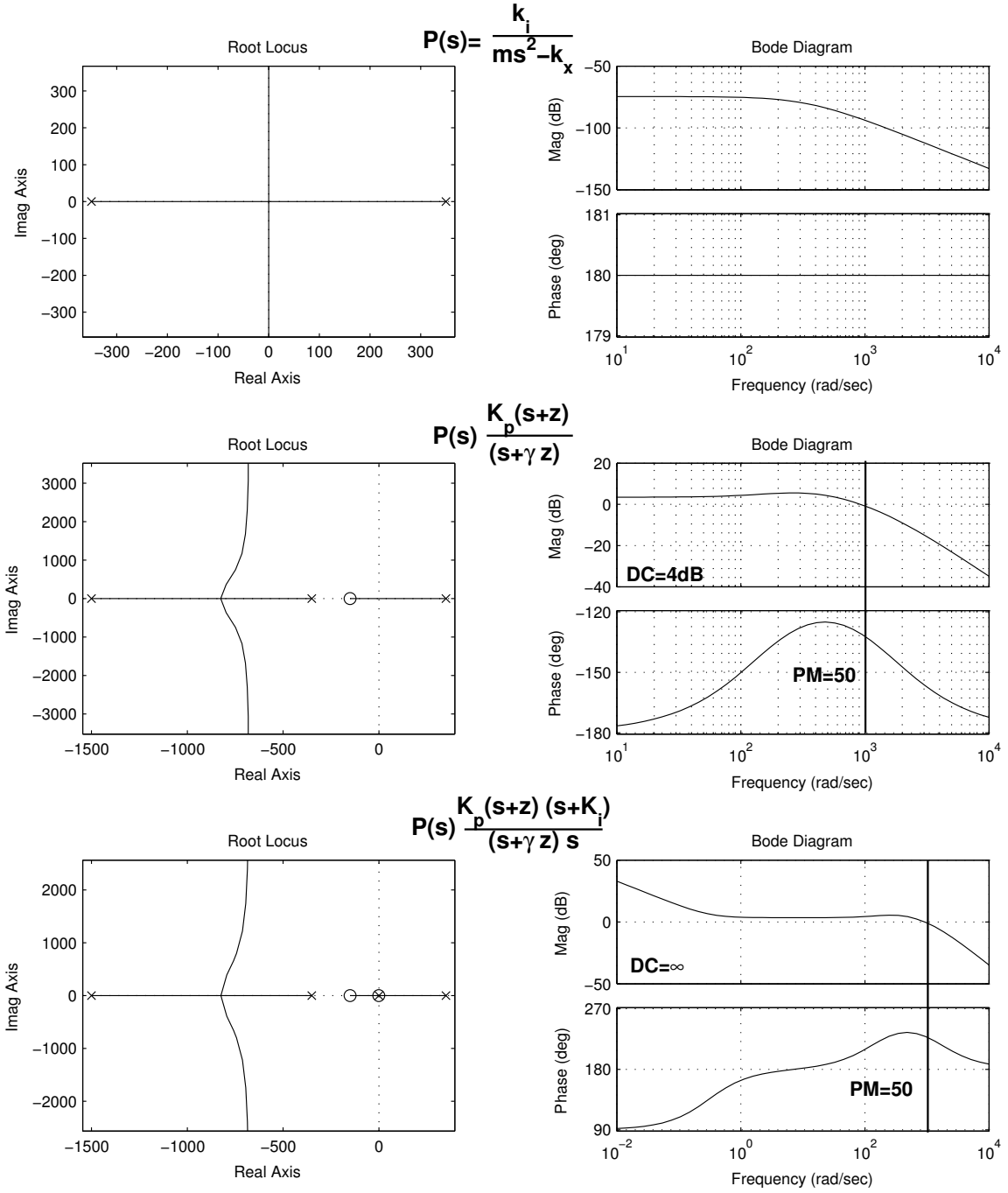

Figure 7.2: Root locus and Bode design of Lead+PI controller. The parameters are $K_p = 8 \times 10^4$ ($K_p = 2.03$ for x in mils), $K_i = 0.3$, $z = 150$, and $\gamma = 10$.

measurement of the steady-state error. Although this roughly eliminates the steady-state error to a step input from the reference to the output, a PI controller is a more robust solution. The PI controller $(s+K_i)/s$ has pole at origin and zero close to origin

so that the magnitude and angular contribution to the root locus is minimal. The third row of Figure 7.2 shows that the PI does not change the root locus (or the PM) significantly for $k_i = 0.3$. However, the pole at the origin introduces infinite DC gain and consequently achieves zero steady-state error to step inputs *and disturbances*.

In summary, a controller of the form

$$\frac{U(s)}{e(s)} = K_p \frac{(s+z)(s+K_i)}{(s+\gamma z)s} \tag{7.35}$$

is required. This has the basic Lead+PI form, however this is implemented in a slightly nonstandard way. It turns out to be difficult to achieve *any* desired transient response to a step input and *simultaneously* achieve zero steady-state error with the typical cascade compensation designs[7]. The control is implemented with the feedback structure of Figure 7.3. In this implementation, cascade lead compensation and unity feedback is employed to stabilize the plant. The feed-forward gain K_0 is selected to be the inverse of the DC gain of Lead/plant closed-loop from $r_0(s)$ to $Y(s)$. Since the plant is not exactly known, K_0 is determined from experiment. This ensures roughly zero steady-state error to a step input. An additional outer PI loop for perfect tracking of a step reference and rejection of constant disturbances is added. Note that the gain K_0 takes most of the work load off of the PI controller when following steps references. The PI control also ensures perfect regulation to zero error.

[7]For example, it can be difficult to achieve a desired overshoot, settling time and zero steady state error for a step input. Zero error may be achieved in steady state, but steady state may take a long time to achieve using a pole at the origin. Further discussion about alternative PID control implementations can be found in [59, 58, 21].

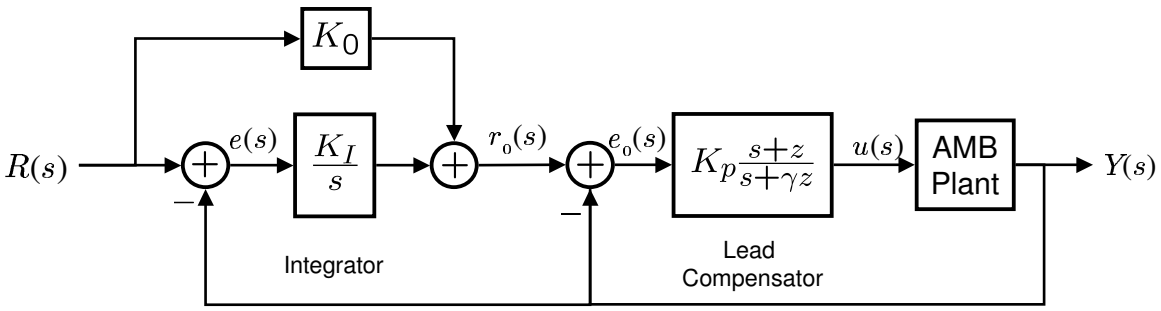

Figure 7.3: Feedback configuration for the Lead+PI control law.

The feedback structure in Figure 7.3 essentially implements the Lead+PI controller of equation (7.35).

$$\begin{aligned} U(s) &= K_p\frac{s+z}{s+\gamma z}e_0(s) \\ &= K_p\frac{s+z}{s+\gamma z}(r_0(s) - Y(s)) \\ &= K_p\frac{s+z}{s+\gamma z}\Big((R(s)K_0 - Y(s)) + \frac{K_i}{s}e(s)\Big) \\ &= K_p\frac{s+z}{s+\gamma z}(\tilde{e}(s) + \frac{K_i}{s}e(s)) \\ &\approx K_p\frac{s+z}{s+\gamma z}\frac{s+K_i}{s}e(s) \end{aligned}$$

Since K_0 is typically close to one, the signal $\tilde{e} \approx e$ and the Lead+PI compensator is implemented. For values of $K_0 \neq 1$, the zero location of the PI controller is slightly perturbed, however this has minimal effect on the performance.

7.4 MIMO Local Asymptotic Stability

The SISO control design is illustrated in Section 7.3. This approach has the benefit of easy design, however, it does not guarantee stability of the MIMO closed-loop system. The coupling evident in the A_ω matrix or the B matrices of the state equations may lead to instability. Indeed, the interconnection of stable systems is not necessarily stable. However, the closed-loop *local* asymptotic stability is easily checked after deriving the closed loop system matrices of the linearized equations. In Section 7.5, *global* asymptotic stability is suggested via simulation of the decentralized linear

control law on the nonlinear plant, however, only local asymptotic stability is achievable in the experiments. The experimental results of Section 8.6 further illustrate the decentralized control approach.

The dynamics of the Lead+PI control laws are first represented in state variable form and then the augmented plant state x_p and controller state x_c is shown to have an asymptotically stable equilibrium point at $\xi = [x_p, x_c] = [0, 0]$.

A lead controller has the transfer function

$$\frac{u(s)}{e_0(s)} = k_p \frac{s+z}{s+\gamma z}$$

where u is the plant input and e is an error signal. The zero is specified by z and γ is a constant to place the pole about 6-10 times further out in the left half plane than the zero. The differential equation for the lead transfer function is

$$\dot{u} + \gamma z u = k_p \dot{e}_0 + k_p z e_0$$

Since the derivative of the input appears, let $x_c = u - k_p e_0$ represent the controller state.

$$\begin{aligned} \dot{u} - k_p \dot{e}_0 &= -\gamma z u + k_p z e_0 \\ x_c &= \int_0^t \frac{d}{d\tau}(u(\tau) - k_p e_0(\tau)) d\tau = \int_0^t \gamma z u(\tau) + k_p z e_0(\tau)\, d\tau \end{aligned}$$

Thus, the state equation of a single Lead controller is given by

$$\dot{x}_c = -\gamma z x_c + z(1-\gamma) k_p e_0 \tag{7.36a}$$

$$u = x_c + k_p e_0 \tag{7.36b}$$

To compactly represent the four parallel lead controllers, let the controller states, control inputs, and tracking error be $x_c = [x_{c1}, ..., x_{c4}]^T$, $u = [u_1, ..., u_4]^T$, $E_0 = [e_{01}, ..., e_{04}]^T$, respectively. Let the zero locations, the pole scaling factors and the loop gains be $z = \text{diag}(z_1, ..., z_4)$, $\Gamma = \text{diag}(\gamma_1, ..., \gamma_4)$, and $K_p = \text{diag}(k_{p1}, ..., k_{p4})$,

respectively. Then the controller state equation has the form

$$\dot{x}_c = -Fx_c + K_pGE_0 \tag{7.37a}$$

$$u = I_4x_c + K_pE_0 \tag{7.37b}$$

with $F = z\Gamma$ and $G = z(I - \Gamma)$.

The plant representation is

$$\dot{x}_p = Ax_p + Bu$$

$$Y = C_px_p$$

First calculate the inner-loop state equation from R_0 to Y in Figure 7.3, where $R_0 = [r_{01}, ..., r_{04}]$. Let the stacked controller plant state be $\Sigma = [x_p, x_c]^T$. Then using the feedback constraint $E_0 = R_0 - Y$, it is easy to verify that the inner-loop of satisfies the state equation

$$\dot{\Sigma} = \begin{bmatrix} A - BK_pC_p & B \\ -K_pGC_p & -F \end{bmatrix} \Sigma + \begin{bmatrix} BK_p \\ K_pG \end{bmatrix} R_0 \tag{7.38}$$

Thus, the MIMO AMB is *locally* asymptotically stabilized with four parallel lead controllers if the system matrix of equation 7.38 is Hurwitz.

The integral portion of the control law is represented with by the simple state equation, $\dot{v} = e$ with $v \in \mathbb{R}^4$. The feedback constraint from Figure 7.3 is $R_0 := K_iv + K_0R$ where $K_i = \text{diag}(k_{i1}, ..., k_{i4})$ and $K_0 = \text{diag}(k_{01}, ..., k_{04})$. Augmenting the state once again gives the closed loop state equation from R to $[\Sigma, v]^T$,

$$\begin{bmatrix} \dot{\Sigma} \\ \dot{v} \end{bmatrix} = \begin{bmatrix} A - BK_pC_p & B & BK_pK_i \\ -K_pGC_p & -F & K_pGK_i \\ -C_p & \mathbf{0}_{4\times4} & \mathbf{0}_{4\times4} \end{bmatrix} \begin{bmatrix} \Sigma \\ v \end{bmatrix} + \begin{bmatrix} BK_pK_0 \\ K_pGK_0 \\ I \end{bmatrix} R \tag{7.39}$$

Thus, the MIMO AMB is *locally* asymptotically stabilized with the decentralized control scheme of Figure 7.3, can follow step inputs with zero steady state error, and reject constant disturbances, if the system matrix of equation (7.39) is Hurwitz.

In summary, decentralized control allows one to proceed as if the plant was represented by four decoupled SISO systems. This approach is motivated by the available sensor measurements and the ease of design. Once four stabilizing Lead+PI controllers are designed for the nominal SISO system, one uses equation (7.39) to check the *local* asymptotic stability of the closed loop MIMO system. Note that it is *not* shown that the four Lead+PI controllers that stabilize their respective nominal SISO models will also stabilize the 4-DOF MIMO AMB. There are definitely situations where MIMO system is unstable when this decentralized approach is used. For example, given a large ω_z, the coupling can destabilize the closed loop MIMO system, even when stable Lead+PI controllers have been designed for each SISO system. This is a shortcoming of the decentralized approach. However, simulation and experimental results furnish evidence of its practicality.

7.5 Simulations

This section presents simulation results of the nonlinear MIMO plant acted on by the decentralized control scheme of Figure 7.3 and Section 7.4. The state is represented by the state space model of equation (7.18).

The plant parameters used for the following simulations are summarized in Table 7.5. Most of these parameters are well-known. The terms marked with an asterisk (*) are calculated from the IronCAD 3D modelling software (from IronCAD LLC.) and are considered to be reasonably accurate. The β_{leak} variable is a guess. All other parameters are measured directly or calculated. The same Lead+PI controller that is used on the real plant is used in the simulations,

$$Lead(s) = k_p \frac{(s+150)}{(s+1500)} \frac{(s+0.3)}{s} \tag{7.40}$$

and are implemented with the scheme shown in Figure 7.3.

Table 7.1: Plant parameters used in simulations.

Parameter	Meaning	Value
g_0	Nominal Airgap length	.508mm (20 mils)
r_0	Radius of rotor	78.74 mm
μ_0	permeability of free space	$4\pi \times 10^{-7}$ H/m
A_p	Area of pole face	.001428 m^2
N	Number of coil turns	60
ℓ	distance along z axis from C to pole face	7.747 mm
ρ_g^*	distance along z axis from C to G	4.51 mm
$\ell_1 = \ell + \rho_g$	Upper moment arm along z axis from G	12.257 mm
$\ell_2 = \ell - \rho_g$	Lower moment arm along z axis from G	3.237 mm
m^*	Mass of rotor	1.807 kg
I_a^*	Axial moment of Inertia	44.317 $\frac{\text{kg}}{\text{cm}^2}$
I_r^*	Radial moment of Inertia	72.878 $\frac{\text{kg}}{\text{cm}^2}$
β_{leak}	Flux-leakage coefficient	0.5

The next few figures illustrate the effects of the control gains on the performance. Each simulation shows the response of the system as the controllers regulate the rotor to $(y_T, x_T, y_B, x_b) = (0, 0, 0, 0)$ from an initially at rest position of $(y_T(0), x_T(0), y_B(0), x_b(0)) = g_0(0.9, -0.9, 0.5, 0.5)$.

The simulation is conducted with the same loop-gain K_p on each control axis. Figure 7.4 shows the effect of increasing $K_p = 2$ to $K_p = 4$. Note that these gains assume the position is measured in mils. As expected, larger loop gains imply shorter settling times.

Figure 7.5 shows a similar initial condition response however, the x_b axis is tracking a 2.5 mil, $0.5Hz$ square wave. Two simulations are conducted for the feed-forward gain $K_0 = 1$ and $K_0 = 0.6$. When $K_0 = 1$, the transient response may be decomposed into two parts. The first part of the transient is due the lead controller and lasts for about the first $0.1s$ after the step occurs. After this quick transient, the tracking error is almost 2 mils. At this point, the integrator action drives the tracking error towards zero, however the rate of decay of the tracking error is slow. Perhaps the rate of decay of the steady-state tracking error could be improved with a lag instead of a PI controller, however, it is easier to reduce the initial large steady-state error that occurs

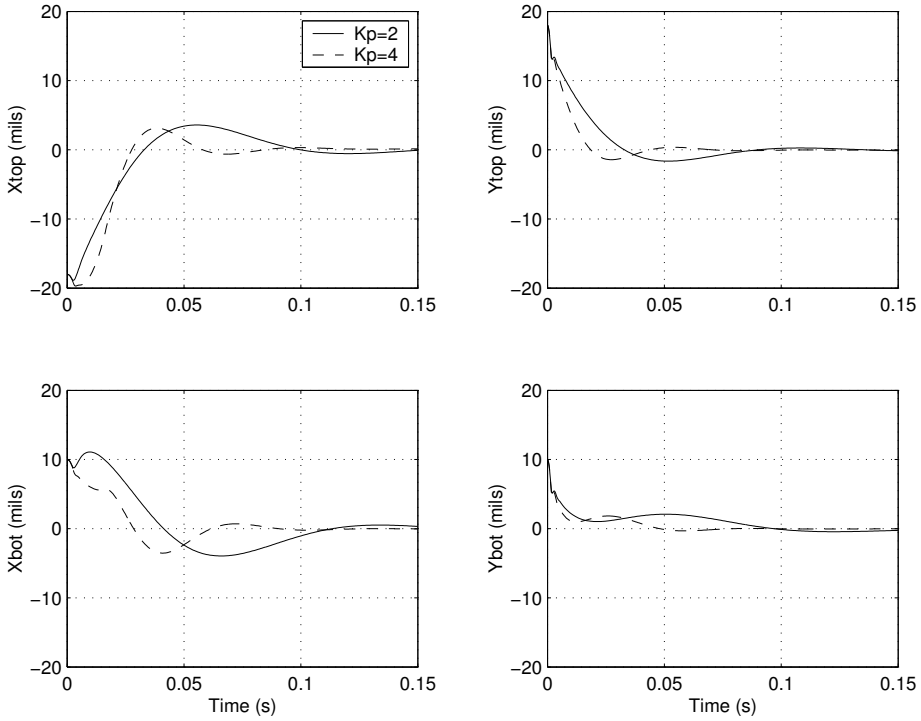

Figure 7.4: Initial condition response with $\omega_z = 0$, and $K_p = 2$ and $K_p = 4$ for each control axis. Position measured in mils.

after the first transient. This is done by changing the feed-forward gain. When $K_0 = 0.6$, the system tracks the square wave with about 20% overshoot and a settling time of about 0.1 seconds with zero steady-state error. This technique takes most of the work load off of the PI controller as far as reference tracking is concerned. However, the PI controller is essential because it is required for eliminating disturbances and for perfect regulation.

One may also observe the coupling of the system in Figure 7.5. The $B_1 \frac{\partial F}{\partial x}$ and $B_1 \frac{\partial F}{\partial I_c}$ matrices in equation (7.33) predict coupling between the top and bottom control axes. They also predict that the x and y control axes are independent. This is verified in Figure 7.5.

Figure 7.6 shows the effects of a spinning rotor. In these simulations, $K_p = 4$ and $K_0 = 1$ for each axis. In the first simulation $\frac{\omega}{2\pi} = 20$Hz. This makes the A_ω term in equation (7.32) non-zero and coupling between each of the four control axes results.

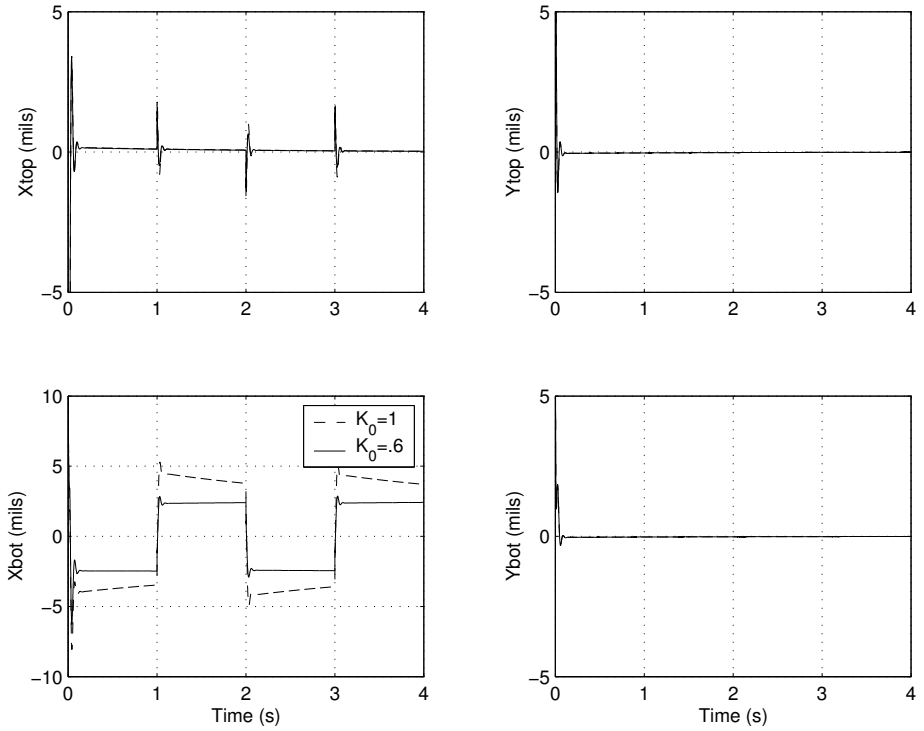

Figure 7.5: Initial condition response and x_b tracking a 2.5 mil square wave with $\omega_z = 0$, $K_p = 2$, and $K_0 = \{1, 0.6\}$.

This manifests itself as an oscillation that decays to zero. Note that the rotor is assumed to be balanced except for the fact that its center of gravity has been shifted in the axial z direction. If the center of gravity had a non-zero x or y component, the rotor imbalance would cause a persistent sinusoidal disturbance. Recall that with the proper selection of gains, the decentralized control approach ensures local asymptotic stability even though it neglects the coupling between the control axes. Keeping the control gains fixed, one sees that increasing the angular velocity to $\frac{\omega}{2\pi} = 33$Hz results in coupling between the control axes that is significant enough to destabilize the system. This illustrates the situation where each Lead+PI controller should stabilize each SISO channel, however, the coupled closed-loop MIMO system is unstable.

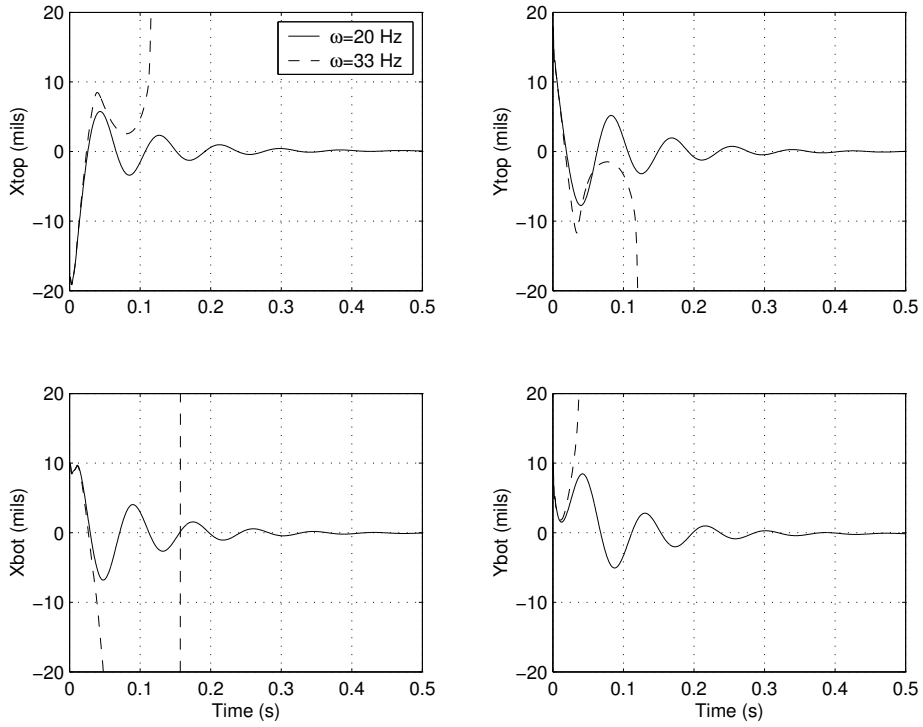

Figure 7.6: Initial condition response with $\omega_z = \{20, 33\}$Hz, $K_i = 1$ and $K_p = 4$ for each control axis.

CHAPTER VIII

EXPERIMENTAL CONTROL LAW VERIFICATION

8.1 Overview of Experimental Results

This chapter presents the experimental validation of the low-loss nonlinear control laws presented in Chapter 4. The PREMAG reaction wheel is stabilized with the decentralized control scheme established in Chapter 7. Current mode amplifiers are used on the x_t, y_t, and y_b axes for linear control and voltage mode amplifiers are employed on the x_b control axis for verification of the low-loss nonlinear control laws. The backstepping, control Lyapunov function, and passivity control laws are investigated with particular attention paid to the power consumption, the total square flux required for regulation, the bearing stiffness, and the control law singularity as a function of the flux bias and the control gains. The linear controller is similarly scrutinized.

There are several practical issues that arise when implementing the control laws on a real magnetic bearing that do not arise in simulation. In the development of the AMB model, it was assumed that when the rotor is centered at $x = y = 0$, the airgap on both sides of the rotor is equal to g_0. In this situation, the zero-force-point (the point at which the bias forces exactly cancel) is at $x = 0$. However, the electromagnet coils do not fit perfectly into the housing and the airgap on one side of the rotor when $x = y = 0$ may not equal the airgap on the other side. Consequently, the zero-force-point is shifted to a new position. Note that amount of shift in the zero-force-point depends on the bias. Thus, in several of the following results, the rotor is often

regulated to a constant position other than $x = y = 0$. Note that when regulating to the zero-force-point, the control currents are approximately zero. Furthermore, it is found that the control laws must be augmented with integral action to regulate to a setpoint with zero steady-state error. The details are presented in Section 8.2.

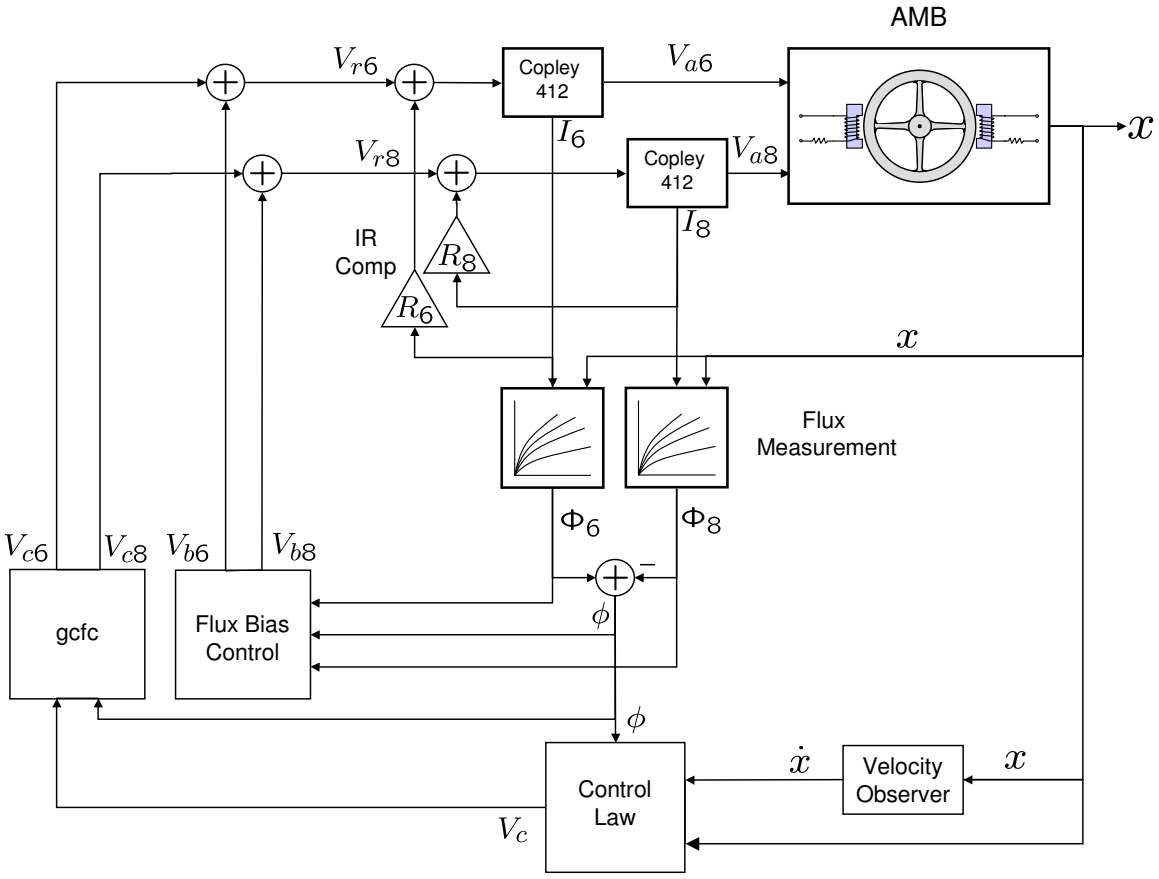

Figure 8.1: Block diagram of the closed-loop control and gcfc implementation for the x_b actuator axis.

Figure 8.1 illustrates the control loop for the nonlinear x_b control axis. The amplifiers operate in voltage mode with software implemented IR compensation. The voltage inputs V_{rj} are composed of a bias component V_{bj} and a control component V_{cj} for $j = 1, 2$. The gcfc switching condition distributes the calculated control voltage V_c to the appropriate electromagnets by monitoring the sign of the generalized flux ϕ. Each nonlinear control law requires the position, the velocity, and the generalized control flux.

Velocity measurements are obtained by filtering the position signal. Since differentiation amplifies noise at high frequency, direct differentiation of the position signal is avoided. A limited differentiation scheme is used. Since the bandwidth of the position control loops are on the order of $20-50$Hz, a filter that roughly matches the derivative up to 200Hz is used. Figure 8.2 shows the transfer function of the derivative and the velocity estimation filter

$$\frac{V(s)}{X(s)} = \frac{(1+b)^2 s}{s^2 + 2bs + b^2}$$

where $b = 2\pi 200$. The filter does introduce some extra phase shift in low frequency but does not affect the control performance significantly.

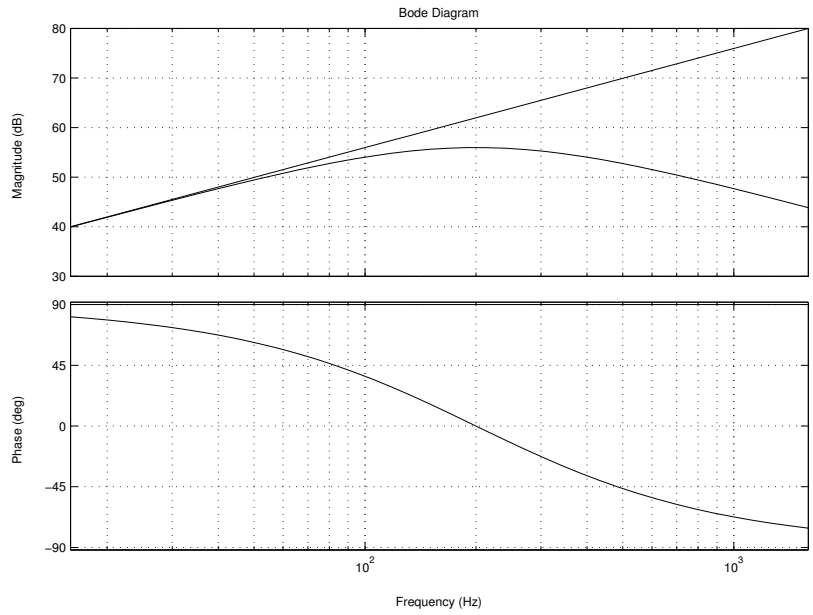

Figure 8.2: Bode plot of approximate derivative filter used for velocity estimation.

Figure 8.3 shows a test of the velocity estimation filter for a sinusoidal and step position signal. The velocity is shown in mils/s and the position is scaled for easy viewing. The estimator successfully reproduces the velocity from the position.

Stability proofs in Chapter 4 assume continuous-time systems, thus, a fast sampling rate is required. The dSPACE board monitors the time required to calculate the control law, referred to as the 'turn-around time". The controller complexity

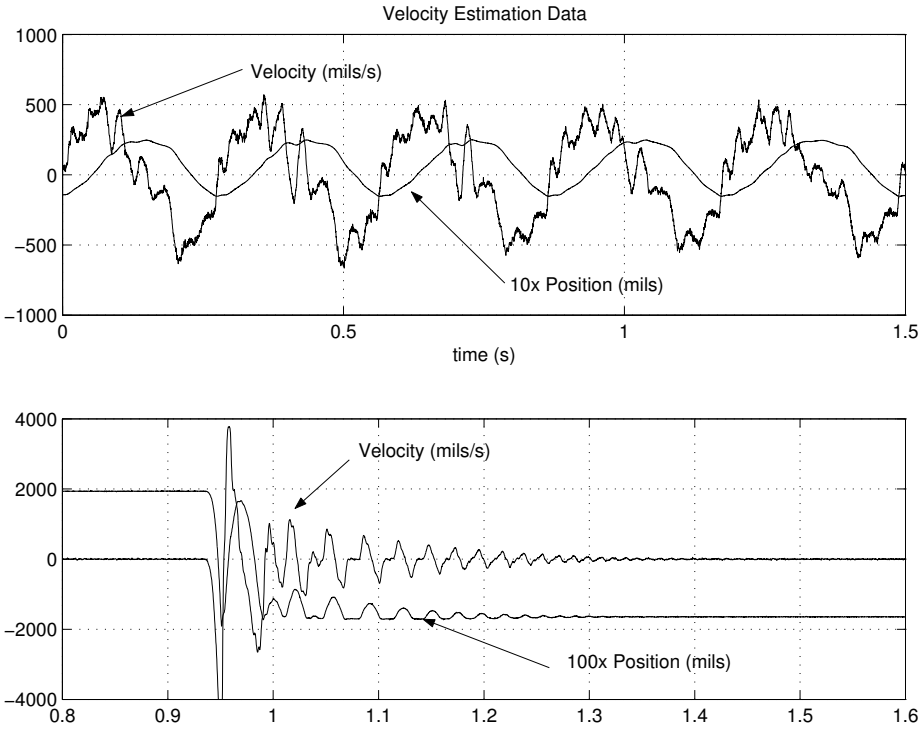

Figure 8.3: Velocity estimation test data.

and the number of signals to be recorded determines the turn-around time. The clf control law is the most complex while the passivity control law is the least complex. The dSPACE board produces an overrun fault if the sampling period is shorter than the turn-around time and execution is halted. In practice, the sampling period is decreased until a fault occurs. A sampling period of $T_s = 165\mu$s is used for each control law. This corresponds to a sampling rate of 6.06kHz. No attempts have been made to simplify the the control law implementations to minimize their turn-around times.

The power consumption and total square flux required for stabilization are of main concern in low-loss magnetic bearing design. Recall that the electromagnetic losses are proportional to the square of the flux: see Section 2.2.2. The power and flux required for stabilization are calculated from the state trajectories. Given any two control laws, it may be difficult to "match" their transient responses, and as a result, it is difficult to obtain fair power and flux consumption figures. Therefore, power

consumption and flux requirements must be calculated based on some steady-state behavior of the system. One such steady-state mode of operation is what this author refers to as the "whirl test". In this test scenario, the bottom of the rotor is regulated to a set point while the top of the rotor is uncontrolled. The x_b axis is implemented with a nonlinear low-loss control law and the y_b axis uses a linear controller. With a tap of the hand, the top of the rotor will whirl about in a roughly circular orbit. This presents a persistent sinusoidal disturbance to the bottom control axes. Figure

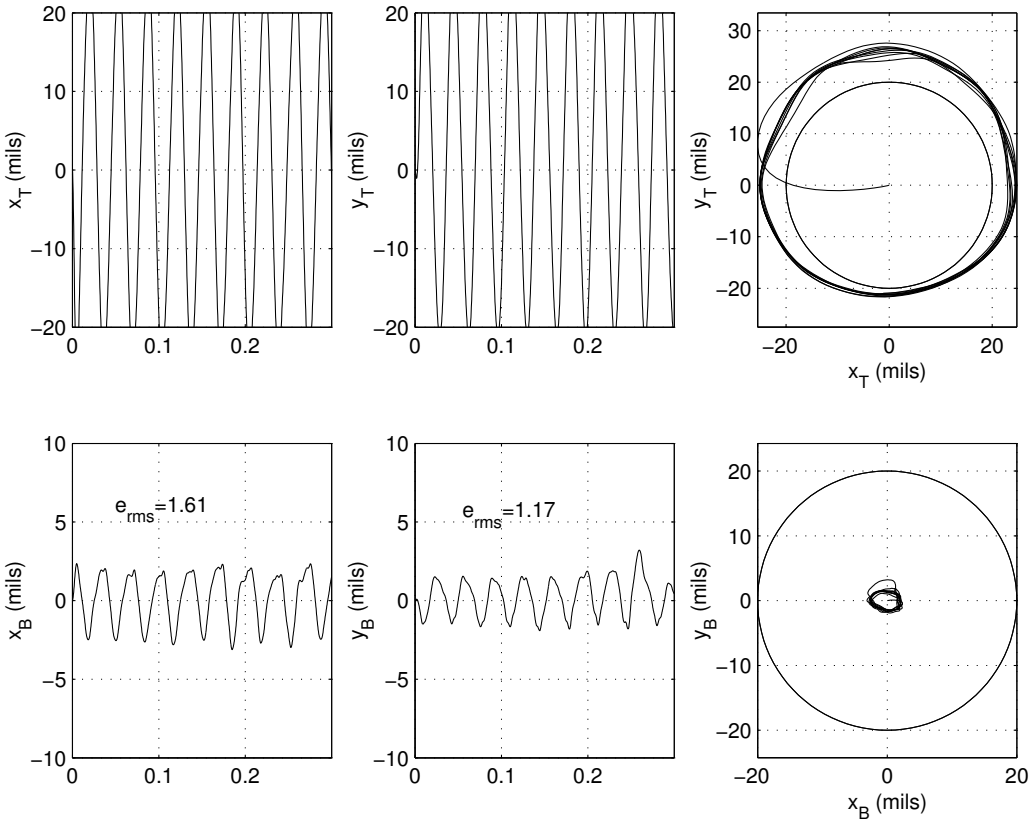

Figure 8.4: Example whirl test. ZB passivity-based control on x_b axis and linear control with $2A$ bias used on y_b axis.

8.4 illustrates a whirl test. The rotor position is illustrated with time and the rotor orbits are seen in the right-hand column. The rms regulation error e_{rms} is used as a performance measure. In this example, the nonlinear passivity controller regulates the x_b position to zero with a rms error of 1.61 mils and the linear controller regulates the

y_b position to zero with a rms error of 1.17 mils. The rms error depends on the control gains and the value of the bias used. Recall that larger bias implies larger actuator gain $\frac{df}{d\phi}$, and therefore affects the closed-loop bearing stiffness. A comparison of the power consumption and flux requirements between different control laws is considered "fair" when the control laws share the same rms regulation error $e_{\rm rms}$. The whirl test is conducted for each control law for several bias levels and control gains so that the power, flux, and stiffness may be investigated over a range of $e_{\rm rms}$ performance values.

Figure 8.5 shows an example of the gcfc implementation during a whirl test. The control voltages, the currents, the fluxes calculated from the flux-lookup tables, the control flux and the tracking error are shown. The rms values of the tracking error, control flux, and total fluxes are calculated for later use.

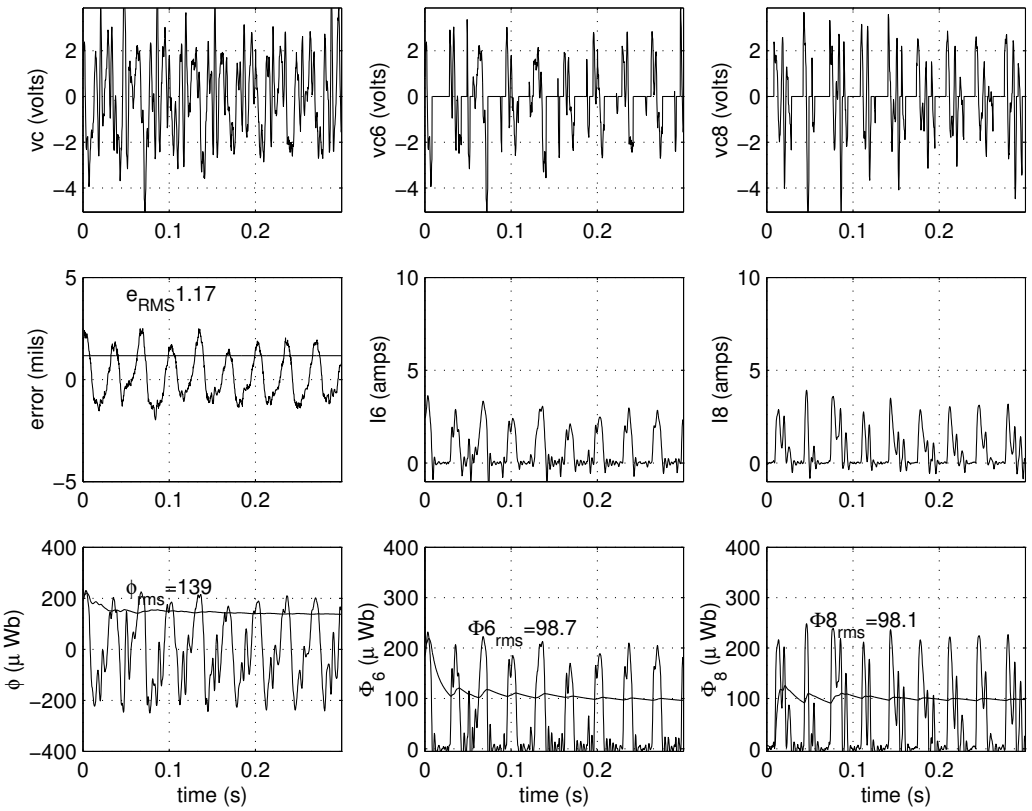

Figure 8.5: Example whirl test using passivity controller $\Phi_0 = 0$: Illustration of gcfc condition during closed-loop control. The rms values of the control flux ϕ and the total fluxes Φ_6 and Φ_8 are calculated for later use.

The instantaneous power analysis of the AMB and FWB was conducted in Section 2.2. Although the instantaneous power is useful for illustrating the power flow of the system, the average (real) or rms power is a more useful tool in determining the power required for operation. Recall the rms value of a signal is calculated with

$$x_{\text{rms}}(t) = \sqrt{\frac{1}{t}\int_0^t x^2(t)dt}$$

This is sometimes referred to as the running or online rms value of a signal. Since the rms value of a signal is basically equivalent to the L_2 norm, the rms value will settle to a constant value for signals with finite energy[1]. The running rms value of the control flux and total fluxes is shown in Figure 8.5. The steady-state value of the running rms value is also displayed.

The instantaneous power supplied to each electromagnet by the control law is

$$P_{supp} = V_{app}I = V_cI + V_bI + I^2\hat{R}$$

where V_cI, V_bI, and $I^2\hat{R}$ are the power required for control, biasing, and replenishment of the Ohmic loss. However, the rms power supplied satisfies

$$|P_{supp}|_2 \leq |V_cI|_2 + |V_bI|_2 + |I^2\hat{R}|_2$$

where $|\cdot|_2$ has been used to indicate the rms value. Therefore, it is difficult to study the rms power supplied to the system in terms of its constituents. Thus,

$$|P_{supp}|_2 = |V_{app}I|_2 \tag{8.1}$$

is used as a measure of the power consumption in each electromagnet. The total power consumption is the sum of the power consumption in each electromagnet. No rotational mechanical power is supplied to the rotor because the angular velocity used in whirl testing is zero.

[1]For periodic signals, the integral is calculated over one period and evaluates to a scalar: $x_{\text{rms}} = \sqrt{\frac{1}{T}\int_0^T x^2(t)dt}$.

The instantaneous power loss in the AMB and FWB is proportional to the square of the flux: see Section 2.2.2. However, the rms power loss is a more useful measure. Thus, to gauge the resulting AMB efficiency if it was to use the particular control law in question, the rms value of the total square flux is calculated. Specifically, the rms value of the total square flux refers to the quantity

$$(\Phi_6^2(t))_{\text{rms}} + (\Phi_8^2(t))_{\text{rms}} \tag{8.2}$$

where Φ_6 and Φ_8 refer to the total flux in each electromagnet on the x_b axis.

The experimental data for the linear, backstepping, clf, and passivity control laws is presented in each section below. Conclusions about the bearing stiffness, power consumption, and flux requirements are drawn from whirl testing and controller regulation data. Step response tracking is shown where appropriate to further illustrate the performance. Although the frequency response of a nonlinear system is not necessarily defined, the response of the PREMAG AMB with any of the nonlinear controllers designed in Chapter 4 to a sinusoidal reference is roughly sinusoidal. The frequency response for each control law is measured to give a rough indication of the bandwidth of the control loop.

There are several interesting trends found in the data. It is evident that the bearing stiffness increases as the flux bias increases. Also, the total flux required for regulation and the total square flux increases with the flux bias. Therefore, the AMB power dissipation increases with flux bias. Interestingly, the power supplied to the bearing for regulation does not necessarily increase with the flux bias. Loosely speaking, the power supplied by the controller is composed mainly of the power required to generate the control flux and the power required to generate the bias flux. In zero-bias (ZB), the control flux may be large. As the bias increases, the power required to implement the flux bias increases. On the other hand, the power required to realize the control flux decreases because of the increase in bearing stiffness. Thus,

there exists[2] a value of the flux bias Φ_0 that minimizes the total power supplied to the bearing. Furthermore, as predicted by simulation, the backstepping control law produces large voltage spikes when operating near the controller singularity (small Φ_0). The clf control law performs better than the backstepping controller in zero bias and the passivity-based control law performs the best. The frequency spectrum of the control signal is used to characterize the performance of the controller when operating near singularity.

8.2 Control Law Modification for Zero Steady-State Error

It is found in the experiments that each of the nonlinear control laws is not able to regulate the rotor to zero with zero steady-state error. The shift in the zero-force-point, as mentioned earlier, will produce a disturbance force on the rotor. Other disturbance forces may arise from the interaction of the other control laws through the coupling between the top and bottom of the rotor control axes. In any case, integral action may be added into the control laws to eliminate the steady-state error. The modifications to each control law are very similar and will only be illustrated in detail for the backstepping controller.

Recall that the open-loop dynamics have the form

$$\dot{x}_1 = x_2 \tag{8.3a}$$

$$\dot{x}_2 = f_2(y) \tag{8.3b}$$

$$\dot{y} = u \tag{8.3c}$$

If $f_2(y)$ is equal to the stabilizing function $\sigma(x_1, x_2)$, the resulting x dynamics are $\ddot{x}_1 = \sigma(x_1, x_2)$ where the designer has the freedom to assign any asymptotically stable dynamics with the choice of σ. Rewriting the open loop dynamics in terms of

[2]This optimal value is yet to be determined.

the backstepping error $\eta := f_2(y) - \sigma(x_1, x_2)$,

$$\ddot{x}_1 = f_2(y) - \sigma(x_1, x_2) + \sigma(x_1, x_2) = \sigma(x_1, x_2) + \eta$$
$$\dot{\eta} = \frac{df_2(y)}{dy}u - \dot{\sigma}(x_1, x_2)$$

Selecting the preliminary feedback

$$u = \Big(\frac{df_2(y)}{dy}\Big)^{-1}(\dot{\sigma}(x_1, x_2) + \nu)$$

the backstepping error dynamics are $\dot{\eta} = \nu$. The auxiliary input ν is selected to make the η dynamics asymptotically stable.

For regulation to $x_1 = x_2 = 0$, choose the stabilizing function as

$$\sigma_r(x_1, x_2) = -k_1 x_1 - k_2 x_2$$

and the auxiliary input as

$$\nu_r = -\gamma\eta$$

where k_1, k_2 and γ are positive control gains. In experiment, it is found that even when regulating to zero, there may be some steady-state error in η when using ν_r. To remedy this, let

$$\nu := -\gamma\eta - \gamma_i \int_0^t \eta dt \tag{8.4}$$

with $\gamma_i > 0$ so that the backstepping error dynamics have the form

$$\ddot{\eta} + \gamma\dot{\eta} + \gamma_i\eta = 0 \tag{8.5}$$

The added integral action ensures that the steady-state error in η is removed. To regulate to a setpoint other than zero with zero steady-state error, let $e = r - x_1$ and let

$$\sigma(x_1, x_2) := k_1 e - k_2 x_2 + k_i \int_0^t e dt \tag{8.6}$$

where k_1, k_2 and k_i are positive control gains[3]. The resulting dynamics are

$$\ddot{x}_2 = k_1\dot{e} - k_2\dot{x}_2 + k_i e + \dot{\eta} \tag{8.7}$$

[3]Note that k_1, k_2, and k_i behave roughly like the proportional, derivative, and integral gains of a PID control law.

Given that $\dot{e} = \dot{r} - x_2$, $\ddot{e} = \ddot{r} - \dot{x}_2$, and $\dddot{e} = \dddot{r} - \ddot{x}_2$, the above dynamics in equation (8.7) may be written in terms of the tracking error,

$$\dddot{e} + k_2\ddot{e} + k_1\dot{e} + k_i e = \dddot{r} + k_2\ddot{r} - \dot{\eta} \tag{8.8}$$

The closed-loop system consisting of the tracking error dynamics of (8.8) and the backstepping error dynamics (8.5) is globally asymptotically stable for constant r. The cascade of two GAS systems with a linear interconnection term is GAS [69]. Thus, tracking to any constant setpoint is possible. In fact, the position will track any reference signal with $\ddot{r} = 0$.

By substituting (8.4) and (8.6) for ν_r and σ_r in the clf and passivity based designs, similar tracking error stability proofs may be constructed.

In the backstepping and clf design, the positive definite matrix P which is the solution to the equation $A^T P + PA < 0$ where

$$A = \begin{bmatrix} 0 & 1 \\ -k_1 & -k_2 \end{bmatrix}$$

is used explicitly in the feedback. To implement the controller so that the control gains k_1 and k_2 can be changed online, the matrix P must be solved analytically in terms of k_1 and k_2. Solving $A^T P + PA = -I$ analytically for P gives

$$P = \frac{1}{2}\begin{bmatrix} \frac{k_1^2+k_1+k_2^2}{k_1 k_2} & k_1 \\ k_1 & \frac{1+k_1}{k_1 k_2} \end{bmatrix} \tag{8.9}$$

8.3 Backstepping Control Results

This section presents the experimental results of the backstepping controller of equation (4.18) which has been modified as described in the previous section. Recall that, when operating with zero flux bias, the backstepping control law is singular on the set $\overline{\mathcal{D}}_1 = \{x \in \mathbb{R}^3 | x_3 = 0\}$. Consequently, infinite voltage signals are commanded when crossing the plane of singularity. In experiment, it is found that large voltage signals

may be commanded even with small, but non-zero flux bias. In terms of regulation performance, the backstepping control law is competitive with the other nonlinear control laws presented in Chapter 4 for large flux bias, however, its ability to regulate the rotor to a setpoint quickly degrades for flux-bias levels less than about 50μWb.

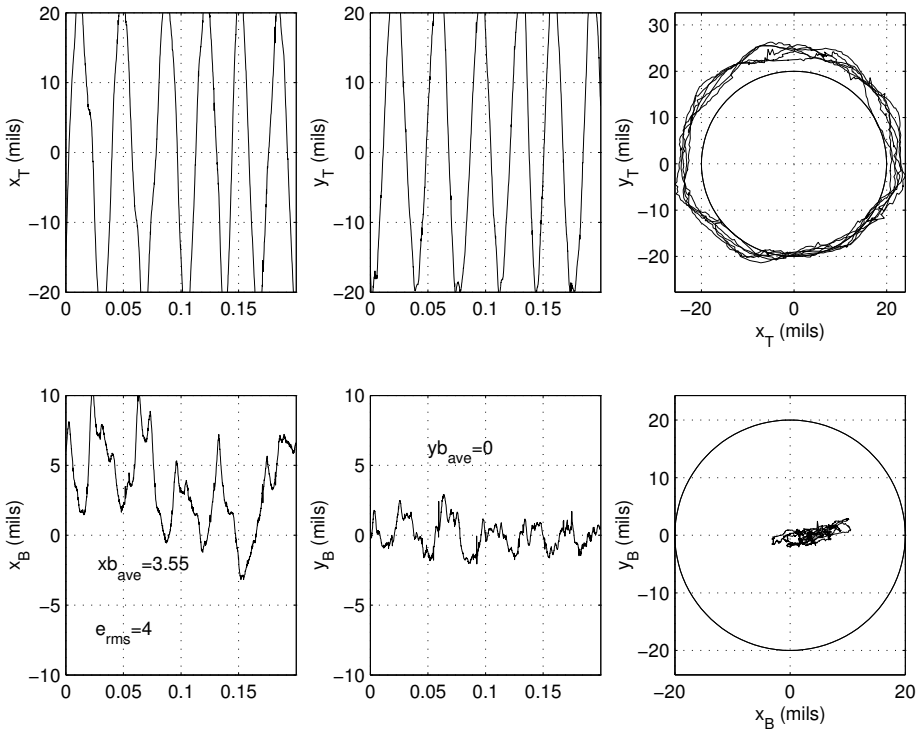

Figure 8.6: Backstepping Whirl Test $\Phi_0 = 0$: x_b axis regulated to 4 mils with a rms regulation error $e_{\text{rms}} = 4$ mils. The poor performance of the ZB Backstepping controller is typical during whirl testing, no matter the value of k_1.

The whirl tests for the backstepping controller are conducted for $\Phi_0 = 0$, 50, 100, and 150μWb. However, the results for ZB operation are not comparable to those of the LB operation. The following figures show that, during whirl testing, the rotor may be consistently regulated to a given setpoint with any desired rms tracking error in the range of about $e_{\text{rms}} \in [.8, 1.5]$ mils by proper selection of the k_1 gain when the flux bias is greater than about 50μWb. However, for ZB operation, the rms tracking error is about $e_{\text{rms}} = 4$ mils for any reasonable choice of k_1 gain. Thus, the ZB data is omitted. Note that for any of the control laws implemented, one can not pick the

control gains too large or the controller may respond to the measurement noise.

Figure 8.6 illustrates this deficiency of the backstepping controller in ZB. The x_b axis is regulated to 4 mils, however, the rms regulation error is about 4 mils. This performance is *not* improved by increasing the k_1 control gain (roughly the proportional gain).

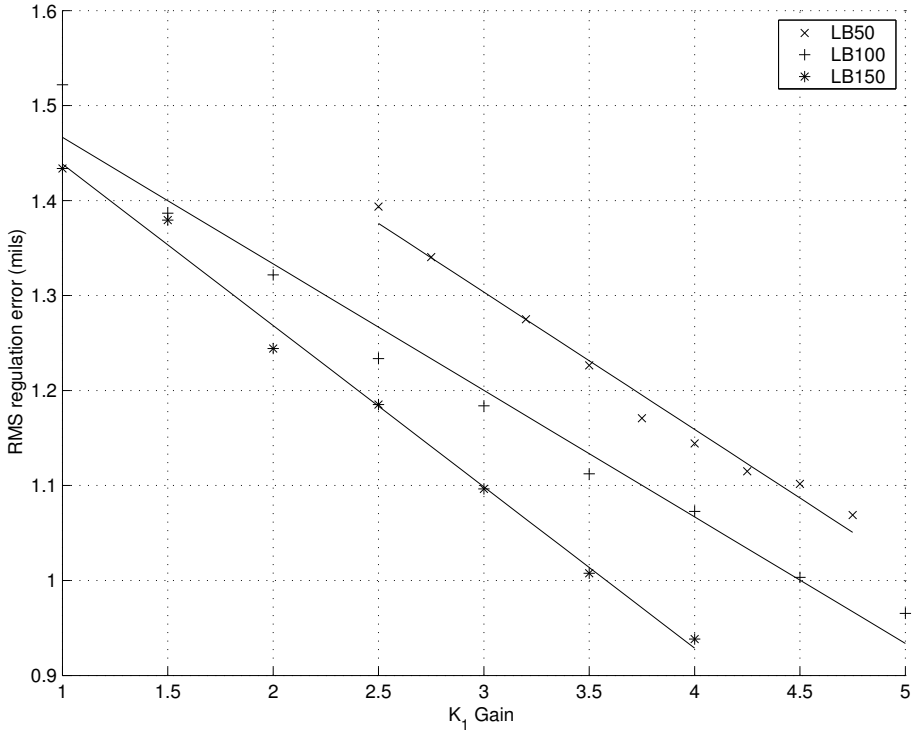

Figure 8.7: Backstepping Whirl Test $\Phi_0 = 50, 100, 150\mu$Wb: The rms regulation error e_{rms} is a linear function of the proportional gain k_1. The proportional gain required to achieve a given e_{rms} decreases as the flux bias increases.

When the bias is increased to values greater than about 50μWb, the whirl test looks similar to that shown in Figure 8.4 and e_{rms} is a linear function of the k_1 control gain. Figure 8.7 illustrates the linear dependence of e_{rms} on the proportional gain for several values of flux bias. The proportional gain required to achieve a given e_{rms} decreases as the flux bias increases. This is due to the fact that the actuator gain $\frac{df}{d\phi}$, where f is the total electromagnet force and ϕ is the control flux, increases with bias. The above may also be interpreted as an increase in bearing stiffness because

$\frac{df}{dx} = \frac{df}{d\phi}\frac{d\phi}{dx}$.

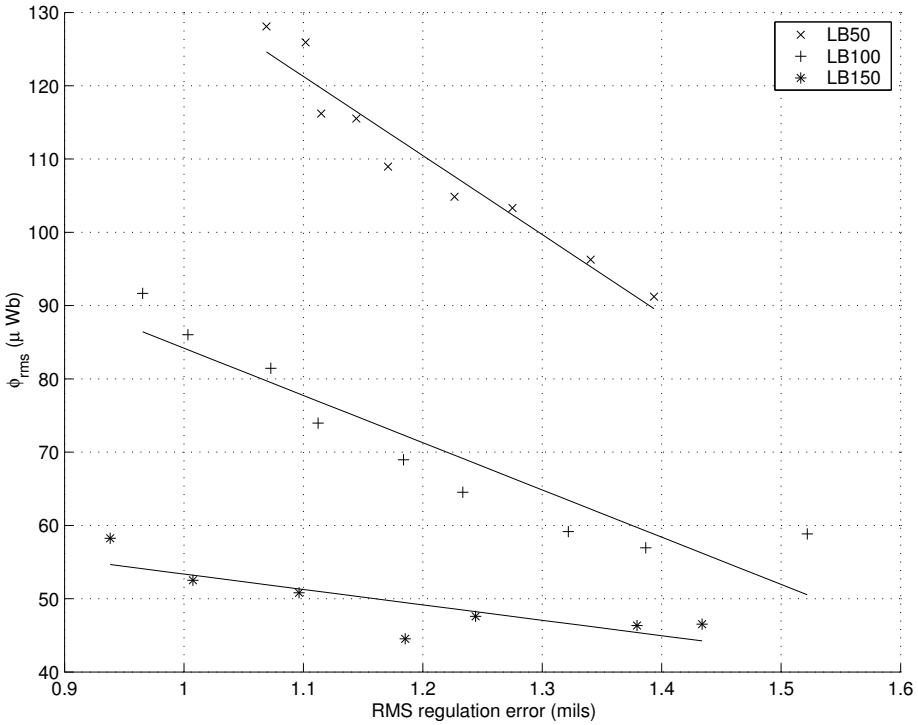

Figure 8.8: Backstepping Whirl Test $\Phi_0 = 50, 100, 150\mu$Wb: The rms value of the control flux ϕ_{rms} vs. rms regulation error e_{rms}. For a given e_{rms}, ϕ_{rms} decreases as Φ_0 increases.

Figure 8.8 shows the linear dependence of the rms control flux ϕ_{rms} on the rms tracking error e_{rms}. For a given flux bias, ϕ_{rms} increases as e_{rms} decreases. This is consistent with the intuition that more control effort is required to regulate the rotor to a tighter position tolerance. The increase in bearing stiffness is also supported by the fact that for a given e_{rms}, ϕ_{rms} decreases as the flux bias Φ_0 increases. Loosely speaking, the bearing becomes more "responsive" as the flux bias increases. Consequently, to perform the same amount of work while regulating the rotor, the required control effort ϕ_{rms} becomes smaller as the flux bias increases.

Figure 8.9 shows the total rms flux $\Phi_{6\text{rms}} + \Phi_{8\text{rms}}$ vs. rms regulation error e_{rms}. Since the total flux is the combination of the control flux and the flux bias in both electromagnets, one expects each curve in Figure 8.8 to be shifted up by $2\Phi_0$. (There is an extra Φ_0 contributed from both of the electromagnets.) For example, $\phi_{\text{rms}} =$

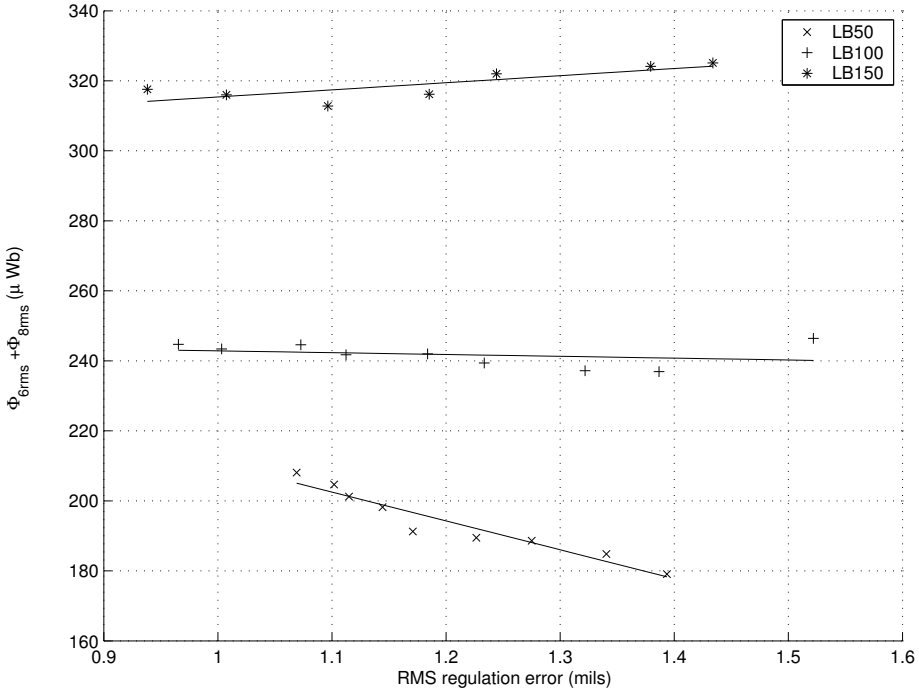

Figure 8.9: Backstepping Whirl Test $\Phi_0 = 50, 100, 150\mu$Wb: The total rms flux $\Phi_{6\text{rms}} + \Phi_{8\text{rms}}$ vs. rms regulation error e_{rms} for several flux bias values.

90μWb for $e_{\text{rms}} = 1.4$ using $\Phi_0 = 50\mu$Wb. Thus, the total flux should be about $90\mu\text{Wb} + 2(50)\mu\text{Wb} = 190\mu\text{Wb}$. One finds the total flux for $e_{\text{rms}} = 1.4$ and $\Phi_0 = 50\mu$Wb in Figure 8.9 to be 180μWb.

Figure 8.10 shows the total square rms flux $(\Phi_6^2)_{\text{rms}} + (\Phi_8^2)_{\text{rms}}$ vs. rms regulation error e_{rms}. Note that $(\Phi^2)_{\text{rms}} \neq (\Phi_{\text{rms}})^2$. Recall that the rms power dissipation is proportional to the square of the flux. As expected, the total square flux increases with increasing flux bias. Thus, one should operate with the smallest flux bias possible to minimize the power loss.

Figure 8.11 shows the total rms power supplied $(P_{6\text{supp}})_{\text{rms}} + (P_{8\text{supp}})_{\text{rms}}$ vs. rms regulation error e_{rms}. Recall that the power supplied is calculated from equation 8.1. The first trend to note is that tighter regulation tolerance requires more power. The trade-off between power consumption and flux bias is also illustrated in this figure. One might expect that the power supplied to the bearing increases as the flux bias

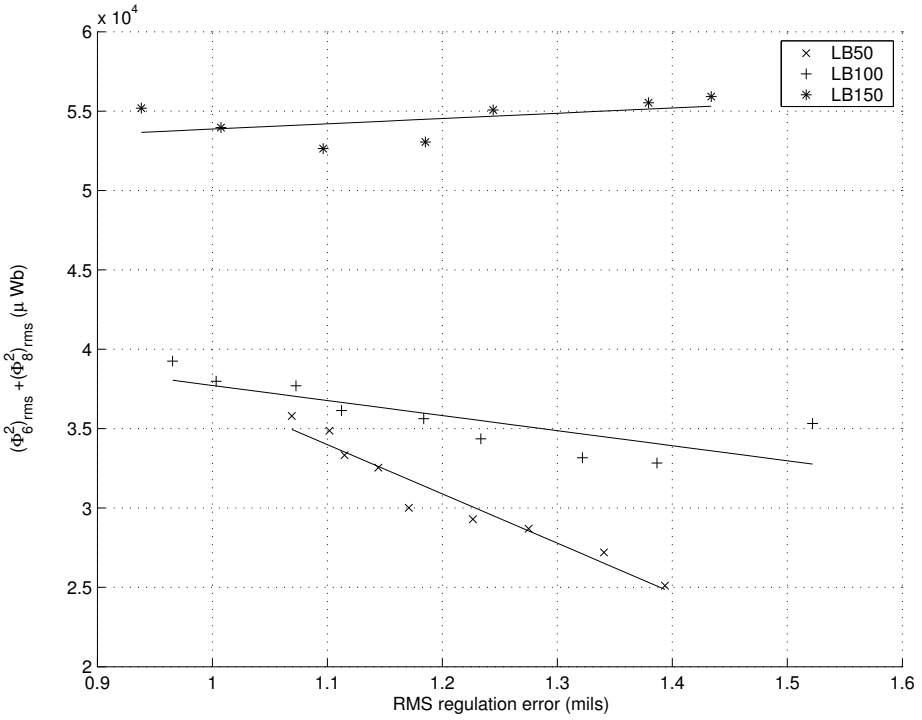

Figure 8.10: Backstepping Whirl Test $\Phi_0 = 50, 100, 150\mu$Wb: The total square rms flux $(\Phi_6^2)_{\rm rms} + (\Phi_8^2)_{\rm rms}$ vs. rms regulation error $e_{\rm rms}$ for several flux bias values.

increases. However, as the flux bias increases, so does the bearing stiffness. Consequently, the rms control flux (a measure of the control effort) decreases. This suggests that there are instances where the reduction in the power required to implement the control flux is greater than the increase in the power required to implement the flux bias. Therefore, one may actually save power by increasing the bias flux. For example, inspecting Figure 8.11, one observes that for $e_{\rm rms} < 1.4$, less power is required by implementing the 100μWb flux bias than when implementing the 50μWb flux bias. Similar statements may be made wherever the different flux bias lines cross. Note also that the slope $(P_{\rm supp})_{\rm rms}/e_{\rm rms}$ decreases as the flux bias increases.

With significant bias levels, the controller performance is acceptable. Figure 8.12 demonstrates the controller tracking a square and a sawtooth wave for $\Phi_0 = 50\mu$Wb with zero steady-state error and acceptable transient performance. The control gains

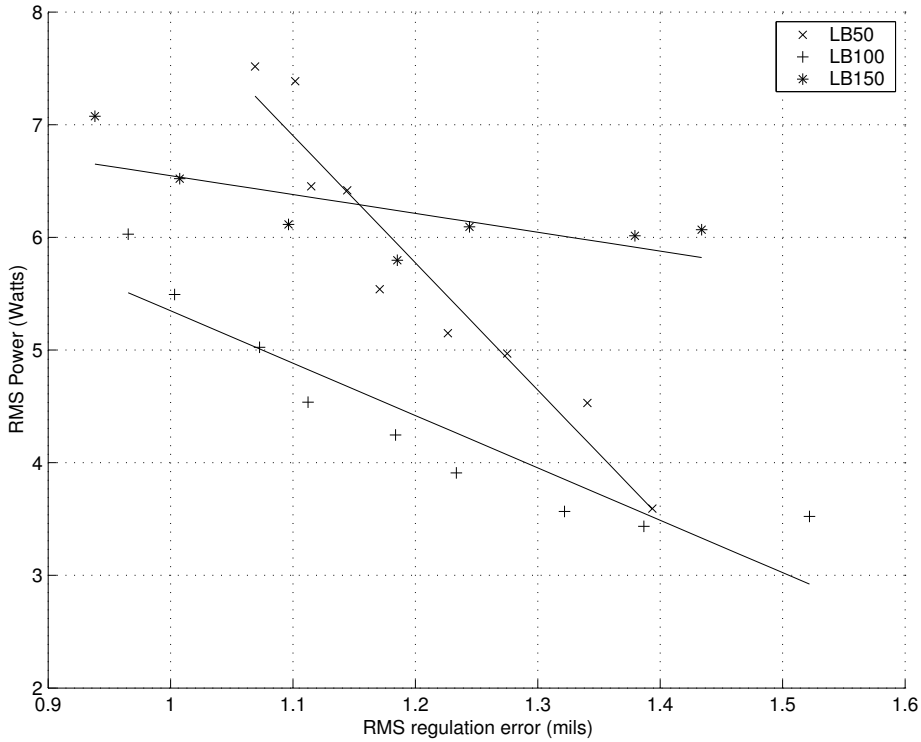

Figure 8.11: Backstepping Whirl Test $\Phi_0 = 50, 100, 150\mu$Wb: The total rms power supplied $(P_{6\text{supp}})_{\text{rms}} + (P_{8\text{supp}})_{\text{rms}}$ vs. rms regulation error e_{rms}.

selected for these figures are $k_1 = 4$, $k_2 = 2$, $k_i = .2$, $\gamma = .5$, $\gamma_i = .1$, and the feed-forward gain $k_0 = 0.83$. Similar results are obtained for larger flux bias levels. Note that the x and y axes are clearly decoupled. However, the reference tracking on the x_b axis presents a disturbance to the x_t axis.

Figure 8.13 shows the measured magnitude frequency response for the backstepping controller using the above gains and several values of the flux bias. The control bandwidth is in the range of $10 - 30$Hz. As the flux bias increases, the bandwidth increases.

Figure 8.14 shows the rotor being regulated to $(x_t, y_t, x_b, y_b) = (4, 0, 4, 0)$ mils with $\Phi_0 = 50\mu$Wb. At $t = 0.2s$, the rotor is spun by hand to present a disturbance. Recall that when the rotor is spinning, there is coupling between each of the control axes. The controllers on each axis successfully reject the disturbance. Although omitted from this presentation, the disturbance is better rejected for larger bias. In fact

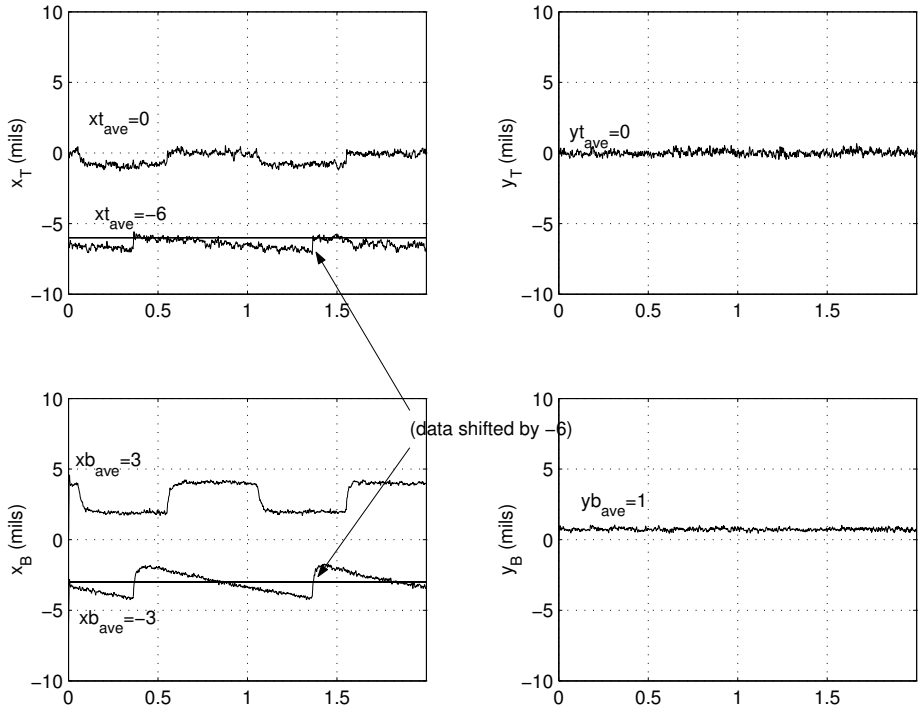

Figure 8.12: Backstepping Controller 1 mil Reference Tracking $\Phi_0 = 50\mu$Wb: Tracking of a 1 mil square and sawtooth reference with 3 mil offset. Note that the data for the sawtooth has been shifted by -6 mils for easy viewing. The following control gains result in zero steady-state error: $k_1 = 4$, $k_2 = 2$, $k_i = .2$, $\gamma = .5$, $\gamma_i = .1$, $k_0 = 0.83$.

for $\Phi_0 = 150\mu$Wb, it is difficult to deflect the rotor's x_b position with an impulse disturbance (a sharp tap with a hard object) or spin disturbance. Although not illustrated, the commanded control voltages are at most $20 - 30$V.

The general trend with the backstepping controller is that the performance degrades significantly as the flux bias decreases to zero. Figure 8.15 shows the backstepping controller with $\Phi_0 = 10\mu$Wb regulating to $(x_t, y_t, x_b, y_b) = (4, 0, 4, 0)$ mils with a spin disturbance introduced before $t = 0$s. The rotor behaves erratically, but briefly recovers between $1.5 - 4$s. Although not explicitly shown, the commanded voltage signal may spike into the hundreds of volts during the erratic behavior. At about 4s, the spin disturbance again causes large spikes in the control law and the rotor vibrates violently. Since the rotor is spinning, coupling exists between all axes. The spasmatic control on the x_b axis injects a large disturbance into the other control

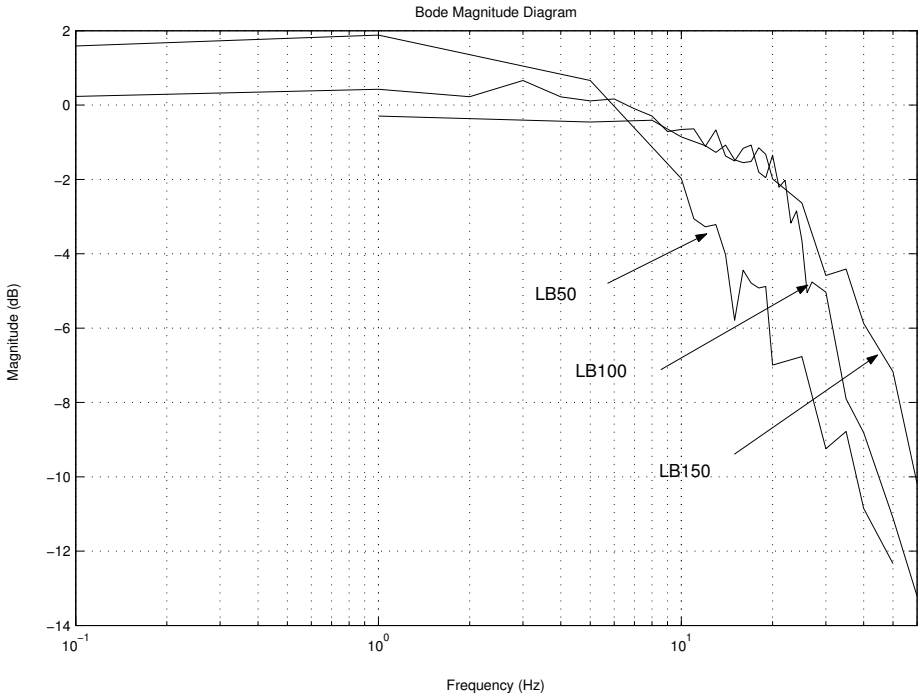

Figure 8.13: Backstepping magnitude frequency response for $\Phi_0 = 50, 100, 150$ μWb: $k_1 = 4$, $k_2 = 2$, $k_i = .2$, $\gamma = .5$, $\gamma_i = .1$. Note bandwidth increases as flux bias increases.

axes. Note that when using zero bias, the controller typically fails to recover from a spin disturbance and the requested control voltage may have spikes on the order of 10^6 volts.

The frequency spectrum is used to obtain an appreciation for the erratic control voltages that the backstepping controller requests when operating in zero bias. Figure 8.16 shows the requested control voltages V_{r6} and V_{r8} produced by the backstepping controller during a sample whirl test with $\Phi_0 = 0$. Note the large control spikes and that these spikes are typically even larger when conducting a regulation test as in Figure 8.15. The frequency spectrum for each requested control voltage is shown. Notice the control signal energy is spread over a very large bandwidth. The Copley 412 amplifiers acting in voltage mode try to make V_{app6} and V_{app8} track V_{r6} and V_{r8}, respectively. However, the bandwidth of the amplifiers in voltage mode is only about $200 - 300$Hz. Only a very small portion of the frequency spectrum of V_{r6} and V_{r8}

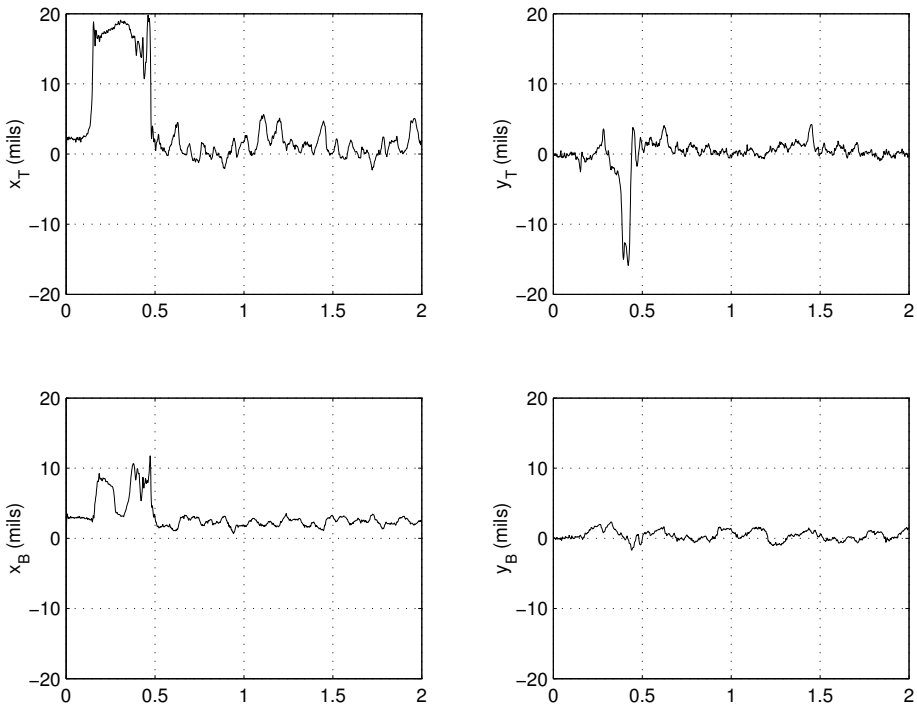

Figure 8.14: Backstepping spin regulation for $\Phi_0 = 50\mu$Wb: Rotor is regulated to $(x_t, y_t, x_b, y_b) = (4, 0, 4, 0)$ mils and spin disturbance introduced at $t = 0.2$s. Control Gains: $k_1 = 4$, $k_2 = 2$, $k_i = .2$, $\gamma = .5$, $\gamma_i = .1$. Each axis is successful at regulating against the spin disturbance.

make it through the amplifier to appear at V_{app6} and V_{app8}. Note that the resulting applied voltages are well within the $\pm$28V voltage saturation range. Note that as the bias increases, the bandwidth of the requested frequency spectrum is much smaller.

8.4 CLF Control Results

This section presents the experimental results of the clf controller of equation (4.35) for $p = 1$. The experimental results for $p > 1$ are similar. The modifications to this control law so that it can regulate to any setpoint with zero steady-state error are similar to those presented in Section 8.2. The stabilizing control law σ in equation (4.14) is replaced by equation (8.6). Defining $\eta = x_3 - u_0(z)$, the function Θ in equation (4.36) is written

$$\Theta(z, x_3) = \gamma\eta$$

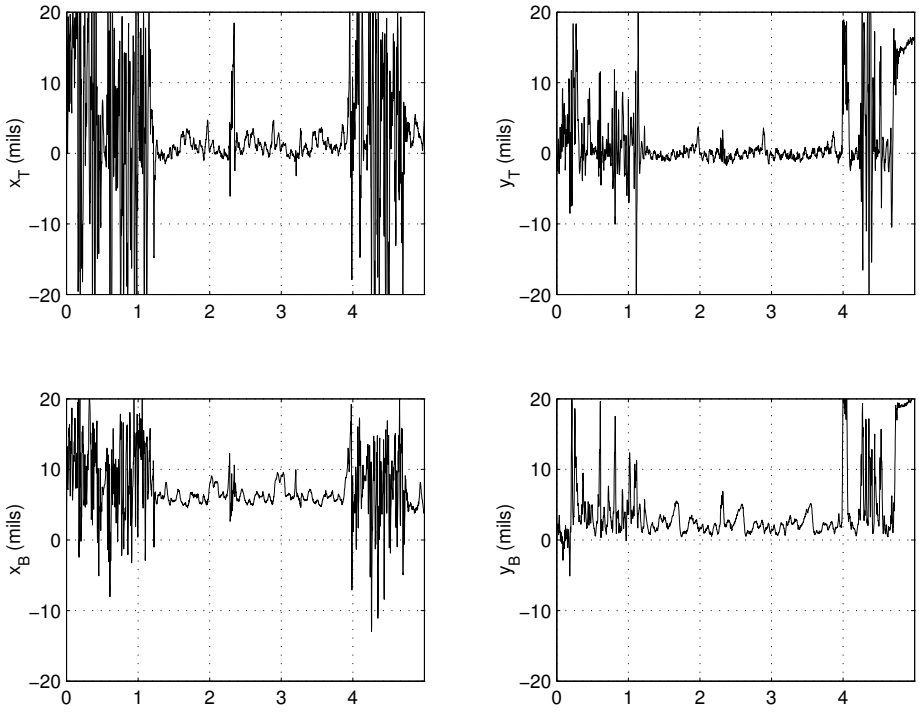

Figure 8.15: Backstepping spin regulation for $\Phi_0 = 10\mu$Wb: Rotor is regulated to $(x_t, y_t, x_b, y_b) = (4, 0, 4, 0)$ mils and spin disturbance introduced before $t = 0$s. Control Gains: $k_1 = 4$, $k_2 = 2$, $k_i = .2$, $\gamma = .5$, $\gamma_i = .1$. Each axis is successful at regulating against the spin disturbance, but often with violent rotor vibrations.

This function is modified to

$$\Theta(z, x_3) = \gamma\eta + \gamma_i \int_0^t \eta dt$$

Recall that, when operating with zero flux bias, the clf control law is singular on the set $D_3 := \{x \in \mathbb{R}^3 | \ x_3 = u_0(z) = 0\}$ where u_0 is defined in equation (4.16). This corresponds to a line in $\mathbb{R}^3$. In experiment, it is found that this singularity is rarely encountered. Note that operation near this singularity does produce some peaks in the requested control voltage, however, the magnitude of these peaks are typically reasonable in amplitude. Note that in zero bias, the clf controller performs much better than the backstepping controller.

The whirl tests for the clf controller are conducted for $\Phi_0 = 0$, 50, 100, and

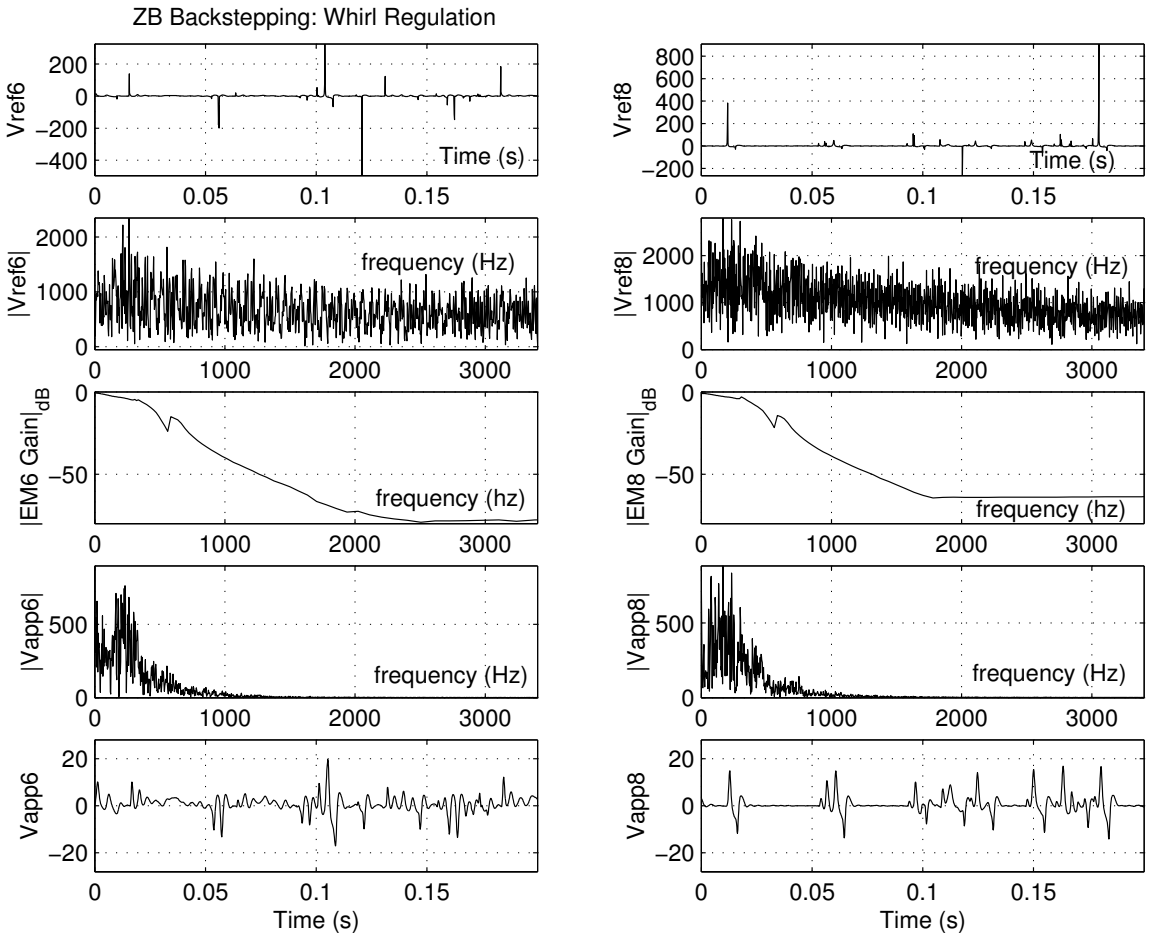

Figure 8.16: Backstepping Whirl Regulation Control Spectrum: $\Phi_0 = 0$. Requested control voltages V_{r6} and V_{r8} and their frequency spectra. The voltage mode amplifiers only have bandwidth of about $200 - 300$Hz. The applied voltage V_{app6} and V_{app8} and their frequency spectra. Compare to Figures 8.24 and 8.34.

150μWb. In contrast to the backstepping controller, the performance of the clf controller in zero bias is comparable to the results in low bias. During whirl testing, the rotor may be consistently regulated to a given setpoint with any desired rms tracking error in the range of about $e_{\text{rms}} \in [.9, 1.5]$ mils by proper selection of the k_1 gain. There is an upper limit to the proportional gain in experiment. When k_1 is too large, the controller seems to respond to the measurement noise and instability results. Figure 8.17 shows the linear dependence of e_{rms} on the proportional gain k_1. To regulate with given e_{rms}, the proportional gain k_1 decreases as the flux bias increases due to the increase in bearing stiffness. Note that the magnitude of the slope of e_{rms}/k_1 also

increases with bias.

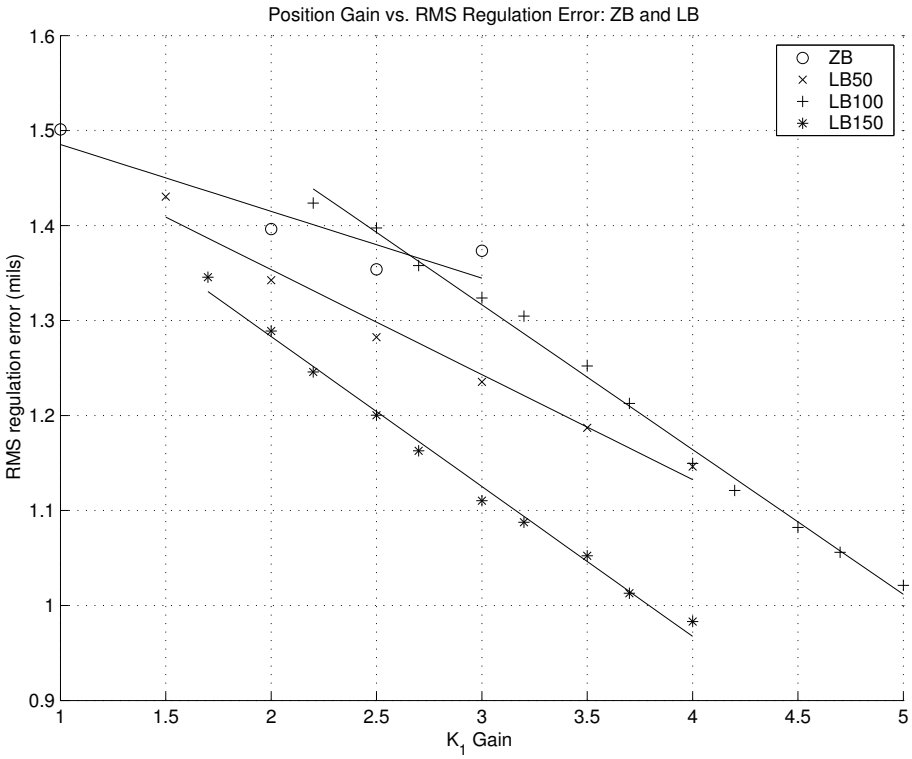

Figure 8.17: Clf Whirl Test $\Phi_0 = 50, 100, 150\mu$Wb: Linear dependence of $e_{\rm rms}$ on proportional gain k_1. To regulate to a given $e_{\rm rms}$, the proportional gain k_1 decreases with increasing flux bias. This is due to the increase in bearing stiffness with increasing flux bias.

Figure 8.18 shows the linear dependence of the control flux $\phi_{\rm rms}$ on the tracking error $e_{\rm rms}$. More control effort is required to regulate the rotor with tighter position tolerance. Note that for a given $e_{\rm rms}$, less control flux is required to regulate the rotor as the flux bias increases. This is due to the increase in actuator gain $\frac{df}{d\phi}$ and the resulting increase in bearing stiffness $\frac{df}{dx} = \frac{df}{d\phi}\frac{d\phi}{dx}$.

Figure 8.19 shows the total rms flux $\Phi_{6\rm rms} + \Phi_{8\rm rms}$ vs. rms regulation error $e_{\rm rms}$. Since the total flux is the combination of the control flux and the flux bias in both electromagnets, one expects each curve in Figure 8.18 to be shifted up by $2\Phi_0$. For example, $\phi_{\rm rms} = 100\mu$Wb for $e_{\rm rms} = 1.4$ mils using $\Phi_0 = 50\mu$Wb. The total flux should be about $100\mu\text{Wb} + 2(50)\mu\text{Wb} = 200\mu$Wb. The resulting total flux found in

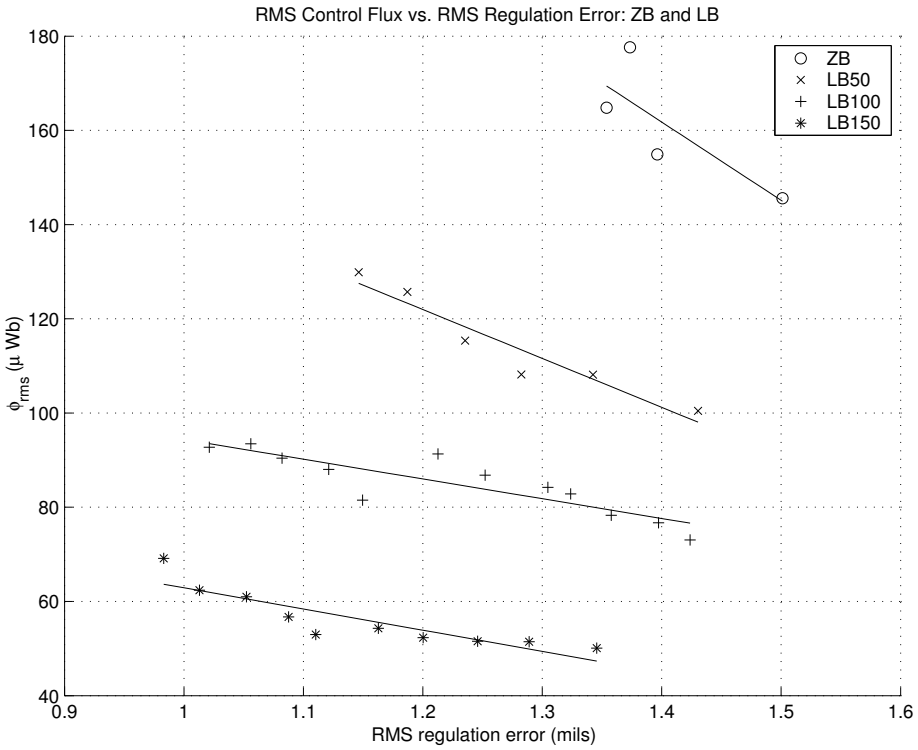

Figure 8.18: Clf Whirl Test $\Phi_0 = 50, 100, 150\mu Wb$: Linear dependence of $\phi_{\rm rms}$ on proportional gain $e_{\rm rms}$. Less control flux is required for regulation to a given $e_{\rm rms}$ as the flux bias increases. This is due to the increase in bearing stiffness with increasing flux bias.

Figure 8.19 for $e_{\rm rms} = 1.4$ mils and $\Phi_0 = 50\mu$Wb is 190μWb. Thus, the total rms flux in each electromagnet is about 45μWb larger than its rms control flux. Similar comparisons may be made for the other flux bias lines.

Interestingly, the zero bias total flux line is also shifted in Figure 8.19 even though zero bias is implemented. The control flux for $e_{\rm rms} = 1.5$ mils is $\phi_{\rm rms} = 145\mu$Wb. The total flux for $e_{\rm rms} = 1.5$ mils is $\Phi_{6\rm rms} + \Phi_{8\rm rms} = 200\mu$Wb. Thus, the total rms flux in each electromagnet is about 27.5μWb larger than expected. Recall that when the voltage mode amplifier operates properly, the coil dynamics are governed by $N\dot{\Phi} = -I(R - \hat{R}) + V_b + V_c$. Thus the total flux is composed of the flux generated by the control signal v_c, the flux generated by the bias signal v_b and the flux generated by the imperfect IR compensation. Since $v_b \equiv 0$ when implementing zero bias, this extra flux must be due to the imperfect IR compensation.

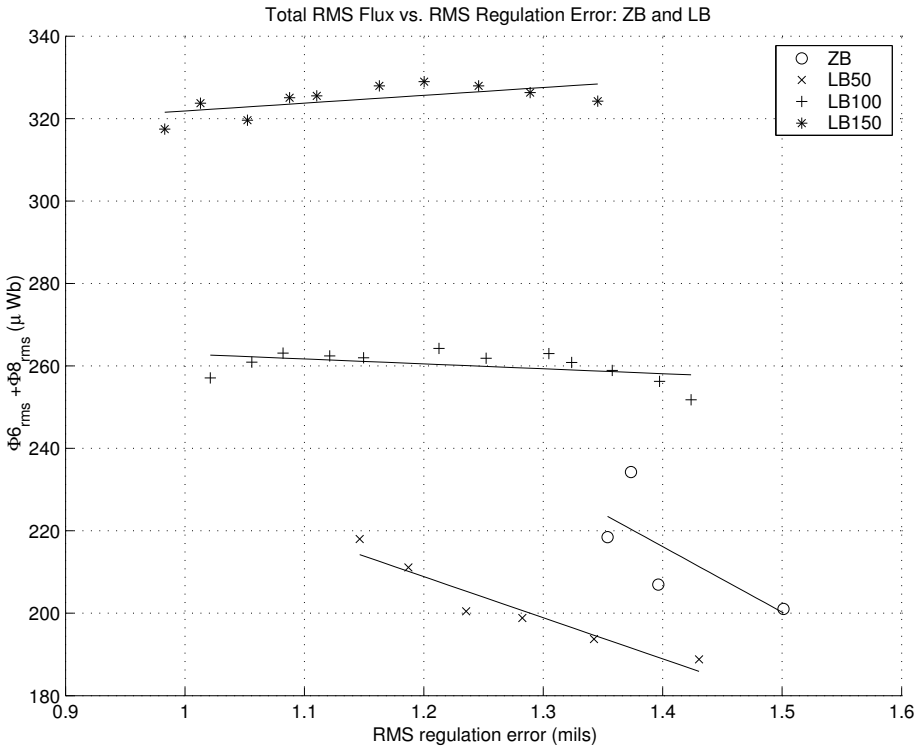

Figure 8.19: Clf Whirl Test $\Phi_0 = 50, 100, 150\mu$Wb: The total rms flux $\Phi_{6\text{rms}} + \Phi_{8\text{rms}}$ vs. rms regulation error e_{rms} for several flux bias values.

Figure 8.20 shows the total rms square flux $(\Phi_6^2)_{\text{rms}} + (\Phi_8^2)_{\text{rms}}$ vs. rms regulation error e_{rms}. The total rms square flux increases with increasing flux bias. Recall that the total rms square flux is proportional to the rms power dissipation due to eddy-current drag losses in the FWB application. Therefore, to operate with minimal losses, one must operate with the smallest flux bias possible.

Figure 8.21 illustrates the total rms power supplied to the bearing $(\Phi_{6\text{supp}})_{\text{rms}} + (\Phi_{8\text{supp}})_{\text{rms}}$ vs. the rms regulation error e_{rms} for several flux bias values. For any value of the flux bias, more power is required to regulate the rotor to a tighter position tolerance. Most interesting about these results is that zero bias takes the most rms power to implement. Furthermore, when regulating the rotor with a position tolerance less than $e_{\text{rms}} = 1.2$ mils, less power is required when implementing the 100μWb flux bias than the 50μWb flux bias. Similar observations may be made wherever the flux bias lines cross. The power savings can be traced to the increase in bearing stiffness

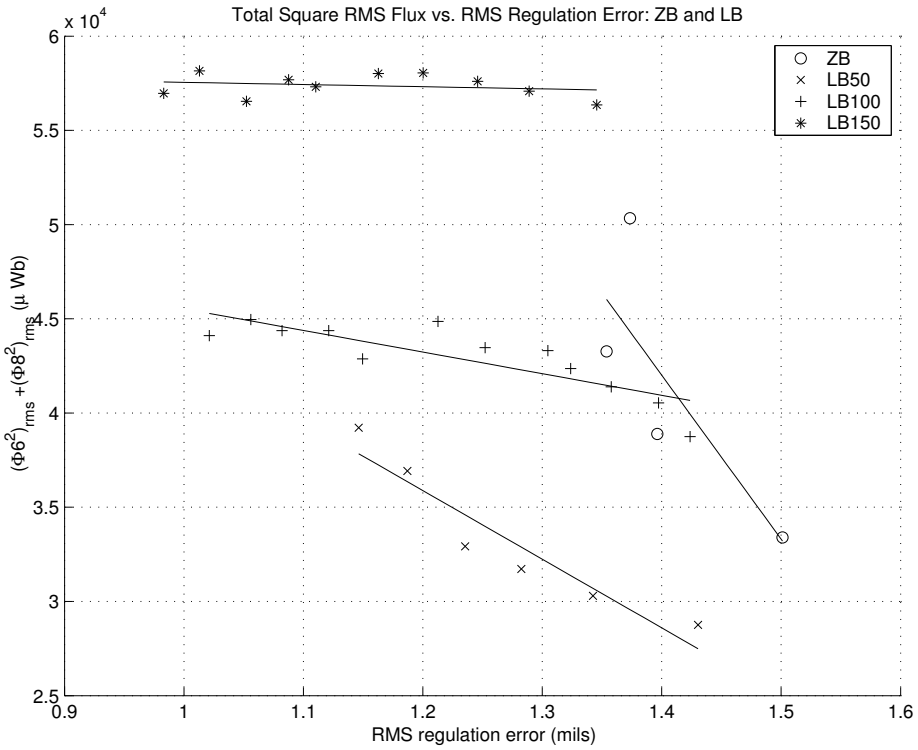

Figure 8.20: Clf Whirl Test $\Phi_0 = 50, 100, 150\mu$Wb: The total rms square flux $(\Phi_6^2)_{\rm rms} + (\Phi_8^2)_{\rm rms}$ vs. rms regulation error $e_{\rm rms}$ for several flux bias values.

as the flux bias increases. Note also that the magnitude of the slope $(P_{\rm supp})_{\rm rms}/e_{\rm rms}$ decreases as the flux bias increases.

Like the backstepping controller, the clf controller has the ability to track square and sawtooth reference signals for $\Phi_0 \geq 50\mu$Wb. These results are similar to those shown in Figure 8.12 and are omitted. Note, however, the clf controller has much better performance when regulating against the spin disturbance than the backstepping controller. Consider Figure 8.22. The rotor is regulated to $(x_t, y_t, x_b, y_b) = (4, 0, 0, 4)$ mils. A very large spin disturbance (rotor is spun by hand) is introduced at $t = 0.5s$. The spin disturbance is applied for $0.5 < t < 1.2$ seconds. Afterwards, the x_b axis position quickly recovers. One observes that the clf regulation performance in zero bias is much better than the backstepping performance with $\Phi_0 = 10\mu$Wb: compare Figure 8.22 to Figure 8.15.

The closed-loop magnitude frequency response of the clf controller is illustrated

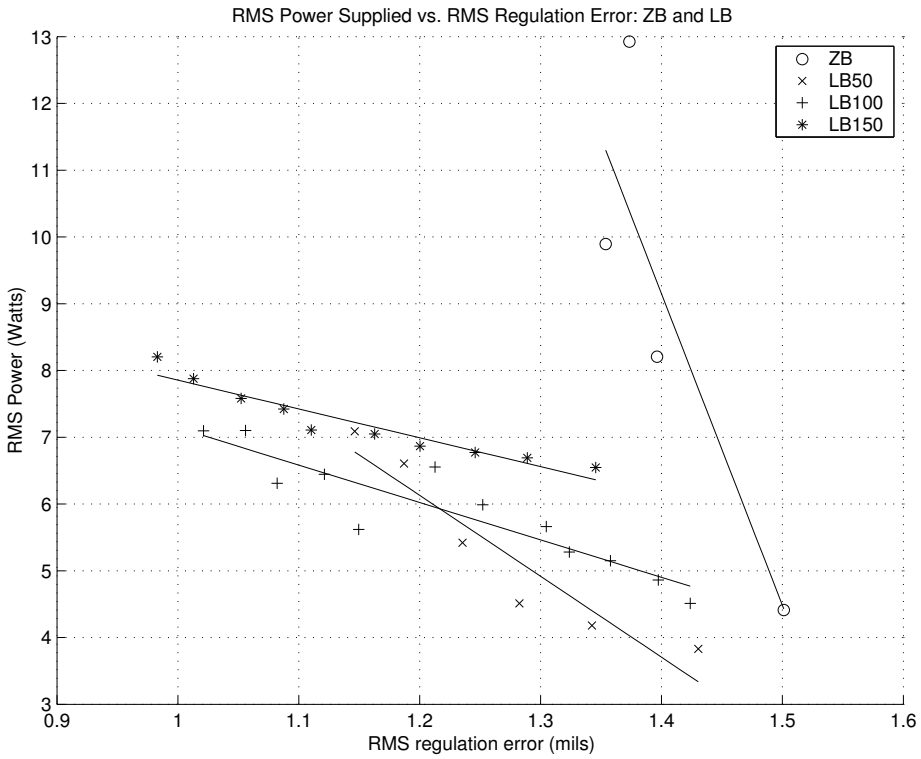

Figure 8.21: Clf Whirl Test $\Phi_0 = 50, 100, 150\mu$Wb: The total rms power supplied $(\Phi_{6\text{supp}})_{\text{rms}} + (\Phi_{8\text{supp}})_{\text{rms}}$ vs rms regulation error e_{rms} for several flux bias values.

in Figure 8.23 for several values of the flux bias. Note that the closed-loop controller bandwidth is on the order of $20 - 30Hz$ for each value of the bias.

Figure 8.24 illustrates the requested control voltages V_{r6} and V_{r8} during zero bias operation of the clf control law. Note that the control law may operate close to the singularity at $D_3 := \{x \in \mathbb{R}^3 |\ x_3 = u_0(z) = 0\}$, but rarely encounters it. Observe that the requested control voltages V_{r6} and V_{r8} often have peaks, however, the magnitude of these peaks are typically less than $10V$. The frequency spectra of V_{r6} and V_{r8} is also shown. The bandwidth of these signals is dramatically less than the bandwidth of the requested control signals generated by the backstepping controller: see Figure 8.16. Since the bandwidth is so small, the Copley 412 voltage-mode amplifiers are successful in making V_{app6} and V_{app8} track V_{r6} and V_{r8}, respectively. Practically the entire requested control voltage signal appears at the coil terminals.

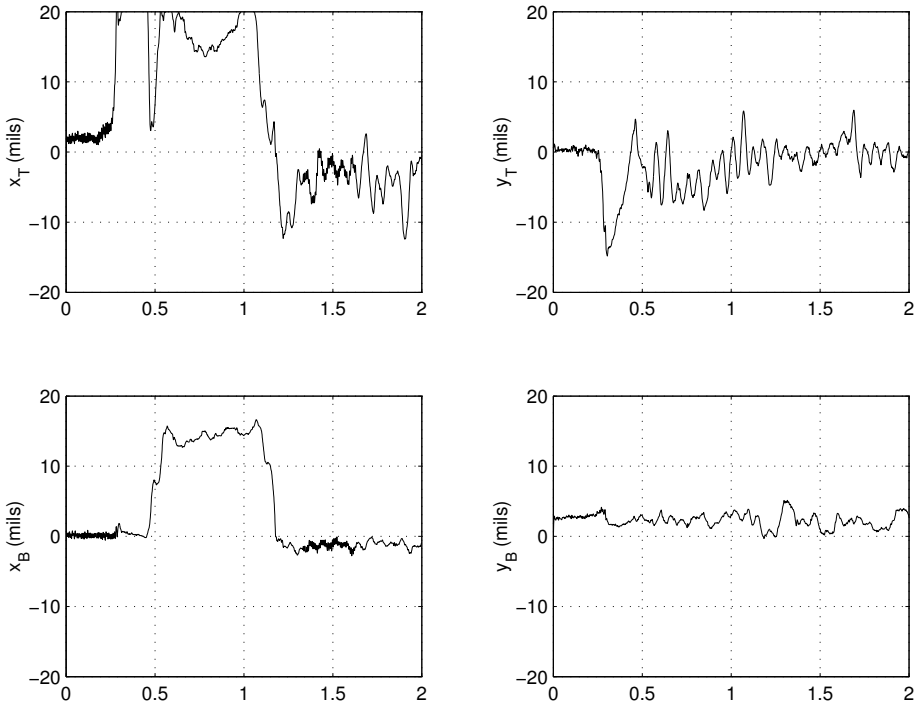

Figure 8.22: Clf spin regulation for $\Phi_0 = 0\mu$Wb: Rotor is regulated to $(x_t, y_t, x_b, y_b) = (4, 0, 0, 4)$ mils and spin disturbance introduced for $0.5 < t < 1.2sec$. Control Gains: $k_1 = 4$, $k_2 = 2$, $k_i = .2$, $\gamma = .5$, $\gamma_i = .1$. Each axis is successful at regulating against the spin disturbance.

8.5 Passivity Control Results

This section presents the experimental results for the passivity-based control law of proposition 6. The modifications to this control law so that it can regulate to any desired setpoint with zero steady-state error are very similar to the modifications presented in Section 8.2. Recall that for the passivity based control law, $u_0(x_1, x_2) := \sigma(x_1, x_2) := -k_1 x_1 - k_2 x_2$. The stabilizing function σ is replaced with equation (8.6). Also the $-\gamma\eta$ term in equation (4.47) of Proposition 6 is replaced by equation (8.4). The stability proof with these modifications is similar to that of Proposition 6.

Recall that the passivity-based control law is completely nonsingular. The performance of this controller is much better than that of the backstepping and clf controller in zero bias. During whirl testing, the rotor may be consistently regulated to a given

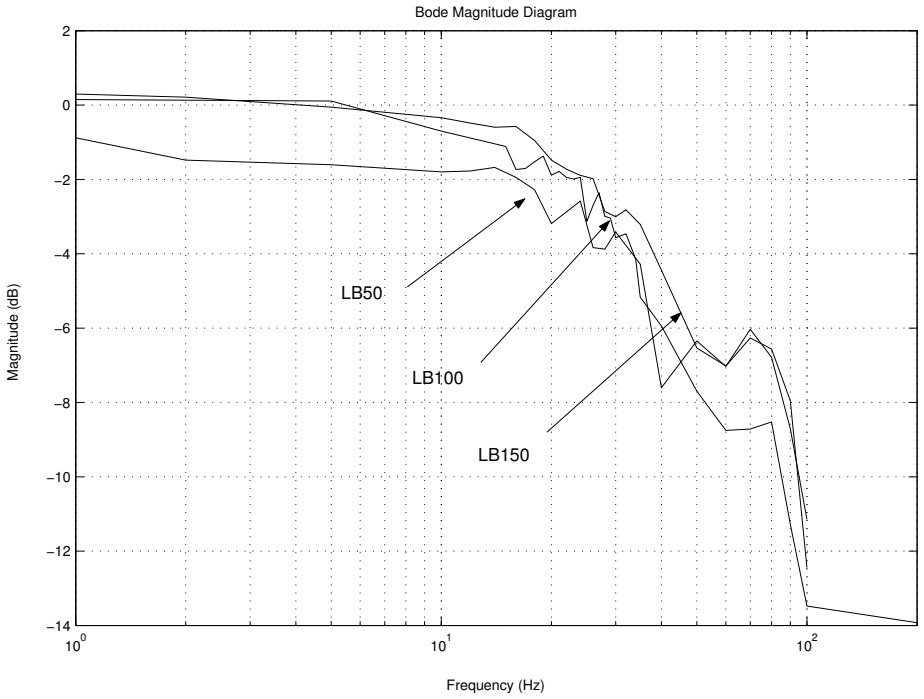

Figure 8.23: Clf magnitude frequency response for $\Phi_0 = 50, 100, 150$ μWb: $k_1 = 4$, $k_2 = 2$, $k_i = .2$, $\gamma = .5$, $\gamma_i = .1$. The bandwidth for each response is on the order of $20 - 30$Hz.

setpoint with any desired rms tracking error in the range of about $e_{\text{rms}} \in [0.9, 1.5]$ mils by proper selection of the k_1 gain. There is an upper limit to the proportional gain in experiment. When k_1 is too large, the controller seems to respond to the measurement noise and instability results. Figure 8.25 shows the linear dependence of e_{rms} on the proportional gain k_1. To regulate with given e_{rms}, the proportional gain k_1 decreases as the flux bias increases due to the increase in bearing stiffness. Note that the magnitude of the slope of e_{rms}/k_1 also increases with bias.

Figure 8.26 shows the linear dependence of the control flux ϕ_{rms} on the tracking error e_{rms}. More control effort is required to regulate the rotor with tighter position tolerance. Note that for a given e_{rms}, less control flux is required to regulate the rotor as the flux bias increases. This is due to the increase in actuator gain $\frac{df}{d\phi}$ and the resulting increase in bearing stiffness $\frac{df}{dx} = \frac{df}{d\phi}\frac{d\phi}{dx}$.

Figure 8.27 shows the total rms flux $\Phi_{6\text{rms}} + \Phi_{8\text{rms}}$ vs. rms regulation error e_{rms}.

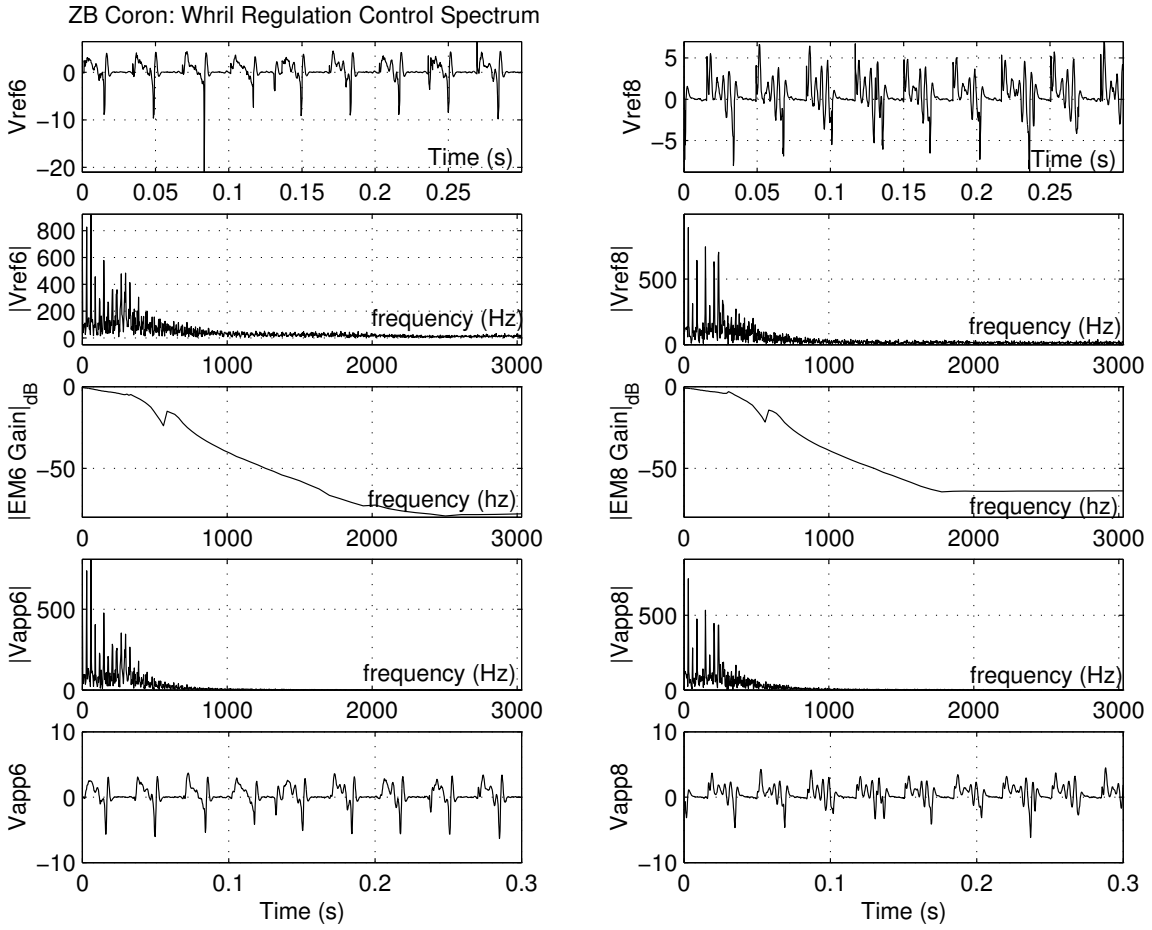

Figure 8.24: Clf Whirl Regulation Control Spectrum: $\Phi_0 = 0$. Requested control voltages V_{r6} and V_{r8} and their frequency spectra. The voltage mode amplifiers have bandwidth of about $200 - 300$Hz. The applied voltage V_{app6} and V_{app8} and their frequency spectra. Compare to Figure 8.16 and 8.34.

Since the total flux is the combination of the control flux and the flux bias in both electromagnets, one expects each curve in Figure 8.26 to be shifted up by $2\Phi_0$. For example, $\phi_{\text{rms}} = 105\mu$Wb for $e_{\text{rms}} = 1.5$ mils using $\Phi_0 = 50\mu$Wb. The total flux should be about $105\mu\text{Wb} + 2(50)\mu\text{Wb} = 205\mu$Wb. The resulting total flux found in Figure 8.27 for $e_{\text{rms}} = 1.5$ mils and $\Phi_0 = 50\mu$WB is 220μWb. Thus, the total rms flux in each electromagnet is about 57μWb larger than its rms control flux. Similar comparisons may be made for the other flux bias lines.

As presented in the clf data, the zero bias total flux line for the passivity data is also shifted in Figure 8.27 even though zero bias is implemented. The control

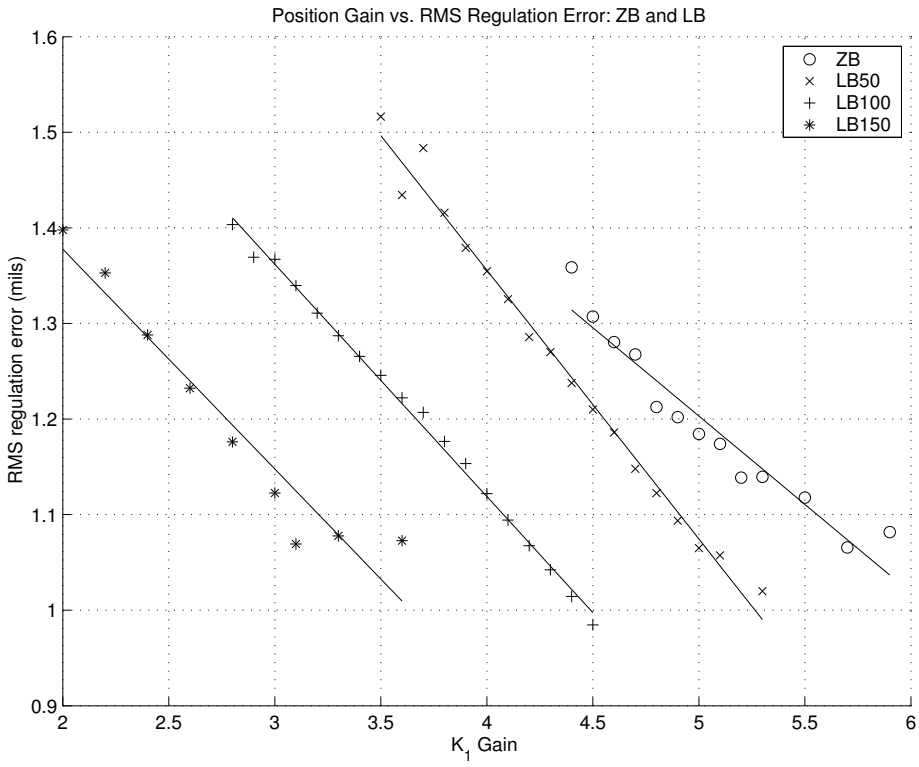

Figure 8.25: Passivity Whirl Test $\Phi_0 = 50, 100, 150\mu$Wb: Linear dependence of $e_{\rm rms}$ on proportional gain k_1. To regulate to a given $e_{\rm rms}$, the proportional gain k_1 decreases with increasing flux bias. This is due to the increase in bearing stiffness with increasing flux bias.

flux for $e_{\rm rms} = 1.3$ mils is $\phi_{\rm rms} = 135\mu$Wb. The total flux for $e_{\rm rms} = 1.3$ mils is $\Phi_{6\rm rms} + \Phi_{8\rm rms} = 185\mu$Wb. Thus, the total rms flux in each electromagnet is about 25μWb larger than expected. As explained in Section 8.4, this extra flux is due to the imperfect IR compensation. Note that the magnitude of the extra flux from the imperfect IR compensation in the clf and passivity-based control are about the same.

Figure 8.28 shows the total rms square flux $(\Phi_6^2)_{\rm rms} + (\Phi_8^2)_{\rm rms}$ vs. rms regulation error $e_{\rm rms}$. The total rms square flux increases with increasing flux bias. Since the total rms square flux is proportional to the rms power dissipation due to eddy-current drag losses in the FWB application, one must operate with the smallest flux bias possible to minimize losses.

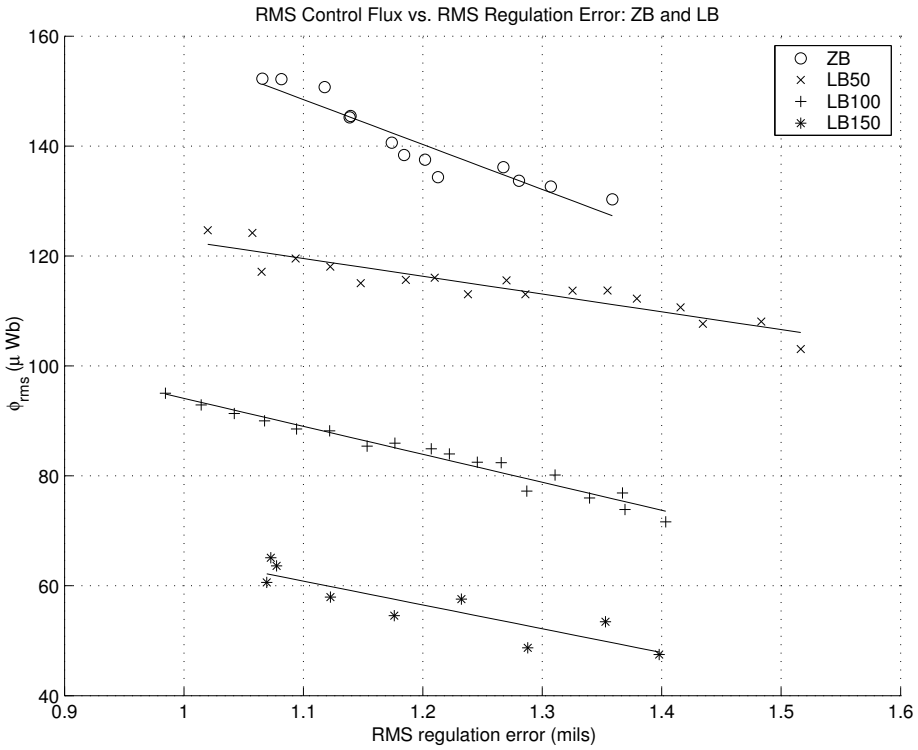

Figure 8.26: Passivity Whirl Test $\Phi_0 = 50, 100, 150\mu$Wb: Linear dependence of ϕ_{rms} on proportional gain e_{rms}. To regulate to a given e_{rms}, the required control flux ϕ_{rms} decreases with increasing flux bias. This is due to the increase in bearing stiffness with increasing flux bias.

Figure 8.29 illustrates the total rms power supplied to the bearing $(\Phi_{6\text{supp}})_{\text{rms}} + (\Phi_{8\text{supp}})_{\text{rms}}$ vs. the rms regulation error e_{rms} for several flux bias values. For any value of the flux bias, more power is required to regulate the rotor to a tighter position tolerance. Note that for $e_{\text{rms}} > 1.1$ mils, the zero bias controller requires the least amount of power to implement. This is in contrast to the clf controller which required the most amount of power to implement in zero bias: see Figure 8.21. As seen in the previous rms power analyses for the backstepping and clf controller, there are instances when the supplied power may be reduced by increasing the flux bias. Recall that as the flux bias increases, so does the bearing stiffness. Consequently, the power required to implement the control flux decreases. Observe that when lines corresponding to different flux biases cross, one should change the bias to save power. Note that for the data presented, it takes less power to implement the 100μWb flux

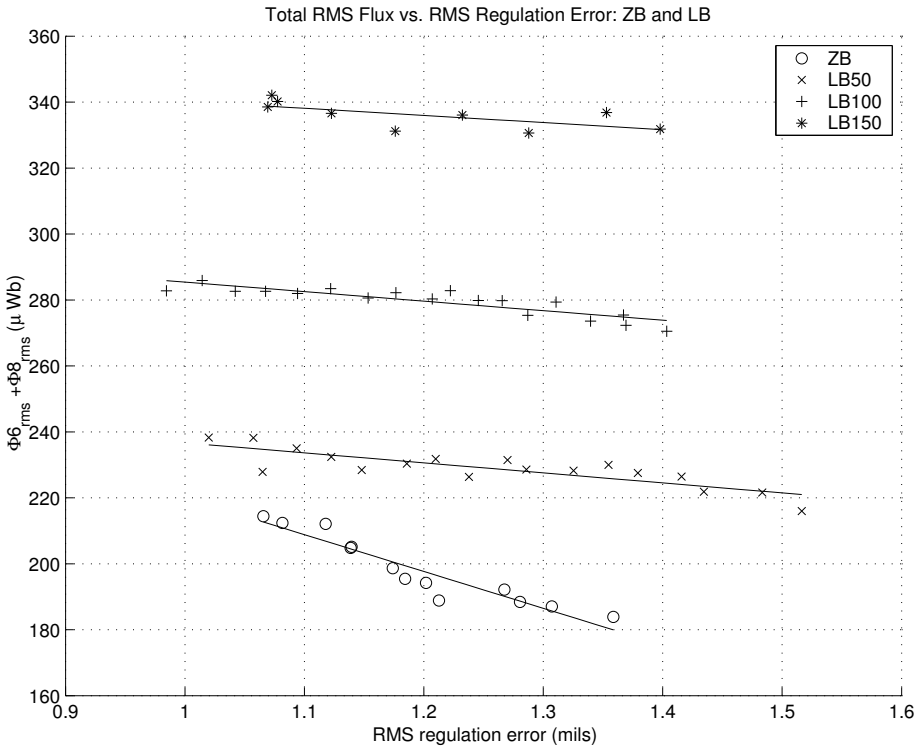

Figure 8.27: Passivity Whirl Test $\Phi_0 = 50, 100, 150\mu$Wb: The total rms flux $\Phi_{6\text{rms}} + \Phi_{8\text{rms}}$ vs. rms regulation error e_{rms} for several flux bias values.

bias than the 50μWb flux bias. However, from looking at the slopes of these two lines, the 50μWb line may require less power for some value of $e_{\text{rms}} < .9$ mils. Also, when $e_{\text{rms}} < 1.1$ mils, the 100μWb flux bias implementation requires less than the zero bias implementation.

Figure 8.30 shows the response of the passivity based controller to a 1 mil square wave reference. The damping of step response increases as the bias increases. In zero bias, the rotor is regulated to $(x_t, y_t, x_b, y_b) = (2, 0, 1.5, 1)$. The controller gains are $k_1 = 3$, $k_2 = 0.5$, $\gamma = 0.5$, $\gamma_i = 0.1$, $k_i = 0.3$. For $k_0 = .68$, the step response on the x_b axis is highly under-damped, but rises from 0.5 mil to 2.5 mil as desired. As expected, the x and y axes are decoupled, but the x_b axis presents a disturbance to the x_t axis. The data for $\Phi_0 = 150\mu$Wb has been shifted down by 7 mils for easy viewing. In this case, the rotor is regulated to $(x_t, y_t, x_b, y_b) = (4, 0, 4, 1)$ and the step response for $k_0 = 0.9$ on the x_b control axis is over-damped and has zero steady-state

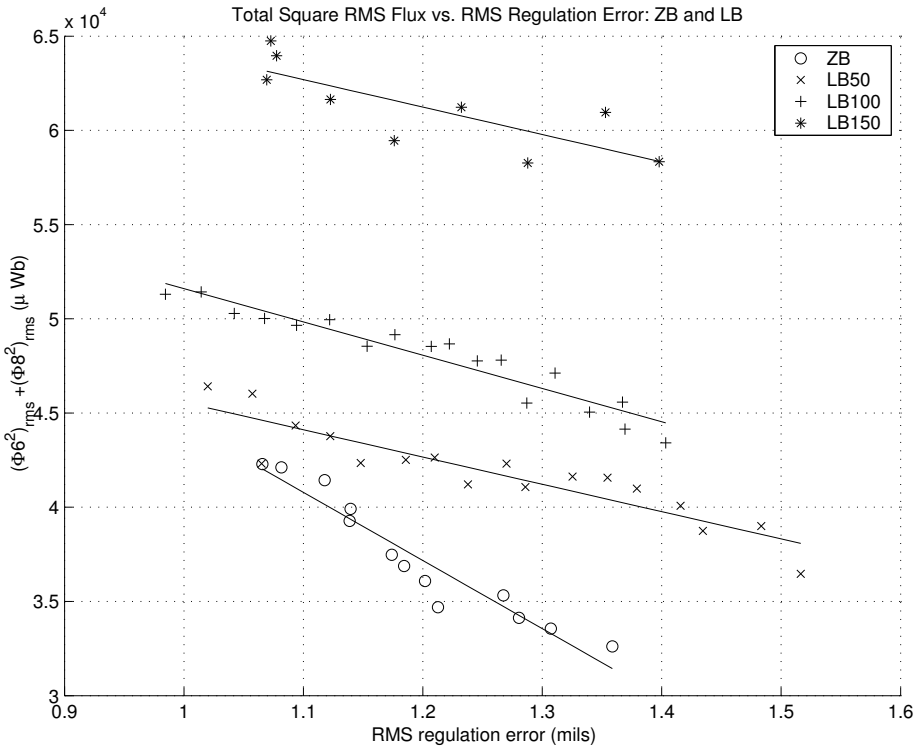

Figure 8.28: Passivity Whirl Test $\Phi_0 = 50, 100, 150\mu$Wb: The total rms square flux $(\Phi_6^2)_{\rm rms} + (\Phi_8^2)_{\rm rms}$ vs. rms regulation error $e_{\rm rms}$ for several flux bias values.

error.

Figures 8.31 and 8.32 illustrate the passivity-based controller's ability to regulate the rotor against disturbances. Specifically, figure 8.31 shows the rotor being regulated to $(x_t, y_t, x_b, y_b) = (6, 0, -3, 0)$ while the rotor is spinning and Figure 8.32 shows the rejection of a large impulse disturbance for $\Phi_0 = 150\mu$Wb. In both situations, the controller is able to keep the rotor stable.

The closed-loop magnitude frequency response of the passivity controller is illustrated in Figure 8.33 for $\Phi_0 = 0$ and $\Phi_0 = 150\mu$Wb. Note that the closed-loop controller bandwidth is on the order of $20 - 30$Hz for each value of the bias.

Figure 8.34 illustrates the requested control voltages $V_{\rm r6}$ and $V_{\rm r8}$ during zero bias operation of the passivity control law. Contrary to the clf and backstepping controllers, the passivity-based control law is completely nonsingular. Observe that the requested control voltages $V_{\rm r6}$ and $V_{\rm r8}$ are less than $10V$. The bandwidth of these

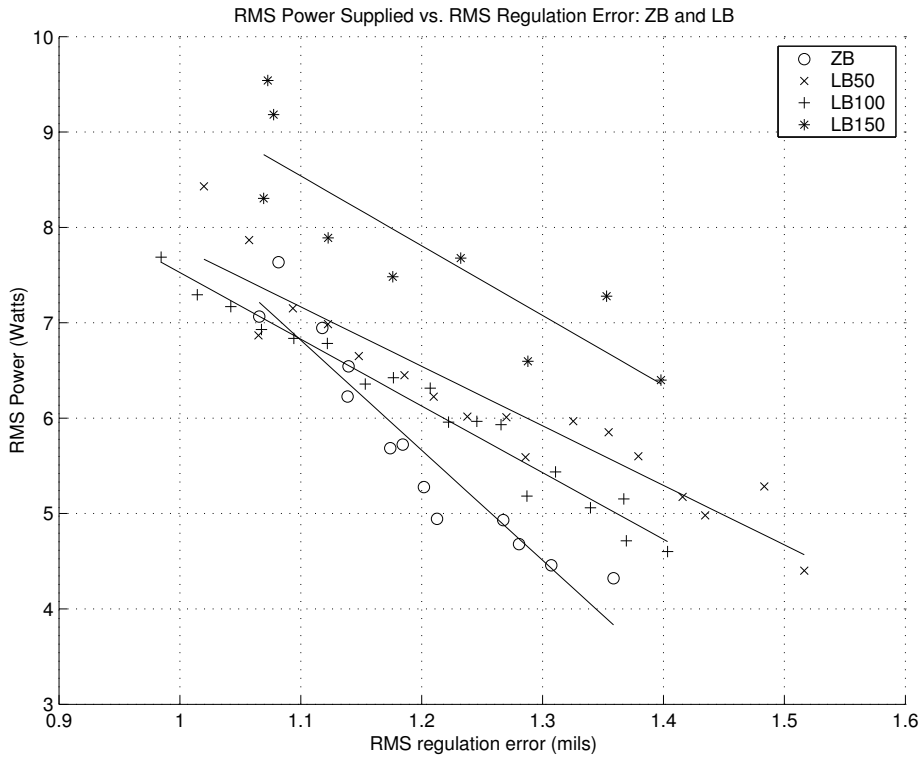

Figure 8.29: Passivity Whirl Test $\Phi_0 = 50, 100, 150\mu$Wb: The total rms power supplied $(\Phi_{6\text{supp}})_{\text{rms}} + (\Phi_{8\text{supp}})_{\text{rms}}$ vs rms regulation error e_{rms} for several flux bias values.

signals is dramatically less than the bandwidth of the requested control signals generated by the backstepping controller and the clf controller: compare to Figures 8.16 and 8.24. Since the bandwidth is so small, the Copley 412 voltage-mode amplifiers are successful in making V_{app6} and V_{app8} track V_{r6} and V_{r8}, respectively. The entire requested control voltage signal appears at the coil terminals.

8.6 Linear Control Results

Each axis, except for the x_b control axis, employs a linear controller using the normal biasing scheme and amplifiers acting in current mode with a current bias in the range of $1.5 - 3.0$ A. The Lead+PI controllers are implemented with the feedback structure shown in Figure 7.3. In all of the results to be presented below, the integral gain is $k_i = 0.3$, the lead zero position is $z = 150$, and the lead pole position is

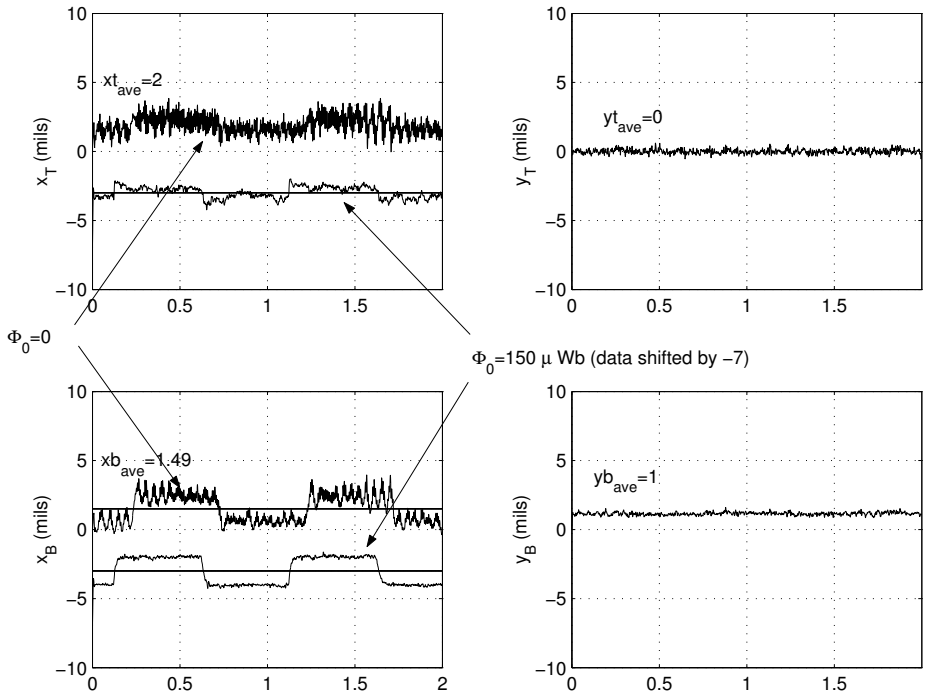

Figure 8.30: Passivity Step Responses for $\Phi_0 = 0, 150\mu$Wb, $k_1 = 3$, $k_2 = 0.5$, $\gamma = 0.5$, $\gamma_i = 0.1$, $k_i = 0.3$: Zero bias results in a highly under-damped step response ($k_0 = .68$). When $\Phi_0 = 150\mu$Wb, the step response is over-damped ($k_0 = .9$).

$\gamma z = 1500$. The controller is illustrated in several situations for various values of k_p. Step responses and frequency response data are used to illustrate the controller behavior. Also, the data illustrates the coupling between the axes and the differences between the inertia of the top and bottom of the rotor. Whirl tests are also conducted for several values of the bias current.

Note that the region of attraction of the AMB using linear control depends on the value of the current bias and this region does not cover the entire operating space. Stated differently, the rotor is only locally asymptotically stable on the linear control axes. (Note that the nonlinear control axis x_b is globally asymptotically stable.) Also, integrator windup can be problematic. For the above reasons, the following steps are taken when initiating the linear controllers. First, the integral gains are initially set to zero and the current bias is turned on. The rotor is pulled towards the closest electromagnet and comes in contact with the catcher bearings at some point. After

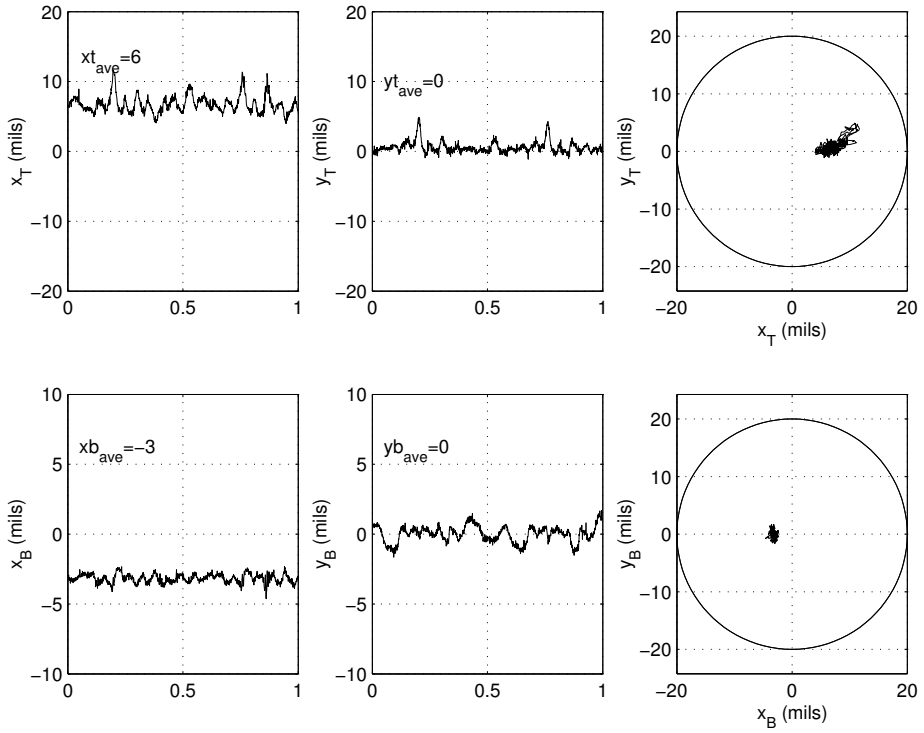

Figure 8.31: Passivity Based Controller for $\Phi_0 = 0$: Regulation of the rotor to a setpoint while the rotor is spinning.

the control is enabled, the linear controller is assisted by giving a slight tap of the hand on the rotor. The rotor is then "caught" by the controllers and held away from the catcher bearings by the lead controller. Tracking to a desired setpoint occurs when the integral gains are turned on.

Note that when using a current bias smaller than about 3 A, the rotor may have difficulty being "caught". To conduct whirl tests with a smaller bias, the rotor is first stabilized with the 3 A bias. The bias is then reduced after the tracking transient.

Since the amplifiers work in current mode, a flux-current-position map similar to the ones constructed in Chapter 6 are used off-line to convert the current and position measurements into flux measurements. This enables comparisons with the nonlinear controllers of the previous sections. Figure 8.35 shows the lookup table for coil 5. The lookup table for coil 7 is similar.

Whirl tests for the linear controller were conducted using a current bias of $I_0 =$

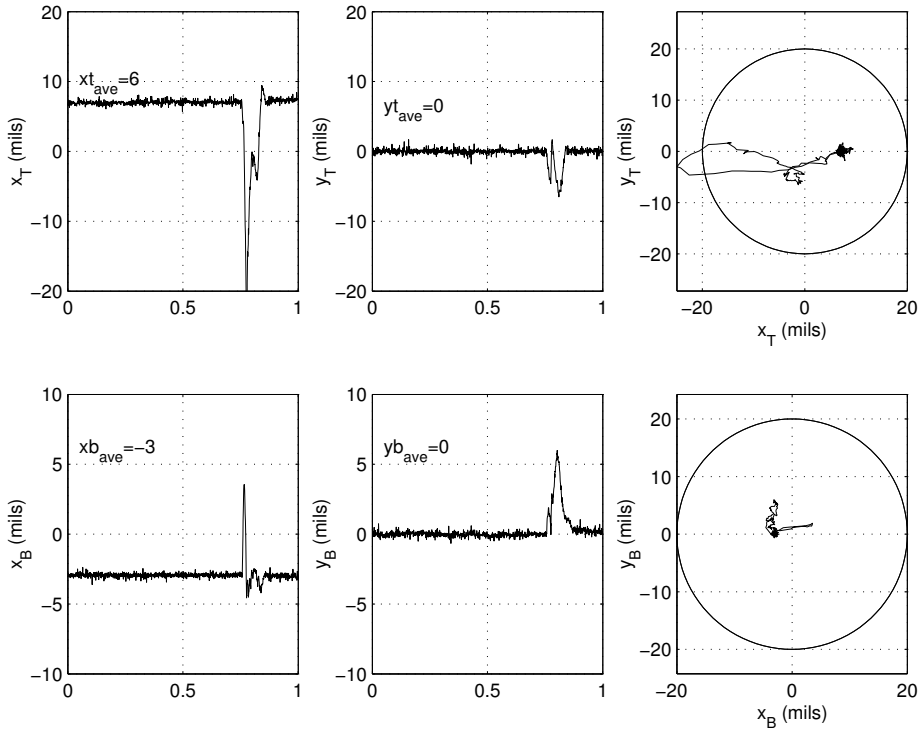

Figure 8.32: Passivity Based Controller for $\Phi_0 = 150\mu$Wb: Rejection of an impulse disturbance while regulating the rotor to $(x_t, y_t, x_b, y_b) = (6, 0, -3, 0)$.

$1.5, 2.0, 2.5$ A. Using Figure 8.35, the flux bias corresponding to the current bias is shown in Table 8.6. Since the inductance changes with position, a current bias produces a range of flux biases depending on the position.

Table 8.1: Correspondence of current and flux bias for linear control.

I_0	**minimum** Φ_0	**maximum** Φ_0
$1.5A$	118μWb	135μWb
$2.0A$	148μWb	168μWb
$2.5A$	172μWb	192μWb

Figure 8.36 shows the linear dependence of rms regulation error e_{rms} on the loop-gain k_p. As expected, the regulation error decreases with increasing loop-gain. Furthermore, the value of k_p required to regulate to a given e_{rms} increases as the current bias increases. This is consistent with the linear control analysis of Section 7.3. Recall that the open-loop pole positions of the linearized SISO AMB with normal biasing

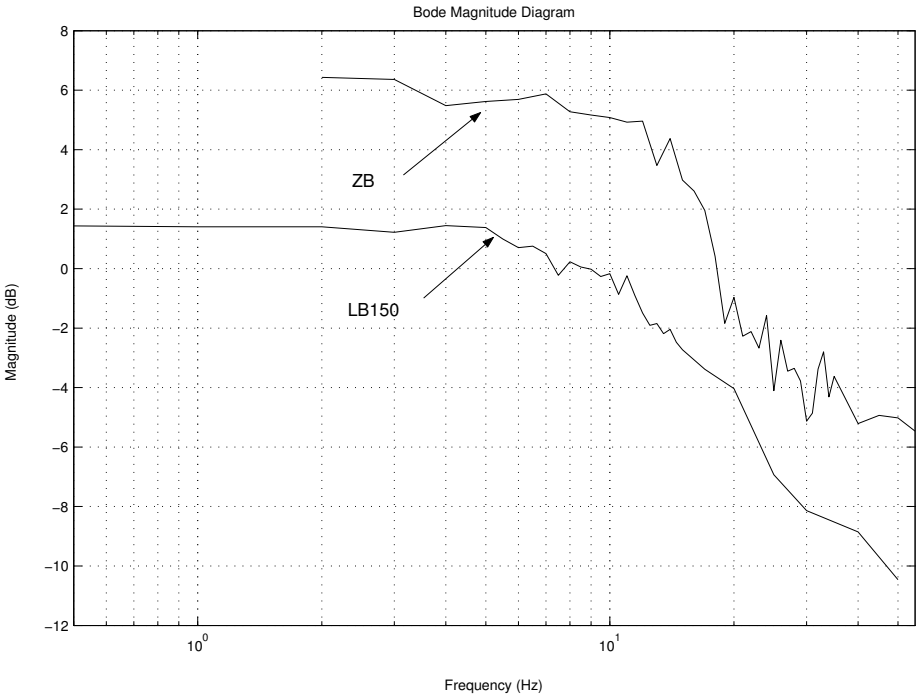

Figure 8.33: Passivity magnitude frequency response for $\Phi_0 = 0, 150$ μWb: $k_1 = 4$, $k_2 = 2$, $k_i = .2$, $\gamma = .5$, $\gamma_i = .1, k_0 = 1$. The bandwidth for each response is on the order of $20 - 30$Hz.

depend directly on the current bias: see Section 7.2.1. The poles are real and symmetric about the $j\omega$ axis and their values increase with bias. When adding the lead controller, increasing the value of k_p moves the open-loop pole in the right half plane along the root locus into the left half plane: see Figure 7.2. Therefore, to achieve the same performance (equivalent to closed loop pole location), a larger loop-gain is required when the current bias increases because the open-loop pole locations are larger.

Figure 8.37 shows the linear dependence of rms control flux ϕ_{rms} on the rms regulation error e_{rms}. As expected, more control effort is required to regulate the rotor with a tighter position tolerance. To regulate the rotor to a given e_{rms}, less control flux is required as the bias current increases. This can be interpreted as an increase in the bearing stiffness.

Figure 8.38 shows the total rms flux $\Phi_{5\text{rms}} + \Phi_{7\text{rms}}$ vs. the regulation error e_{rms}.

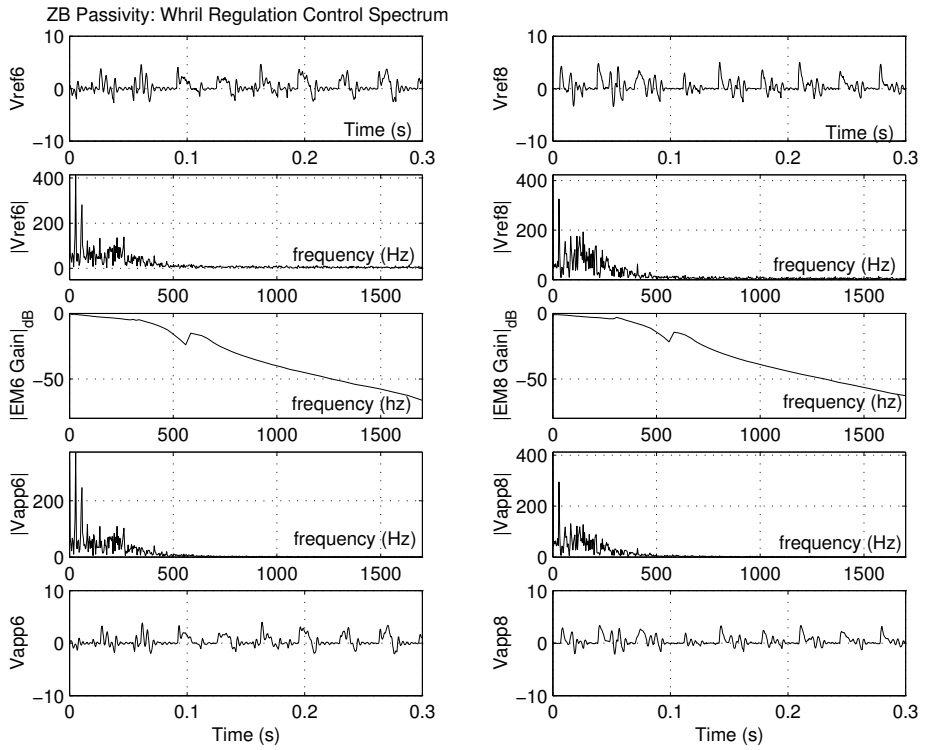

Figure 8.34: Passivity Whirl Regulation Control Spectrum: $\Phi_0 = 0$. Requested control voltages $V_{\rm r6}$ and $V_{\rm r8}$ and their frequency spectra. The voltage mode amplifiers have bandwidth of about $200 - 300$Hz. The applied voltage $V_{\rm app6}$ and $V_{\rm app8}$ and their frequency spectra. Compare to Figure 8.16 and 8.24.

Since the control flux in the normal biasing scheme is perturbed symmetrically, the total flux is independent of the regulation error. Recall that under normal biasing scheme, $\Phi_5 + \Phi_7 = 2\Phi_0$. Thus, the total flux value shown in Figure 8.38 divided by two corresponds to the flux bias. Indeed, for $I_0 = 1.5$ A, $255/2 = 127.5\mu$Wb is within the range of flux biases recorded in Table 8.6. Similarly, the measured flux bias for $I_0 = 2.0$ A and $I_0 = 2.5$ A are 160μWb and 182μWb, respectively. These are also in the range predicted by Table 8.6.

The total rms square flux $(\Phi_5^2)_{\rm rms} + (\Phi_7^2)_{\rm rms}$ is shown in Figure 8.39. The total rms square flux increases with increasing flux bias. Since the total rms square flux is proportional to the rms power dissipation due to eddy-current drag losses in the FWB application, one must operate with the smallest flux bias possible to minimize losses. However, recall that the normal biasing scheme becomes uncontrollable as the

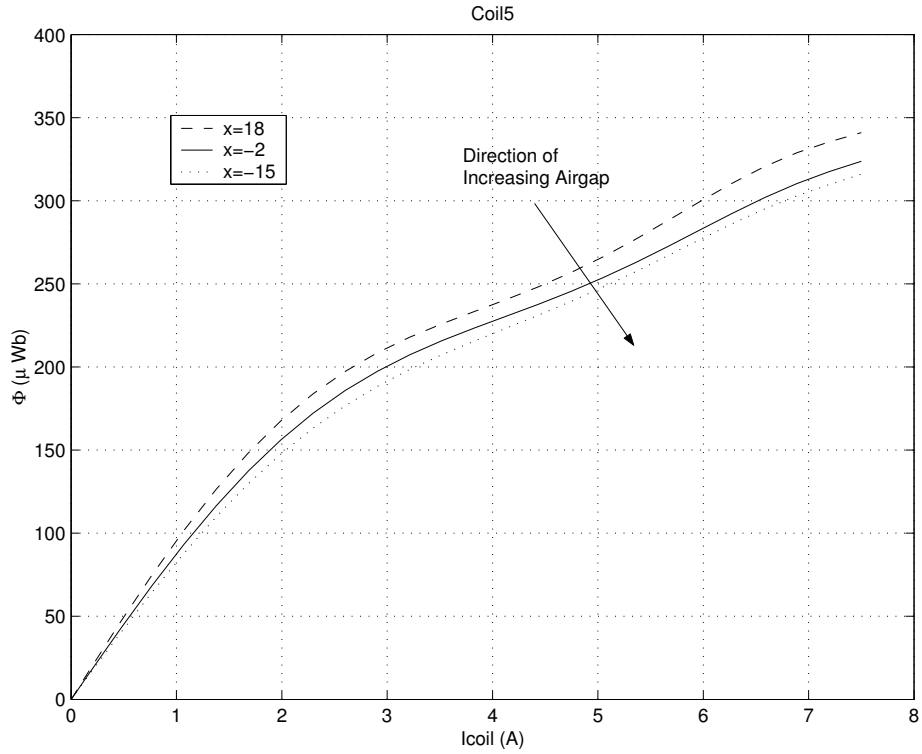

Figure 8.35: The flux-current-position lookup table for electromagnet 5. The data for electromagnet 7 is similar.

flux bias reduces to zero.

Figure 8.40 shows the total rms power supplied $(\Phi_{5\text{supp}})_{\text{rms}} + (\Phi_{7\text{supp}})_{\text{rms}}$ vs. the rms regulation error e_{rms} for several values of current bias. As expected, the more power is required to regulate the rotor to a tighter position tolerance. Contrary to the power curves of the nonlinear controllers using the gcfc condition, the total rms power curves for the linear controller using normal biasing are parallel. Thus, there are no instances when an increase of the current bias results in a reduction in power.

The next few figures illustrate the step responses of the system. Figure 8.41 illustrates the regulation of the rotor position to $(x_t, y_t, x_b, y_b) = (4, 0, 0, 0)$ mils. A 1 mil step reference is injected into y_b control axis. For the loop gain set to $k_p = 5$, the system responds with zero steady-state error, minimal overshoot and a rise time of about $T_r = 0.02$ s. The feed-forward gain is set to $K_0 = 0.88$. Note that the x axis is

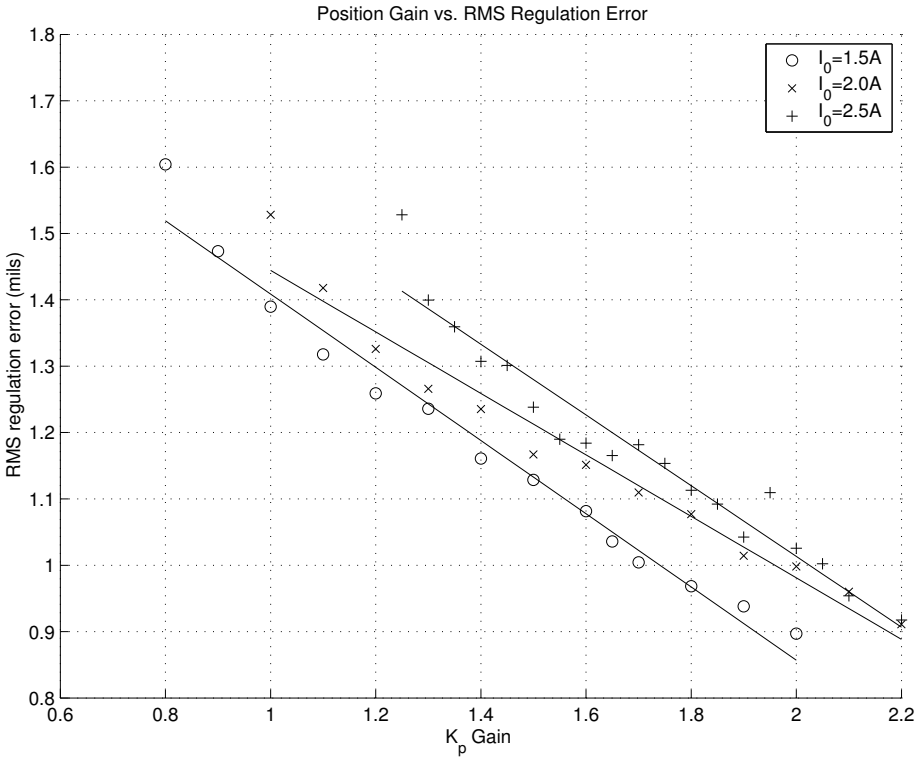

Figure 8.36: Linear Whirl Test for $I_0 = 1.5, 2.0, 2.5$ A: Linear dependence of rms regulation error e_{rms} on the loop-gain k_p.

decoupled from the y axis and step response on the y_b axis presents about a 0.5 mil square wave disturbance on the y_t axis.

For comparison, Figure 8.42 shows the regulation of the rotor to $(x_t, y_t, x_b, y_b) = (4, 0, 0, 0)$ mils, however, a 1 mil step response is superimposed on the y_t control axis. With the loop-gain set to $k_p = 2.5$, the system has zero steady-state error and a rise time of $T_s = 0.02$ s. The feed-forward gain is $k_0 = .75$. Observe that the y_t step response introduces about a 0.1 mil square wave disturbance into the y_b control axis.

The magnitude of the disturbance seen in Figure 8.41 due to the 1 mil square wave tracking is much larger than the magnitude of the disturbance seen in Figure 8.42. This can be explained by the fact that the rotor is "bottom-heavy" and the translational inertia of the bottom of the rotor is heaver than the translational inertia of the top of the rotor.

Figure 8.43 shows the closed-loop magnitude frequency responses of the y_b control

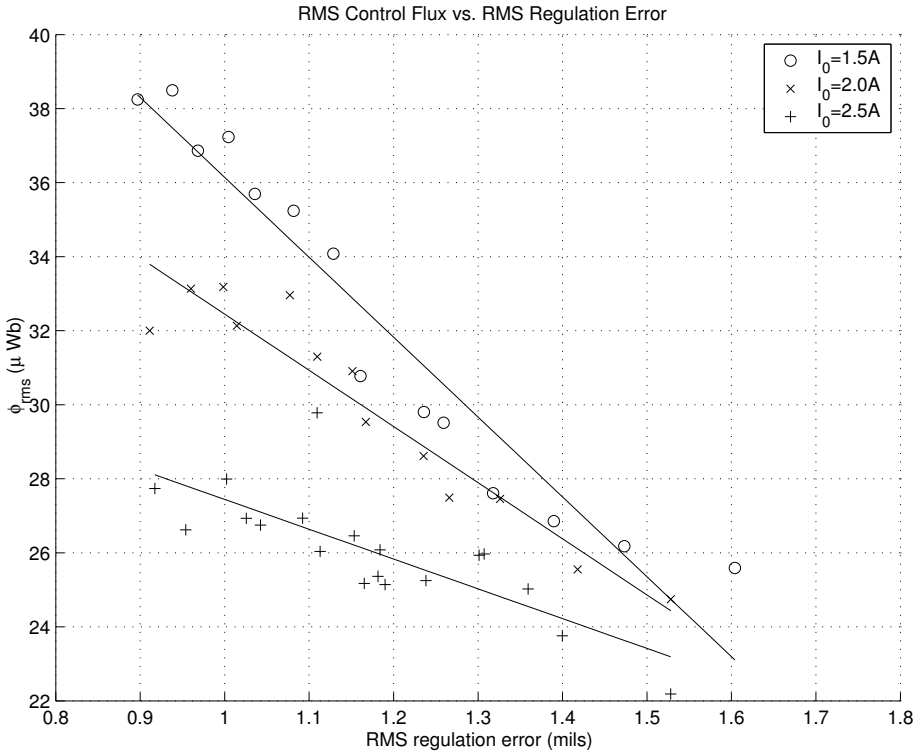

Figure 8.37: Linear Whirl Test for $I_0 = 1.5, 2.0, 2.5$ A: Linear dependence of rms flux $\phi_{\rm rms}$ on the rms regulation error $e_{\rm rms}$.

axis for loop-gains $k_p = 2, 5$. For $k_p = 5$ and $k_p = 2$, the bandwidth is about 40Hz and 10Hz, respectively. For $k_p = 2$, the bandwidth is a little harder to define due to the large hump in the frequency response.

Figure 8.44 shows the closed-loop magnitude frequency responses of the y_t control axis for loop-gains $k_p = 1, 1.5, 2.5$. For $k_p = 2.5$ and $k_p = 1.5$, the bandwidth is about 55Hz and 40 Hz, respectively. For $k_p = 1$, the bandwidth is a little harder to define due to the large hump in the frequency response. However, the overall trend is that the bandwidth increases with loop-gain. Note that the bandwidth in the y_t control axis tends to be larger than the bandwidth in the y_b control axis. Again, this can be traced to the "bottom-heaviness" of the rotor.

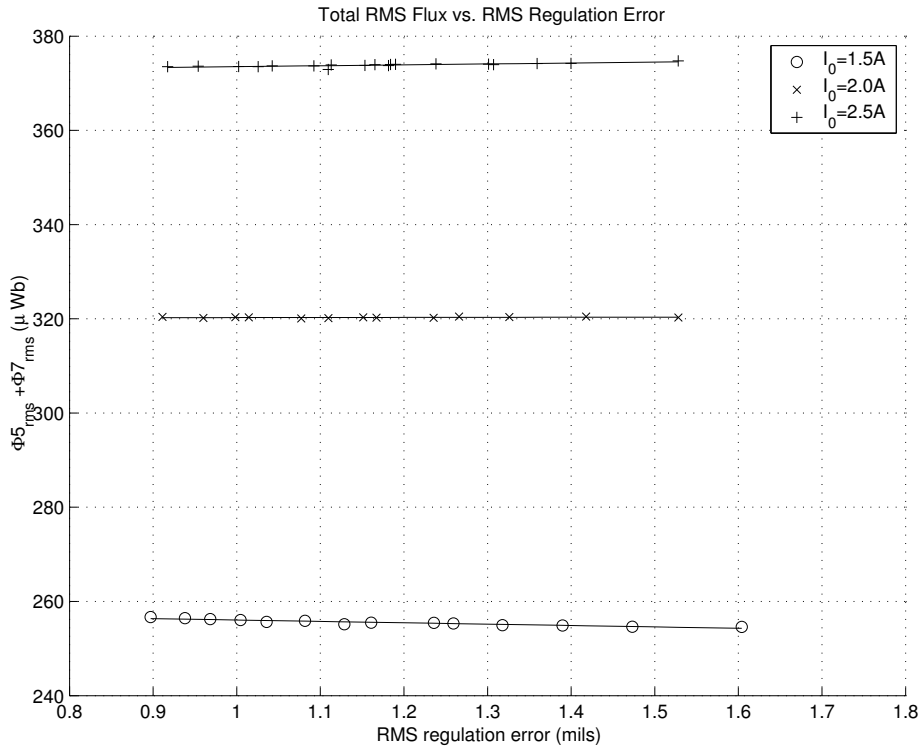

Figure 8.38: Linear Whirl Test for $I_0 = 1.5, 2.0, 2.5$ A: The total rms flux $\Phi_{5\text{rms}} + \Phi_{7\text{rms}}$ vs. the rms regulation error e_{rms}. Since the normal bias scheme is used, the total flux is always constant: $\Phi_5 + \Phi_7 = 2\Phi_0$.

8.7 CFS vs. GCFC: Total RMS Square Flux Comparison

Section 2.2.2 and, in particular, Table 2.1 claim that the losses in the AMB FWB application are minimized if the total square flux required for regulation is minimized. It is desirable to know which bias scheme, the cfs or the gcfc, is more efficient in producing the required flux for rotor regulation and under what conditions this is true. Section 3.3 performs a static force analysis to address this question. That is, a constant force is produced from both bearings F_n and F_g, and a comparison between the gcfc and cfs schemes is considered "fair" when $F_n = F_g$: see Section 3.3 for details. Since the gcfc condition is intended to be used in low-bias mode (and sometimes zero-bias mode), it is likely that the flux bias used in the cfs scheme will be greater than that of the gcfc scheme. As defined in Section 3.3, $\alpha = \Phi_{0n}/\Phi_{0g}$

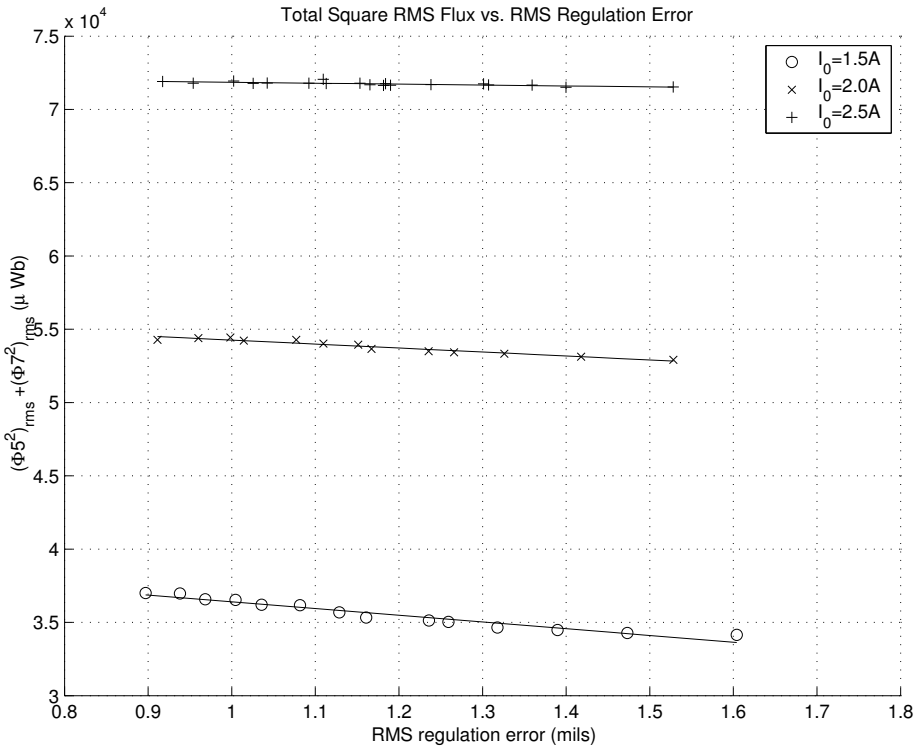

Figure 8.39: Linear Whirl Test for $I_0 = 1.5, 2.0, 2.5$ A: The total rms square flux $(\Phi_5^2)_{\rm rms} + (\Phi_7^2)_{\rm rms}$ vs. the rms regulation error $e_{\rm rms}$.

is used to parameterize the comparison by measuring the ratio of the flux biases. Furthermore, since it is likely that the flux bias will be small in the gcfc scheme, the parameter $\beta = \phi_g/\Phi_{0g}$ is used to measure the size of the control flux in relation to the size of the bias. It is anticipated that the gcfc mode in low-bias will operate with $\alpha > 1$ and $\beta > 1$. Figure 3.3 predicts that as α and β increase, or equivalently, as the flux bias Φ_{0g} decreases, that the ratio T_n/T_g becomes greater than unity. This means that the gcfc scheme is more efficient in producing the required flux for operation than the cfs scheme as the flux bias Φ_{0g} is reduced.

The above analysis is might be considered somewhat artificial because it only considers how much flux is required to produce a desired force at a given time and does not consider the dynamics of the system. To have a more realistic comparison, the total rms square flux required to regulate the rotor during whirl testing using the constant flux sum (cfs) bias scheme is compared to that of the gcfc bias scheme. In this

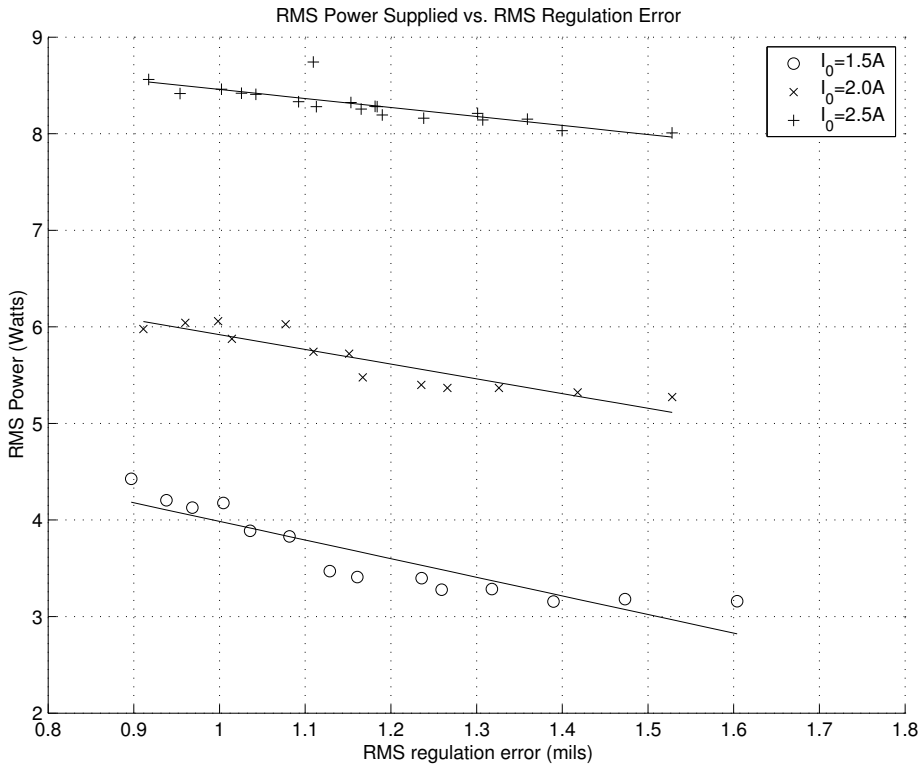

Figure 8.40: Linear Whirl Test for $I_0 = 1.5, 2.0, 2.5$ A: The total rms power supplied $(\Phi_{5\text{supp}})_{\text{rms}} + (\Phi_{7\text{supp}})_{\text{rms}}$ vs. the rms regulation error e_{rms}.

chapter, comparisons are made between the different controllers under whirl testing conditions. Since the disturbance is roughly periodic, the force required to regulate the rotor is also roughly periodic. The magnitude of the periodic force compensation signal produced by the actuator determines the amplitude of the roughly periodic regulation error e. Thus, a measure of the "size" of the regulation error is also a measure of the actuator force. The rms measure for size of a signal is convenient because it averages out the time dependence of the signal and it is easy to calculate for the system operating under the steady-state whirl conditions. The comparisons made between controllers are considered "fair" if the they have the same rms regulation error e_{rms}. Thus, the constraint $F_n = F_g$ used in the static analysis is roughly equivalent to different control laws sharing the same e_{rms}.

Since the passivity-based control law has the best performance of the nonlinear

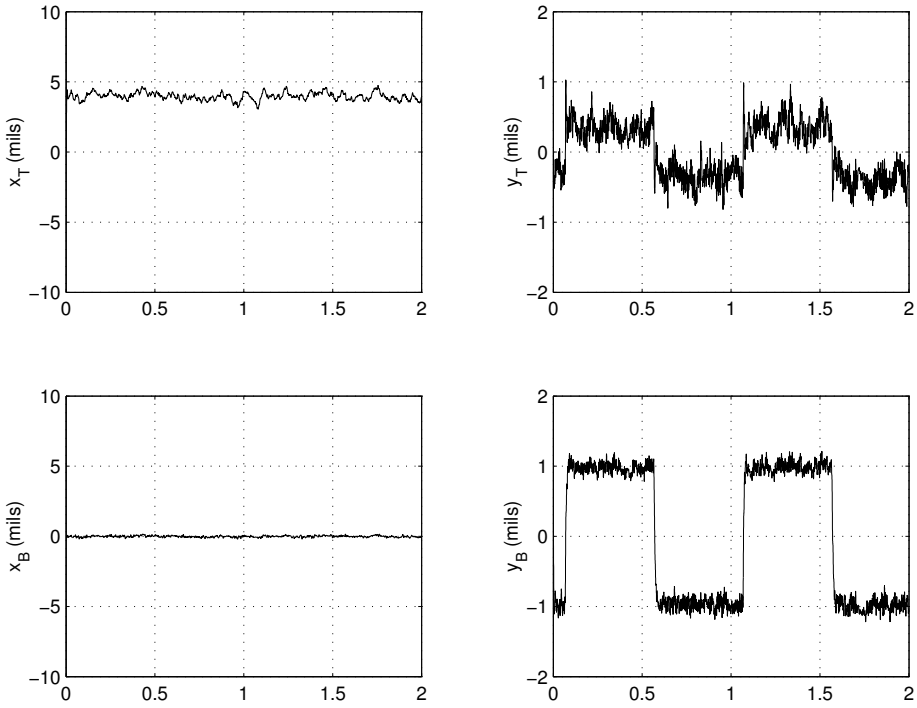

Figure 8.41: Rotor regulated to $(x_t, y_t, x_b, y_b) = (4, 0, 0, 0)$ mils. A 1 mil step response is superimposed on the y_b control axis with $k_p = 5$, $k_i = 0.3$, $k_0 = 0.88$.

controllers (which use the gcfc bias scheme) studied, its results will be compared to those of the linear control which uses the cfs scheme. The parameter $\alpha = \Phi_{0n}/\Phi_{0g}$ has the same interpretation in this comparison as it does in the static analysis. The parameter β in this comparison is defined using the rms control flux $\beta_{\rm rms} = \phi_{\rm rms}/\Phi_{0g}$. However, the range of achievable $\beta_{\rm rms}$ in experiment is limited by the dynamics of the system. One can not vary $\beta_{\rm rms}$ continuously as in the static analysis. Figure 8.26 shows the dependence of $\phi_{\rm rms}$, and hence $\beta_{\rm rms}$, on $e_{\rm rms}$. Furthermore, the increase in bearing stiffness as Φ_0 is increased means that the $\phi_{\rm rms}$ (and $\beta_{\rm rms}$) required to achieve a desired force is smaller with increasing bias. In addition, Figure 8.25 illustrates the relationship between the regulation error $e_{\rm rms}$ and the proportional gain k_1. Recall that in experiment, the k_1 gain is selected to produce a particular $e_{\rm rms}$. It is found in experiment that the controller starts responding to measurement noise and instability results when k_1 is too large. Of course, k_1 can not be set to zero and the performance

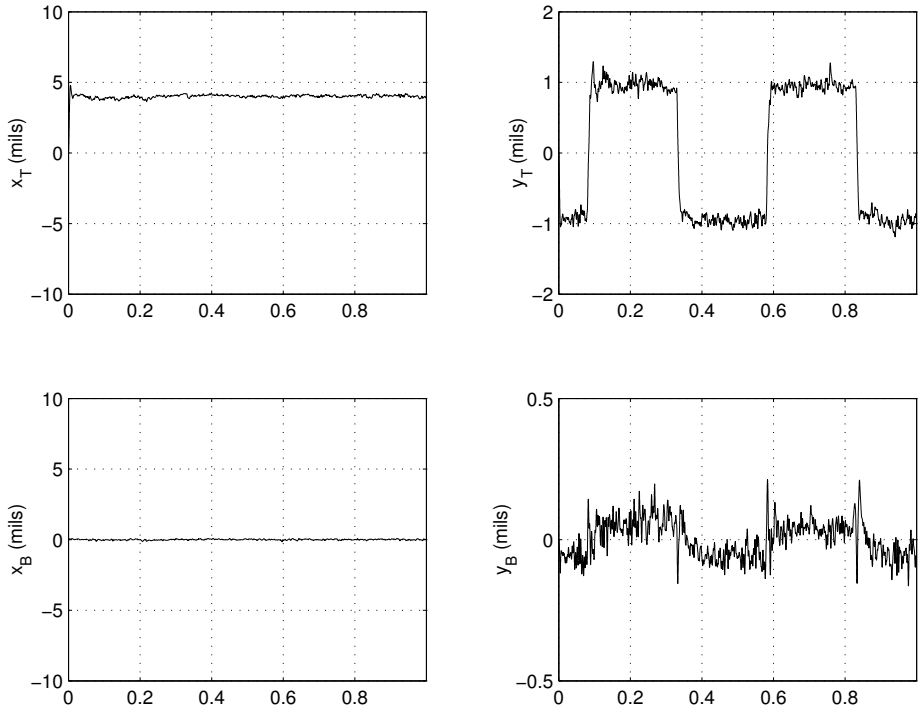

Figure 8.42: Rotor regulated to $(x_t, y_t, x_b, y_b) = (4, 0, 0, 0)$ mils. A 1 mil step response is superimposed on the y_t control axis with $k_p = 2.5$, $k_i = 0.3$, $k_0 = 0.75$.

will most likely degrade to the point where the rotor bumps into the catcher bearings if k_1 is too small[4]. Thus, the $\beta_{\rm rms}$ parameter is more precisely written as $\beta_{\rm rms} = \phi_{\rm rms}(e_{\rm rms}(k_1), \Phi_{0g})/\Phi_{0g}$.

Figures 8.28 and 8.39 show the total rms square flux vs. $e_{\rm rms}$ for the passivity and linear controllers, respectively. These quantities are the whirl test version of the total square flux for normal biasing T_n and the total square flux for gcfc biasing T_g of the static analysis. That is, Figures 8.28 and 8.39 plot $(T_g)_{\rm rms}$ and $(T_n)_{\rm rms}$ vs. $e_{\rm rms}$, respectively. Since $\beta_{\rm rms}$ depends linearly on $e_{\rm rms}$ (see Figures 8.26 and 8.37) $(T_g)_{\rm rms}$, $(T_n)_{\rm rms}$, and hence, $(T_n)_{\rm rms}/(T_g)_{\rm rms}$ may be plotted vs. $\beta_{\rm rms}$. This is conducted for many values of α since several Φ_{0g} and Φ_{0n} are used. The gcfc and cfc modes of operation require less flux, and are therefore more efficient than the cfs mode in regulating the rotor to a given $e_{\rm rms}$ when $(T_n)_{\rm rms}/(T_g)_{\rm rms} > 1$.

[4]No tests have been conducted to exactly determine what this lower limit might be.

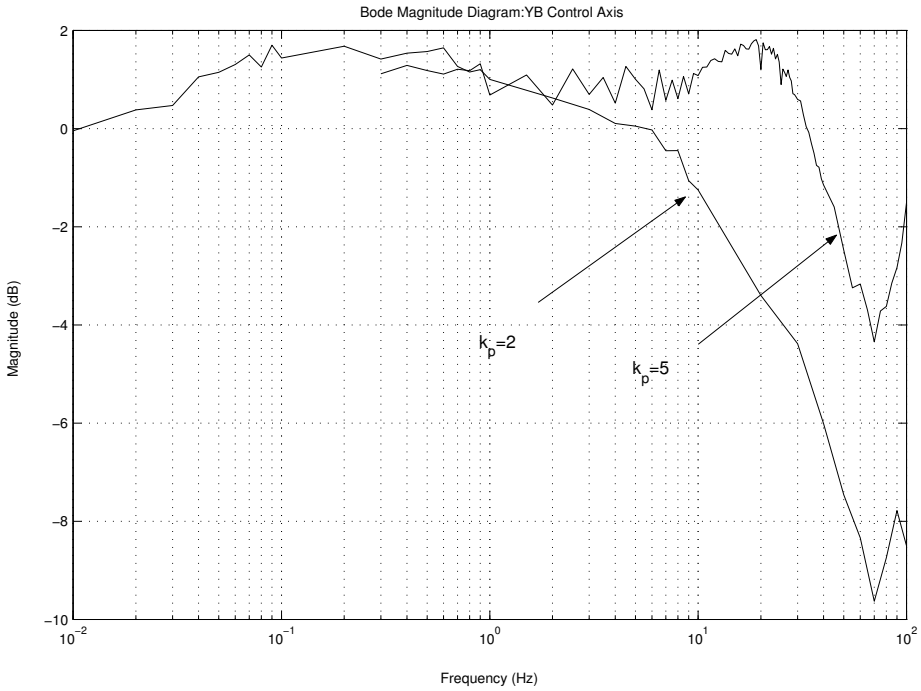

Figure 8.43: Measured closed-loop magnitude frequency response of y_b control axis for loop-gains $k_p = 2, 5$. For each data set, $k_i = .3$, $k_0 = 1$, $\gamma = 10$, and $z = 150$.

Figure 8.45 plots $(T_n)_{\rm rms}/(T_g)_{\rm rms}$ vs. $\beta_{\rm rms}$ for several values of α. Recall that the dynamics limit the achievable range of $\beta_{\rm rms}$ and data taken only defines $\beta_{\rm rms}$ on several short intervals. $\beta_{\rm rms}$ increases with increasing $\phi_{\rm rms}$ because $\beta_{\rm rms} = \frac{\phi_{\rm rms}}{\Phi_{0g}}$. Also, $\beta_{\rm rms}$ increases as Φ_{0g} decreases. Three different values of α are used for each value of Φ_{0g}. This data, illustrated with dark lines, is overlayed the theoretical predictions. The dotted lines represent T_n/T_g in equation (3.21) for several values of α. The data fits the overall trend predicted by the theoretical model, however, there is some discrepancy between the rms analysis and the static analysis.

Figure 8.46 shows a close up of each set of data for different values of Φ_{0g}. Note that for $\Phi_{0g} = 0$, α and β are not defined. $\overline{\beta}$ as defined in Section 3.3 is used to parameterize the ratio. Recall that the cfs condition is not defined for $\overline{\beta} > 2$. Since the rms values of the flux are being employed, the cfs condition is not defined for $\overline{\beta}_{\rm rms} > \sqrt{2}$. As expected, in zero bias, the cfc is more efficient than the cfs scheme for every value of Φ_{0n}. Note that the experimental data matches the theoretical

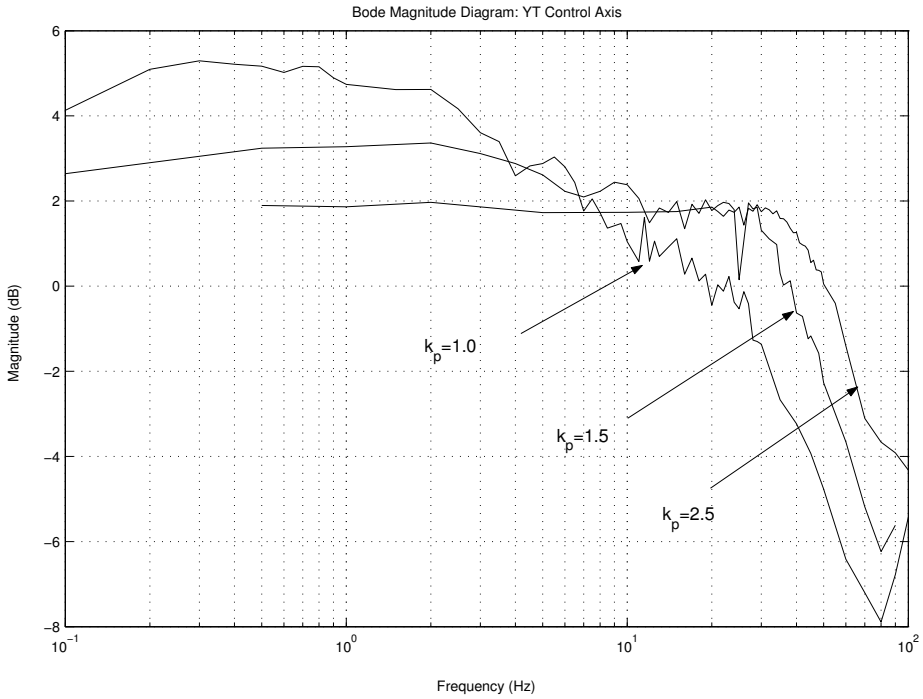

Figure 8.44: Measured closed-loop magnitude frequency response of y_t control axis for loop-gains $k_p = 1, 1.5, 2.5$. For each data set, $k_i = .3$, $k_0 = 1$, $\gamma = 10$, and $z = 150$.

prediction very closely.

To reiterate and clarify the above analysis, efficiency ratio compares the total square flux required to regulate the rotor to a given e_{rms} value. When this ratio is greater than one, the gcfc mode is more efficient at producing the required flux for regulation than the cfs mode. When this ratio is less than one, the converse is true. The efficiency ratio is used as a tool to distinguish between which mode of biasing incurs less operating losses as outlined in Table 2.1. Note that this ratio does not draw any conclusions about the electrical power supplied. In fact, from the data in Figure 8.29, the minimum rms power supplied using the passivity controller is about $4W$. Figure 8.40 shows that the rms power supplied is less than $4W$ for most of the cfs operation using $I_0 = 1.5A$. Thus, there are instances where the gcfc mode may be more efficient in producing the required flux, however, the cfs mode may require less electrical power. For instance, in zero bias, the cfc mode for $e_{\text{rms}} = 1.3$ is more efficient in producing the flux required for regulation. However, the rms power

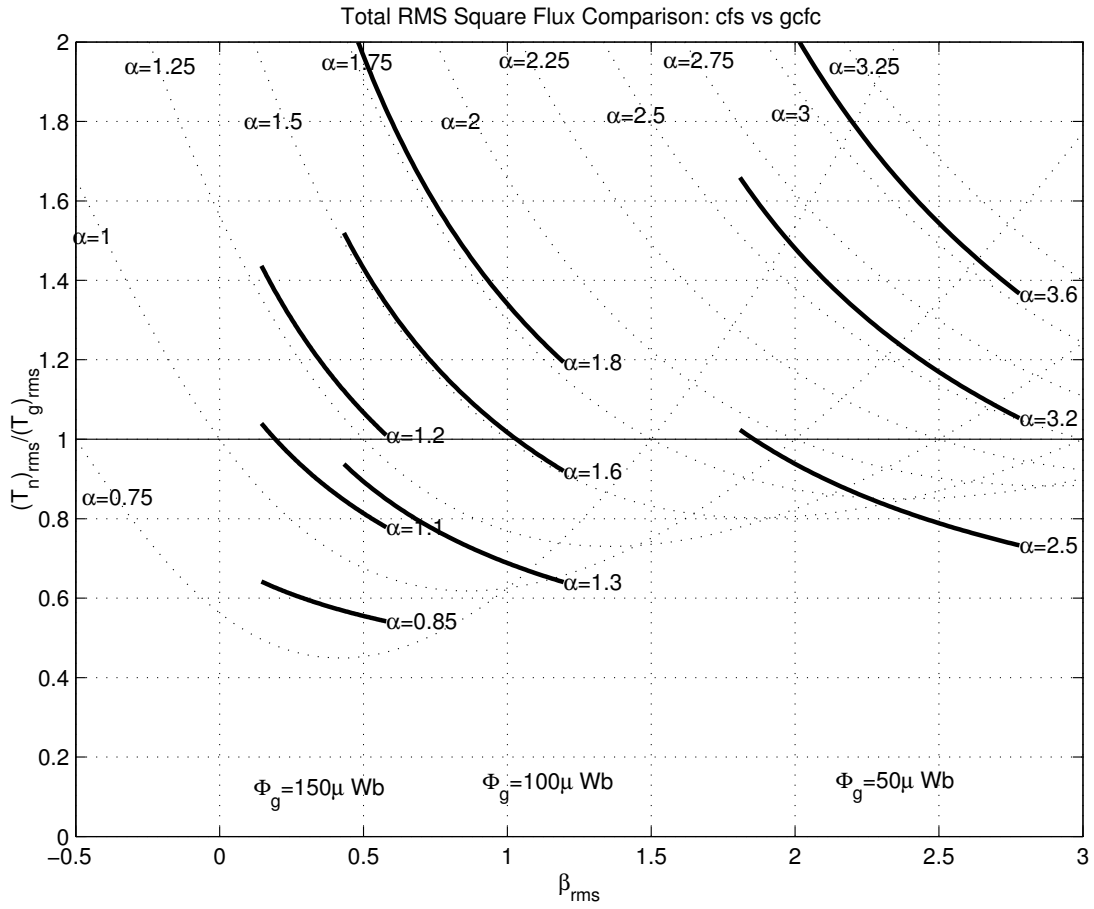

Figure 8.45: Total Square Flux Comparison cfs vs. gcfc: total square flux ratio $(T_n)_{\rm rms}/(T_g)_{\rm rms}$ plotted against the control flux ratio $\beta = \frac{\phi_{\rm rms}}{\Phi_{0g}}$ for several values of the competing flux bias ratio $\alpha = \frac{\Phi_{0n}}{\Phi_{0g}}$. The gcfc bias mode is more efficient than the cfs bias mode at regulating to a given $e_{\rm rms}$ when $(T_n)_{\rm rms}/(T_g)_{\rm rms} > 1$.

required for the cfs mode is $3.5W$ whereas the rms power required for the cfc mode is $4.5W$.

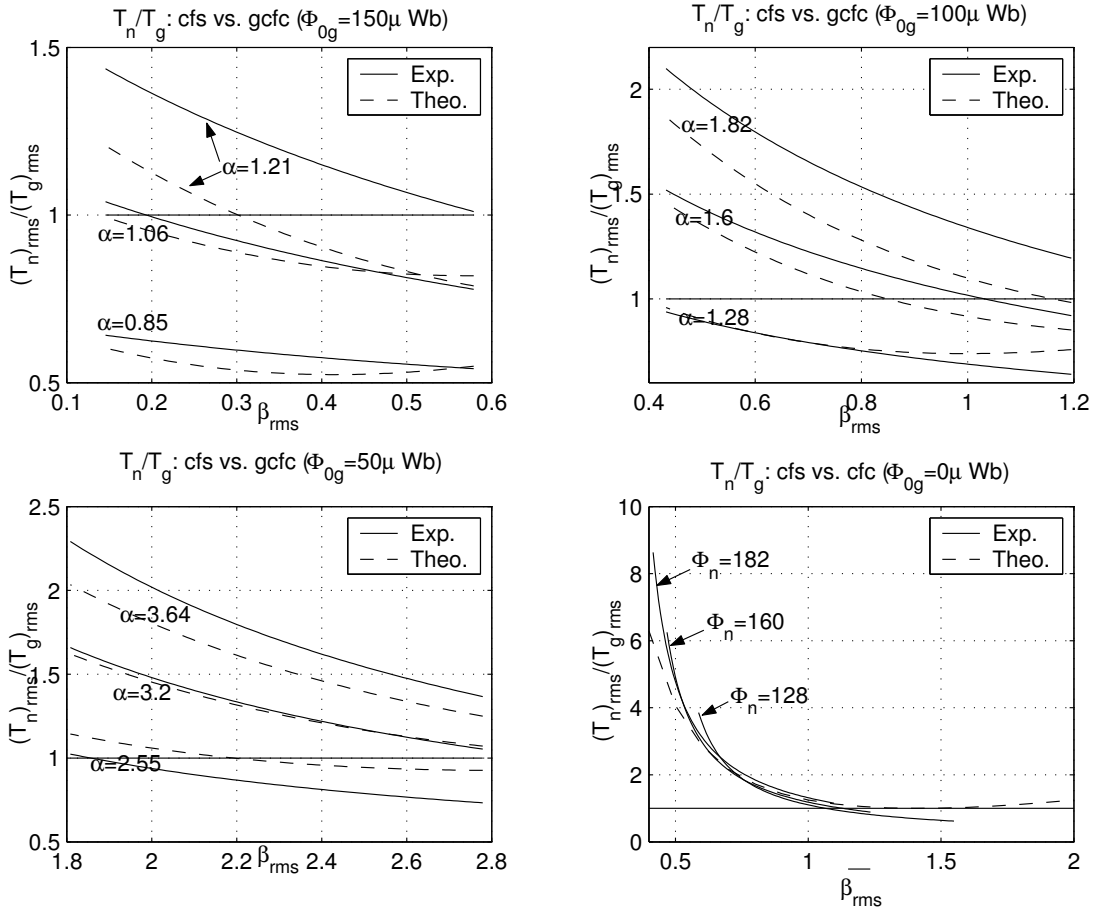

Figure 8.46: Total Square Flux Comparison cfs vs. gcfc: total square flux ratio $(T_n)_{\rm rms}/(T_g)_{\rm rms}$ plotted against $\beta_{\rm rms}$ for several values of the cfs flux bias Φ_{0n}. Note that α and β are not defined for $\Phi_{0g} = 0$.

CHAPTER IX

CONCLUSIONS AND FUTURE WORK

9.1 Summary and Conclusions

This dissertation offers *new theoretical and experimental results* to the current body of literature on low-loss AMB design. Flux measurement is a central issue in this thesis. The construction of a flux-current-position lookup table facilitates the measurement of the flux at low frequency, including DC. Since control design is primarily concerned with low-frequency phenomena (i.e. regulation, transient design, disturbance rejection), low-frequency flux reconstruction is important. In fact, reconstruction all the way down to DC is vital for flux-bias implementation. Furthermore, there are several advantages to using the flux (as opposed to the current) to model the electromagnetic actuators. Some of these advantages include a simplification of the equations-of-motion and prediction of the AMB forces even when the electromagnets operation in saturation, as is often the case in AMB operation.

Assuming that precise flux measurements are available, the newly developed *generalized complementary flux condition* (gcfc) may be imposed on the electromagnets of a given actuator axis. This bias technique was developed to support low-loss control designs for AMBs and the FWB application in particular. To minimize AMB and FWB operating losses (that is, power supplied the bearing and reaction wheel that is wasted), one must minimize the total square flux required for operation. This implies operation with zero flux bias (ZB). Linear control using the constant-flux-sum (cfs) bias technique becomes uncontrollable as the flux bias Φ_0 is reduced to zero. Thus, nonlinear control is required. The standard method for ZB operation is the complementary flux condition (cfc) where the product of the total flux in opposing

electromagnets is held at zero: $\Phi_1(t)\Phi_2(t) = 0\ \forall t$. However, this mode of operation has physical limitations, namely, a limited force-slew rate limit for small flux levels. Furthermore, several of the standard nonlinear control design techniques have a singularity in the control law in ZB. The gcfc condition allows the introduction of a small flux bias to pacify the flux slew-rate limit while at the same time, keeps the power-saving switching strategy of the cfc. The total flux has the form $\Phi_j = \Phi_0 + \phi_j$ for $j = 1, 2$ and the complementarity is imposed on the control fluxes $\phi_1\phi_2 = 0$. In this work, the flux bias is implemented with voltage mode amplifiers and an additional flux-feedback PI control-loop. Theoretical analysis and experimental results show that under typical operating conditions (i.e. Φ_0 small), the gcfc bias scheme is more efficient at producing the required force than the standard cfs bias scheme. Stated differently, the gcfc often produces a given required force with less total square flux than the cfs scheme. Consequently, the gcfc scheme will have less operating losses than the cfs scheme under typical operating circumstances. This is illustrated in Figures 8.45 and **??** where the passivity-based controller implementing gcfc is compared to a linear controller implementing the cfs.

Since the operating losses are proportional to the bias flux, operation with low-flux bias (LB) is typical in the gcfc scheme. However, the question enviably arises, "How small can the bias be before LB operation effectively becomes ZB operation?" Also, since several of the standard nonlinear control designs have a singularity in ZB, how small may Φ_0 become before the effects of operating near the singularity are apparent? Recall that the singularity manifests itself as an infinite voltage command. The answers posed to these questions in the literature sometimes employ an ad-hoc solution. For example, the requested control voltage may be artificially saturated [8, 50, 15]. Other authors have tried to live with the singularity by cranking up the bias when voltage saturation is detected [30, 31, 22]. This thesis is different in that instead of trying to live with the ZB singularity, it removes it altogether.

Consequently, ZB and very small LB operation is greatly improved. The clf-based control law of Section 4.3 has a singularity space that is a line in $\mathbb{R}^3$ as opposed to the typical plane of singularity in $\mathbb{R}^3$ for the standard nonlinear controllers. Even better, the passivity-based controllers of Section 4.4 are completely nonsingular.

Some readers may question the practical value of the improvements to ZB operation. For example, if an infinite voltage is commanded it will never actually be implemented because of the voltage saturation inherent in the voltage-mode amplifiers. Furthermore, there is nothing fundamentally wrong with operating the amplifiers in saturation. In addition, the simulation results of Figure 4.8 show that the introduction of voltage saturation (with a reasonable choice of V_{sat}) into the dynamics only seems to introduce a minor time delay or increase in the settling time. However, experimental results suggest that amplifier bandwidth is the performance limiting factor in ZB operation as opposed to voltage saturation. Figures 8.16, 8.24, and 8.34 show the voltage references V_r, the voltages realized by the Copley 412 amplifiers V_{app}, their frequency content, and the magnitude response of the voltage-mode amplifiers. Although the backstepping control law requests voltages on the order of 10^3 in Figure 8.16, the realized applied voltage V_{app} never actually saturates ($V_{\text{sat}} = 28V$). The performance of the backstepping controller is limited because it requests a voltage signal V_r that has its energy spread out over a wide range in the frequency spectrum. Only a very small percentage of the requested control voltage makes it through the 200Hz bandwidth of the Copley 412 voltage-mode amplifiers. In contrast, most of the clf-based V_r and all of the passivity-based V_r make it through the limited bandwidth of the amplifiers. That is, the control laws with the smallest singularity spaces require the least amount of amplifier bandwidth to implement.

The gcfc is intended to be operated in LB to alleviate the ZB singularity, but how large of a bias is required before an increase in bearing stiffness is observed? To address this question, whirl tests were conducted for several control gains and bias

levels. It is seen that the bearing stiffness increases with the bias. Indeed, since the bearing is more responsive for a larger bias, the rms control flux required to regulate the rotor to a given rms regulation error e_{rms} decreases with bias. This is illustrated in Figures 8.8, 8.18, and 8.26. In addition to studying the stiffness properties, the total rms flux and total rms square flux increases with bias. This implies that operating losses increase with bias (as expected).

Several practical issues are addressed in this work. Resistance compensation is implemented in software with the voltage mode amplifiers. Recall that the power $I^2\hat{R}$ is supplied to the bearing to replenish the Ohmic power loss I^2R. It is found that a good resistance estimate $\hat{R}$ is critical to have the ability to directly assign $\dot{\Phi}$ with V_r. Moreover, the value of $\hat{R}$ must be less than the true resistance R or the voltage-mode amplifiers may be destabilized. Furthermore, the IR compensation in opposing electromagnets must be properly tuned so that the responsiveness of each opposing electromagnet is "matched". Unmatched IR compensation results in asymmetric generalized flux reconstruction. In addition, bandwidth-limited differentiation scheme is employed to estimate the velocity from position measurements and the measured position and currents are heavily filtered to ensure clean flux measurements. Also, the control laws are augmented with integral action to guarantee tracking to any setpoint with zero steady-state error. Additionally, a passive magnetic bearing was constructed for vertical rotor support based on a trial and error design.

9.2 Future Work

Although this work presents a comprehensive treatment of low-loss AMB design and implementation, several issues may be revisited in the future to achieve better results or extend upon those presented here. Several suggestions for future work are listed below:

- **GCFC Bias Strategy Evaluation:** In this work, theoretical and experimental comparisons of the total square flux are made between the gcfc and the standard cfs flux bias scheme. The comparisons are parameterized by $\alpha = \Phi_{0n}/\Phi_{0g}$ and $\beta = \phi/\Phi_{0g}$ where α measures the relative size of the flux bias used in either scheme and β measures the ratio of the control flux to the bias flux. This comparison characterizes only one facet of the AMB's performance, namely, the efficiency with respect to power dissipation. The practical limits to the performance of magnetic bearings include the peak load capability, the slew rate, the gain bandwidth product, and the dynamic load capabilities. These characterizations are described in [53, 4, 1, 71, 70, 18, 93, 92, 44], for example. Such measures have become the standards of AMB performance. To promote the gcfc to the greater AMB control community, the above performance limitations of the gcfc should be evaluated and compared to the cfs and cfp bias schemes.

- **Flux Measurement:** Flux measurements in this work are obtained by using a standard integrating search coil technique using low-frequency sinusoidal excitations to construct $\Phi - I$ curves for a range of x values. Search coils are limited in that they can not sense a constant flux. To recover the DC portion of the flux, DC magnetization curves are fit to the low-frequency excitation $\Phi - I$ curves. The lookup tables consist of the DC magnetization curves for several rotor positions. Thus, the flux-current-position lookup tables have a limited flux-measurement bandwidth. Since the positioning feedback loops in this work also have a limited bandwidth (i.e. less than 100Hz), the limited flux-measurement bandwidth did not pose any serious problems. Investigations should be conducted in which the measurement bandwidth of the flux lookup table is determined. This bandwidth will help determine the achievable closed-loop positioning system bandwidth. Furthermore, work by Keith [32] and Maslen [52] suggest that the bandwidth can be improved by combining the

measurements of a flux lookup table and a search coil. Essentially, the wide-band flux is constructed from a weighted sum of the DC measurements (from a lookup table) and the AC measurements (from an online search coil). Note that search coils are easily integrated into the design of the magnetic actuator if it thought to do so from the start.

An observer may also be used to reconstruct the flux from the measured signals (typically position and the electromagnet currents). Tsiotras and Arcak construct a reduced order flux observer which uses only velocity measurements in [80]. Although this design is successful in simulation, its practicality has not been evaluated in a realistic setting. For example, velocity is typically estimated instead of directly measured. The flux estimator performance may be degraded with respect to improper velocity measurement and measurement noise. Baloh in [1] also proposes a flux estimation scheme which measures only the applied voltage and the measured current. The airgap is considered as time-varying parameter and an observer for the resulting time-varying linear system is constructed. The typical unsaturated reluctance model is assumed to related flux to current: $NI = \mathcal{R}(x)\varphi$. The error between the measured current i and the current estimate $\hat{i}(x, \hat{\varphi})$ is used to correct the flux estimate $\hat{\varphi}$. The performance of these methods in a realistic setting is yet to be determined.

- **Adaptive IR Compensation:** It was seen in Section 5.5.3 that the IR compensation technique requires a good estimate $\hat{R}$ of R so that $R - \hat{R}$ is small. The coil resistance is measured to be about 0.5Ω, however, this value may change with large current levels due to core heating. Furthermore, since the IR compensation is conducted in an open-loop fashion, the amplifier may be destabilized when $\hat{R} > R$. In addition, the online estimate

$$\hat{R}(t) = LPF(s)\frac{V_{\text{app}}(t) - V_{\text{coil}}(t)}{I(t)}$$

in which the calculated resistance is heavily low-pass filtered is shown to be unreliable in all but the simplest test situations. This is due to the fact that the estimate is infinite when $I(t) = 0$. However, it should be possible to construct an online resistance estimate via standard parameter estimation methods [27].

- **Mutual Inductance and Actuator Modelling:**

  It was seen in Section 5.5.4 that mutual inductance exists between the opposing electromagnets on a given control axis. This has consequences on the implementation of the complementary flux condition (cfc). Although one may implement the complementary current condition (ccc), the mutual inductance prevents one from implementing the cfc precisely. A small flux may exist in the coil which is assumed to be at rest. In this work, experiments showed that one could satisfactorily assign the flux in both electromagnets simultaneously. Hence, the effects of mutual inductance were neglected.

  More precise control of the actuator flux may be obtained if the mutual inductance is considered explicitly. In general, the coupling between the actuators is modelled with an inductance matrix.

$$\begin{bmatrix} N\varphi_6 \\ N\varphi_8 \end{bmatrix} = \begin{bmatrix} L_6(x) & M(x) \\ M(x) & L_8(x) \end{bmatrix} \begin{bmatrix} I_6 \\ I_8 \end{bmatrix}$$

  Let $\Lambda = [N\varphi_6, N\varphi_8]^T$, $I = [I_6, I_8]^T$, $R = [R_6, R_8]^T$, $V_A = [V_{\text{app1}}, V_{\text{app2}}]^T$, and $\mathcal{M}$ be the inductance matrix. Then, $\Lambda = \mathcal{M}I$. The flux lookup tables constructed in Chapter 6 model the diagonal terms in the inductance matrix as a function of x. Similar lookup tables may be constructed for the mutual inductance (off-diagonal) terms. $\mathcal{M}$ for any system is invertible: see Proposition 9. Thus, the coupled actuator dynamics have the form

$$\dot{\Lambda} = -RI + V_A = -R\mathcal{M}^{-1}\Lambda + V_A$$

The complementary flux condition (cfc) could be obtained by designing V_A as tracking controller so that Λ tracks Λ_{des}. One then assigns Λ_{des} according to the cfc. In this case, the cfc would be obtained "asymptotically fast" due to the tracking transient.

In the PREMAG magnetic bearing, there may be significant coupling between all eight electromagnet coils. The above coupled actuator framework could accommodate such a situation. However, before one proceeds with such an undertaking, better studies of the core modelling and coupling via finite element analysis is warranted. No such studies have been conducted.

- **System Identification:** A better model of the open-loop system will elicit more precise control performance. Recall that the 1-DOF linearized model of the AMB operating with the constant-current-sum (ccs) bias scheme presented in Section 7.2.1 is

$$P(s) = \frac{K_i}{ms^2 - K_x}$$

and

$$c = \frac{\beta_{\text{leak}}\mu_0 A_g N^2}{4}, \qquad K_x = \frac{4cI_0^2}{g_0^3}, \qquad K_i = \frac{4cI_0}{g_0^2}$$

The constant $\beta_{\text{leak}} \in (0, 1)$ is unknown and directly affects the open-loop pole positions. Furthermore, the mass m of the rotor is not exactly known. Its weight could be measured directly, but this requires disassembly of the rotor hub and removal of the rotor shaft. Concerns about damaging the DC motor contained in the rotor hub prevented this task. Thus, the value of m in Table 7.5 is an estimate. Furthermore, the state equation based on airgap dynamics which allows for a decentralized control approach has several effective mass variables, m_1, m_2, and m_3 defined in equation (7.14). Recall that these parameters capture the "bottom-heaviness" of the rotor. The predicted closed-loop frequency response behavior may be matched to the measured closed-loop frequency response data

by tuning the model parameters.

- **Additional Control Algorithms:** The PREMAG reaction wheel may be used as a test bed for whole range of AMB control design algorithms. For example, the low-loss control algorithms developed in [80] which are based on feedback passivation, the nonlinear small-gain theorem, and nested saturation designs may be experimentally evaluated in the future.

  Currently, the rotor is stabilized by a decentralized control scheme where three control axes are linearly controlled (with amplifiers in current mode) and the fourth is the low-loss nonlinear test bed (with amplifiers in voltage mode). It was found that the regulation along the nonlinear axis was easier to implement than along a linear axis because the nonlinear control laws under test are globally asymptotically stable (GAS). The local asymptotic stability of the linear control axes is sometimes troublesome on system startup. That is, the initial conditions of rotor may not lie within the region of attraction of the linear controllers and the rotor may require some help (i.e. a tap of the hand on the rotor) at system initialization before the regulation kicks in. To remedy this, nonlinear GAS control algorithms could be implemented on each axis. Recall that the decentralized control presented in Chapter 7 neglects the coupling between the control axes. It is likely that better performance is attainable by using a MIMO control scheme, especially when rotor gyroscopic effects become significant at large ω.

  Several control implementation issues could be further investigated. The study of the nonlinear control designs in this thesis are more interesting when using amplifiers in voltage mode. However, the equivalent low-loss control designs using current mode are much easier to implement. It is unclear at this point what the practical trade-offs are between current-mode and voltage-mode operation.

For example, there may exist hardware limitations that determine the operating mode of choice. Future work could focus on determining these trade-offs by comparison of both modes. In addition, studies could be conducted to minimize control law calculation time to obtain faster sampling rates.

Recall that the DC motor mounted in the rotor hub used for spinning the rotor is in need of some minor repair. This work deemed these repairs low-priority because the low-loss control algorithms may be verified without spinning the rotor. However, several interesting studies may be conducted once these repairs are made. First, disturbance rejection of the rotor imbalance, which is synchronous with ω, may be studied. Several methods based on generalized notch filters, repetitive control, and estimation of the fourier components of the rotor imbalance exist in the current literature: see [42, 40, 41, 13, 76], for example. Also, spin down tests of the rotor may be conducted to investigate the eddy-current drag phenomena. Recall that this rotor has been spin tested up to 28krmp. However, high-speed spin testing requires the investment in a containment system and vacuum chamber. Furthermore, the epoxy used to glue the NdFeB magnets to the bottom of the rotor in the construction of the vertical support passive magnetic bearing may fail for large ω. Further safety studies must be conducted before high-speed rotor spin tests are implemented. Perhaps more structurally sound method exists to attach the NdFeB magnets to the bottom of the rotor.

- **Optimal Flux Bias Selection**

  The most interesting problem for future study is the selection of an optimal flux bias for power consumption, power loss, and bearing stiffness trade-offs. Recall that minimization of the power loss and minimization of the power consumption are different problems. Power dissipation (loss) is minimized in zero bias

operation however the bearing stiffness and force slew-rate are compromised. Furthermore, the results in Chapter 8 show that the rms power supplied to the bearing (i.e. the power consumption) may actually decrease when the bias is increased. This tends to be the case for tighter rotor regulation tolerances (for smaller values of e_{rms}).

Recall that the power supplied is $P_{\text{supp}} = V_{\text{app}} I = V_b I + V_c I + I^2 \hat{R}$ where $V_b I$, $V_c I$, and $I^2 \hat{R}$ are the power required to implement the bias flux Φ_0, the control flux ϕ, and the IR compensation. Experiments suggest that the power required for IR compensation is smaller than that required for bias and control flux implementation. It is sensible to presume that the power required to implement the bias P_b is proportional to Φ_0 and is independent of the control parameters. In addition, experimental evidence illustrates that for a given e_rms, the rms value of the control flux decreases with an increasing bias. Moreover, the rms value of the control flux increases as e_{rms} decreases (i.e. as the rotor is regulated to tighter position tolerances). Thus, it is sensible to presume that the power required to implement the control flux P_ϕ is inversely proportional to Φ_0 and e_{rms}. Figure 9.1 speculates the dependence of P_b, P_ϕ and P_{supp} on the bias flux Φ_0 for several values of e_{rms}. If this is indeed the case, then an optimal value of Φ_0^* exists for each value of e_{rms}. Note that the bearing could consume very low power and be highly efficient by operating with $\Phi_0 = 0$ and accepting a larger regulation error tolerance.

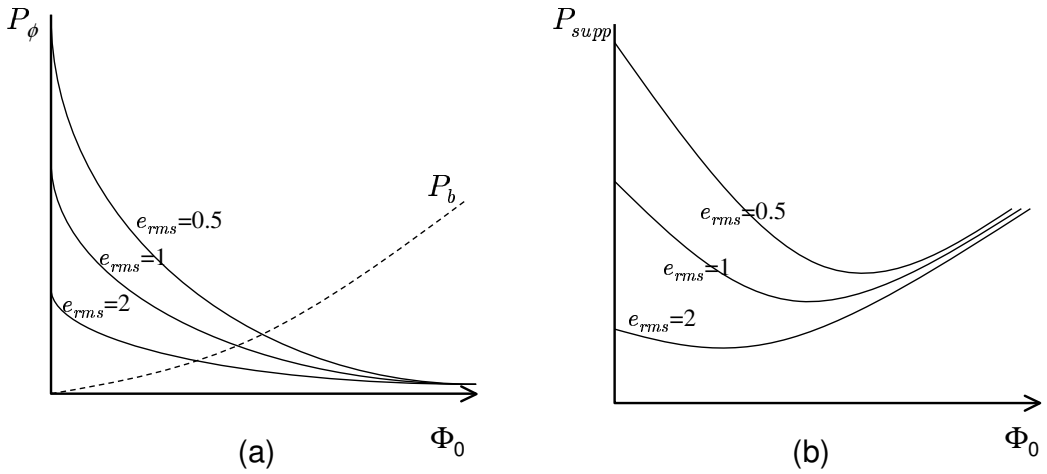

Figure 9.1: Hypothesized dependence of P_b, P_ϕ and $P_{\rm supp}$ on the bias flux Φ_0 for several values of $e_{\rm rms}$.

APPENDIX A

PROPERTIES OF THE FUNCTION $X^{[q]}$

This short appendix introduces an operator for convenient notation. Let the function

$$\text{sgn}(x)x^q = x^{[q]} \tag{A.1}$$

It is easy to verify that the above function has the following properties.

1. $x^{[q]}x^{[p]} = x^{p+q}, \qquad x^{[q]}x^p = x^{[p+q]}$

2. $\frac{x^{[p]}}{x^{[q]}} = x^{p-q}, \qquad \frac{x^{[p]}}{x^q} = x^{[p-q]}$

3. $\frac{dx^{[p]}}{dx} = px^{[p-1]}, \qquad \int x^{[p]} = \frac{x^{[p+1]}}{p+1}$

4. If a scalar function $f(x) \in H_p$ then $f(x)^{[q]} \in H_{pq}$.

5. $x^{[q]} \in \mathcal{C}^0$ for $q > 0$.

6. $x^{[q]} \in \mathcal{C}^1$ for $q \geq 2$.

7. If q is an odd integer, then $x^{[q]}$ is an even function.

8. If q is an even integer, then $x^{[q]}$ is an odd function.

APPENDIX B

BACKGROUND ELECTROMAGNETIC THEORY

This appendix presents a comprehensive treatment of the basic analysis tools required to derive the dynamics of and the force generated by simple electromechanical machinery. Most of this material is adapted from [11, 20, 6]. All electromagnetic phenomena are governed by Maxwell's[1] laws. Maxwell built upon the observations of Ampère, Gauss, and Faraday to construct a concise theory of electromagnetic waves. These laws are very general and describe such diverse topics as wave propagation, light polarization, light refraction and total internal reflection, transmission lines, antennas, and radar, just to name a few. They are

$$\oint_{\mathcal{C}} \overrightarrow{E} \cdot \overrightarrow{d\ell} = -\frac{d}{dt} \int_{\mathcal{S}} \overrightarrow{B} \cdot d\overrightarrow{S} \tag{B.1a}$$

$$\oint_{\mathcal{C}} \overrightarrow{H} \cdot \overrightarrow{d\ell} = \int_{\mathcal{S}} \overrightarrow{J} \cdot d\overrightarrow{S} + \frac{d}{dt} \int_{\mathcal{S}} \overrightarrow{D} \cdot d\overrightarrow{S} \tag{B.1b}$$

$$\oint_{\mathcal{S}} \overrightarrow{D} \cdot d\overrightarrow{S} = \int_{V} \rho \, dv \tag{B.1c}$$

$$\oint_{\mathcal{S}} \overrightarrow{B} \cdot d\overrightarrow{S} = 0 \tag{B.1d}$$

where $\overrightarrow{E}$ is the electric field strength, $\overrightarrow{H}$ is the magnetic field strength, $\overrightarrow{B}$ is the magnetic flux density, $\overrightarrow{D}$ is the electric flux density, $\overrightarrow{J}$ is the current density, and ρ is the electric charge density. In addition, the flux densities are typically related to

[1] James Clerk Maxwell (1831-1879): British physicist and mathematician. He is best known for discovering the connection between light and electromagnetic waves, but also contributed to the kinetic theory of gasses, described the composition of the rings of Saturn and demonstrated how the human eye sees color.

the field strengths by

$$\overrightarrow{B} = \mu \overrightarrow{H}, \qquad \overrightarrow{D} = \varepsilon \overrightarrow{E}$$

where μ is called the magnetic permeability and ε is called the electric permittivity. The units of the quantities in Maxwell's Laws are listed in Table B.1.

Table B.1: Quantities in Maxwell's Laws

Symbol	Quantity	Units
$\overrightarrow{E}$	Electric Field	$\frac{\mathrm{N}}{\mathrm{C}}$
$\overrightarrow{H}$	Magnetic Field	$\frac{\mathrm{A}}{\mathrm{m}}$
$\overrightarrow{D}$	Electric Flux Density	$\frac{\mathrm{A}}{\mathrm{m}}$
$\overrightarrow{B}$	Magnetic Flux Density	$\mathrm{T} = \frac{\mathrm{N}}{\mathrm{Am}}$
$\overrightarrow{J}$	Current Density	$\frac{\mathrm{A}}{\mathrm{m}^2}$
ρ	Charge Density	$\frac{\mathrm{C}}{\mathrm{m}}$
ε_0	permittivity of vacuum	$8.85 \times 10^{-12} \frac{\mathrm{F}}{\mathrm{m}}$
μ_0	permeability of vacuum	$4\pi \times 10^{-7} \frac{\mathrm{H}}{\mathrm{m}}$

Maxwell's Law's are far too general for the purposes of this chapter and the next few sections simplify their application to the study of electromechanical machinery and electromagnets. Equation (B.1c) is Gauss's statement of the conservation of electric charge. In typical electromechanical machines, the electric charge density ρ and the electric flux density $\overrightarrow{D}$ are zero. Thus, equation (B.1c) is disregarded. Section B.1 presents the tools of magnetostatics, the study of steady-state magnetic fields. These tools are credited to Ampère[2] and Gauss[3]. Ampère's Law (equation (B.1b) is Maxwell's generalization of Ampère's Law) establishes that currents create magnetic fields and Gauss's Law for magnetism (equation (B.1d)) is concerned with the conservation of magnetic flux. Under certain conditions, the application of these

[2]André Marie Ampère (1775-1836): French physicist, mathematician and natural philosopher. His findings on electricity and magnetism were published in *Recueil d'observations électrodynamiques* (Collection of Observations on Electrodynamics, 1822) and in *Théorie des phénomènes électrodynamiques* (Theory of Electrodynamic Phenomena, 1826).

[3]Johann Carl Friedrich Gauss (1777-1855): German mathematician. One of the most prolific mathematicians ever, he produced over 500 documents on subjects including the fundamental theorem of algebra, number theory, probability, differential geometry, geodesy, magnetism, electrostatics, astronomy and optics.

laws to the analysis of magnetic structures is analogous to circuit analysis. Section B.2 introduces magnetodynamics, the study of changing magnetic fields. Faraday's[4] Law (equation (B.1a)) dominates this topic and is the basis for electromagnet dynamic modelling. It relates the rate of change of magnetic flux through a coil of wire to the voltage induced at the coil terminals. Since most practical electromagnets employ a magnetic core, a discussion of the core loss and nonlinearity is included in Section B.3. The relationship between coil current, magnetic flux and bearing airgap is of major importance to the practical application of the techniques in this thesis and is clearly delineated.

Finally, the generation of force in magnetic circuits is discussed. There are two schools of thought when studying magnetic forces. One paradigm is to take a close look at the physical mechanisms that produce the magnetic forces. Electromagnetic forces arise when magnetic fields interact with the dipoles of magnetic materials or when an electron is moving through a magnetic field. Through the application of Maxwell's laws and material physics, an extraordinarily detailed and complex picture of the microscopic dynamics involved to create the magnetic forces may arise. The other school of thought is to study the energy stored in the magnetic field of the electromechanical machine and realize that forces are created when electrical energy is converted to mechanical energy through the medium of the magnetic field. Both of these approaches have advantages. One produces a detailed picture of the physical mechanisms involved, but can be very cumbersome. The other produces a macroscopic view of the net force generated in terms of the change in the stored magnetic energy. This *energy method* is very general and applies to practically all electromechanical machinery.

[4]Michael Faraday (1791-1867): British physicist and chemist. He is known for his laws of electrolysis, the isolation of Benzene in 1825, introducing the concepts of magnetic lines of force or flux, and his Law of Induction. His contributions are documented in the volumes entitled *Experimental Researches in Electricity (1839, 1844, 1855)* and *Experimental Researches in Chemistry and Physics (1858)*. He is considered by many to be one of the greatest experimental physicists.

Section C presents the Lorentz equation- which describes the forces felt by moving charges in magnetic fields- and how it is used in the analysis of simple machines. The complex physical mechanisms that govern the force created by interactions between magnetic fields and magnetic materials will not be covered in this discussion. Section D gives an introduction to the energy method.

B.1 Magnetostatics: Ampère's Law, Guass's Law for Magnetism, and Magnetic Circuits

Maxwell's laws are very general and have too complex to be used in simple situations. Fortunately, they may be simplified when appropriate and even boil down to circuit-like analysis laws. Magnetostatics is the study of steady-state or constant magnetic fields. It is assumed that the current densities and the magnetic or electric field strengths involved in the field analysis are constant. Magnetostatics is governed by equations (B.1b) and (B.1d) of Maxwell's Laws. Equation B.1b is a generalization of the law that was first stated by Ampère. The term $d/dt \int_{\mathcal{S}} \overrightarrow{D} \cdot d\overrightarrow{S}$ establishes how magnetic fields are created by changing electric fields and is of primary interest in the study of electromagnetic radiation. However, since the electric field strength is constant in magnetostatics, the term $d/dt \int_{\mathcal{S}} \overrightarrow{D} \cdot d\overrightarrow{S}$ in equation (B.1b) is zero. In this case, equation (B.1b) reduces to Ampère's Law.

$$\oint_{\mathcal{C}} \overrightarrow{H} \cdot \overrightarrow{d\ell} = \int_{\mathcal{S}} \overrightarrow{J} \cdot d\overrightarrow{S}, \qquad \nabla \times \overrightarrow{H} = \overrightarrow{J} \tag{B.2}$$

For completeness, the integral form and differential form have been stated[5] .

[5]Recall that conversion between the integral and differential forms of Maxwell's equations is conducted by applying the Divergence Theorem and Stokes Theorem for vector fields.

Divergence Theorem: For a vector field $\overrightarrow{V}$ and a closed surface $\mathcal{S}$, the flux integral of $\overrightarrow{V}$ through a *closed* surface equals the integral (or the sum total) of the divergence throughout the volume that the surface encloses. $\oint_{\mathcal{S}} \overrightarrow{V} \cdot d\overrightarrow{S} = \int \nabla \cdot \overrightarrow{V} dv$.

Stokes Theorem: For a vector field $\overrightarrow{V}$ and a closed curve $\mathcal{C}$, the circulation integral of $\overrightarrow{V}$ equals the integral (or the sum total) of the curl of $\overrightarrow{V}$ over any surface that has the contour $\mathcal{C}$ as its boundary. $\oint_{\mathcal{C}} \overrightarrow{V} \cdot \overrightarrow{d\ell} = \int (\nabla \times \overrightarrow{V}) \cdot d\overrightarrow{S}$.

Ampère's law establishes the connection between the current carried in a wire and the magnetic field generated by that current. Mathematically, it states that the line integral around any closed path $\mathcal{C}$ of the *magnetic field strength* $\overrightarrow{H}$ is equal surface integral of the *current density* $\overrightarrow{J}$ over any surface S which has $\mathcal{C}$ as its boundary. Ampère's may be restated as the circulation integral of the magnetic field strength about a closed curve is the flux integral of the current density $\overrightarrow{J}$ through a surface bounded by that curve. The differential form of Ampère's law states that the curl of the magnetic field is equal to the current density. That is, a current density (or a current) causes the magnetic field to curl (locally rotate). Note that the magnetic field curls in the direction to coincide with the right hand rule. If one grasps a current carrying wire with their right hand and thumb pointing in the direction of the current, the field curls in the direction of the fingers. This leads to the well known fact that the magnetic field about a current carrying wire forms in concentric circles.

The following example illustrates the application of Ampère's law on a toroidal magnetic core with a rectangular cross-section. The example will be revisited several times to facilitate understanding of magnetic circuits.

Example B.1. *(Application of Ampère's Law [6])*
The application of Ampère's law is demonstrated by studying a toroidal core with rectangular cross-section with a coil tightly wrapped around it. Calculate the magnetic field strength as a function of the radius from the center of the core. See Figure B.1.

Solution: *For simplicity, assume that the coil is tightly wrapped around the core and there are enough turns to completely cover the core. In this case, one assumes two thin layers of uniform current density* $\overrightarrow{J}$ *into* ($\bigotimes$) *and out of the page* ($\bigodot$) *in Figure B.1b. The radii of the layers of the core are marked* $r_a, ..., r_d$.

Symmetry is employed to analyze this problem. Obviously, choose cylindrical coordinates with unit vectors $\hat{r}$, $\hat{\theta}$, *and* $\hat{z}$ *for the radial, angular and axial directions. The*

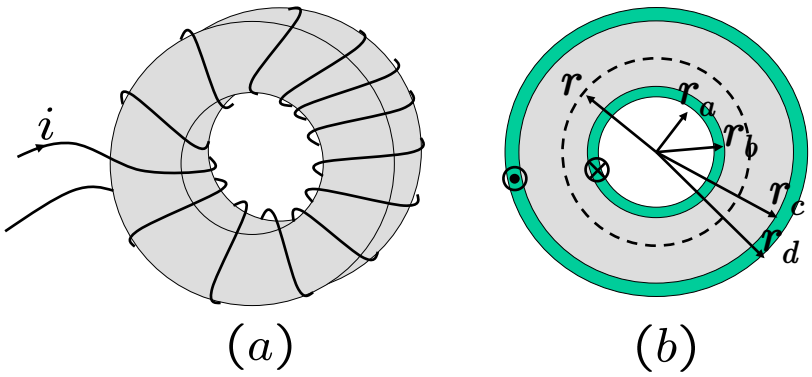

Figure B.1: **(a)** Toroidal core with coil wrapped around it. **(b)** Cross section of core.

uniform current density assumption leads to a symmetrical magnetic field strength H *with respect to* θ*.*

To evaluate Ampère's Law, a circular contour of radius r *is selected to make the integration easy. The dotted circular contour shown in Figure B.1b has a tangent vector that is perpendicular to two of the three cylindrical unit vectors.*

$$\begin{aligned} \oint_{\mathcal{C}} \overrightarrow{H}\,\overrightarrow{d\ell} &= \oint (H_r\hat{r} + H_\theta\hat{\theta} + H_z\hat{z}) \cdot (r\hat{\theta}d\theta) \\ &= \int_0^{2\pi} H_\theta r d\theta = 2\pi r H_\theta \end{aligned} \tag{B.3}$$

The evaluation of the RHS of Ampère's Law inside the core reduces to the total current piercing the surface defined by the circular contour $\mathcal{C}$*.*

$$\int_{\mathcal{S}} \overrightarrow{J} \cdot d\overrightarrow{S} = Ni \tag{B.4}$$

Thus, the magnetic field strength is

$$\overrightarrow{H} = \frac{Ni}{2\pi r}\hat{\theta} \tag{B.5}$$

Note that direction of the field is in the $\hat{\theta}$ *direction, but the polarity (clockwise or counter-clockwise) has not been specified. It it determined by the right-hand-rule for coils, a generalization of the right-hand-rule for wires. If one wraps their fingers in the direction that the current encircles the core, then the field direction in the core is*

in the direction of the thumb. Thus, in this example, the field direction is clockwise. The magnetic field as a function of the radius is

$$
\begin{aligned}
H &= 0 && r \le r_a \\
H &= \frac{Ni}{2\pi r}\frac{r^2 - r_a^2}{r_b^2 - r_a^2} && r_a \le r \le r_b \\
H &= \frac{Ni}{2\pi r} && r_b \le r \le r_c \\
H &= \frac{Ni}{2\pi r}\Big(1 - \frac{r^2 - r_c^2}{r_d^2 - r_c^2}\Big) && r_c \le r \le r_d \\
H &= 0 && r \ge r_d
\end{aligned}
\tag{B.6}
$$

This function is illustrated in Figure B.2. Note that the analysis excludes consideration of the end-turns of the coil. The magnetic field strength increases as more current is enclosed in the $\mathcal{C}$ contour and decreases with radius.

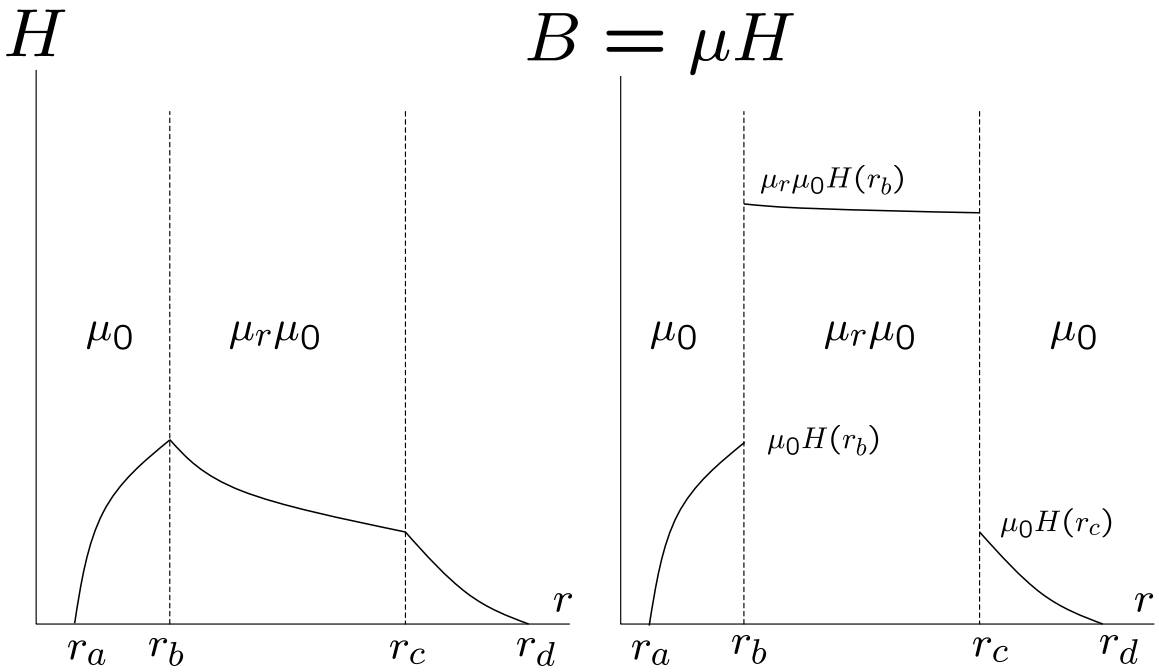

Figure B.2: Variation of the H and B field (it is symmetric wrt θ) as a function of the radius. Note that the B field is discontinuous because of the change in material.

The *magnetic flux density* $\overrightarrow{B}$, measured Tesla (T := $\frac{\text{Wb}}{\text{m}^2}$), is a function of the magnetic field strength $\overrightarrow{H}$ and medium that the field passes through. Ferromagnetic

materials (ones that include iron, or are alloys of iron and cobalt, tungsten, nickel, or aluminum, for example) have a strong magnetic flux-focusing effect. For an isotropic material (magnetic properties independent of direction), the flux density $\overrightarrow{B}$ measures how the magnetic field has been magnified inside the material and is often defined by the *permeability* μ.

$$\overrightarrow{B} = \mu_0 \mu_r \overrightarrow{H} \qquad \left[\mathrm{T} = \frac{\mathrm{Wb}}{\mathrm{m}^2}\right] \tag{B.7}$$

where μ_0 is the permeability of free space ($\mu_0 = 4\pi \times 10^{-7}\mathrm{H/m}$) and μ_r is the relative permeability, which is cataloged for several materials[6]. Note that in Example B.1, the B field shown in Figure B.2 is discontinuous because of the abrupt change of material.

The other workhorse of magnetostatics is Guass's law for magnetism. It is a statement about the conservation of *magnetic flux* φ, a quantity closely related to the magnetic flux density $\overrightarrow{B}$. The magnetic flux is obtained by integrating the flux density over some surface area. It is often represented schematically with magnetic flux lines. One can visualize these lines by scatting some iron filings near a strong permanent magnet. The magnetic flux density measures how closely packed these flux lines are in a given cross-sectional area. Note that $\overrightarrow{B}$ is a vector and φ is a scalar.

$$\varphi = \int_{\mathcal{S}} \overrightarrow{B} \cdot d\overrightarrow{S} \qquad [Wb] \tag{B.8}$$

Gauss's Law for magnetism in integral and differential form is

$$\oint_{\mathcal{S}} \overrightarrow{B} \cdot d\overrightarrow{S} = 0, \qquad \nabla \cdot \overrightarrow{B} = 0 \tag{B.9}$$

Since the surface integral of $\overrightarrow{B}$ is the flux, Gauss's law states that the total flux passing through a *closed surface* is zero. That is, no *net* flux enters or leaves a closed surface. In differential form, it states the the divergence of the magnetic field is zero.

[6]Typical values of the relative permeability for ferromagnetic materials is in the range of $10^3 - 10^5$.

In other words, there are no point sources of flux for magnetic fields. This is in contrast to Gauss's law for electricity which states that the divergence of the electric flux density is equal to the electric charge density, $\nabla \cdot \overrightarrow{D} = \rho$.

Example B.2 illustrates the relationship between flux and flux density and motivates the magnetic circuit approach to analysis of magnetic structures.

Example B.2. *(Flux in Toroidal Core [6])*
Obtain the flux density and the flux in the core of Example B.1.

Solution: *Integrate the flux density over the rectangular cross-sectional area. Since H is a function of r (see equation (B.5) in Example B.1), the magnetic field strength varies across the cross-sectional area. To simplify matters, evaluate $B(r) = \mu H(r)$ at $r = (r_b + r_c)/2$ and assume that B has this constant value over the entire cross sectional area. When neglecting the variation of B with respect to r in this way, little error is incurred in the calculation of the flux. Inspecting Figure B.2, one observes that, in a core with a large permeability μ, the percent change of B as a function of radius is very small: see Figure B.2. B is roughly constant in the core due to the large permeability. Let H_c be*

$$H_c = \frac{Ni}{2\pi((r_0 + R_i)/2)} = \frac{Ni}{\ell_c} \tag{B.10}$$

where ℓ_c is length along the mean flux-path. The flux density is given by

$$B_c = \mu H_c = \frac{\mu Ni}{\ell_c}$$

and the flux is

$$\varphi = \int_{\mathcal{S}} \overrightarrow{B} \cdot d\overrightarrow{S} = B_c A_c = \frac{\mu Ni A_c}{\ell_c} = \frac{Ni}{\ell_c/\mu A_c} \tag{B.11}$$

where A_c is the cross-sectional area of the core.

Looking closely at equation (B.11), one notes that the flux in the core is related to the current in the coil by a constant that depends only on the physical geometry

of the core and the core material. It makes sense to group these constants into one quantity called the *reluctance* $\mathcal{R}$.

$$\mathcal{R} = \frac{Ni}{\varphi}, \qquad \left[\frac{\text{A}}{\text{Wb}}\right] \tag{B.12}$$

The product of the current and the number of turns of the coil is called the magnetomotive force (mmf:$= Ni$). It has units of Ampère$A$ or Ampère-turns $A-t$ depending if N is considered a dimensionless quantity. In this work, mmf will have units of Ampère. From Example B.2, the reluctance of the core is given by

$$\mathcal{R} = \frac{\ell}{\mu A} = \frac{\text{length in direction of flux}}{\mu(\text{Area} \perp \text{to flux})}$$

This expression is similar to the resistance of a wire in terms of its geometry.

$$R = \frac{\rho \ell}{A} = \frac{\ell}{\sigma A}$$

with ρ and σ the resistivity and conductivity, respectively.

Equation B.12 motivates the analysis of magnetic structures via circuit analysis techniques. In this analogy, equation (B.12) plays the role of Ohm's law where $\mathcal{R}$ is the resistance, φ is the current and the mmf is the voltage. In fact, the name magnetomotive force is dubbed after the electromotive force (emf), a quantity which is defined as a voltage source. Carrying this analogy further, Kirchhoff's current law (kcl) states that the total current entering a node (or more generally, any closed surface) is zero. This is the expression of Gauss's law for magnetism if flux substituted for current. Kirchhoff's voltage law (kvl) says that the sum of the voltage drops around a loop must balance the sum of the voltage increases. Referring to equation (B.10), one may think of Ni as a mmf increase and $H_c \ell_c$ as a mmf drop. Thus, Ampère's law may be interpreted as the sum of the mmf drops around a loop equals the mmf supplied to the magnetic circuit.

$$\oint_{\mathcal{C}} \overrightarrow{H} \cdot \overrightarrow{d\ell} = \sum_k H_k \ell_k = Ni$$

In summary, the definition of reluctance, Gauss law for magnetism, and amperes law are analogous to ohms law, kcl and kvl, respectively.

Remark 3. *(Large Permeability and the Magnetic Circuit Assumption)*
The simplified analysis of the magnetic circuit approach is possible because the value of μ_r is typically very large, $10^3 - 10^5$ for ferromagnetic materials. Thus, the flux density outside of the highly permeable material may be neglected. That is, assume that there is no leakage flux and that all of the important flux is concentrated in "the circuit". For example, in Figure B.1b, the magnetic circuit approach assumes that the leakage flux density in the range $r < r_a$ and $r > r_d$ is negligible. In general, ferromagnetic materials exhibit nonlinear behavior and the value of μ_r depends on the value of H and its past values (the hysteresis phenomenon). However, the relatively high value of μ_r enables one to linearity approximate B with respect to H (and thus pick a constant μ_r). This hysteresis-masking effect is discussed at length in Section B.3.

Example B.3. *(Application of Magnetic Circuit Concept [20])*
Find the mmf required to produce a flux density of $0.5Wb/m^2$ in the airgap of the magnetic circuit shown in Figure B.3. The constants are $g = 0.1\text{cm}$, $\ell_c = 6\text{cm}$, $A_c = 1\text{cm}^2$, and $\mu_r = 10^4$. Since the permeability of the core is large, assume that there is no leakage-flux. That is, the magnetizing flux occupies only the core and the airgap. Solve this problem using Maxwell's equations and the magnetic circuit approach.

Preliminary Comments: *Obviously, this example is different than Example B.2 in that it has an airgap. Simplifying assumptions are typically made about the behavior of the flux density in the airgap. Before doing so, one can study the situation with Gauss's law. To apply Gauss, a closed surface is required. Consider two cross-sectional areas of the core defined at any two points p_1 and p_2 along the mean-flux path ℓ_c. Let the closed surface be bounded by the core and the two cross-sectional*

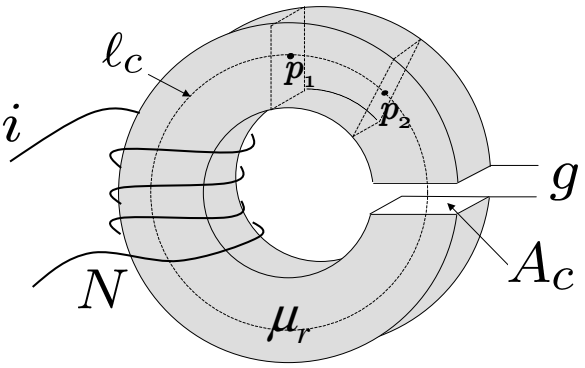

Figure B.3: Toroidal core with airgap.

areas: See Figure B.3.

$$\oint_{\mathcal{S}} \overrightarrow{B} \cdot d\overrightarrow{S} = \int_{p_1} \overrightarrow{B} \cdot d\overrightarrow{S}_1 + \int_{p_2} \overrightarrow{B} \cdot d\overrightarrow{S}_2 + \int_{\text{core}} \overrightarrow{B} \cdot d\overrightarrow{S}_{\text{core}} = 0$$

where the subscripts p_1, p_2 and core of the surface integrals refer to the cross-sectional areas at p_1 and p_2 and the surface of the core. The no-leakage flux assumption implies that the flux inside the core is parallel the the mean flux path, thus, $\overrightarrow{B} \cdot d\overrightarrow{S}_{\text{core}} = 0$. Let $\hat{n}_1$ and $\hat{n}_2$ be the normal vectors to the cross-sectional areas.

$$\begin{aligned}
\oint_{\mathcal{S}} \overrightarrow{B} \cdot d\overrightarrow{S} &= \int_{p_1} \overrightarrow{B} \cdot d\overrightarrow{S}_1 + \int_{p_2} \overrightarrow{B} \cdot d\overrightarrow{S}_2 \\
&= \int_{p_1} \overrightarrow{B} \cdot \hat{n}_1 dS_1 + \int_{p_2} \overrightarrow{B} \cdot \hat{n}_2 dS_2 \\
&= \int_{p_1} \overrightarrow{B} \cdot \hat{n}_1 dS_1 - \int_{p_2} \overrightarrow{B} \cdot \hat{n}_1 dS_2 \\
&= \varphi_1 - \varphi_2 = 0
\end{aligned}$$

This means that the flux at any two points in the magnetic circuit is the same. This means that flux is constant throughout the magnetic circuit.

Now consider the airgap. Recall that a highly permeable material tends to focus the flux. When the flux passes from a highly permeable region to a lowly permeable region, the flux spreads out. This fringing effect, a decrease in the flux density, appears as a bulge in the magnetic field in the vicinity of the airgap. Note, the flux density varies continuously as it crosses the gap: See Figure B.4. One observes that the

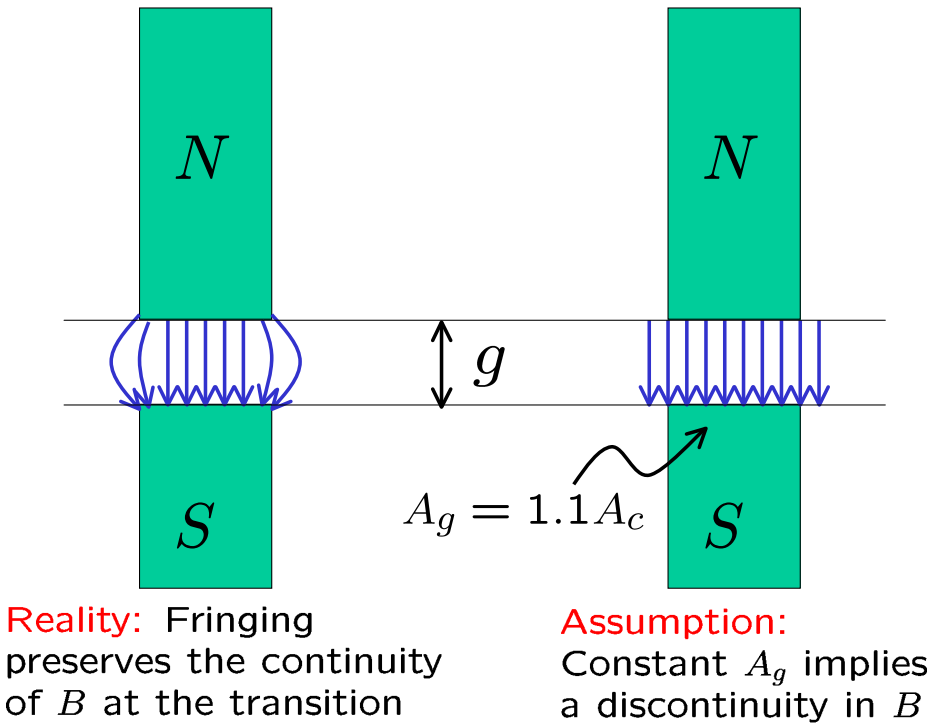

Figure B.4: Fringing in the airgap occurs because flux and flux density are continuous and the airgap cross-sectional area is effectively changing. A constant airgap assumption implies a flux-density discontinuity at the transition.

number of flux lines crossing a given cross-sectional area is much less in the airgap as it is in the core. Now, applying the above analysis to a surface with p_1 *in the core and* p_2 *in the airgap, one finds* $\varphi_{\text{core}} = \varphi_{\text{gap}}$ *and* $B_c A_c = B_g A_g$*. The fringing in the airgap could be captured, for example, by allowing the effective cross-sectional area of the airgap to vary continuously,* $B_g = B_c A_c / A_g(x)$ *with* $x \in [0, g]$*. However, the fringing is typically neglected and only roughly approximated by a constant airgap cross-section which is slightly larger than that of the core. This cross-section is assumed to apply for the entire length of the airgap. For example, let* $A_g = 1.1 A_c$*. This captures the reduction in flux density but artificially introduces a discontinuity in* B*. To see this,*

apply Gauss to find

$$\phi_c = \phi_g$$

$$B_c A_c = B_g A_g$$

$$B_c A_c = B_g 1.1 A_c$$

$$B_c = 1.1 B_g$$

Because the approximate airgap cross-sectional area applies for the entire length of the airgap, a discontinuity in the B field must occur at the transition from iron to air. This discontinuity is an artifact of the assumption. In reality, the fringing in the B field preserves its continuity. It is important not to let the conclusions drawn from simplifying assumptions cloud the understanding of the underlying physics.

Solution: *Apply Ampère's Law.*

$$\begin{aligned} Ni &= \oint \overrightarrow{H} \cdot \overrightarrow{d\ell} \\ &= H_c \ell_c + H_g g \\ &= \frac{B_c}{\mu_0 \mu_r} \ell_c + \frac{B_g}{\mu_0} g \\ &= \frac{B_g A_g}{\mu_0 \mu_r A_c} \ell_c + \frac{B_g}{\mu_0} g \\ &= \frac{(0.5Wb)(1.1)}{(10^4)(4\pi \times 10^{-7}\text{H/m})}(.06\text{m}) + \frac{(0.5\text{Wb})}{4\pi \times 10^{-7}\text{H/m}}(.001\text{m}) \\ &= 2.63 + 398 = 401\text{A} \end{aligned}$$

Thus, a 100 turn coil with 4.01 A could be used to set the required flux density.

Resolve the problem using magnetic circuit assumptions. The equivalent magnetic circuit for this magnetic structure is simple. Since the permeability of the core is large, the reluctance of the core is negligible. This is analogous to neglecting the resistance of the wires in circuit analysis. Thus, the magnetic circuit is just the reluctance of the airgap in parallel with the mmf source. Thus,

$$Ni = \varphi_g \mathcal{R}_g = B_g A_g \mathcal{R}_g = B_g A_g \frac{g}{\mu_0 A_g} = (0.5\text{Wb}) \frac{.001\text{m}}{4\pi \times 10^{-7}\text{H/m}} = 398\text{A}$$

This approach says that a 100 turn coil with 3.98 A could be used to set the required flux density. This approach requires much less work and a gives very close approximation to the answer given by applying Ampère. It is typically the case in magnetic circuits that the airgap reluctance dominates the core reluctance and the magnetic circuit approach is well justified. Indeed, the reluctances are

$$\mathcal{R}_g = \frac{g}{\mu_0 A_g} = 7.2343 \times 10^6 \frac{\text{A}}{\text{Wb}}, \qquad \mathcal{R}_c = \frac{\ell_c}{\mu_0 \mu_r A_c} = 4.7746 \times 10^4 \frac{\text{A}}{\text{Wb}}$$

and the gap reluctance dominates by a factor of 100. This is due the presence of μ_r in the denominator of $\mathcal{R}_c$. Consequently, only a mmf of $H_c \ell_c = \varphi R_c = 2.63$ A is required to excite the core, however, a mmf of $H_g g = \varphi R_g = 398$ A is required to energize the airgap.

Remark 4. *(Magnetic Circuit Approach vs. Maxwell's laws)*
It should be apparent from the previous example that the magnetic circuit approach is only an approximate technique and depends heavily on the relative magnitudes of the permeabilities (or equivalently, the reluctances). Note that if the core was made out of a non-ferromagnetic material, the magnetic circuit approach would be totally inappropriate. Furthermore, it often depends on using rule of thumb factors to accommodate for factors such as fringing. The power of the magnetic circuit approach is in its ability to quickly produce good approximations and to allow the user to draw conclusions based on familiar circuit analysis ideas. However, in many cases, one must resort to directly applying Ampère's Law and the continuity of the magnetic flux.

The following example illustrates circuit analysis techniques on a multi-flux-path magnetic structure.

Example B.4. *(A Multi-Path Magnetic Circuit [20])*
The magnetic circuit in Figure B.5 has two parallel airgaps. Find the inductance, the total flux, the individual fluxes and the flux densities in the airgaps.

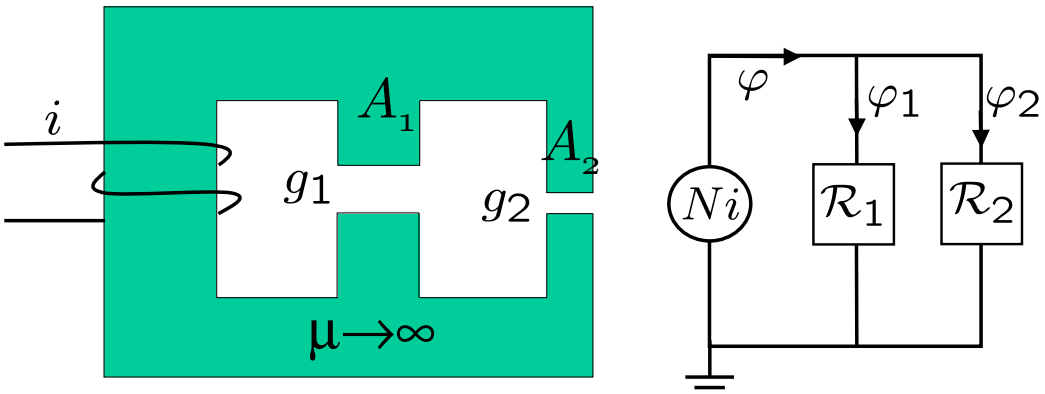

Figure B.5: Magnetic structure and equivalent magnetic circuit.

Solution: *The equivalent magnetic circuit is shown in Figure B.5. The flux generated by the mmf splits and feeds into the two airgaps. Each reluctance is given by*

$$\mathcal{R}_1 = \frac{g_1}{\mu_0 A_1}, \qquad \mathcal{R}_2 = \frac{g_2}{\mu_0 A_2}$$

To find the total flux φ, calculate the total reluctance. $\mathcal{R}$ is given by the parallel combination of $\mathcal{R}_1$ and $\mathcal{R}_2$.

$$\mathcal{R} = \frac{\mathcal{R}_1 \mathcal{R}_2}{\mathcal{R}_1 + \mathcal{R}_2}$$

Thus, the total flux is

$$\varphi = \frac{Ni}{\mathcal{R}} = \frac{N(\mathcal{R}_1 + \mathcal{R}_2)}{\mathcal{R}_1 \mathcal{R}_2} i$$

Since the reluctances are in parallel, the flux-divider rule, which is equivalent to the well known current-divider rule from circuit theory, can be used to find the individual fluxes φ_1 and φ_2 from φ. Applying the flux-divider rule

$$\begin{aligned} \varphi_1 &= \varphi \frac{\mathcal{R}_2}{\mathcal{R}_1 + \mathcal{R}_2} \\ &= Ni \frac{(\mathcal{R}_1 + \mathcal{R}_2)}{\mathcal{R}_1 \mathcal{R}_2} \frac{\mathcal{R}_2}{\mathcal{R}_1 + \mathcal{R}_2} \\ &= \frac{Ni}{\mathcal{R}_1} \end{aligned} \qquad \begin{aligned} \varphi_2 &= \varphi \frac{\mathcal{R}_1}{\mathcal{R}_1 + \mathcal{R}_2} \\ &= Ni \frac{(\mathcal{R}_1 + \mathcal{R}_2)}{\mathcal{R}_1 \mathcal{R}_2} \frac{\mathcal{R}_1}{\mathcal{R}_1 + \mathcal{R}_2} \\ &= \frac{Ni}{\mathcal{R}_2} \end{aligned}$$

Note that fluxes could have also been directly obtained with Ohm's law if one realizes that the mmf across both reluctances is the same. The individual flux densities are

given by

$$B_1 = \frac{\varphi_1}{A_1} = \frac{\mu_0 N i}{g_1}, \qquad B_2 = \frac{\varphi_2}{A_2} = \frac{\mu_0 N i}{g_2}$$

The inductance, which is defined in Section B.2, for the magnetic circuit is

$$L := \frac{N^2}{\mathcal{R}} = \mu_0 N^2 (\frac{A_1}{g_1} + \frac{A_2}{g_2}) = L_1 + L_2$$

B.2 Magnetodynamics: Faraday's Law

Ampère's law and Gauss's law for magnetism describe steady-state phenomena (i.e. magnetostatics). Faraday's law governs magnetodynamics. Consider again the basic example of a coil and the circular core with rectangular cross-section. Faraday's law relates the rate of change of flux inside the core to the voltage induced at the terminals of an *ideal* coil. If the core is highly permeable, magnetic circuit assumptions are valid and one considers only the flux inside the core. Previously stated in equation (B.1a) of Maxwell's laws, Faraday's law is restated and interpreted here.

$$\oint \overrightarrow{E} \cdot \overrightarrow{d\ell} = -\frac{d}{dt} \int_{\mathcal{S}} \overrightarrow{B} \cdot \overrightarrow{ds}$$

To apply Faraday to a coil, select the contour of integration $\mathcal{C}$ for the circulation integral to coincide with one turn of the coil. The surface of integration for the flux integral is the cross-sectional area of the coil.

Recall that the electric field $\overrightarrow{E}$ has units of N/C. The integral the electric field with respect to position results in units of Nm/C = J/C := V = volts. The voltage is a potential energy density per unit charge. Each winding on the coil constitutes a loop in which a voltage will be induced.

$$v_{\text{turn}} = -\frac{d}{dt} \int \overrightarrow{B} \cdot \overrightarrow{ds} = -\frac{d\varphi}{dt}$$

The total coil voltage is then given by

$$v_{\text{coil}} = -N \frac{d\varphi}{dt} \tag{B.13}$$

where the flux φ is assumed to link all of the N turns. Equation (B.13) is similar to the form in which it was stated by Faraday. Note that a coil may be used in to modes. When used as an electromagnet, the coil voltage is the input and the resulting flux is the output. When the coil is used as the secondary of a transformer, the changing flux is assumed as the input and the induced voltage is the output.

The negative sign, which governs the voltage polarity, makes equation (B.13) consistent with Len's law. It says that if the terminals a and b in Figure B.6 are shorted so that current can flow, then the changing flux induces a current in the direction to *oppose* the change of flux. To illustrate, suppose that in the Figure B.6, the flux is increasing ($\frac{d\varphi}{dt} > 0$) in the direction shown. Then, if the terminals are shorted, current must be induced so that it generates flux to oppose the changing flux. Using the right-hand-rule, downward flux is generated by current flowing from

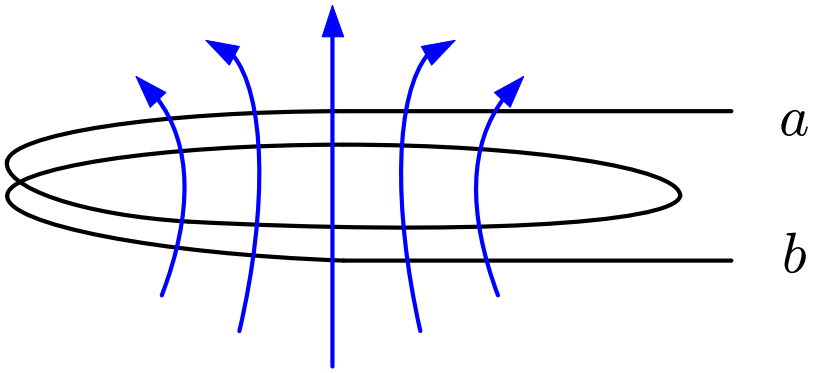

Figure B.6: A single coil in presence of magnetic field.

terminal b, through the coil, and then to terminal a. In this case, one views the input as the changing flux and the output as the induced voltage at ab. When the coil is viewed from an external perspective as in the secondary of a transformer, terminal a should be marked as positive and terminal b should be marked as negative because current flows out of terminal a and into b as viewed from the outside. When viewed as an electromagnet, flux is produced upward in accordance with the right-hand-rule when current flows from terminal a to b. Again, terminal a is marked positive and b

negative.

Using *flux-linkage*, defined as $\lambda = N\varphi$, Faraday's law becomes

$$\dot{\lambda} = v_{\text{coil}}$$

The *inductance* is defined as the ratio of flux-linkages to current,

$$L = \frac{\lambda}{i} \tag{B.14}$$

Assumption 1. *In general, when using permeability or inductance, a linearized model for the core is implicitly assumed and the nonlinear characteristics are neglected.*

Using the inductance in Faraday's law,

$$v_{\text{coil}} = \frac{d\lambda}{dt} = L\frac{di}{dt} + \frac{dL}{dt}i$$

Of course, if L is constant, one obtains the law for the inductor. Inductance is related to the reluctance by

$$L = \frac{\lambda}{i} = \frac{N\varphi}{i} = \frac{N}{i}\frac{Ni}{\mathcal{R}} = \frac{N^2}{\mathcal{R}}$$

Also, expressing the inductance in terms of geometry of the magnetic circuit,

$$L = \frac{N^2\mu_0 Ag}{\ell_c} \tag{B.15}$$

Equation (B.15) is used as a basic inductor design equation for toroidal inductors.

B.3 Electromagnet Core Nonlinearity

In Section B.1, the flux density B was defined with the simple relation

$$\overrightarrow{B} = \mu_0\mu_r\overrightarrow{H}$$

This linear relationship is quite often very useful. When the permeability of the magnetic material is large and the levels of current in the coil are small, a linear relationship between B and H may be appropriate. Also, in a gapped magnetic

circuit, the airgap reluctance often dominates the core reluctance. A perfectly good engineering approximation may be to neglect the core reluctance. However, there are situations when the core nonlinearity is significant. When the magnetic circuit is excited with large current or flux levels, the magnetic core may saturate. Also, in magnetic circuits with moveable parts, like a magnetic bearing for instance, the reluctance of the airgap may reduce to a level comparable to that of the core when the airgap is small. In this case, it may be inappropriate to neglect the core reluctance. The following sections illustrate the complexity of the core nonlinearity and outline when it may be appropriate to neglect it.

B.3.1 Magnetic Materials and Hysteresis

In ferromagnetic materials, the $\overrightarrow{B}$ field is related to the $\overrightarrow{H}$ field by a *hysteresis function*. A typical BH curve is shown in Figure B.7a. Starting at the origin, an increase in H produces an increase in B until saturation B_{sat} at a value of H_{max}, typically somewhere between 1.0-2.0 T (determined by material). The B field increases because the applied magnetic field is realigning the magnetic domains in the material so that they generally point in the same direction. The B field saturates when all of the domains are aligned. As H is decreased, a different path is followed. At $H = 0$, there is some residual flux density. This is known as the *remanence* or *residual flux density*.

When the excitation field/current is turned off, the magnetic domains do not get randomized. The magnetic moments naturally align themselves along certain directions related to the crystal structure of the material. These directions are known as the *axes of easy magnetization*. When the magnetizing field is cut off, the domains choose the axis closest to the direction of the magnetizing field. A net magnetization results. This is the cause of the remanent flux density and the hysteresis effect. The magnetic field must be reduced a negative value called the *coercive force* to eliminate

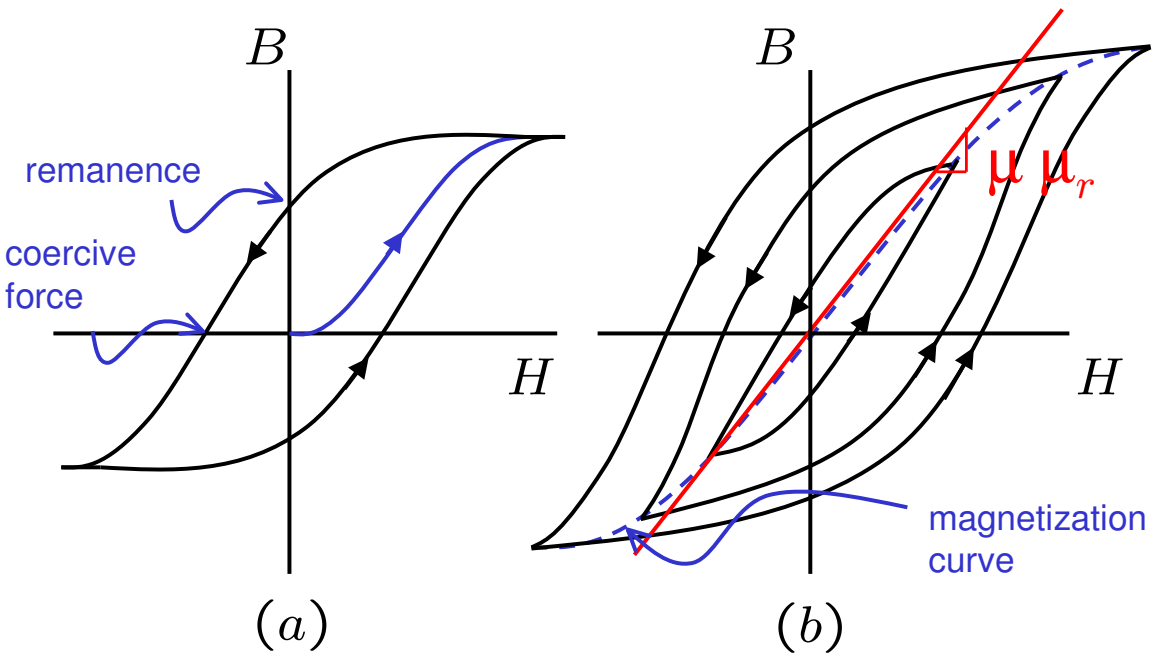

Figure B.7: Hysteresis curves: **(a)** Illustration of one hysteresis curve, the definitions of remanent flux and coercive force **(b)** a family of hysteresis curves, the magnetization curve, and the permeability approximation

the remanence. By further reducing $H = -H_{\max}$ and then to $H = H_{\max}$, a full hysteresis loop is traversed. Hysteresis exists because it takes energy to realign these magnetic domains. The amount of energy expended per cycle is determined by the area enclosed by the Hysteresis curve[7].

Materials with large coercivities, hard materials, make good permanent magnets while materials with small coercivities, soft materials, make good temporary magnets. Electromagnet cores are made from soft materials so that the electromagnet has a smaller coercivity to overcome when trying to produce a desired force. Because soft cores have smaller coercivities, they should also have smaller energy loss per cycle.

Note, however, the hysteresis behavior is more complex. If the direction of H is reversed (when $H \neq H_{\max}$) a new hysteresis curve is started. The commonality between the family of curves generated by different values of $H_{\max}$ is the line that

[7]Actually, the area enclosed by the BH curve is the volumetric energy density loss per cycle. Energy analysis is discussed at length in Section D.

connects the end points of the curves. This curve, shown dotted in Figure B.7b, is called the *(DC) magnetization curve* and is a function of only the material. Also shown is a linear approximation to this curve. This line has a slope that corresponds to the permeability μ. The permeability is a good estimate to the DC magnetization curve for values of H in which the core is not in saturation. It is a poor estimate when the core saturates or when the area enclosed by the BH curve is large. As will be shown in Section B.3.2, eddy-current generation within the core causes the area enclosed by the BH curve to increase. The increase in enclosed area is directly proportional to the excitation frequency. Thus, when constructing the DC magnetization curve from experimental data, the frequency of sinusoidal excitation should be small[8] to avoid corruption of the BH curve from eddy currents: see further discussion on BH curve generation in Chapter 6.

To construct a BH curve for a core, one may use an amplifier in current mode or voltage mode. In voltage mode, the amplifier is used to set V_{coil} to be sinusoidal. Faraday's law dictates that the flux will also be sinusoidal. In general, the resulting current is nonlinear. Note that for small peak values of the magnetizing flux, the resulting current may look like an amplitude scaled, phase-shifted sinusoid, and thus, a linear model for the BH curve may be a good approximation. However, as the peak magnetizing flux increases, the saturation and the larger enclosed area of the hysteresis curve severely distort the current. Illustrated in Figure B.8, the voltage V_{coil} and flux φ are sinusoidal and always 90° out of phase. However, the current and the flux relationship is quite complex. The $\varphi - I$ curve[9] is shown to the right. The flux and current rise and fall together, however, to say that they are in phase would be incorrect. The flux and current peak together but *do not share zero crossings*. This fact is very important when trying to determine the flux from current and airgap

[8]Note that the "DC" in DC magnetization curve means low frequency.

[9]This curve is equivalent to the BH curve because B and H can be calculated from the Ampère's law and the definition of flux density (see Section B.1).

measurements as described in Chapter 6. To illustrate this fact, several key times have been identified in Figure B.8. At time t_1, the the flux and current peak together. As the sinusoidal flux decreases, the current passes through zero for a non-zero value of the flux (t_2 on the figure). As the flux decreases to zero, the current becomes positive.

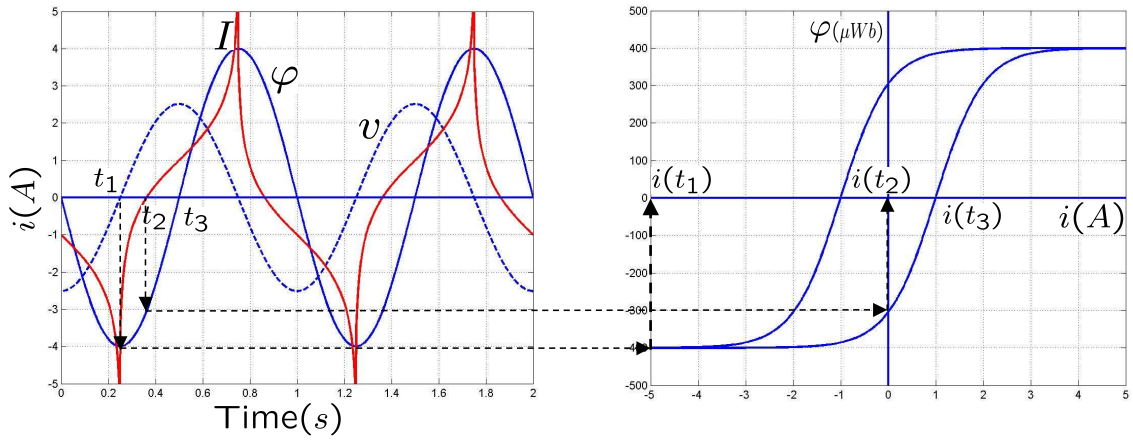

Figure B.8: Example of AC nonlinear core excitation in voltage mode with corresponding $\varphi - I$ curve. Note that the signals have been scaled to make viewing easier. Use a voltage mode amplifier to set a $1Hz$ ($\omega = 2\pi$) sinusoidal excitation $v_{\text{coil}} = -\omega 400\cos(\omega t)$ mV: v is displayed in volts above. By Faraday, the flux is $\varphi = \int v_{\text{coil}} dt = -400\sin(\omega t)$ μWb: $\frac{\varphi}{100}$ is plotted above. The current, shown in Amps, is related to the flux by the $\varphi - I$ curve.

One may also use an amplifier in current mode to construct a BH or $\varphi - I$ curve. In this mode, the current is commanded to be sinusoidal. As in voltage mode, the current and the flux peak together, but have different zero crossings. For small excitation currents, each signal may be sinusoidal and a linear model for the BH relationship may be appropriate. However, as the current level increases the flux in the core saturates and the voltage signal is highly distorted.

Observe that the quantities of permeability, inductance and reluctance are all tools used to estimate the DC magnetization curve. The nonlinear behavior is grossly approximated with a straight line. Depending on what is plotted, this straight line is given one of the following names: reluctance, inductance, or permeability. Consider

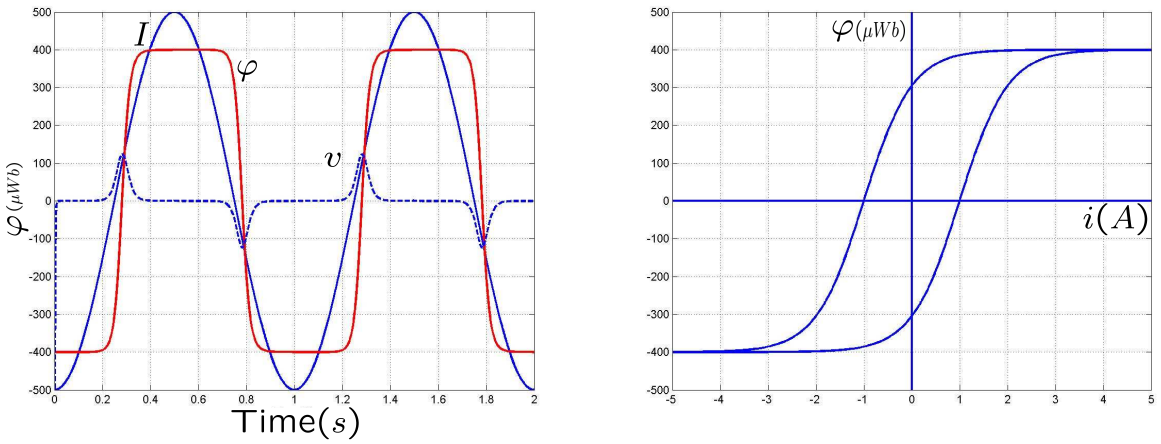

Figure B.9: Example of AC nonlinear core excitation in current mode with corresponding $\varphi - I$ curve. Note that the signals have been scaled to make viewing easier. The current is set to a 1Hz ($\omega = 2\pi$) sinusoidal excitation $I = 5\sin(\omega t)$ A: $100I$ is shown above. φ in μWb is shown unscaled. Faraday relates the voltage to the flux $v = \dot{\varphi}$: $10v$, with v in mV, is plotted above.

Figure B.10 where plots of the BH curve, the $\varphi - NI$ curve, and the $\lambda - I$ curve are shown. These plots model the same phenomenon, but with the axis re-scaled. See Table B.2 for a summary.

Table B.2: Permeability, reluctance and inductance comparison

	Permeability	scale by	**Reluctance**	scale by	**Inductance**
vertical axis	B	A_c	φ	N	λ
horizontal axis	H	ℓ_c	Ni	$1/N$	i

B.3.2 Magnetic Core Losses

The losses in the magnetic material are due to two factors. The eddy-current losses and hysteresis losses. Eddy-current losses are ohmic in nature. Hysteresis losses are due the the fact that it takes energy to realign the magnetic domains in the core material.

Eddy currents are a direct consequence of Faraday's law. A laminated magnetic core and cross-section are shown in Figure B.11. For the direction of the current shown, the $\overrightarrow{B}$ field is increasing into the page. Note that the eddy currents themselves produce an additional flux! Moreover, this additional flux is *always* directed to oppose

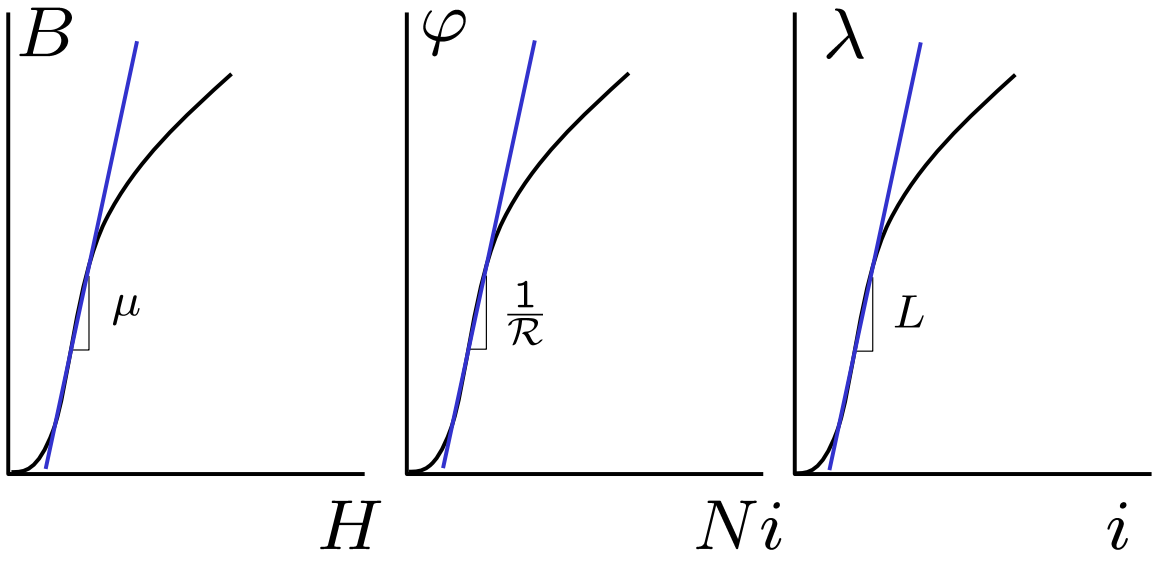

Figure B.10: Comparison of Reluctance, Inductance and Permeability. They are all the same thing, just plotted on re-scaled axes. See Table B.2.

the changing flux. This fact, as stated in Section B.2, is a consequence of Len's law and is the source of the minus sign in Faraday's law. Since the eddy currents are induced to oppose the direction of the increasing magnetic field, the eddy currents produce a field that is out of the page. Using the right hand rule, the eddy currents are shown counterclockwise in the Figure B.11.

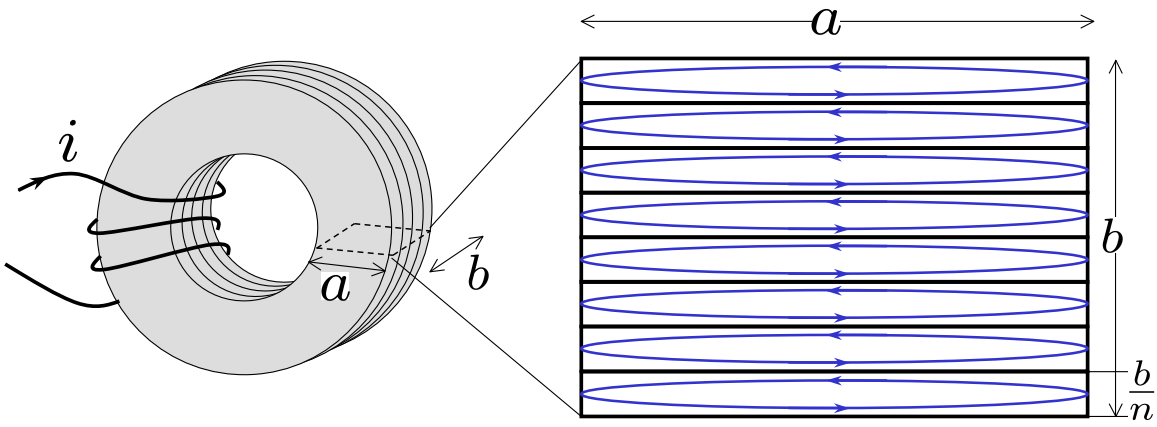

Figure B.11: Laminated magnetic core and cross-section. The flux is increasing into the page. Eddy-currents are induced in the direction shown.

Lamination of the iron core reduces eddy-currents. The core is constructed of thin sheets of magnetic material that are separated with thin coatings of highly resistive

material. Such a coating may consist of a thin layer of oxidation and a sealant or varnish. A typical lamination in a power application ranges from $0.5 - 5\ mm$. The ratio of the actual magnetic material to the actual cross sectional area is called the stacking factor. The stacking factor increases as the lamination thickness decreases.

Faraday is now evaluated on a lamination to determine the eddy-current power dissipation. Let the path of integration for

$$\oint \overrightarrow{E} \cdot \overrightarrow{d\ell} = -\int \frac{d\overrightarrow{B}}{dt} \cdot \overrightarrow{ds}$$

be the perimeter of a lamination. The minus sign is accounted for by taking E in the direction of eddy-current flow. Assume thin laminations: $a >> b/n$ where $A_c = ab$ and n is the number of laminations. The circulation integral under the thin lamination assumption becomes

$$\oint \overrightarrow{E} \cdot \overrightarrow{d\ell} \approx 2aE$$

where the value of the electric field is assumed constant along the perimeter. Assuming a uniform flux density over the lamination cross section,

$$\int \frac{d\overrightarrow{B}}{dt} \cdot \overrightarrow{ds} = \frac{dB}{dt} a \frac{b}{n}$$

Thus,

$$E = \frac{dB}{dt}\frac{b}{2n} \tag{B.16}$$

Note that the value of E depends linearly on the lamination thickness $t_\ell \equiv b/n$. The power loss *per unit volume* of the lamination is $\sigma E(t)^2$, where σ is the conductivity: Recall the DC power loss in resistors is $\frac{V^2}{R}$. The *average* value of $\sigma E(t)^2$ over the lamination relates to the real power loss.

$$\begin{aligned}(E^2)_{ave} &= \frac{\int_0^{b/2n}\left(\frac{dB}{dt}\right)^2 y^2 dy}{\frac{b}{2n}} \\ &= \frac{2n}{b}\left(\frac{dB}{dt}\right)^2 \frac{y^3}{3}\Big|_0^{b/2n} \\ &= \frac{1}{3}\left(\frac{dB}{dt}\right)^2\left(\frac{b}{2n}\right)^2 \end{aligned} \tag{B.17}$$

Now consider the special case of sinusoidal time variation of the flux density.

$$B = B_{\max}\sin(\omega t + \psi), \qquad \frac{dB}{dt} = \omega B_{\max}\cos(\omega t + \psi)$$

$$\left(\frac{dB}{dt}\right)^2 = \frac{4\pi^2 f^2 B_{\max}^2}{2}[1 + \cos(2\omega t + 2\psi)]$$

Using the above in equation (B.16), and taking the time average over one period, the *power loss per unit volume* in Watts per cubic meter is

$$p_e = \frac{\sigma}{6}\pi^2 f^2 B_{max}^2 t_\ell^2 \qquad [\mathrm{W/m^3}]$$

Typically, the above is written as

$$p_e = K_e(f B_{max} t_\ell)^2 \qquad [\mathrm{W/m^3}] \tag{B.18}$$

which shows how the eddy-current loss depends on the excitation frequency, the lamination thickness, and the amplitude of the excitation flux density. The constant K_e depends on the conductivity.

The energy loss per unit volume *per cycle* is also important.

$$w_e = \frac{p_e}{f} = K_e f(B_{\max} t_\ell)^2 \qquad [\mathrm{J/m^3}] \tag{B.19}$$

Since the energy loss in each cycle is proportional to the area enclosed by the BH curve, equation (B.19) suggests that the area inside of the hysteresis curve increases with frequency. This is illustrated in Figure B.12.

Losses due to hysteresis are more difficult to deal with analytically and empirical relationships are customarily used. It is determined – typically at low frequency to avoid interference from eddy-current effects – that the area inside the BH curve is proportional to $B_{\max}^q$ where q is empirically determined. The energy dissipated due to hysteresis loss per cycle per unit volume is

$$w_h = K_h(B_{\max})^q \qquad [\mathrm{J/m^3}] \tag{B.20}$$

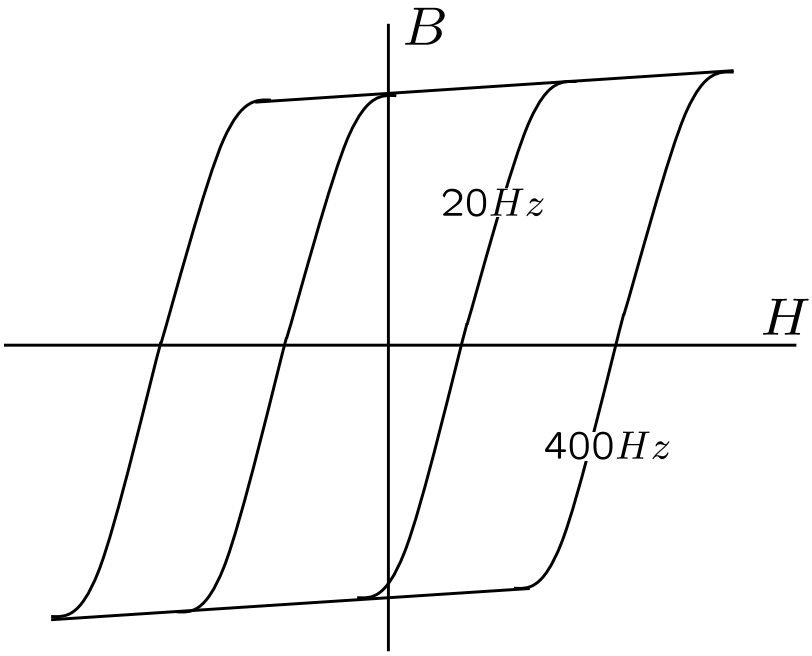

Figure B.12: Effects of eddy-current losses on the BH curve with frequency.

and the power loss per unit volume is then

$$p_h = f w_h = K_h f (B_{\max})^q \qquad [\mathrm{W/m^3}] \tag{B.21}$$

The constant q ranges from $1.5 - 2.5$ and is cataloged for materials. Thus, the total power losses per unit volume is the sum of the hysteresis and eddy-current losses.

$$p = p_h + p_e \qquad [\mathrm{W/m^3}]$$

Manufacturers publish core loss charts with their product. The total core loss is usually given per unit volume or per unit weight. Charts are plotted as total power loss as a function of $B_{\max}$ (with f as a parameter) or plotted vs f (with $B_{\max}$ as a parameter).

B.3.3 Effect of Airgap on Hysteresis Nonlinearity

The introduction of an airgap into a magnetic circuit affects the nonlinear behavior of an electromagnet in several interesting ways. With a closed core as in Example B.1, hysteresis dominates the AC behavior of the magnetic circuit. When an airgap

is introduced as in Example B.3 and Figure B.3, the hysteresis effect is masked by the airgap reluctance [32]. To see this, again consider the magnetic circuit of Figure B.3 where $A_c = A_g = 1\text{cm}^2$, $\ell_c = 6\text{cm}$, $\mu_r = 10^4$. The relationship between the excitation mmf and the resulting flux is studied for several values of g.

Using Ampère's law to analyze the circuit, one obtains

$$\begin{aligned} NI &= H_c\ell_c + H_g g \\ &= H_c(B_c)\ell_c + \frac{B_g}{\mu_0} g \end{aligned}$$

where H_c and H_g are the core and gap magnetic field strength, respectively. In the second equation, the function $H_c(B_c)$ represents the nonlinear hysteretic relationship between H and B in the core. Also, the air presents no nonlinearity and the linear relation, characterized by the permeability of free space, $B_g = \mu_0 H_g$ holds. Since the core has a large relative permeability and the airgap is small compared to ℓ_c, it is temporarily assumed that all the flux passes through the core and the airgap (i.e. no leakage-flux), $\varphi_g = \varphi_c = \varphi$. In this case, conservation of flux dictates

$$\varphi = B_g A_g = B_c A_c$$

Plugging into Ampère's Law, the following nonlinear equation relating φ and I is found

$$\begin{aligned} NI &= H_c(\frac{\varphi}{A_c})\ell_c + \frac{\varphi g}{\mu_0 A_g} \\ &= H_c(\frac{\varphi}{A_c})\ell_c + \varphi\mathcal{R}_g \end{aligned} \tag{B.22}$$

In words, equation (B.22) states that the mmf NI supplied by the coil drops across the airgap and the core. As in magnetic circuit analysis, the airgap drop in terms of reluctance is φR_g. The mmf drop across the core is calculated from the core nonlinear BH curve: such data can be obtained from manufacturer's specifications. Thus, given the manufacturers data, equation (B.22) estimates the effect of adding an airgap into the magnetic circuit on the $\varphi - I$ curve.

To illustrate the effect of adding an airgap into a magnetic circuit, the following equation is used to represent the BH curve nonlinearity in place of manufacturer's specifications

$$B(H) = 2B_{\text{sat}}\Big(\frac{1}{1+e^{-\alpha(H+h_c)}} - \frac{1}{2}\Big) \tag{B.23}$$

where $B_{\text{sat}} = 2T$ is the saturation flux density, $h_c = \pm 500\text{A/m}$ is the coercive force, and $\alpha = .004$ relates to the slope of the BH curve at $B = 0$. Recall that the core nonlinearity is represented by a *family* of BH curves where each loop depends on the amplitude of the excitation. The largest BH loop (one which encloses the most area) is generated by an excitation that drives the core into saturation. Consider a magnetic field excitation $H_{\max}\cos(\omega t)$ that drives the core just into saturation with $H_{\max} = 2000\text{A/m}$. When H is increasing, $h_c = -500\text{A/m}$. When H is decreasing, $h_c = 500\text{A/m}$. This BH loop is shown in Figure B.13a.

The core nonlinearity can also be examined via the flux and the mmf. Rescaling the axes ($\varphi = BA_c$ and mmf$= H_c\ell_c$) in Figure B.13a, this map is shown in Figure B.13b. This particular $\varphi - NI$ curve saturates at $\Phi_{sat} = 200\mu\text{Wb}$ when $NI = 150\text{A}$. Note that the mmf that corresponds to the coercive force is $mmf_c = h_c\ell_c = 30\text{A}$.

The effect of adding an airgap is illustrated in Figure B.13c where equation (B.22) has been evaluated for $g = 0, 5, 10, 20, 30$, and 40 mils. The total reluctance of the circuit increases when an airgap is present, thus, more mmf is required to generate the same level of flux. Since $\mathcal{R}_g = g/\mu_0 A_g$, the magnetic circuit reluctance will increase with airgap. Also, since $\varphi/NI = 1/\mathcal{R}$, the slope (for instance the slope at $\varphi = 0$) of the $\varphi - NI$ curve will decrease as the airgap and reluctance increase. This is observed in Figure B.13c.

Note that the remanent flux $\varphi_r = A_c B_r$ reduces as the airgap increases. Recall that this is the residual magnetization of the core when the excitation field is turned off. On the other hand, the coercive force (and mmf_c) is independent of the airgap. As a result, the area enclosed by the $\varphi - NI$ curve appears to be independent of

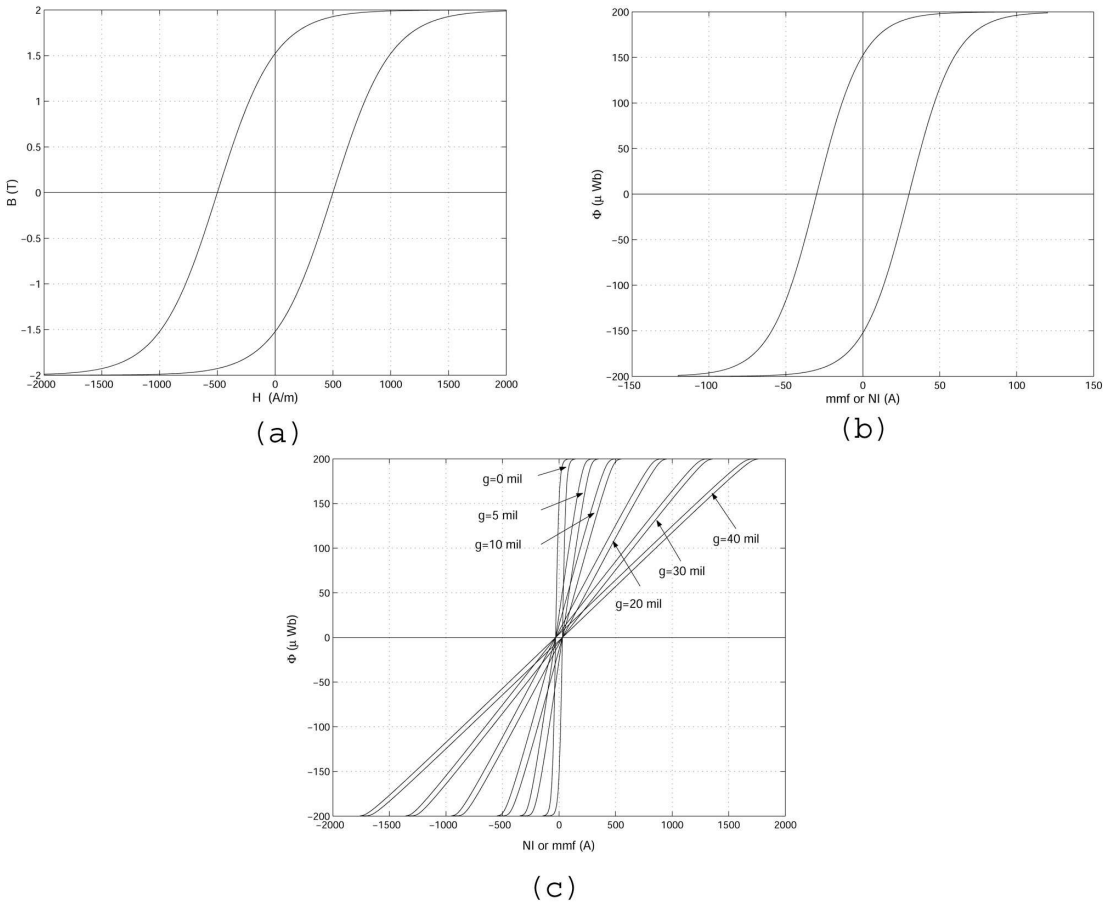

Figure B.13: **(a)** BH curve generated by equation (B.23). **(b)** The corresponding $\varphi - NI$ curve. **(c)** Several $\varphi - NI$ curves for airgap values $g = 0, 5, 10, 20, 30, 40$ mils.

the airgap. This is consistent with the fact that core loss (directly proportional to the enclosed area) depends only on loss mechanisms related to the core material and structure, not on the airgap.

Note that for a material with a small coercive force, the hysteresis curve would appear very "thin" (i.e., it would not enclose much area) in Figure B.13c. The DC magnetization curves for each value of g may be a good estimate of the hysteresis nonlinearity in this case. In such a situation, the complex hysteresis nonlinearity reduces to a saturation nonlinearity. Moreover, as the airgap increases, the mmf required to excite the core is a very small percentage of that required to magnetize the airgap. This is further motivation to neglect the multi-valued nature of the hysteresis

nonlinearity and estimate the nonlinear behavior with the DC magnetization curves[10]. To make this clear, consider equation (B.22) again, however, approximate the BH curve with $B_c = \mu_0 \mu_r H_c$ for values of H_c that do not saturate the core.

$$NI = \varphi \frac{\ell_c}{\mu_0 \mu_r A_c} + \varphi \frac{g}{\mu_0 A_g} = \varphi(\mathcal{R}_g + \mathcal{R}_c)$$

Since $\mu_r = 10^4$, the core reluctance is much smaller than the gap reluctance, leading to nearly a linear relationship between φ and I. The airgap reluctance dominates the RHS of equation (B.22) in practically all instances, except when the airgap is very small. As a consequence of the airgap dominance, the percentage of the supplied mmf Ni that drops across the airgap is much larger than that required to excite the core since

$$\frac{\varphi \mathcal{R}_g}{Ni} >> \frac{\varphi \mathcal{R}_c}{Ni}$$

It is this airgap dominance that enables one to apply magnetic circuit analysis rules to magnetic circuits *that are not in saturation.*

In realistic situations, the assumption of zero leakage-flux is not always valid. Figure B.14a illustrates the difference between the measured airgap flux, the leakage flux, and the fringing flux. The main flux leaves the face of the electromagnet and reaches the target to create the electromagnet force. A flux sensor is typically placed in the airgap or as close a possible to the face of the electromagnet pole to measure this flux. Fringing flux leaves the electromagnet, not necessarily through the pole face, spreads out resulting in reduced flux density, and also reaches the target to contribute to the EM force. However, since this flux spreads out, it may not be detected by the flux sensor when the fringing is significant. Leakage flux leaves the EM through surfaces other than the pole face and does not interact with the target. This flux is not detected by the flux sensor.

[10]In such a situation when it is appropriate to neglect the hysteresis, the flux and the mmf practically share the same zero crossings. This fact becomes important when trying to measure the flux from current and position measurements: see Chapter 6

In Figure B.13c, the saturation flux level is constant for each airgap length. However, as the airgap increases, the flux fringing and leakage increase. Since less flux crosses the sensor path, the saturation knee appears to be lower for increasing airgap. This is illustrated in Figure B.14b. Note that this variation of the flux-saturation

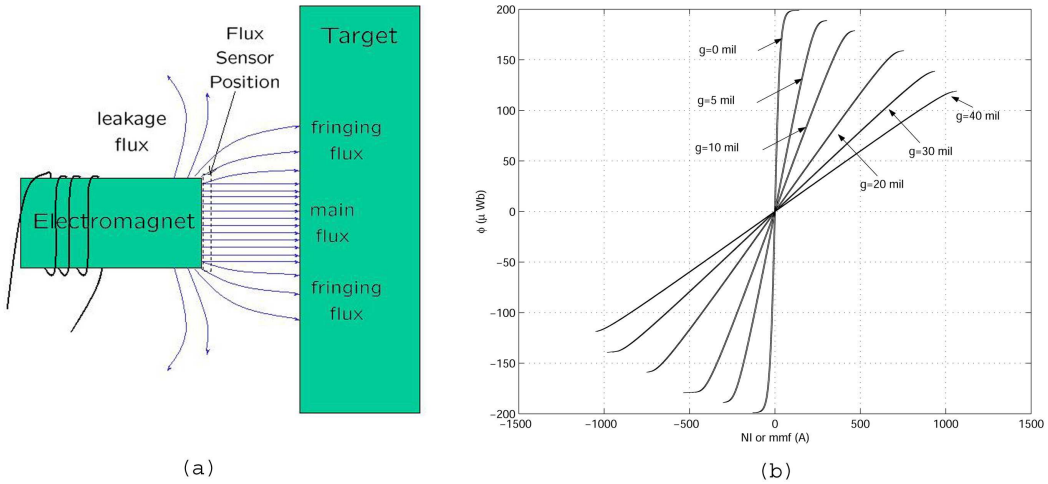

Figure B.14: (a) Illustration of main flux, fringing flux, and leakage flux. **(b)** Due to increased flux leakage and fringing, the saturation knee gradually gets lower as the airgap increases.

knee with position may be modelled by

$$\varphi_a = \rho(g)\varphi \tag{B.24}$$

where φ is the magnetic circuit flux, φ_a, called the *airgap flux*, is the flux that crosses the airgap to interact with the target, and $\rho(g)$ is an airgap-dependent *flux-spreading* or *flux-leakage* function. It has the form

$$\rho(g) = \frac{1}{\rho_1 + \rho_2 g} \tag{B.25}$$

where the constants ρ_1 and ρ_2 are determined from experiment.

APPENDIX C

THE LORENTZ EQUATION

The force on an electric charge is governed by the Lorentz equation

$$\overrightarrow{F} = q(\overrightarrow{E} + \overrightarrow{v} \times \overrightarrow{B}) \tag{C.1}$$

The electric force is in the direction of the electric field and the magnetic force is perpendicular to the $v - B$ plane. For a positive charge q, the right hand rule for cross products indicates the direction of the magnetic force. Recall that the thumb, index finger and middle finger point in the direction of $\overrightarrow{v}$, $\overrightarrow{B}$, and $\overrightarrow{F}$, respectively. On the other hand, if q is a negative charge, the force will be in the opposite direction (or one could employ the left hand).

In machines, free charges are rarely encountered and one is more concerned about the net force a current-carrying wire feels in the presence of a magnetic field. Recall that the total charge in a volume of wire is neutral: the fixed positive charge of the metal lattice is countered by the "free", gas-like electrons. Forces on the moving electrons are transmitted to the lattice structure by Coulomb forces. The convention of positive current flow (holes) is assumed in the following discussion. Recall that the current in terms of the charge density ϱ and charge drift velocity v_d is

$$i = \varrho v_d \tag{C.2}$$

Note that a positive charge density has the same magnitude but opposite drift velocity of a negative charge density. The drift velocity of the electrons for typical current levels is relatively slow, 10^{-4}m/s. However, the current flow in a wire can increase very rapidly because of the extraordinarily high charge density in metals. The number

of electrons in the valance band of copper is on the order of 10^{29}e/m^3 resulting in a charge density of about 10^{10}C/m^3. Thus, you can flip a switch and have a lamp turn on almost instantly, but walk across the room to the lamp itself before the actual electrons at the switch get there.

To find the net force on the wire due to the forces on the electrons, consider a differential length of wire with linear charge density ϱ. The charge in this differential element of a thin conductor is thus given by $q = \varrho d\ell$. The differential force due to this differential current element is

$$\begin{aligned} d\overrightarrow{F} &= q(\overrightarrow{v_d} \times \overrightarrow{B}) \\ &= \varrho d\ell(\overrightarrow{v_d} \times \overrightarrow{B}) \\ &= id\ell(\frac{\overrightarrow{v_d}}{v_d} \times \overrightarrow{B}) \\ &= i\overrightarrow{d\ell} \times \overrightarrow{B} \qquad [\text{N}] \end{aligned} \tag{C.3}$$

With the simple situation of the B field at right angles to the conductor, the familiar equation for the force felt by a conductor in the presence of an external uniform field is obtained.

$$F = BiL \qquad [\text{N}] \tag{C.4}$$

If the conductor cross-sectional area is not negligible, a more general approach with any medium having a current density $\overrightarrow{J}$ is used. Defining a volumetric charge density ς, the current density is

$$\overrightarrow{J} = \varsigma \overrightarrow{v}_d \qquad [\text{A/m}^2]$$

The differential force generated by a differential volume dV with charge $q = \varsigma dV$ is

$$\begin{aligned} d\overrightarrow{F} &= q(\overrightarrow{v_d} \times \overrightarrow{B}) \\ &= \varsigma dV(\overrightarrow{v_d} \times \overrightarrow{B}) \\ &= dV(\varsigma\overrightarrow{v_d} \times \overrightarrow{B}) \\ &= dV(\overrightarrow{J} \times \overrightarrow{B}) \qquad [\text{N}] \end{aligned} \tag{C.5}$$

Thus the volumetric force density is given by

$$\overrightarrow{f} = \frac{d\overrightarrow{F}}{dV} = \overrightarrow{J} \times \overrightarrow{B} \qquad [\mathrm{N/m^3}] \tag{C.6}$$

When using (C.3), (C.5), or (C.6), the total force on the conductor is found by integrating the differential force over some line segment or volume. The following examples illustrate the application of this equation and introduce two fundamental DC machines: the DC motor and the DC (linear) generator.

Example C.1. *(Force between two thin wires)*

Two thin wires are carrying current i and are separated by a distance d. The are relatively long and are parallel to each other. Find the force on one due to the other. Figure C.1 shows two wires carrying current in opposite directions and the corresponding B fields generated.

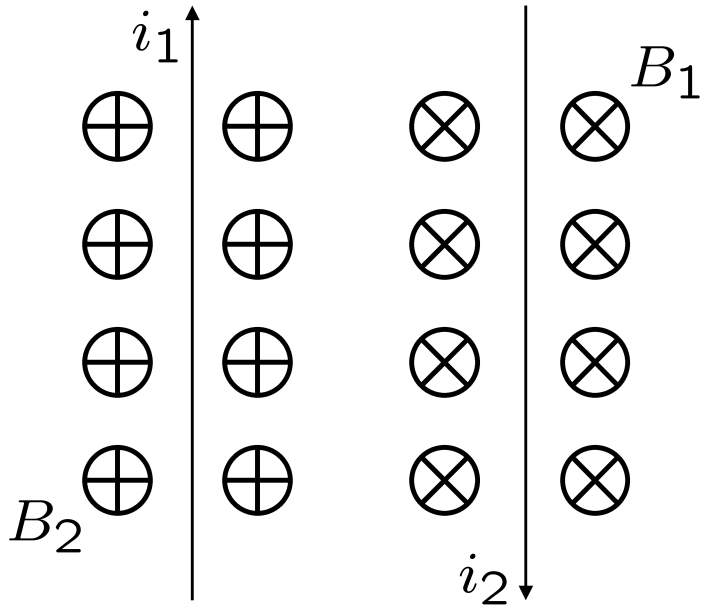

Figure C.1: Two current-carrying wires separated by distance d. The B field from i_1 and i_2 are represented by $\otimes$ and $\oplus$, respectively.

The B field around a wire is $\overrightarrow{B} = \mu_0 \overrightarrow{H}$ where H determined by Ampère's law.

$$\overrightarrow{B}_1 = \mu_0 \overrightarrow{H} = \frac{\mu_0 i_1}{2\pi d}\hat{\theta}$$

Thus, the magnitude of the force per unit length of wire on wire 2 due to wire 1 is

$$f_2 = \frac{F_2}{L} = Bi_2 = \frac{\mu_0 i_1 i_2}{2\pi d}$$

Applying the right hand rule to the wires, the force is attractive for currents in opposite directions and repulsive for currents in the same directions. This is very similar to Coulomb's Law for charges.

Example C.2. *(Fundamental Example of DC Machine [6])*

This example illustrates the basics of all DC machines. It is a 4 pole DC motor. Find the torque generated on the rotor per pole. Figure C.2 shows the geometry.

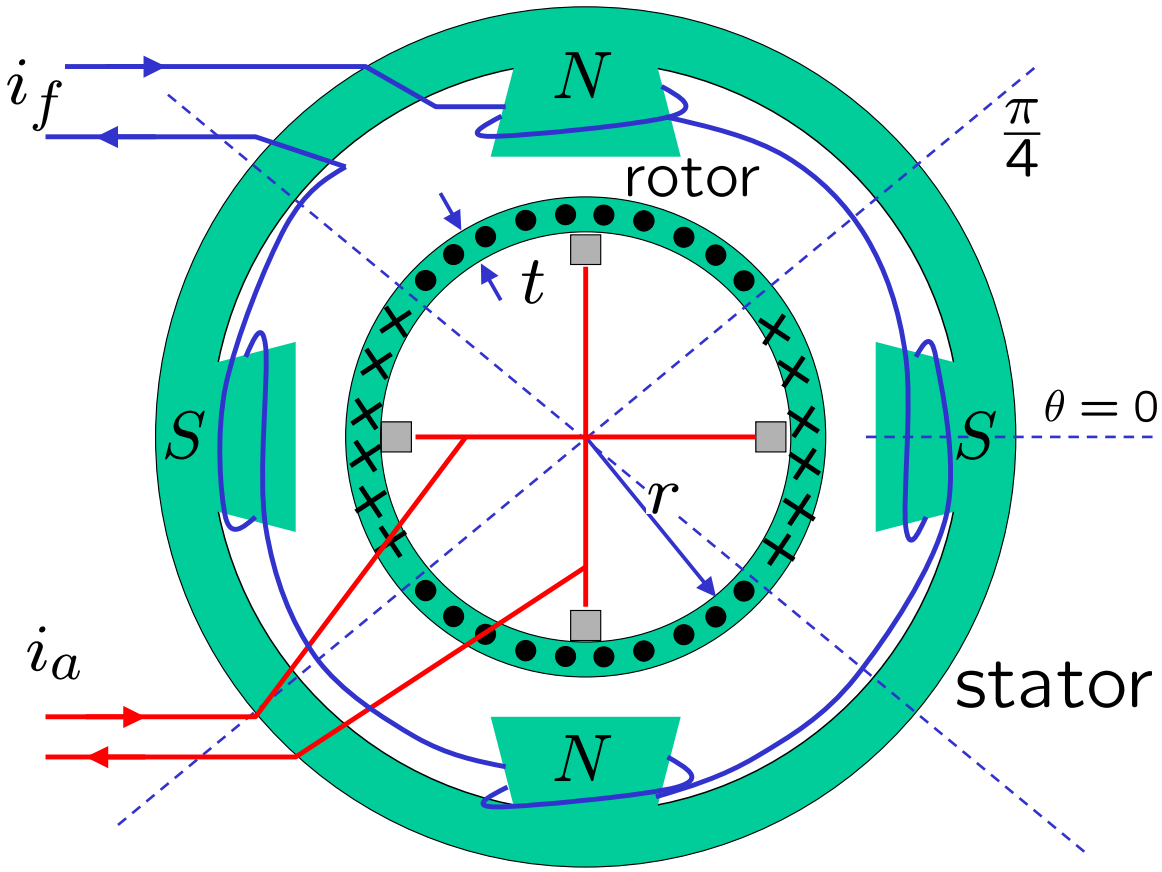

Figure C.2: Geometry of a 4 pole DC motor. The field is generated by coils in this example, but may be generated by permanent magnets. Also, only one set of commutation brushes is shown. Brushless DC motors commute the currents electronically.

Solution: *The field circuit on the stator generates a stationary (not changing with time) B field. The radial component of the B field, evaluated at a given radius*

r, is a periodic function of θ. An example B field at a given radius is shown in Figure C.3. Note that the B field is relatively constant under a pole. If the B field is evaluated at a a larger radius, the value of $B_{\max}$ will increase, but the shape of the wave form will not change much.

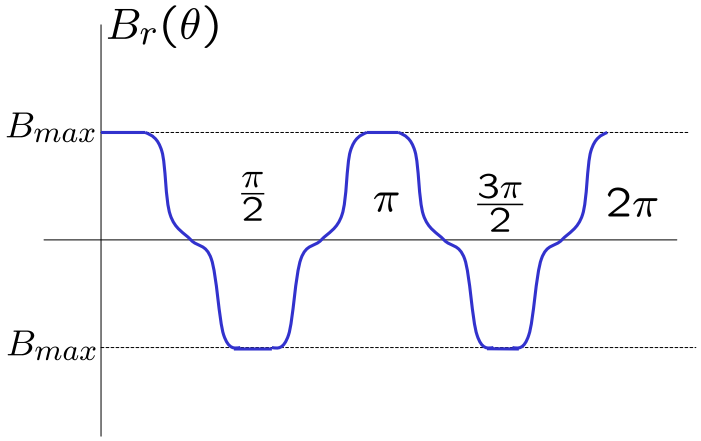

Figure C.3: $B(\theta)$ for the DC machine of Example C.2.

Note that the B field has half wave symmetry. That is,

$$B(\theta) = B(\theta \pm \frac{4\pi}{P}) = -B(\theta \pm \frac{2\pi}{P}) \tag{C.7}$$

where P is the number of poles of the machine.

The armature winding of the machine is the winding that has the major voltage induced in it (if used as a generator). In the case of a DC machine, the armature winding is on the rotor. It is on the stator for most ac machines. The rotor winding on a DC machine is typically distributed in slots on the rotor periphery. The stationary brushes (only one set is shown) supply armature current i_a to the moving conductors in such a way so that the current distribution (into and out of the page in Figure C.2) stays fixed in space, regardless of the position of the rotor. This is the essence of the conventional DC machine.

Assume that the axial length of the machine is long enough to implement a 2D analysis (to neglect end-effects). Note that the armature current i_a produces a field to distort the stator field, however, good design practices minimize this effect and

it is neglected here. The effect of the slots in the rotor to hold the armature wires are also neglected. The winding is regarded as a belt of armature conductors with a uniform thickness t around the periphery of a perfectly round rotor.

By assuming that t is small compared to r, the torque is developed using $F = BiL$. *If the total number of uniformly distributed armature conductors is* Q, *then the number of conductors in an incremental arc length is* $dQ = Qrd\theta/2\pi r = (Q/2\pi)d\theta$. *If each conductor carries* i_c, *the contribution to the total torque by a differential arc length at position* θ *is*

$$dT = rBiL = rB(\theta)i_c\frac{Q}{2\pi}d\theta L \qquad [\text{Nm}]$$

where L *is the axial length of the winding. (By neglecting the end effects, one assumes that* $B(\theta)$ *is constant along the length of the machine.) The total torque is found by integrating from* $\theta = -\pi/P$ *to* $\theta = \pi/P$ *where* P *is the number of poles of the machine. Thus, the torque per pole is given by,*

$$T_p = \frac{Q}{2\pi}i_c\int_{-\pi/P}^{\pi/P} B(\theta)Lrd\theta \qquad [\text{Nm}]$$

Note that the integral in the expression is the total flux per pole.

$$\Phi_p = \int_{-\pi/P}^{\pi/P} B(\theta)Lrd\theta \qquad [\text{Wb}]$$

Thus the total torque is

$$T = PT_p = \frac{PQ}{2\pi}i_c\Phi_p$$

Note that the armature winding is typically constructed with many parallel paths. Thus, $i_c = i_a/a$ *where* i_a *is the armature terminal current. Then the torque becomes*

$$T = \frac{PQ}{2\pi a}i_a\Phi_p \qquad [\text{Nm}]$$

This says that the torque is directly proportional to the armature current and the pole flux.

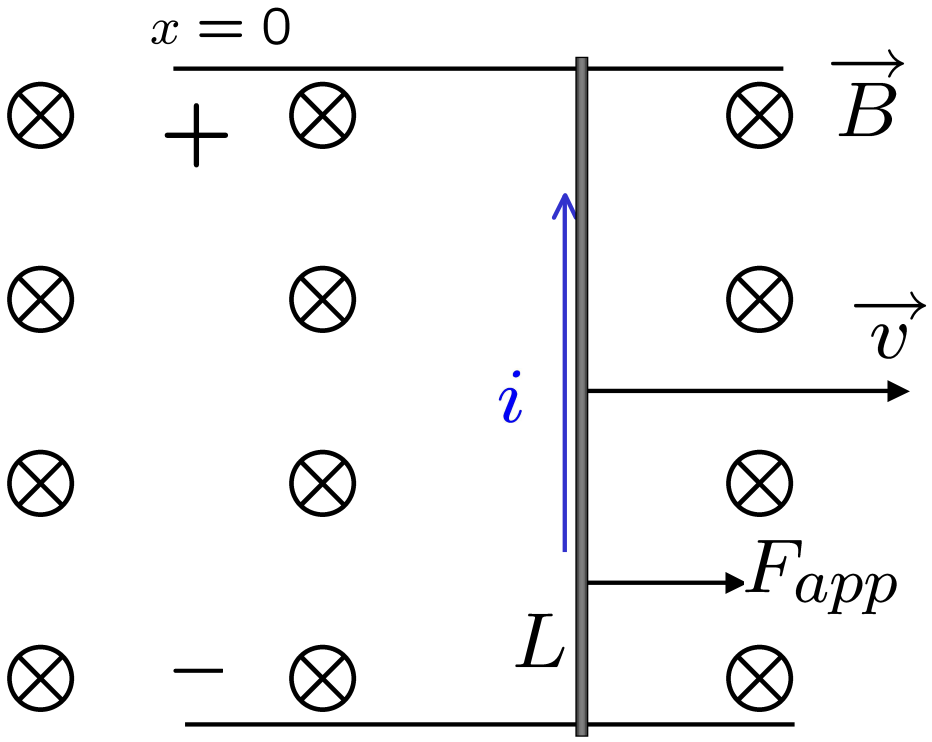

Figure C.4: Geometry for the linear generator.

Example C.3. *(Linear Generator [6])*

Figure C.4 shows a metal bar of length L being pushed along two metal rails by an external force F_{app} so that linear velocity v is constant. This apparatus is in the presence of a B field pointing into the page. Find the voltage e induced at the rail terminals. This voltage is sometimes called the motional emf. Also, what is the external force applied so that the velocity v is constant.

Solution: *$F = qvB$ may be used to find the answer. By the right hand rule, if the terminals were short circuited, the current would flow upwards. Here the bar is seen as a power source that delivers voltage or current to whatever device is connected to the rail terminals. Thus, the top of the bar should be marked as $+$ and the bottom of the bar marked as $-$. This is the essence of a generator: mechanical energy $(1/2mv^2)$ produces electrical power ei through the medium of the magnetic field.*

The energy or work[1] *it takes to move the electron up is*

$$W = F \cdot s = (qvB)(L) \qquad [\text{J}]$$

Thus, the voltage induced, also known as the potential energy or work per unit charge, is

$$e = \frac{W}{q} = LBv \qquad [\text{V}] \tag{C.8}$$

One could also use Faraday to derive the motional emf. Faraday relates the voltage across coils to the changing flux through the coil. In Figure C.4, the rails and the bar form the 1 turn coil which has a cross-sectional area that is increasing with time.

The the area of the coil is Lx*. Applying Faraday,*

$$e = \dot{\varphi} = B\dot{A} = BL\dot{x} = vBL$$

By Len's law, the current induced if the coil was short circuited is always in the direction to oppose the change in flux. If the current flows counterclockwise through the coil when the terminals are shorted, then the B *field induced is out of the page (directly opposite to the external* B *field.) For this reason, the induced emf is sometimes called a back emf.*

When current flows in the bar and the bar moves through the magnetic field, the bar will experience a force according to $F_{\text{induced}} = Li \times B$*. By the right hand rule, this force points in the* $-x$ *direction. Thus, the external force that must be applied to the bar to produce the constant velocity* v *must cancel the induced force. Thus,*

$$F_{\text{app}} = -F_{\text{induced}} = \frac{e}{R}LB = \frac{L^2B^2v}{R}$$

where R *is the resistance of the bar plus the resistance of the load that is connected to the terminals. Since the force is proportional to the velocity, it is called an electromagnetic drag force.*

[1] *Note that no work is done by the magnetic field moving the charge along the rails because the force and displacement are perpendicular.*

An analysis very similar to the one in Example C.3 is used to find the power loss in a flywheel battery due the electromagnetic drag: See Chapter 2.

APPENDIX D

ENERGY ANALYSIS OF MAGNETIC CIRCUITS

To quickly facilitate understanding of the energy method fundamentals, Example B.1 of the toroidal coil is revisited. This is good starting point for investigating energy storage because it is unencumbered by an airgap or moving magnetic circuit components. Afterwards, the energy analysis concepts of general electromechanical machines are presented.

Example D.1. *(Energy Stored in Toroidal Inductor [20])*
Again consider the pedagogic example of the rectangular cross section toroidal core with a winding as in Example B.1. Find the energy stored in the magnetic field of this inductor.

***Solution**: Consider the instantaneous power delivered to (i.e. the supply rate) the circuit.*

$$p(t) = i(t)v(t)$$

where i and v are the terminal current and voltage. Using Faraday's law,

$$p(t) = i(t)\frac{d\lambda}{dt}$$

By expressing current as a function of λ (consider the third graph in Figure B.10), one can separate variables and integrate to get the energy W supplied to the circuit.

$$dW = p(t)dt = i(\lambda)d\lambda$$

$$W = \int_{t_1}^{t_2} p(t)dt = \int_{\lambda_1}^{\lambda_2} i(\lambda)d\lambda$$

See Figure D.1a for a graphical representation of this integral. The shaded area in this figure corresponds to the energy delivered W_{12} to the circuit in time $t \in [t_1, t_2]$.

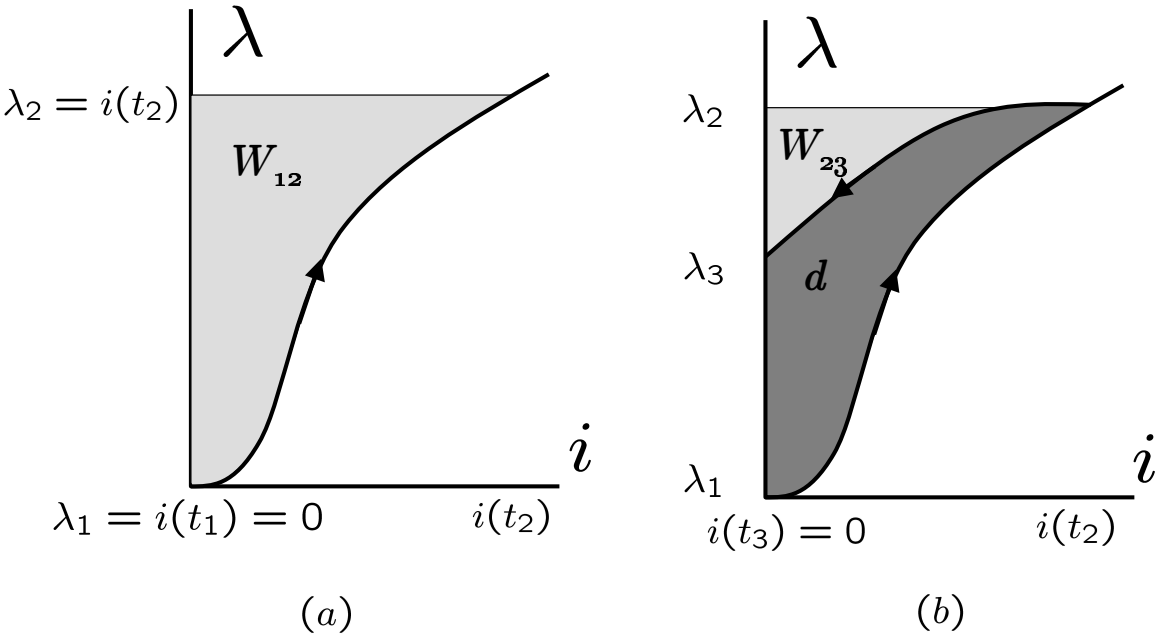

Figure D.1: **(a)** The energy W_{12} supplied to the magnetic circuit for $t \in [t_1, t_2]$. **(b)** The energy extracted W_{23} and energy dissipated d for $t \in [t_2, t_3]$.

As the current is reduced back to zero in time $t \in [t_2, t_3]$, the flux-linkage follows the hysteresis curve. To calculate the energy supplied to the circuit in time $t \in [t_1, t_3]$ the following integrals are used.

$$W_{t_1,t_2}^{\text{supplied}} = \int_{\lambda(t_1)}^{\lambda(t_2)} i(\lambda) d\lambda, \qquad t \in [t_1, t_2]$$

$$W_{t_2,t_3}^{\text{supplied}} = \int_{\lambda(t_2)}^{\lambda(t_3)} i(\lambda) d\lambda = -\int_{\lambda(t_3)}^{\lambda(t_2)} i(\lambda) d\lambda, \qquad t \in [t_2, t_3]$$

The negative sign is introduced to make the interval of integration increasing. Negative supplied energy may be thought of as energy extracted. Thus, the energy supplied to the circuit during $t \in [t_1, t_3]$ is the energy supplied minus the energy extracted.

$$W = W_{t_1,t_2}^{\text{supplied}} - W_{t_2,t_3}^{\text{extracted}} = \int_{\lambda(t_1)}^{\lambda(t_2)} i(\lambda) d\lambda - \int_{\lambda(t_3)}^{\lambda(t_2)} i(\lambda) d\lambda$$

Since more energy is supplied than extracted, there must be some energy dissipated in the magnetic circuit: See d in Figure D.1b. It turns out that this excess energy is

converted to heat in the core (via eddy-current losses or the energy it takes to realign the magnetic domains). Thus, the area enclosed by the curve is the energy dissipated in the core. During steady-state cyclic operation, the area inside the hysteresis loop corresponds to the energy loss per cycle. The energy that can be extracted is the energy that has been stored in the magnetic field: See W_{23} in Figure D.1b.

Since the hysteresis phenomenon may be represented with different variables (see Figure B.10), the energy stored may be expressed in different variables. Changing variables of integration $\lambda = N\varphi$,

$$W = \int_{\lambda_0}^{\lambda_f} i(\lambda) d\lambda = \int_{N\varphi_0}^{N\varphi_f} Ni(\varphi) d\varphi$$

This relates the stored energy to the magnetic circuit variables. Revisiting the rectangular toroid and assuming the H and B are uniform over the cross section, the energy stored is

$$d\varphi = A_c dB, \qquad Ni = H\ell_c$$

$$W = \int_{B_0}^{B_f} H(B)\ell_c A_c dB = \ell_c A_c \int_{B_0}^{B_f} H(B) dB$$

These concepts are summarized in Figure D.2. Note that the integral of $H(B)$ gives energy density w per unit volume, not energy W.

Example D.1 serves to quickly illustrate the application of the energy method to a toroidal inductor. This method integrates the power supplied to the magnetic circuit- a quantity which is typically known- to find the energy stored in the magnetic field. It also shows how the energy stored in the inductor is related to the area under the $\lambda - i$ ($\varphi - Ni$, or BH) curve and how hysteresis represents an energy loss. Note that for a lossy inductor, one with hysteresis or eddy-current loss, that the energy stored in the inductor depends on how the core is excited. In Example D.1, the current is increased from zero to $I_{\max}$ and then back to zero, as in Figure D.1b. Suppose, for example, that the current was excited as follows: $i(t_1) = 0$, $i(t_2) = I_{\max}/2$, $i(t_3) = I_{\max}/4$, $i(t_4) = I_{\max}$, and finally $i(t_5) = 0$. Then a different hysteresis curve would be traversed

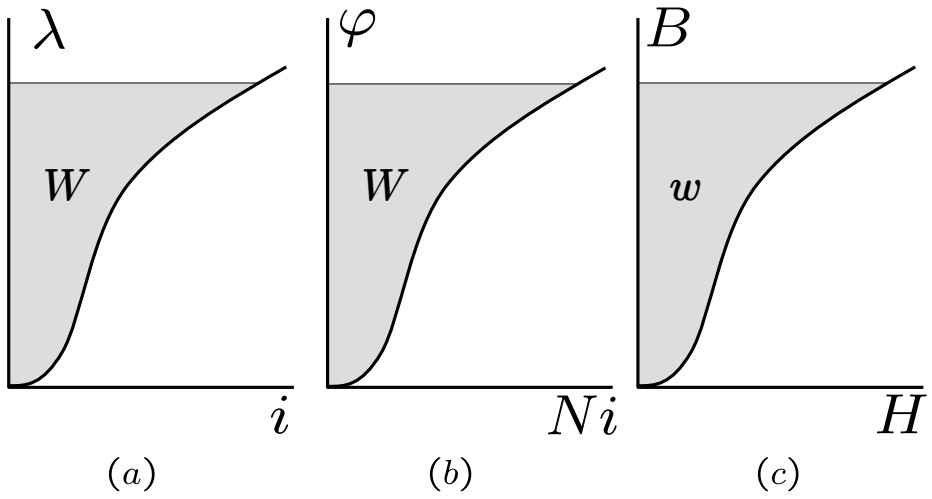

Figure D.2: Comparison of energy supplied to circuit for different magnetic circuit variables. Note that part (c) shows the energy density per unit volume.

resulting in a different amount of core loss than in Figure D.1b: the energy stored is different for the two paths followed through the $\lambda - i$ plane. However, if the inductor is considered lossless and an inductance is assigned ($\lambda = Li$), then only one (linear) path in the $\lambda - i$ can be traversed and the energy stored in the inductor only depends on the final value of the current. This issue of path-dependence in energy analysis is of central concern and is discussed in the sequel.

D.1 Determining the Energy Stored in the Magnetic field

Recall from basic physics that energy is considered a positive scalar quantity and is a measure of the system's ability to do work (work and energy have units of Joules, J). The first law of thermodynamics says that energy in a system is conserved, that is, energy is transformed from one form into another. Note that the definition of the "system" is an important concept. For example, the energy (or heat) stored in a hot cup of coffee dissipates with time. This simple system seemingly contradicts the first law of thermodynamics. Of course, if one broadens the definition of the system to be the coffee cup and the surrounding air, then the energy in the coffee cup is

transferred to the air and the energy of the coffee-air system is conserved. Thus, the identification of systems where energy is conserved is paramount in energy analysis.

When electromechanical systems are used as motors, electrical energy is converted to mechanical energy and vice versa when they are used as generators. The medium in which the energy is converted is the magnetic field. Thus, energy analysis applied to electromechanical systems is concerned with the energy stored in the magnetic field. Figure D.3 schematically shows the energy conversion relationship. Observe that f and x are the magnetic force applied to and the position of the moving members of the magnetic circuit, respectively. Note that the multi-input, multi-output (MIMO) systems can be represented by considering the quantities shown as vectors.

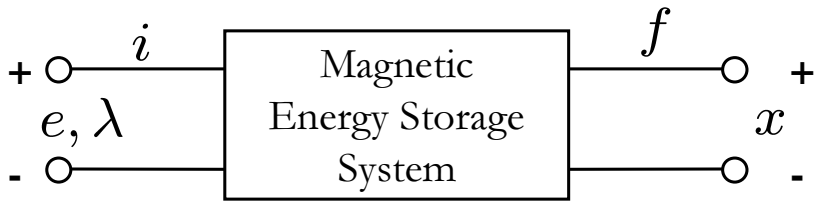

Figure D.3: Energy conversion schematic. The electrical terminals are on the left and the mechanical terminals are on the right. The magnetic field is the medium in which electrical power ei is converted to mechanical power fv.

The first law of thermodynamics states that the electrical energy supplied to the system during a period of length T is converted to mechanical work, the increase in energy stored in the magnetic field and heat.

$$W_{\text{supplied}} = W_{\text{mechanical}} + \Delta W_{\text{field}} + W_{\text{heat}}$$

Since the energy is a scalar quantity, the change in energy stored in the magnetic field during the time T is the difference between the final and initial energy. Thus, the energy stored in the magnetic field is

$$\Delta W_{\text{fld}} = W_{fld}(T) - W_{\text{fld}}(0) = W_{\text{supplied}} - W_{\text{mechanical}} - W_{\text{heat}} \tag{D.1}$$

where the energy supplied increases the energy stored in the magnetic field. The mechanical work is done by the magnetic circuit and thus decreases the energy stored

in the magnetic field. The energy converted to heat also reduces the energy stored in the magnetic field. In magnetic circuits, core loss and coil resistance tend to heat up the core and coil.

In general, the thermal energy loss is difficult to quantify. For example, the resistance of the coil depends on the temperature. As the coil heats up, the resistance changes and consequently, the rate of coil heating changes. Furthermore, Example D.1 showed that the core loss in a nonlinear inductor depends on the excitation. These issues make equation (D.1) difficult to work with in a quantifiable way. In general, the following inequality is true.

$$W_{\text{fld}}(T) - W_{\text{fld}}(0) \leq W_{\text{supplied}} - W_{\text{mechanical}} \tag{D.2}$$

This equation is called the Dissipation Inequality and is fundamental in energy analysis. It says that energy stored in the system is less than the net the energy supplied. Therefore, there must be some energy that has been dissipated. If this relationship holds with equality (an "=" instead of "$\leq$" in equation (D.2)), then the system is called *lossless*. This concept is very general and practical. In fact, it is implemented in Chapter 4 to derive stabilizing control laws for the 1-DOF AMB.

Typically the electrical power and the mechanical power are measurable quantities. Recall that the electrical power is ei and the mechanical power is fv. Thus, it is more convenient to work with power instead of energy as in equation (D.2). Since power is the time rate of change of energy, one may be tempted to differentiate equation (D.2) to obtain an equation in terms of power. However, *one can not differentiate an inequality*!

To address this challenge, energy analysis strives to identify systems where the energy storage is *lossless*. This seemingly cripples this approach because realistic systems have losses. However, lossy processes can often be *modelled* so that the loss mechanism is separated from the energy storage mechanism. Of course, one can not physically remove the coil resistance from the coil or eliminate the magnetic hysteresis

from a realistic core. Nevertheless, coils are often *modelled* as ideal cores with external winding resistances and transformer cores are *modelled* as ideal cores in cascade with filters to estimate the core loss or leakage flux. In summary, energy analysis often narrows its definition of a physical system to one that is lossless, represents it as a 2-port network as in Figure D.3, and then connects external components to the network to represent the losses of the process.

Since the magnetic energy storage system considered is lossless, one may differentiate equation (D.2) because it actually holds with equality. Rewriting the dissipation inequality in terms of power,

$$W_{\text{fld}}(T) - W_{\text{fld}}(0) = \int_0^T \tfrac{dW_{fld}}{dt} dt = \int_0^T (ei - fv) dt \tag{D.3a}$$

$$= \int_{W(0)}^{W(T)} dW_{fld} = \int_0^T \left(\tfrac{d\lambda}{dt} i(\lambda,x) - f(\lambda,x)\tfrac{dx}{dt}\right) dt \tag{D.3b}$$

$$W_{\text{fld}}\big(\lambda(T),x(T)\big) - W_{\text{fld}}\big(\lambda(0),x(0)\big) = \int_{\lambda(0)}^{\lambda(T)} i(\lambda,x) d\lambda - \int_{x(0)}^{x(T)} f(\lambda,x) dx \tag{D.3c}$$

In equation (D.3b), Faraday has been used to express the voltage in terms of the flux-linkage. Also, λ and x have been assumed as the independent variables. Note that equation (D.3c) states that the change in energy stored in the magnetic field is equal to the line integrals on the RHS for some path through the $\lambda - x$ plane. Since our system is lossless, the *line integrals are independent of the path chosen and the stored energy only depends on the initial and final values of* λ *and* x. This observation is the essence of the practicality and versatility of the energy method. It allows one to choose the simplest path to evaluate the integrals on the RHS of equation (D.3c).

With out loss of generality, let $\lambda(0) = 0$ and $W_{fld}(0, x) = 0$. Furthermore, since the magnetic field is necessary to generate a magnetic force, $f(\lambda, x)|_{\lambda=0} = 0$. To find the energy stored in the magnetic field as one increases (λ, x) from zero to their final values (λ_T, x_T): consider Figure D.4. The integral over path c is the same as the integral over path ab.

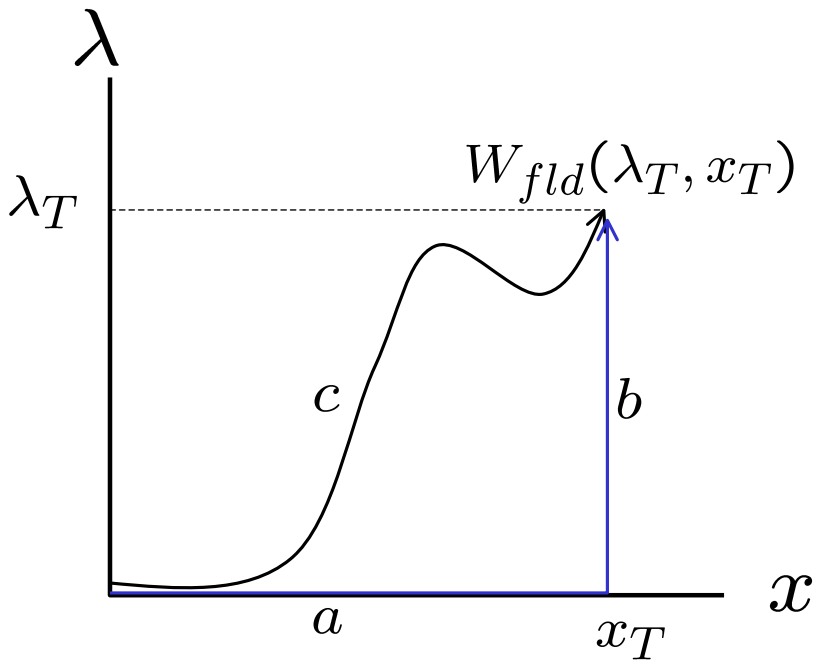

Figure D.4: Path independence of the line integral.

$$W_{\text{fld}}(\lambda_T, x_T) = \int_c dW_{\text{fld}} = \int_a dW_{\text{fld}} + \int_b dW_{\text{fld}}$$

The integral is simpler to calculate on path ab.

$$\begin{aligned} W_{\text{fld}}(\lambda_T, x_T) &= \int_a i(\lambda, x)d\lambda - \int_a f(\lambda, x)dx + \int_b i(\lambda, x)d\lambda - \int_b f(\lambda, x)dx \\ &= 0 - \int_a 0dx + \int_b i(\lambda, x)d\lambda + 0 \end{aligned}$$

Along path a, $d\lambda = 0$ and $\lambda(0) = 0$. If the flux-linkage is zero, the magnetic field is null and $f(0, x) = 0$. Along path b, $dx = 0$. The integral simplifies to

$$W_{\text{fld}}(\lambda_T, x_T) = \int_0^{\lambda_T} i(\lambda, x_T)d\lambda \tag{D.4}$$

Thus, the energy stored in the magnetic field for any position x, can be calculated from knowledge of only the current as a function of λ and x. The path independence allows one to calculate the stored energy *without a priori knowledge of the force.*

In equation D.3c, the electrical differential input power could be represented as $NI(\varphi)d\varphi$ or the electrical input power density as $H(\overrightarrow{B})dB$. These are equivalent descriptions of the energy and they are selected as a matter of preference or convenience.

The equivalent forms of the stored magnetic energy are

$$W_{\text{fld}}(\varphi_0) = \int_0^{\varphi_0} Ni(\varphi)d\varphi \tag{D.5}$$

and

$$W_{\text{fld}}(B_0) = \int_V \Big(\int_0^{B_0} \overrightarrow{H}(\overrightarrow{B}) \cdot \overrightarrow{dB} \Big) dV \tag{D.6}$$

Note that the energy density equation is the most general in the sense that is it integrating vector quantities. Also note the presence of the dot product because one is interested in the magnetic field intensity and flux density that are in the same direction. (In an extremely complex magnetic circuit situation, the permeability can be a function of the position and may make the H and B fields linearly independent.)

Now, consider the simple case when hysteresis, saturation, and eddy current losses are neglected. That is, let $\lambda = L(x)i$. Additional results are obtained by recalling that $L(x) = N^2/\mathcal{R}(x)$ and that $\lambda = N\varphi$.

$$\begin{aligned} W_{\text{fld}}(\lambda, x) &= \int_0^{\lambda} i(\xi, x_0)d\xi = \int_0^{\lambda} \frac{\xi}{L(x)} d\xi \\ &= \frac{1}{2}\frac{\lambda^2}{L(x)} = \frac{1}{2}\mathcal{R}(x)\varphi^2 \end{aligned} \tag{D.7}$$

If a homogeneous permeability is assumed, $B = \mu H$,

$$W_{\text{fld}}(B) = \int_V \Big(\int_0^{B} \overrightarrow{H}(\overrightarrow{\beta}) \cdot \overrightarrow{d\beta} \Big) dV = \int_V \frac{1}{2}\frac{B^2}{\mu} dV \tag{D.8}$$

D.2 Relationship Between Magnetic Force and Stored Energy

To find the relationship between the force and the stored energy, re-examine the virtual work or the infinitesimal stored magnetic energy.

$$dW_{\text{fld}}(\lambda, x) = id\lambda - f_{fld}dx$$

By the chain rule,

$$dW_{\text{fld}}(\lambda, x) = \frac{\partial dW_{fld}}{d\lambda} d\lambda + \frac{dW_{\text{fld}}}{dx} dx$$

Since λ and x are independent variables, one compares like terms in the above equations to discover that

$$i = \frac{\partial W_{\text{fld}}(\lambda, x)}{d\lambda} \tag{D.9}$$

and

$$f_{fld} = -\frac{\partial W_{\text{fld}}(\lambda, x)}{dx} \tag{D.10}$$

Equation (D.9) states that for a fixed x, the current sets the rate of increase in the stored energy for a change in the flux-linkage. Likewise, equation (D.10) states that the force is the rate of decrease of the stored energy with respect to an increase in the position. Stated differently, the *force acts in the direction x to decrease the stored energy*.

Equations (D.4), (D.9) and (D.10) form the basis of the energy method. This technique is quite powerful in its ability to calculate the forces and torques acting in a very complex system. Given the current in terms of the flux, one uses equation (D.4) to find the stored energy. With the stored energy in hand, the force is found by calculating the partial derivative with respect to the position. However, one should realize that a detailed description of the force producing mechanisms is not given by this method. It only calculates the force that corresponds to the change in the system energy. It is a macroscopic viewpoint of the microscopic phenomena that are taking place. The forces themselves are produced by the well-known Lorentz forces on current carrying elements or by the interaction of the magnetic fields with the of the dipoles in the magnetic material.

The differential stored energy may be expressed in terms of i instead of λ as the independent variable. This is possible because i and λ depend on each other and one can arbitrarily select one as the independent variable. The current is often selected as the independent variable because current measurements are readily available. The stored energy that is calculated from the selection of i as the independent variable is called the *co-energy*. The co-energy $\overline{W}_{\text{fld}}(i, x)$ is related to the energy $W_{\text{fld}}(\lambda, x)$ by

the following relationship[1].

$$W_{\text{fld}}(\lambda, x) + \overline{W}_{\text{fld}}(i, x) = i\lambda \tag{D.11}$$

Using this transformation, the differential co-energy is

$$\begin{aligned} d\overline{W}_{\text{fld}}(i, x) &= d(i\lambda) - dW_{\text{fld}}(\lambda, x) \\ &= \lambda di + id\lambda - id\lambda - -fdx \\ &= \lambda di + fdx \end{aligned}$$

Via chain rule

$$d\overline{W}_{\text{fld}}(i, x) = \frac{\partial \overline{W}_{\text{fld}}(i, x)}{\partial i} di + \frac{\partial \overline{W}_{\text{fld}}(i, x)}{\partial x} dx$$

By comparison of the above equations,

$$\lambda = \frac{\partial \overline{W}_{\text{fld}}(i, x)}{\partial i} \tag{D.12}$$

and

$$f = \frac{\partial \overline{W}_{\text{fld}}(i, x)}{\partial x} \tag{D.13}$$

Equation (D.12) states that the flux-linkage sets the rate at which the co-energy increases with increasing current. Equation (D.13) states that *the force acts in the direction to increase the stored co-energy.*

Integrating the differential stored co-energy, one finds the total co-energy stored in the magnetic field. Without loss of generality, let $i(0) = 0$ and $\overline{W}_{\text{fld}}(0, x) = 0$. Furthermore, since the magnetic force acts through the medium of the magnetic field and the current generates the magnetic field, the magnetic force must be zero when the current is zero, $f(i, x)|_{i=0} = 0$. Again, using the principle of path independence in the $i - x$ plane, first integrate $d\overline{W}(i, x)$ along $i(0) = 0$ from $x = 0$ to $x = x_T$ and then integrate along $x = x_T$ from $i = 0$ to i_T. Along the $i(0) = 0$ path, $di = 0$ and

[1]Recall that $[i\lambda] = \text{AWb} = \text{ATm}^2 = \text{A}\frac{\text{N}}{\text{Am}}\text{m}^2 = \text{Nm} = \text{Joules}$

no force can be generated because the magnetic field is null. Along $x = x_T$, $dx = 0$. Thus,

$$\overline{W}_{\text{fld}}(i_T, x_T) = \int_0^{i_T} \lambda(i, x_T) di \tag{D.14}$$

Similarly, in terms of the energy density HB,

$$\overline{W}_{\text{fld}}(H_0) = \int_V \Big(\int_0^{H_0} \overrightarrow{B}(\overrightarrow{H}) \cdot \overrightarrow{dH} \Big) dV \tag{D.15}$$

Assuming linear behavior and neglecting hysteresis and saturation, $\lambda = L(x)i$, $L = N^2/\mathcal{R}(x)$ and $\lambda = N\varphi$.

$$\begin{aligned} \overline{W}_{\text{fld}}(i, x) &= \int_0^i \lambda(\xi, x_0) d\xi = \int_0^i L(x) \xi d\xi \\ &= \frac{1}{2} L(x) i^2 = \frac{1}{2} \frac{(Ni)^2}{\mathcal{R}(x)} \end{aligned} \tag{D.16}$$

Assuming a homogeneous permeability $B = \mu H$,

$$\overline{W}_{\text{fld}}(H_0) = \int_V \Big(\int_0^{H_0} \overrightarrow{B}(\overrightarrow{H}) \cdot \overrightarrow{dH} \Big) dV = \int_V \frac{1}{2} \mu H_0^2 dV \tag{D.17}$$

Table D.2 summarizes the actions of the force on the movable magnetic elements and the effects that are induced. Observe that the forces always act to decrease the

Table D.1: Action of the forces on stored energies in terms of $L(x)$ and $\mathcal{R}(x)$.

	$W_{\text{fld}}(\lambda, x)$	$\overline{W}_{\text{fld}}(i, x)$	$f = -\frac{\partial W}{\partial x}$	$f = \frac{\partial \overline{W}}{\partial x}$
$L(x)$	$\frac{1}{2}\frac{\lambda^2}{L(x)}$	$\frac{1}{2} L(x) i^2$	increases inductance	increases inductance
$\mathcal{R}(x)$	$\frac{1}{2}\mathcal{R}(x)\varphi^2$	$\frac{1}{2}\frac{(Ni)^2}{\mathcal{R}(x)}$	decreases reluctance	decreases reluctance

stored energy and increase the stored co-energy. Consequently, the force is generated in the direction that increases the inductance and decreases the reluctance. Thus, the force arranges the movable members of the magnetic circuit to maximize the inductance and minimize reluctance. Moreover, if the movable member is has several degrees of freedom in motion, the force is generally

$$f = -\nabla_x W(\lambda, x) = \nabla_x \overline{W}(i, x)$$

where ∇_x is the gradient.

Remark 5. *(Comments on the Energy/Co-energy Relationship [20])*

Recall that the energy and co-energy are related by

$$W(\lambda, x) + \overline{W}(i, x) = i\lambda$$

For a linearly assumed relationship between λ and i, $\lambda = L(x)i$, the numerical values of the energy and co-energy are identical. Indeed,

$$\frac{1}{2}\frac{\lambda^2}{L(x)} + \frac{1}{2}L(x)i^2 = L(x)i^2 = \lambda i$$

However, for a current-flux relationship that is nonlinear, the energy and cos-energy are not equal. From equations (D.4) and (D.14) one constructs the graph in Figure 5. Observe that $W = \int i(\lambda, x)d\lambda$ is the area to the left of the curve. Likewise, since the co-energy is $\overline{W} = \int \lambda(i, x)di$, the co-energy is the area under the curve.

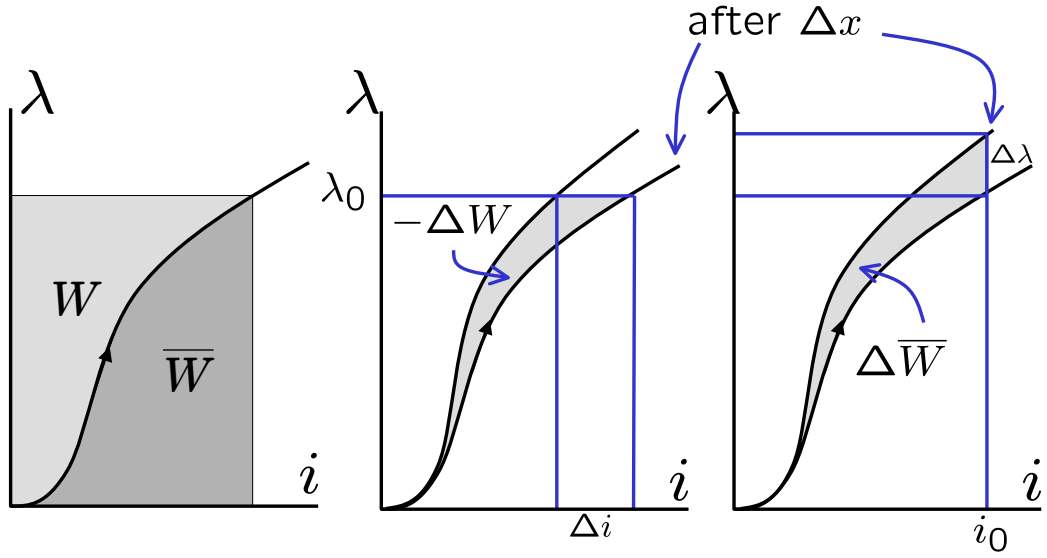

Figure D.5: **(a)** Relationship between energy and co-energy, **(b)** change in energy with respect to x, **(c)** change in co-energy with respect to x

To double check that the force is unique, whether determined form the energy or co-energy, inspect Figure 5, parts (b) and (c). A change in the energy $-\Delta W$ due to a change in x is shown in (b) while holding the flux-linkage constant. This is represented by the area between the two curves. Note that since $\lambda \approx L(x)i$, the

change in $L(x)$ induces a change in i since λ is held constant. Likewise, a change in the co-energy $\Delta\overline{W}$ with x while holding the current constant is illustrated in part (c). Again, since the current is a function of the position and the flux-linkage, the flux-linkage experiences a change corresponding to the change in x. The difference in these two areas is a small triangle with sides Δi and $\Delta\lambda$. Since $\Delta\lambda$ and Δi go to zero as $\Delta x \to 0$, these two areas match. Thus, $lim_{\Delta x\to 0} - \Delta W/\Delta x = lim_{\Delta x\to 0}\Delta\overline{W}/\Delta x$ and the force is unique.

The following examples demonstrate the practical application of the energy method to find the force in common magnetic circuits. Note that the forces generated in the following examples arise from the complex interaction of the magnetic field and the dipoles of the ferromagnetic material. The calculation of the force from the energy method is direct and avoids complex field and magnetic material theory.

Example D.2. *(Basic Solenoid [20])*
The diagram in Figure D.6 shows a simple Solenoid. Calculate the force using the energy and co-energy. Assume that the permeability of the target and the core are very large. The cross-sectional area is $A = wd$ where w is shown and d is the depth of the core. Consider h to be much larger than g.

Solution: *Since the core and target permeability is large, the magnetic field intensity in the core is minimal $H = B/\mu$ and the magnetic field of the airgap is comparatively large. Thus, a magnetic circuit approach is justified.*

The energy and co-energy are

$$W(\lambda, x) = \frac{1}{2}\frac{\lambda^2}{L(x)} = \frac{1}{2}\mathcal{R}(x)\varphi^2, \qquad \overline{W}(i, x) = \frac{1}{2}L(x)i^2 = \frac{1}{2}\frac{N^2 i^2}{\mathcal{R}(x)}$$

where the $R(x)$ and $L(x)$ refer to the reluctance and inductance of the airgap. Recall the reluctance is

$$\mathcal{R} = \frac{\text{length in direction of flux}}{\mu_0 \text{ area } \perp \text{ to flux}}$$

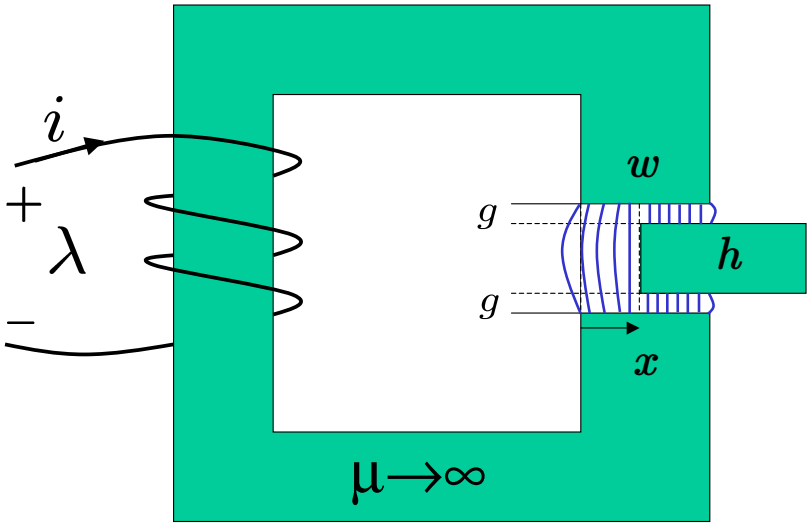

Figure D.6: A simple solenoid with constant airgap length $2g$. The cross-sectional area is $A = wd$.

The airgap has 3 parts, the 2 gaps of length g and the gap of length $h + 2g$. The 2 airgaps between the core and the plunger are important and the gap of length $h + 2g$ is neglected because it is considered fringe field.

The reluctance is

$$\mathcal{R}(x) = \frac{2g}{\mu_0 dw(1 - \frac{x}{w})}, \qquad x \in [0, w)$$

Plugging into the energy equations

$$W(\lambda, x) = \frac{g\varphi^2}{\mu_0 dw(1 - \frac{x}{w})} = \frac{g\lambda^2}{N^2\mu_0 dw(1 - \frac{x}{w})}, \qquad x \in [0, w)$$

and

$$\overline{W}(i, x) = \frac{N^2 i^2 \mu_0 dw(1 - \frac{x}{w})}{4g} \qquad x \in [0, w)$$

The force calculated from the energy is

$$f = -\frac{\partial W}{\partial x} = -\frac{\varphi^2}{2}\frac{d\mathcal{R}(x)}{dx} = -\frac{g\varphi^2}{\mu_0 dw^2(1 - \frac{x}{w})^2}, \qquad x \in [0, w)$$

$$f = \frac{\partial \overline{W}}{\partial x} = -\frac{N^2 i^2 \mu_0 d}{4g}$$

Note the very interesting result. The force when expressed in terms of the current does not depend on the displacement x. Thus, could linearize the actuator here if $\sqrt{i}$ is

commanded instead of i. When expressing the force as a function of the flux or flux-linkage, the force explicitly depends on x and the actuator force is more challenging to control precisely. Also, since the force always reduces the reluctance, the force is generated to pull the plunger towards $x = 0$.

Remark 6. *(Using $f = \frac{\partial W}{\partial x}$)*

Note that it is very important to express the energy as a function of the flux-linkage and position before taking the derivative. If $\lambda = L(x)i$ is substituted into W and then the derivative with respect to x is calculated, one would be differentiating the expression for $L(x)$ also. The product $L(x)i = \lambda$ would not be held constant when calculating the derivative wrt x. Similar remarks could be made about expressing the co-energy in terms of the current and position before taking derivatives wrt x.

Example D.3. *(Electromagnet Force on Target [6])*

Figure D.3 shows a simple electromagnet pulling on a target. Find the force from the energy and co-energy. Do not neglect the reluctance of the core and discuss the consequences.

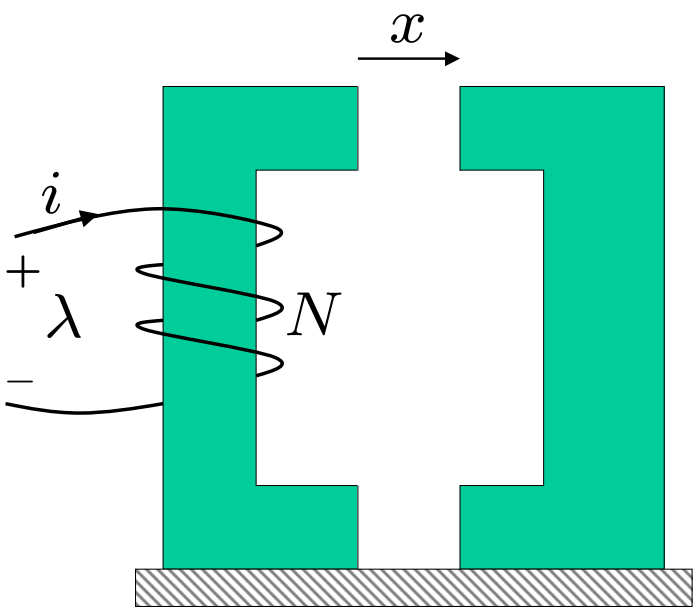

Figure D.7: A simple electromagnet pulling on a ferromagnetic target.

Solution: *The energy $W(\lambda, x)$ and the force are*

$$W(\lambda, x) = \frac{1}{2}\frac{\lambda^2}{L(x)} = \frac{1}{2}\frac{\lambda^2 \mathcal{R}(x)}{N^2}, \qquad f = -\frac{\lambda^2}{2N^2}\frac{d\mathcal{R}(x)}{dx}$$

where the reluctance where $R(x)$ refers to the total reluctance of the circuit. This is

$$\mathcal{R}(x) = R_{\text{core}} + \frac{2x}{\mu_0 A_g}$$

Here, R_{core} is the reluctance of the core when $x = 0$. If the pieces have a mean length of $\ell_c/2$ then the reluctance of the core is

$$\mathcal{R}_{\text{core}} = \frac{\ell_c}{\mu_0 \mu_r A}$$

The reluctance of the core is very small because the core is highly permeable, however, when x is very small, the reluctance of the gap and the core are comparable. Evaluating the energy and force,

$$W(\lambda, x) = \frac{\lambda^2}{2N^2}\Big(\mathcal{R}_{\text{core}} + \frac{2x}{\mu_0 A}\Big)$$

and

$$f = -\frac{\lambda^2}{N_2 \mu_0 A} = -\frac{\varphi^2}{\mu_0 A} \tag{D.18}$$

Note here that the stored energy depends on the reluctance of the core, but the force does not (R_{core} is constant wrt x).

Re-calculating the solution using the co-energy,

$$\begin{aligned}\overline{W}(i, x) &= \frac{1}{2}L(x)i^2 = \frac{1}{2}\frac{N^2 i^2}{\mathcal{R}(x)} \\ &= \frac{N^2 i^2}{2}\frac{1}{\mathcal{R}_{\text{core}} + \frac{2x}{\mu_0 A}}\end{aligned}$$

The force is

$$\begin{aligned}f = \frac{\partial \overline{W}(i, x)}{\partial x} &= \frac{N^2 i^2}{2}\frac{d}{dx}\Big(\mathcal{R}_{\text{core}} + \frac{2x}{\mu_0 A}\Big)^{-1} \\ = -\frac{N^2 i^2}{\mu_0 A}\frac{1}{\Big(\mathcal{R}_{\text{core}} + \frac{2x}{\mu_0 A}\Big)^2} &= -\frac{N^2 i^2}{\mu_0 A}\frac{1}{R(x)^2}\end{aligned} \tag{D.19}$$

Note that here, the force is expressed as a function of x and the reluctance of the core. Note that as $x \to 0$, the force would be infinite if the core reluctance term was neglected. Thus, including the core reluctance will saturate the force as a function of position.

Remark 7. *(Electromagnet Force Saturation)*

Using magnetic co-energy, the saturation of the force with respect to position x in equation (D.19) is explicitly accounted for by the presence of the core reluctance. When $x = 0$, the force is finite for a given current. If one neglected the reluctance, the force in equation (D.19) is unbounded for $x = 0$. Using magnetic energy, the force does not depend on position and equation (D.18) does not make any prediction about the saturation with respect to x. Thus, it appears as if the electromagnet behaves differently depending on how one models the energy storage. One must appreciate that in reality, the force will saturate irrespective to the manner in which it is modelled, because the electromagnet core will eventually saturate for a large enough flux or current excitation. Since the energy and co-energy relationships used to derive the forces above implicitly assume that the core is not in saturation, the forces that are predicted will not saturate. To obtain a more precise model of the force for an electromagnet driven into saturation, one may use equation (D.18) in terms of the flux. However, the flux-based model of the force needs to include a description of the flux saturation with respect to current and position.

Typically, the saturation flux density B_{sat} of a material is known. One considers cross-sectional area of the magnetic circuit to see how much flux it can hold given a saturation flux density. Note that if the cross-sectional area of the magnetic circuit varies, the minimum area determines the maximum flux: $\Phi_{\text{sat}} = B_{\text{sat}} A_{\min}$.

D.3 Energy Analysis of Multiply Excited Systems: Mutual Inductance

Consider systems with several sets of electrical input and mechanical output terminals. A two input system is easily generalized to an n input one. Assume that $x \in \mathbb{R}^3$ for generality. The energy method is generalized in a straight-forward way for application to multiply excited systems. Stored energy is expressed in terms of the flux-linkages or the currents (co-energy) and the mechanical output $x \in \mathbb{R}^3$. The differential stored energy for this two input system is

$$dW(\lambda_1, \lambda_1, x) = i_1(\lambda_1, \lambda_2, x)d\lambda_1 + i_2(\lambda_1, \lambda_2, x)d\lambda_2 - fdx$$

Generally, the currents and force are

$$i_1 = \frac{\partial W(\lambda_1, \lambda_2, x)}{\partial \lambda_1}$$
$$i_2 = \frac{\partial W(\lambda_1, \lambda_2, x)}{\partial \lambda_2}$$
$$f = -\nabla_x W(\lambda_1, \lambda_2, x)$$

Path independence is the key to making the calculation of the stored energy manageable. The best approach is to use a path so that the force term drops out of the integrals. This conveniently occurs when $\lambda_1 = \lambda_2 = 0$ because there is no field. So first, hold these at zero and integrate with respect to the position along a path in $\mathbb{R}^3$. Then hold the position constant ($dx = 0$) and integrate over the fluxes. This composite path is sketched in Figure D.3.

The stored energy is

$$W(\lambda_{10}, \lambda_{20}, x_0) = \int_0^{\lambda_{20}} i_2(\lambda_1 = 0, \lambda_2, x_0)d\lambda_2 + \int_0^{\lambda_{10}} i_1(\lambda_1, \lambda_2 = \lambda_{20}, x_0)d\lambda_1$$

If the relationships between the inductances and currents are assumed linear,

$$\lambda_1 = L_{11}i_1 + L_{12}i_2$$
$$\lambda_2 = L_{21}i_1 + L_{22}i_2$$

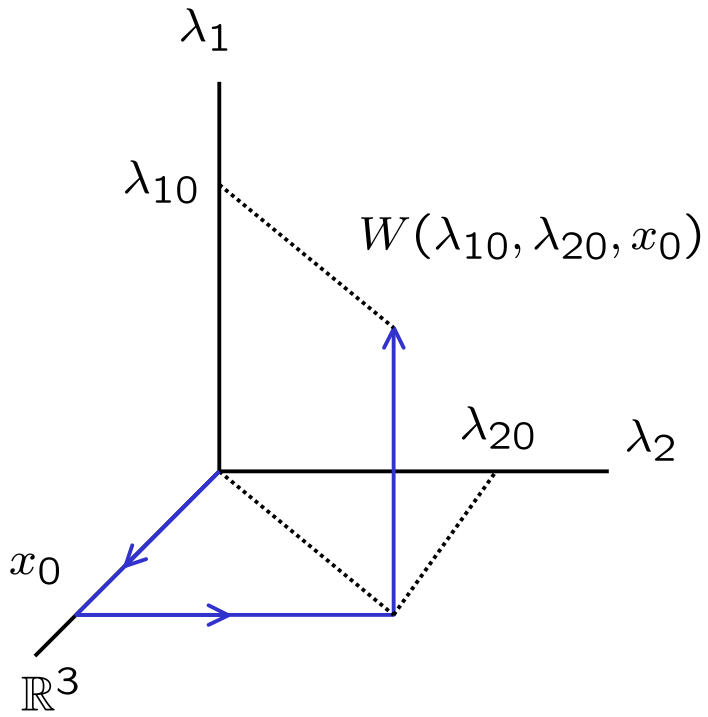

Figure D.8: The path for the line integral evaluation of the stored magnetic energy in multiply excited systems.

with $L_{12} = L_{21} = M$ and M is called the *mutual inductance*. To collect this into matrix form, let $\Lambda, I \in \mathbb{R}^2$ and $L \in \mathbb{R}^{2\times 2}$. Then the linear relationship between the current and flux-linkage is $\Lambda = LI$. Calculating the current $I = L^{-1}\Lambda$ or

$$i_1 = \frac{L_{22}\lambda_1 - L_{12}\lambda_2}{det(L)}, \qquad i_2 = \frac{-L_{21}\lambda_1 - L_{11}\lambda_2}{det(L)}$$

Using these equations, the energy is

$$\begin{aligned} W(\lambda_{10}, \lambda_{20}, x_0) &= \int_0^{\lambda_{20}} \frac{L_{11}\lambda_2}{det(L)} d\lambda_2 + \int_0^{\lambda_{10}} \frac{L_{22}\lambda_1 - L_{12}\lambda_{20}}{det(L)} \lambda_1 \\ &= \frac{L_{11}\lambda_{20}^2}{2det(L)} - \frac{L_{12}\lambda_{10}\lambda_{20}}{det(L)} + \frac{L_{22}\lambda_{10}^2}{2det(L)} \\ &= \frac{1}{2}\lambda^T L^{-1}\lambda \end{aligned}$$

The differential co-energy is

$$d\overline{W}(i_1, i_2, x) = \lambda_1 di_1 + \lambda_2 di_2 + f dx$$

$$\lambda_1 = \frac{\partial \overline{W}(i_1, i_2, x)}{\partial i_1}$$
$$\lambda_2 = \frac{\partial \overline{W}(i_1, i_2, x)}{\partial i_2}$$
$$f = \nabla_x \overline{W}(i_1, i_2, x)$$

By the same line of reasoning, path independence is used find the co-energy.

$$\overline{W}(i_{10}, i_{20}, x_0) = \int_0^{i_{20}} \lambda_2(i_0 = 0, i_2, x_0) di_2 + \int_0^{i_1} \lambda_1(i_1, i_2 = i_{20}, x_0) di_1$$

Using the linear relations for the flux linkage and current,

$$\begin{aligned}\overline{W}(i_1, i_2, x) &= \frac{1}{2} L_{11} i_1^2 + L_{12} i_1 i_2 + \frac{1}{2} L_{22} i_2^2 \\ &= \frac{1}{2} i^T L i\end{aligned}$$

As in the scalar case, the energy and co-energy are related by

$$\begin{aligned}W(\lambda, x) + \overline{W}(1, x) &= \frac{1}{2} \lambda^T L^{-1} \lambda + \frac{1}{2} I^T L I \\ &= \frac{1}{2} I^T L^T L^{-1} L I + \frac{1}{2} I^T L I \\ &= \frac{1}{2} I^T L^T I + \frac{1}{2} I^T L I = I^T L I \\ &= (LI)^T I = \lambda^T I\end{aligned}$$

In multiply excited systems, the energy and force equations are the multidimensional versions of the scalar equations previously found. The fundamental difference in MIMO systems is that one input terminal may affect several output terminals. This is modelled by the mutual inductance. The following proposition and examples serve to familiarize the reader with mutual inductance.

Proposition 9. *(Symmetric Inductance Matrix [6])*

The inductance matrix for a coupled, multi-coil system is always symmetric.

Proof. Suppose a system has two coupled coils. A system with more coils is easily

generalized. It is governed by the linear system

$$\lambda_1 = L_{11}i_1 + L_{12}i_2$$

$$\lambda_2 = L_{21}i_1 + L_{22}i_2$$

Let $\Lambda = [\lambda_1, \lambda_2]^T$ and let $I = [i_1, i_2]^T$. The stored co-energy is $\overline{W} = \frac{1}{2}I^T L I$. Suppose that I is increased from zero to $I = [i_1, i_2]$ and measure the stored energy. Since the integral is path independent, calculate the energy stored for two different paths and set them equal. First, follow path 1: $I = [0, 0] \rightarrow [i_1, 0] \rightarrow [i_1, i_2]$.

$$S_{p1} = \frac{1}{2}L_{11}i_1^2 + L_{12}i_1 i_2 + \frac{1}{2}L_{22}i_2^2$$

Then follow path 2: $I = [0, 0] \rightarrow [0, i_2] \rightarrow [i_1, i_2]$.

$$S_{p2} = L_{21}i_2 i_1 + \frac{1}{2}L_{22}i_2^2 + \frac{1}{2}L_{11}i_1^2$$

Setting these equal gives

$$L_{12} = L_{21} := M$$

□

Example D.4. *(Finding the Mutual Inductance [20])*
The magnetic circuit of Figure D.9 has two windings and two airgaps. The core can be assumed of infinite permeability. The core dimensions are shown in the figure.

(a) Let $i_1 = I_1$ and $i_2 = 0$. Calculate B_1 and B_2 of the airgaps, λ_1 and λ_2 of the coils.

(b) Repeat part (a) however, let $i_2 = I_2$ and $i_1 = 0$.

(c) Repeat part (a) however, let $i_1 = I_1$ and $i_2 = I_2$.

(d) Find the self- and mutual-inductances of the windings.

Solution:

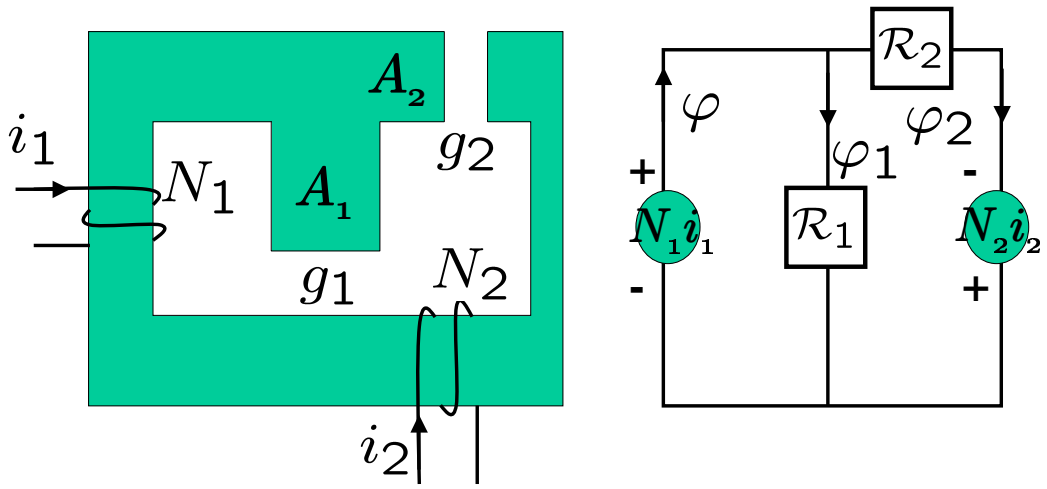

Figure D.9: Problem 1-12 in [20].

(a) Using the equivalent circuit, zero-out the $N_2 i_2$ mmf source and observe that the mmf $N_1 i_1$ is applied directly across $\mathcal{R}_1$ and $\mathcal{R}_2$. Thus,

$$\varphi_1 = \frac{N_1 I_1}{\mathcal{R}_1}, \qquad \varphi_2 = \frac{N_1 I_1}{\mathcal{R}_2}$$

The flux densities are

$$B_1 = \frac{\phi_1}{A_1} = \frac{\mu_0 N_1 I_1}{g_1}, \qquad B_2 = \frac{\phi_2}{A_2} = \frac{\mu_0 N_1 I_1}{g_2}$$

The flux-linkage is

$$\lambda_1 = N_1 \varphi = N_1(\varphi_1 + \varphi_2) \qquad \lambda_2 = N_2 \varphi_2$$
$$= N_1^2 \frac{I_1}{\mathcal{R}_1} + N_1^2 \frac{I_1}{\mathcal{R}_2} \qquad = N_2 N_1 \frac{I_1}{\mathcal{R}_2}$$

(b) With the $N_1 i_1$ voltage source shorted, no flux may flow through $\mathcal{R}_1$ and all of the flux flows through $\mathcal{R}_2$. Thus,

$$\varphi_1 = 0, \qquad \varphi = \varphi_2 = \frac{N_2 I_2}{\mathcal{R}_2}$$

The flux densities are

$$B_1 = 0, \qquad B_2 = \frac{\mu_0 N_2 I_2}{g_2}$$

Finally, the flux linkage is

$$\lambda_1 = N_1\varphi = N_1\varphi_2 = \frac{N_1N_2I_2}{\mathcal{R}_2} \qquad \lambda_2 = N_2\varphi_2 = \frac{N_2^2I_2}{\mathcal{R}_2}$$

(c) The flux-linkages are easily found by superposition

$$\lambda_1 = N_1^2I_1(\mathcal{R}_1||\mathcal{R}_2) + \frac{N_1N_2I_2}{\mathcal{R}_2}$$
$$\lambda_2 = \frac{N_1N_2I_1}{\mathcal{R}_2} + \frac{N_2^2I_2}{\mathcal{R}_2}$$

(d) Define $\lambda = [\lambda_1,\ \lambda_2]^T$ *and* $i = [i_1,\ i_2]^T$. *Then* $\lambda = \mathbf{L}i$ *where* $\mathbf{L}$ *is*

$$\mathbf{L} = \begin{bmatrix} L_1 & M \\ M & L_2 \end{bmatrix}, \qquad L_1 = N_1^2\mathcal{R}_1||\mathcal{R}_2, \qquad L_2 = \frac{N_2^2}{\mathcal{R}_2}, \qquad M = \frac{N_1N_2}{\mathcal{R}_2}$$

Problem 1. *(P1-14 [20]: Solenoid 1 example used as a generator)*
Consider the solenoid of Example D.2, except that it is used as a generator instead of a motor. To do this, excite the airgap field by using a constant current I_0 *through the coil. Wrap another coil of* N_2 *turns around the core in the same direction. The voltage* v_2 *induced at the terminals of this new coil as the plunger is moved is the output of the generator. Assume that the* g *airgaps are constant and both the yoke and the plunger are considered infinite permeability. Note that* $x(t) \in [0, w]$.

(a) find the mutual inductance of the coils as a function of the plunger position.

(b) find the voltage $v_2(t)$ *if* $x(t) = \frac{w}{2}(1 + \epsilon\sin(\omega t))$ *for some* $\epsilon \in (0, 1)$.

To find the inductances, express the flux-linkages in terms of the currents. Using amperes law,

$$\varphi = \frac{N_1i_1 + N_2i_2}{\mathcal{R}(x)}$$

Since $\lambda_1 = N_1\varphi$ *and* $\lambda_2 = N_2\varphi$, *then*

$$\lambda_1 = \frac{N_1^2i_1 + N_1N_2i_2}{\mathcal{R}(x)}$$
$$\lambda_2 = \frac{N_1N_2i_1 + N_2^2i_2}{\mathcal{R}(x)}$$

Thus, the mutual inductance is $M = N_1 N_2/\mathcal{R}(x)$. *Find the open-circuit voltage* v_2 *when* $i_1 = I_0$.

$$\lambda_2(t) = Mi_1 = \frac{N_2 N_1 I_0}{\mathcal{R}(x(t))}$$

where

$$\mathcal{R}(x) = \frac{2g}{\mu_0 dw(1 - \frac{x}{w})}$$

was calculated in Example D.2. Faraday gives the voltage as

$$v_2 = \frac{d\lambda_2}{dt} = -\frac{\mu_0\ dw\ N_2 N_1 I_0}{4g}\ \omega\epsilon\cos(\omega t)$$

APPENDIX E

FILTER CONSTRUCTION

The design of the filters used for signal conditioning is carried out in two programs: Electronics Workbench Multisim 2001 and Ultiboard 2001 (student versions). Multisim is a schematic capture circuit simulation program. This program is very much like Simulink in usage except instead of a block library there is a database of manufacturers parts (thousands of them). Associated with each part is a schematic diagram, a detailed SPICE (a circuit simulation language) model, a footprint of the physical dimensions of the part, and several other parameters. Once the schematic diagram is wired up, one can connect the multimeter (DC measurements), the spectrum analyzer (for frequency response simulation), the function generator, and the oscilloscope virtual instruments just like one uses the scope block in Simulink.

When simulation studies are complete, the design is automatically imported to printed circuit board (PCB) layout program Ultiboard. The footprints from the manufacturer's data is also passed to Ultiboard. The user manually organizes the layout of the components on PCB and then an automatic trace routing program takes over and designs the trace layout. The filters constructed in this work are simple one-sided (one copper side) PCB with through-hole components. However, Ultiboard may has the ability to route up to 32 layer PCBs and use surface mount components. For hobby/workshop use, only boards as complex as a two-sided PCB are practical.

To make the PCB, the copper trace layout is printed with a standard laser printer using a special paper from Pulsar (www.pulsar.gs). The toner transfer paper allows

one to transfer the image directly onto the copper of a raw[1] printed circuit board using a household iron. Pulsar also offers a special applicator machine for high quality image transfers. The plastic in the toner is an etch resistant material. After the toner trace image is transferred to the board, the board is immersed in Ferric Chloride to eat away the exposed copper. The etching time is about 20 minutes with gentle rubbing using a sponge and plastic gloves. The PCB traces are made from the copper that is protected under the toner mask. Once the board is etched, the toner is removed with acetone, the component holes are drilled with a Dremel Drill Press, and the board is sprayed with a green enamel as a protective coating. Finally the components are soldered in place.

The figures below illustrate the process.

[1]This is just a fiberglass board that is completely coated with copper on one or two sides.

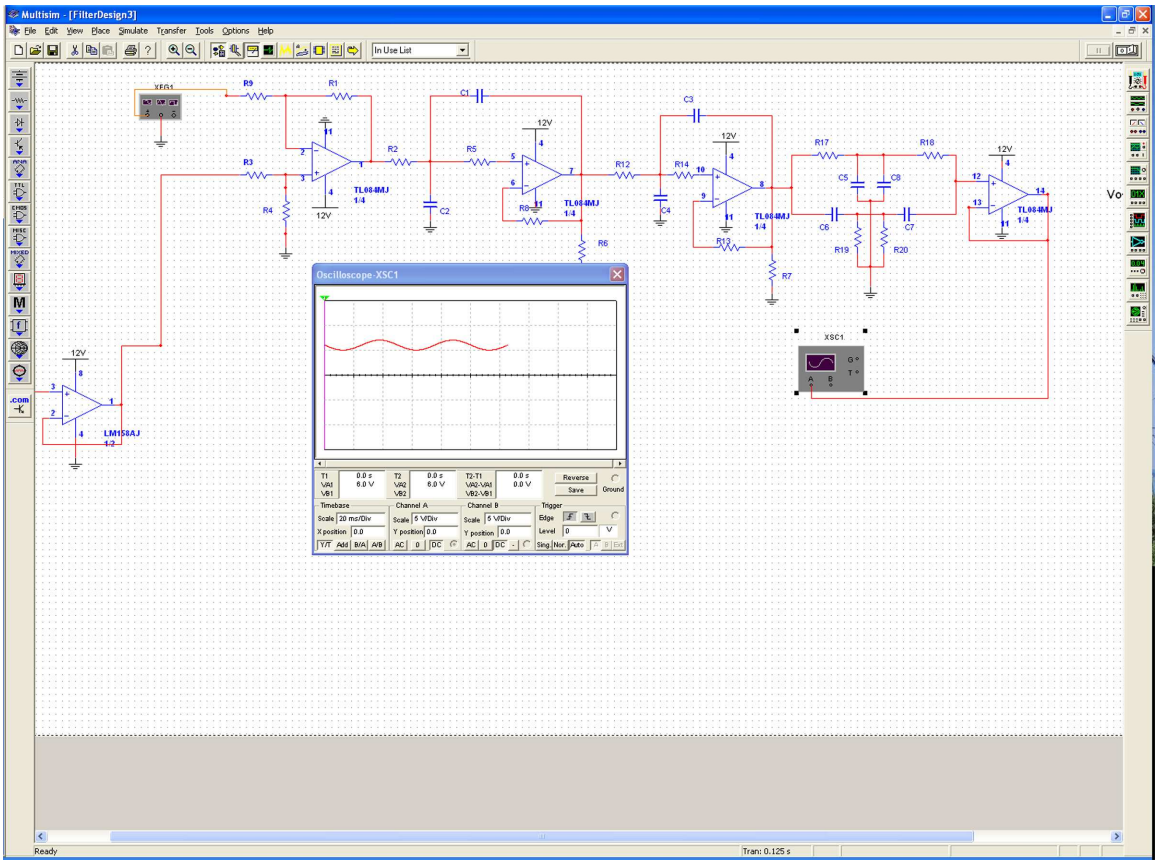

Figure E.1: Multisim is used for the filter design and simulation. The component data base is shown on the left, the instrument selector on the right, the schematic in the background and the oscilloscope readout in the small display.

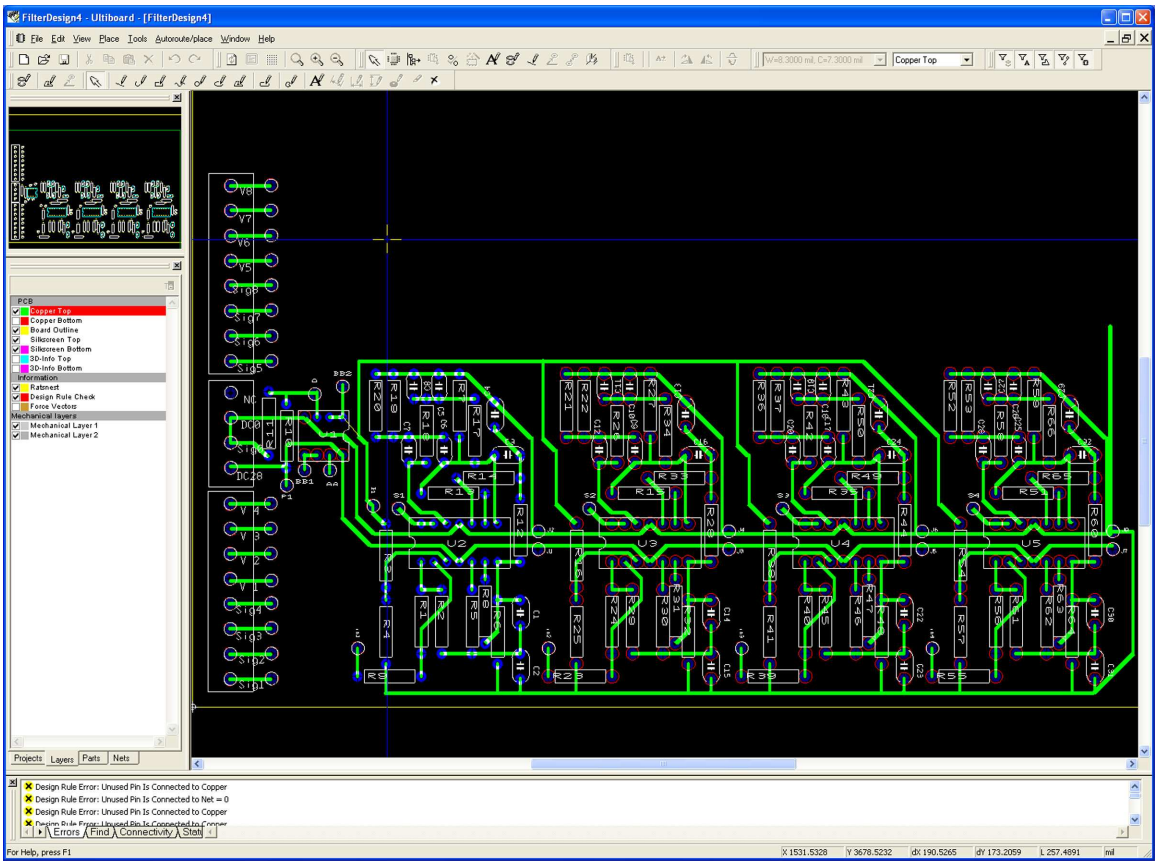

Figure E.2: Ultiboard uses the footprint data from the Multisim component data base to make a Printed Circuit Board Layout. The copper traces are shown in green and the components in white.

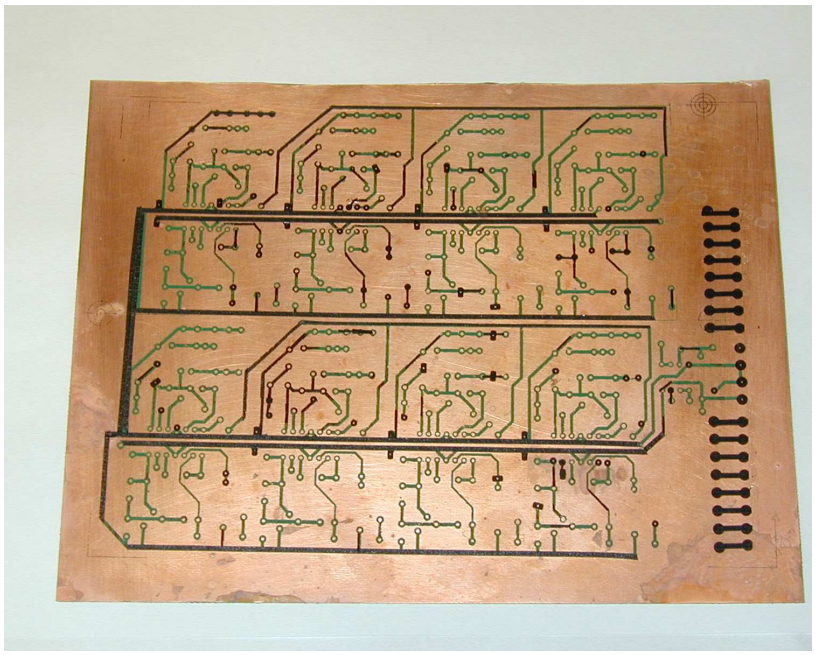

Figure E.3: Using an ordinary household iron, the toner image is transferred from the special Toner Transfer Paper to mask the traces on the raw, copper-clad circuit board. The toner appears in black. On top of the toner is an additional protective green layer to prevent "pitted" traces. Also used are direct rub-on transfer decals to repair any toner traces that have been damaged or did not transfer. This board is now ready to be immersed into the Ferric Chloride etchant.

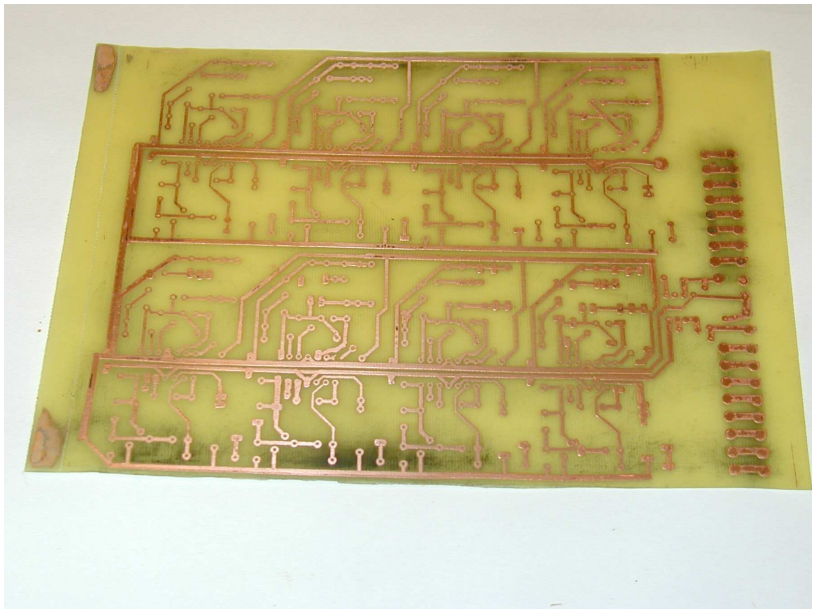

Figure E.4: The etched printed circuit board. This board is now ready for drilling. Five large drill holes will be added to accommodate the PCB standoff posts used when mounting the board.

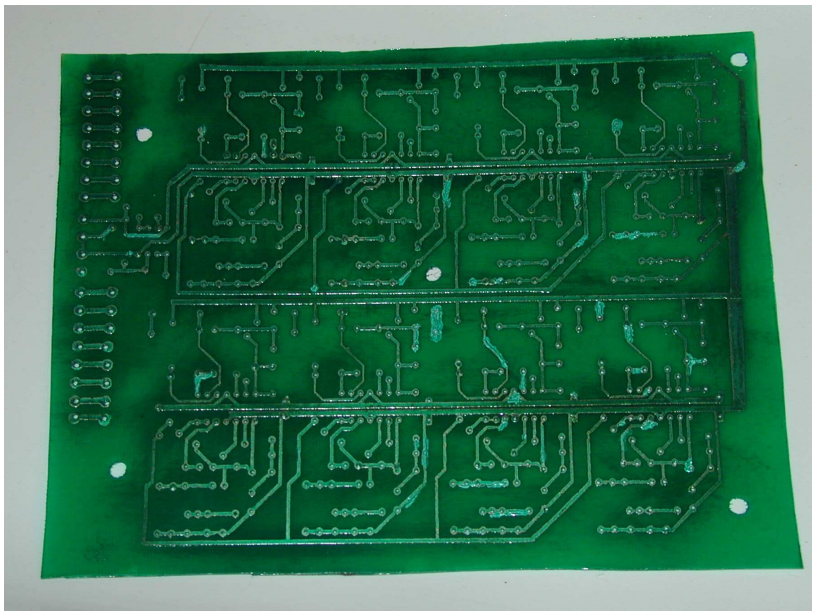

Figure E.5: After drilling the component holes, the board is sprayed with a green enamel. This acts as an insulator and also as a solder mask. It also gives the board a professional look. At this point, one could apply another toner transfer to the board, called the silkscreen layer. This outlines the locations of the parts and acts as a placement guide.

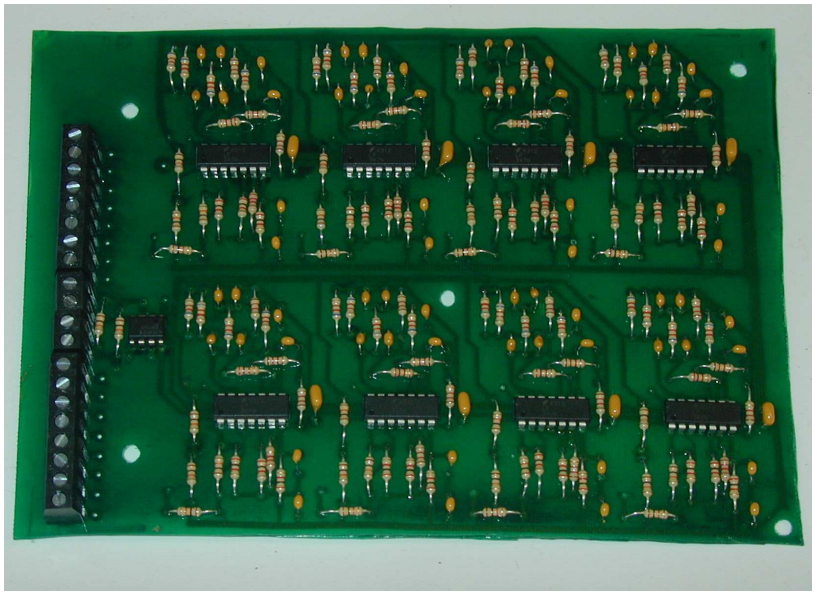

Figure E.6: This is the finished board. All that needs to be done is mount it in the amplifier box and wire the power, ground, input and output. These signals come into the terminal block on the left of the board. The bias reference voltage is set by the LM358 amplifier on the left. Each LF347 chip (the longer chips) holds 4 opamps and implements, along with the components above and below it, one filter. Eight filter circuits are implemented on one board.

REFERENCES

[1] Baloh, M., *Time-Varying Feedback Linearization of Magnetic Bearing Actuators*. PhD thesis, University of Virginia, 2001.

[2] Barnes, L., Hardin, J., Gross, C. A., and Wasson, D., "An eddy current braking system," in *(25th) Southeastern Symposium on System Theory*. Tuscaloosa, AL.

[3] Bartle, R. G., *Elements of Real Analysis*. New York, NY: John Wiley and Sons, 1976.

[4] Bornstein, K., "Dynamics load capabilities of active electromagnetic bearings," *Transactions of the ASME Journal of Tribology*, vol. 113, pp. 598–603, 1991.

[5] Bowler, M. E., "Flywheel energy systems: Current status and future prospects," in *Magnetic Material Producers Association Joint Users Conference*. Michael E. Bowler is Vice-President-Manufacturing Trinity Flywheel Power Systems Inc., San Francisco, CA.

[6] Brown, D. and Hamilton III, E. P., *Electromechanical Energy Conversion*. Macmillian Publishing Company.

[7] Charara, A. and Caron, B., "Magnetic bearing: Comparison between linear and nonlinear functioning," in *Proceedings of the 3rd International Symposium on Magnetic Bearings*, pp. 451–463, 1992.

[8] Charara, A., De Miras, J., and Caron, B., "Nonlinear control of a magnetic levitation system without premagetization," *IEEE Transactions on Control Systems Technology*, vol. 4, pp. 513–523, Sept. 1996.

[9] Chellaboina, V. and Haddad, W. M., "A unification between partial stability and stability theory for time-varying systems," *IEEE Control Systems Magazine*, vol. 22, pp. 66–75, 2002.

[10] Cho, D., Kato, Y., and Spilman, D., "Sliding mode and classical controllers in magnetic levitation systems," *IEEE Control Systems Magazine*, vol. 14, no. 2, pp. 4–12, 1994.

[11] Coren, R. L., *Basic Engineering Electromagnetics an Applied Approach*. Englewood Cliffs, NJ: Prentence-Hall, Inc., 1989.

[12] Costic, B. T., de Queiroz, M. S., Dawson, D. M., and Fang, Y., "Energy management and attitude control strategies using flywheels," in *Proceedings of the 40th IEEE Conference on Decision and Control*, pp. 2639–2643, Dec. 2001. Orlando, FL.

[13] Costic, B. T., de Queiroz, M. S., and M., D. D., "A new learning control approach to the active magnetic bearing benchmark system," in *Proceedings of the American Control Conference*, pp. 2639–2643, 2000. Chicago, IL.

[14] Darling, J. and Burrows, C. R., "The control of propeller-induced vibrations in ship transmission shafts," in *Proceedings of the 2nd International Symposium on Magnetic Bearings*. Tokyo, Japan.

[15] de Queiroz, M. S. and Dawson, D. M., "Nonlinear control of active magnetic bearings: A backstepping approach," *IEEE Transactions on Control Systems Technology*, vol. 4, pp. 545–552, Sept. 1996.

[16] de Queiroz, M. S., Dawson, D. M., and Canbolat, H., "A backstepping-type controller for a 6-dof active magnetic bearing system," in *Proceedings of the 35th IEEE Conference on Decision and Control*, pp. 3370–3375, 1996.

[17] Dussaux, M., "The industrial applications of active magnetic bearing technology," in *Proceedings of the 2nd International Symposium on Magnetic Bearings*, pp. 33–38, 1990.

[18] El Rifai, M. O. and Youcef-Toumi, K., "Achievable performance and design trade-offs in magnetic levitation control," in *1998 5th International Workshop on Advanced Motion Control. Proceedings*, pp. 586–591, 1998. Coimbra, Portugal.

[19] Fausz, J., "Control issues in simultaneous attitude control and energy storage." Air Force Research Labs Summer Seminar Series on Structures and Control., June 2001.

[20] Fitzgerald, A. E., Kingsley Jr., C., and Umans, S. D., *Electric Machinery*. New York, NY: McGraw-Hill, Inc., fifth ed., 1990.

[21] Franklin, G. F., Powell, J. D., and Emami-Naeini, A., *Feedback Control of Dynamic Systems*. Upper Saddle River, NJ: Prentence-Hall, Inc., fourth ed., 2002.

[22] Ghosh, J., Mukherjee, D., M., B., and Paden, B., "Nonlinear control of a benchmark beam balance experiment using variable hyperbolic bias," in *Proceedings of the American Control Conference*, pp. 2149–2153, 2000. Chicago, IL.

[23] Herbner, R., Beno, J., and Walls, A., "Flywheel batteries come around again," *IEEE Spectrum*, pp. 46–51, Apr. 2002.

[24] Higuchi, T., Horikoshi, A., and Komori, T., "Development of an actuator for super clean rooms and ultra high vacua," in *Proceedings of the 2nd International Symposium on Magnetic Bearings*, pp. 115–122, July 1990. Tokyo, Japan.

[25] Horowitz, P. and Hill, W., *The Art of Electronics*. Cambridge Press, second ed., 1980.

[26] Howe, D., Mason, P., Mellor, P. H., Wu, Z. Y., and Atallah, K., "Flywheel peak power buffer for electic/hybrid vehicles," in *Proceedings of Electric Machines and Drives Conference*, pp. 508–510, May 1999. Seattle, WA.

[27] Ioannou, P. A. and Sun, J., *Robust Adaptive Control*. Upper Saddle River, NJ: Prentence-Hall, Inc., 1996.

[28] Isidori, A., *Nonlinear Control Systems*. Communication and Control Engineering, New York, NY: Springer-Verlag, third ed., 1995.

[29] Isidori, A., *Nonlinear Control Systems II*. Communication and Control Engineering, New York, NY: Springer-Verlag, 1999.

[30] Johnson, D., *Alternative Operating Modes for Magnetic Bearing Control*. PhD thesis, State University of New York at Buffalo, 1995.

[31] Johnson, D., Brown, G. V., and Inman, D. J., "Adaptive variable bias magnetic bearing control," in *Proceedings of the American Control Conference*. Philadelphia, PA.

[32] Keith, F. J., *Implicit Flux Feedback Control for Magnetic Bearings*. PhD thesis, University of Virginia, 1993.

[33] Kenny, A., *Nonlinear Electromagnetic Effects on AMB Performance and Power Losses*. PhD thesis, Texas A and M University, 2001.

[34] Khalil, H. K., *Nonlinear Systems. Second Edition*. Upper Saddle River, NJ: Prentence-Hall, Inc., 1996.

[35] Knospe, C., "The nonlinear control benchmark experiment," in *Proceedings of the American Control Conference*, pp. 2134–2138, 2000. Chicago, IL.

[36] Knospe, C., Markert, R., Fittro, R., Hoffmann, K., and Laier, D., "Control aspects of active magnetic bearings," in *14th Triennial IFAC World Congress*, pp. 418–423, July 1999. Beijing, China.

[37] Knospe, C. and Yang, C., "Gain-scheduled control of a magnetic bearing with low bias flux," in *Proceedings of the 36th IEEE Conference on Decision and Control*, pp. 418–423, 1997.

[38] Knospe, C. R. and Collins, E. G., "Introduction to the special issue on magnetic bearing control," *IEEE Transactions on Control Systems Technology*, vol. 4, no. 5, pp. 481–483, 1996.

[39] Knospe, C. R. and Fittro, R. L., "Control of a high speed milling spindle via mu-synthesis," in *Proceedings of the 1997 IEEE International Conference on Control Applications*, pp. 912–917, 1997. Hartford, CT.

[40] Knospe, C. R., Hope, R. W., Fedigan, S. J., and Williams, R. D., "Experiments in the control of unbalance response using magnetic bearings," *Mechatronics*, vol. 5, no. 4, pp. 385–400, 1995.

[41] Knospe, C. R., Hope, R. W., Tamer, S. M., and Fedigan, S. J., "Robustness of adaptive unbalance control of rotors with magnetic bearings," *Journal of Vibration and Control*, vol. 2, no. 1, pp. 33–52, 1996.

[42] Knospe, C. R. and Humphris, R. R., "Control of unbalance response with magnetic bearings," in *Proceedings of the American Control Conference*, pp. 211–215, 1992. Chicago, IL.

[43] Krstić, M., Kanellakopoulos, I., and Kokotović, P., *Nonlinear and Adaptive Control Design*. Series on Adaptive and Learning Systems for Signal Processing, Communications, and Control, New York, NY: Wiley-Interscience, 1995.

[44] Kubota, T. and Youcef-Toumi, K., "Limitation of linear controllers for the precision magnetic bearing with uncertainties," in *Proceedings of the American Control Conference*, pp. 2224–2228, June 1998. Philidelphia, PA.

[45] Lévine, J., Lottin, J., and Ponstart, J. C., "A nonlinear approach to the control of magnetic bearings," *IEEE Transactions on Control Systems Technology*, vol. 4, pp. 524–544, Sept. 1996.

[46] Li, L., "Linearizing magnetic bearing actuators by constant current sum, constant voltage sum, and constant flux sum," *IEEE Transactions on Magnetics*, vol. 35, pp. 528–535, Jan. 1999.

[47] Li, L. and Mao, J., "Feedback linearization of magnetic bearing actuators for a uniform upper bound of force slew rate," in *IEE Proceedings of Electric Power Applications*, vol. 146, pp. 378 –382, July 1999.

[48] Li, L., Shinshi, T., and Shimokohbe, A., "Asymptotically exact linearizations for active magnetic bearing actuators in voltage control configuration," *IEEE Transactions on Control Systems Technology*, vol. 11, pp. 528–535, Mar. 2003.

[49] Lin, Z. and Knospe, C., "A saturated high gain control for a benchmark experiment," in *Proceedings of the American Control Conference*, pp. 2644–2648, June 2000. Chicago, Illinois.

[50] Lottin, J., Mouille, P., and Ponsart, J. C., "Nonlinear control of active magnetic bearings," in *Proceedings of the 4th International Symposium on Magnetic Bearings*, pp. 101–106, Aug. 1994.

[51] Lozano, R., Brogilato, B., Egeland, O., and Maschke, B., *Dissipative Systems Analysis and Control Theory and Applications*. Communication and Control Engineering, London, England: Springer-Verlag, 2000.

[52] Maslen, E., "Magnetic bearings." Notes on Magnetic Bearings, University of Virginia, Jan. 1999.

[53] Maslen, E., Herman, P., Scott, M., and Humphris, R., "Practical limits to the performance of magnetic bearings: Peak force, slew rate, and displacement sensitivity," *Transactions of the ASME Journal of Tribology*, vol. 111, pp. 331–336, 1989.

[54] Matsumura, F. and Kobayashi, H., "Fundamental equation for horizontal shaft magnetic bearing and its control system design," *Electrical Engineering in Japan*, vol. 101, no. 3, pp. 123–130, 1981.

[55] Mittal, S. and Menq, C., "Precision motion control of a magnetic sspension actuator using a robust nonlinear compensation scheme," *IEEE/ASME Transactions on Mechatronics*, vol. 2, pp. 268–280, Dec. 1997.

[56] Mohamed, A. M. and Emad, F. P., "Nonlinear oscillations in magnetic bearing systems," *IEEE Transactions on Automatic Control*, vol. 38, no. 8, pp. 1242–1245, 1993.

[57] Nijmeijer, H. and van der Schaft, A. J., *Nonlinear Dynamical Control Systems*. New York, NY: Springer-Verlag, 1990.

[58] Ogata, K., *Discrete-Time Control Systems*. Upper Saddle River, NJ: Prentence-Hall, Inc., second ed., 1995.

[59] Ogata, K., *Modern Control Engineering*. Upper Saddle River, NJ: Prentence-Hall, Inc., fourth ed., 2002.

[60] Ortega, R., Loría, A., Nicklasson, P. J., and Sira-Ramírez, H., *Passivity Based Control of Euler-Lagrange Systems: Mechanical, Electrical and Electromechanical Applications*. Communication and Control Engineering, London, England: Springer-Verlag, 1998.

[61] Ota, M., Andoh, S., and Inoue, H., "Mag-lev semiconductor wafer transporter for ultra-high-vacuum environment," in *Proceedings of the 2nd International Symposium on Magnetic Bearings*, pp. 109–114, July 1990. Tokyo, Japan.

[62] Pichot, M. A., Kajs, J. P., Murphy, B., Ouroua, A., Rech, B. M., Hayes, R. J., Beno, J. H., Buckner, G. D., and Palazzolo, A. B., "Active magnetic bearing designs for energy storage systems for combat vehicles," *IEEE Transactions on Magnetics*, vol. 37, no. 1, pp. 318–323, 2001.

[63] Praly, L., d'Andréa-Novel, B., and Coron, J. M., "Lyapunov design of stabilizing controllers for cascaded systems," *IEEE Transactions on Automatic Control*, vol. 36, no. 10, pp. 1177–1181, 1991.

[64] Rao, D., "Precision magnetic bearing systems final report for contract no. f29601-97-c-0044," tech. rep., Precision Magnetic Bearing Systems, 36 Green Mountain Drive, Cohoes, NY 12047, 2000.

[65] Richie, D., Tsiotras, P., and Fausz, J., "Flywheel simultaneous attitude control and energy storage using a vscmg configuration," in *Proceedings of the 2000 IEEE International Conference on Control Applications*, pp. 991 –995, Sept. 2000. Ancorage, Alaska, USA.

[66] Richie, D., Tsiotras, P., and Fausz, J., "Simultaneous attitude control and energy storage using vscmgs: Theory and simulation," in *Proceedings of the American Control Conference*, vol. 5, pp. 3973 –3979, 2001.

[67] Richie, D., Tsiotras, P., and Fausz, J., "Variable speed control moment gyroscope workbench: a new simulation tool for tomorrow's spacecraft," in *20th Digital Avionics Systems Conference*, vol. 2, pp. 497–508, Oct. 2001.

[68] Scherpen, J. M. A., van der Kerk, B., Klaassens, J. B., Lazeroms, M., and Kan, S., "Nonlinear control for magnetic bearings in deployment test rigs: Simulation and experimental results," in *Proceedings of the 37th IEEE Conference on Decision and Control*, pp. 2613–2618, 1998. Tampa, FL.

[69] Sepulchre, R., Janković, M., and Kokotović, P., *Constructive Nonlinear Control*. Communication and Control Engineering, London, England: Springer-Verlag, 1997.

[70] Siegwart, R., Larsonneur, R., and Traxler, A., "Design and performance of a high speed milling spindle in digitally controlled active magnetic bearings," in *Proceedings of the 2nd International Symposium on Magnetic Bearings*. Tokyo, Japan.

[71] Siegwart, R. and Traxler, A., "Performance and limits of amb-actuators illustrated on an electromagnetically suspended milling spindle," in *Proceedings of the Intersociety Energy Conversion Engineering Conference*, vol. 3, pp. 494–499.

[72] Sivrioglu, Nonami, K., Kubo, A., and Takahata, R., "Nonlinear adaptive control of a flywheel rotor-amb system with unknown parameter," in *Proceedings of the 8th International Symposium on Magnetic Bearings*, pp. 593–598, Aug. 2002. Mito, Japan.

[73] Smith, R. D. and Weldon, W. F., "Nonlinear control of a rigid rotor magnetic bearing system: Modeling and simulation with full state feedback," *IEEE Transactions on Magnetics*, vol. 31, pp. 973–980, Mar. 1995.

[74] Sontag, E. D., "A universal consruction of artstein's theorem on nonlinear stabilization," *Systems and Control Letters*, vol. 13, pp. 117–123, 1989.

[75] Teel, A. and Arcak, M., Aug. 2000. private communication.

[76] Tomizuka, M., "Zero phase error tracking algorithm for digital control," *ASME Journal of Dynamic Systems, Measurement, and Control*, vol. 109, pp. 65–68, 1987.

[77] Torries, M., Sira-Ramirez, H., and Escobar, G., "Sliding mode nonlinear control of magnetic bearings," in *Proceedings of the 1999 IEEE International Conference on Control Applications*, pp. 743–748, 1999.

[78] Troung, L. V., Wolff, F. J., and Dravid, N. V., "Simulation of flywheel electrical system for aerospace applications," in *Proceedings of 35th Intersociety Energy Conversion Engineering Conference*, July. Las Vegas, NV.

[79] Trumper, D. L., Weng, M. C., and Ritter, R. J., "Magnetic suspension and vibration control of beams for non-contact processing," in *Proceedings of the 1999 IEEE International Conference on Control Applications*, pp. 551–557, 1999. Kohala Coast Island, Hawaii.

[80] Tsiotras, P. and Arcak, M., "Low-bias control of amb subject to voltage saturation: State-feedback and observer designs," in *Proceedings of the 41st IEEE Conference on Decision and Control*, pp. 2474–2479, Dec. 2002. Las Vegas, NV.

[81] Tsiotras, P. and Velenis, S., "Low-bias control of amb's subject to saturation constraints," in *Proceedings of the 2000 IEEE International Conference on Control Applications*, pp. 138–143, Sept. 2000. Anchorage, Alaska.

[82] Tsiotras, P. and Wilson, B. C., "Zero- and low-bias control designs for active magnetic bearings," *IEEE Transactions on Control Systems Technology*, vol. 11, pp. 889–904, Nov. 2003.

[83] Tsiotras, P., Wilson, B. C. D., and Bartlett, R., "Control of a zero-bias magnetic bearing using control lyapunov functions," in *Proceedings of the 39th IEEE Conference on Decision and Control*, pp. 4048–4053, 2000. Sidney, Austraila.

[84] Undisclosed, "Models 412, 413, 421, 422, 423, 432 dc brush servo amplifiers," tech. rep., Copley Controls Corp., 2002. Data sheet available at http://www.copleycontrols.com.

[85] Undisclosed, "Models 5121, 5131, 5211, 5221, 5231, 5321 dc brushless servo amplifiers," tech. rep., Copley Controls Corp., 2002. Data sheet available at http://www.copleycontrols.com.

[86] Vorotnikov, V. I., *Partial Stability and Control*. Boston, MA: Birkhäuser, 1988.

[87] Weiler, E. J., "Nasa space sciences stragetic plan," tech. rep., NASA Space Science Enterprise, 2000.

[88] Williams, A. B. and Taylor, F. J., *Electronic Filter Design Handbook*. New York, NY: McGraw-Hill, Inc., third ed., 1995.

[89] Wouterse, J. H., "Critical torque and speed of eddy current brake with widely separated soft iron poles," in *IEE Proceedings B (Electric Power Applications)*, vol. 138, pp. 153–158, July 1991.

[90] Yang, C. and Knospe, C., "Optimal control of a magnetic bearing without bias flux," in *Proceedings of the American Control Conference*, pp. 1534–1538, June 1997. Albuquerque, NM.

[91] Yang, C., Knospe, C., and Tsiotras, P., "Optimal control of a magnetic bearing without bias flux using finite voltage," *Optimal Control Applications and Methods*, vol. 19, pp. 227–246, 1998.

[92] Yea, T. J. and Youcef-Toumi, K., "Achievable performance of magnetically levitated rotating machines," in *13th Triennial IFAC World Congress*, pp. 451–456, 1996. San Francisco, CA.

[93] Youcef-Toumi, K. and Reddy, S., "Dynamic analysis and control of high speed and high precision active magnetic bearings," *ASME Journal of Dynamic Systems, Measurement, and Control*, vol. 114, pp. 623–632, 1992.

VITA

Brian Christopher David Wilson was born in Buffalo, NY, 1973. He received a B.S. degree in electrical engineering from SUNY Buffalo in 1996 and a Masters degree in electrical engineering for the Georgia Institute of Technology (Georgia Tech), Atlanta, in 1998.

In the summer of 2001, he participated in the Air Force Research Labs Space Scholars Program at Kirtland AFB, NM. He is currently a Ph.D. candidate with the School of Electrical and Computer Engineering at Georgia Tech. His current research interests include analytical dynamics, nonlinear control theory, electromechanical machines, active magnetic bearings, and electronic instrumentation.